

# THE ENVIRONMENT OF GALAXIES AND GROUPS OF GALAXIES

Owain Snaith

A THESIS SUBMITTED IN PARTIAL FULFILMENT  
OF THE REQUIREMENTS FOR THE DEGREE OF  
DOCTOR OF PHILOSOPHY

Jeremiah Horrocks Institute for Astrophysics and Supercomputing  
University of Central Lancashire

May 2011

# Declaration

The work presented in this thesis was carried out in the Jeremiah Horrocks Institute for Astrophysics and Supercomputing, University of Central Lancashire.

I declare that while registered as a candidate for the research degree, I have not been a registered candidate or enrolled student for another award of the University or other academic or professional institution.

I declare that no material contained in the thesis has been used in any other submission for an academic award and that the thesis solely my own work.

Parts of this thesis are undergoing revision with Monthly Notices of the Royal Astronomical Society at the time of writing - specifically Chapter 5, Chapter 1 section 4 and parts of Chapter 2, etc. Some changes have been made to the text of the paper as of writing, but some passages remain the same.

# Abstract

## Abstract

In this thesis, we employ two numerical tools - semi-analytical models and N-body plus hydrodynamical simulations of large scale structure and individual galaxies - to explore the underlying physics governing the formation and evolution of groups of galaxies, and the role of environment in generating polar structures around disk galaxies.

Using phenomenological models of baryonic physics imposed upon large-scale dissipationless simulations of the Universe, semi-analytic models (SAMs) are one of the principal methods used to model large samples of model galaxies. We sought to examine the properties of groups of galaxies with a range of densities using SAMs applied specifically to the industry-standard Millennium Run; for this work, we make use of the well-known Munich and Durham models, and their descendants.

We are especially interested in how group properties change as we change the linking length of our Friends-of-Friends group finder. We compare the group populations and richness in these models and compare them both with observations and high-resolution N-body simulations. This leads us to the conclusion that the Durham models produce a much larger population of compact objects than the Munich models. We also explore the group dynamics and morphology as a function of density.

We compare the luminosity distributions of galaxy groups using publicly available SAMs in order to explore the group environment. We find a characteristic “wobble” in the group galaxy luminosity function in the De Lucia et al. (2006) model that is not present in the Durham models, the former of which is consistent with observations. When we explore the magnitude gap distribution between

first- and second-ranked galaxies, we find a turnover in the De Lucia et al. model that is not present in either the Durham models or the observations.

We interpret the above observations in terms of the different galaxy lifetimes in the two models and find that there is a longer-lived galaxy population in the Durham models than exists in the Munich models.

We next examine the properties of a polar disc galaxy simulated using cosmological initial conditions with the gravitational N-body/hydrodynamical code **GASOLINE**. We found a noticeable “kink” aligned with the major axis of the dark matter halo at the radius of the inner galaxy disc, due to the dominance of stars. This is not visible in the dark matter halos of more traditional galaxies. We also note that the angle of the minor axis of the dark halo then aligns to the polar disc and remains tightly correlated out to the virial radius. We also identify the last major merger as being responsible for the polar disc shape, as the angular momentum of the interaction is perpendicular to the angular momentum of the inflowing gas.

# Contents

<b>Declaration</b>	<b>2</b>
<b>Abstract</b>	<b>3</b>
<b>Acknowledgements</b>	<b>23</b>
<b>1 INTRODUCTION</b>	<b>24</b>
1.1 Description of content . . . . .	26
1.2 Structure formation . . . . .	27
1.3 Numerical Methods . . . . .	31
1.3.1 Initial Conditions . . . . .	31
1.3.2 N-body Codes . . . . .	33
1.3.3 Hydrodynamics with GASOLINE . . . . .	36
1.3.4 Halo finding . . . . .	39
1.4 Semi-analytic Models . . . . .	41
1.4.1 Merger Trees . . . . .	41
1.4.2 Description of the Models . . . . .	42
1.4.3 Durham Models: Bower et al. (2006; D_B06); Font et al. (2008; D_F08) . . . . .	46
1.4.4 Munich Models: De Lucia et al. (2006; M_D06); Bertone et al. (2007; M_B07) . . . . .	47

1.5	N-body data . . . . .	50
1.6	Types of Group & Observational Data. . . . .	50
1.6.1	Loose groups . . . . .	51
1.6.2	Tucker et al. (2000) . . . . .	52
1.6.3	Yang et al. (2007,2008) . . . . .	53
1.6.4	Tago et al. (2008; T08); Tago et al. (2010; T10) . . . . .	54
1.6.5	Compact Groups . . . . .	55
1.6.6	Barton et al. (1996) . . . . .	56
1.6.7	Allam et al. (2002) . . . . .	57
<b>2</b>	<b>DISTRIBUTION AND RICHNESS OF GROUPS</b>	<b>58</b>
2.1	Introduction . . . . .	58
2.2	Group Finding Algorithm and the construction of group catalogues for the present work. . . . .	59
2.2.1	Synthetic group catalogues . . . . .	60
2.3	Global properties . . . . .	63
2.3.1	Spatial Distribution . . . . .	63
2.3.2	Group Richness . . . . .	70
2.4	Correlation Functions of Groups . . . . .	73
2.5	Summary . . . . .	78
<b>3</b>	<b>GROUP PROPERTIES</b>	<b>80</b>
3.1	Introduction . . . . .	80
3.2	Group Properties . . . . .	81
3.2.1	Harmonic Radius . . . . .	81
3.3	Velocity Dispersion . . . . .	86
3.4	Crossing time . . . . .	89
3.5	Group Types . . . . .	91

3.6	Galaxy distribution . . . . .	94
3.7	Group Shape . . . . .	96
3.8	Environment of Groups . . . . .	104
3.8.1	Observations . . . . .	108
3.8.2	Correspondences . . . . .	108
3.9	Conclusion . . . . .	113
<b>4</b>	<b>BRIGHTEST CLUSTER GALAXIES</b>	<b>114</b>
4.1	Introduction . . . . .	114
4.2	Method . . . . .	116
4.3	Results . . . . .	118
4.3.1	Identifying clusters . . . . .	118
4.3.2	Subhalo . . . . .	118
4.3.3	Most Massive Cluster Members . . . . .	122
4.4	In the SDSS survey . . . . .	124
4.5	Discussion & Conclusion . . . . .	125
<b>5</b>	<b>LUMINOSITY FUNCTIONS</b>	<b>128</b>
5.1	Introduction . . . . .	128
5.2	Luminosity Function of FoF Groups . . . . .	130
5.3	In SAMs . . . . .	135
5.4	Conditional Luminosity Function . . . . .	136
5.5	Magnitude Gap . . . . .	144
5.6	Satellite-Satellite Mergers . . . . .	152
5.7	Conclusions . . . . .	153
<b>6</b>	<b>MERGER TREES</b>	<b>156</b>
6.1	Introduction . . . . .	156
6.2	Calculating Merging times . . . . .	157

6.2.1	Munich . . . . .	157
6.2.2	Durham . . . . .	158
6.3	Dynamical Friction Time . . . . .	158
6.3.1	Munich . . . . .	158
6.3.2	Durham . . . . .	159
6.4	Method . . . . .	160
6.5	Merging times . . . . .	165
6.5.1	Merged galaxies . . . . .	165
6.5.2	Satellite galaxies . . . . .	165
6.6	Conclusion . . . . .	168
<b>7</b>	<b>POLAR DISC GALAXY</b>	<b>169</b>
7.1	Introduction . . . . .	169
7.1.1	Motivation . . . . .	171
7.1.2	Simulation . . . . .	172
7.1.3	Orientation of the disc . . . . .	174
7.2	Polar disc galaxy . . . . .	176
7.3	Evolution of discs . . . . .	178
7.4	Star formation . . . . .	179
7.4.1	SFR . . . . .	179
7.4.2	Metallicity . . . . .	183
7.4.3	Stellar Age . . . . .	185
7.4.4	Summary . . . . .	186
7.5	Halo Shape . . . . .	187
7.5.1	Introduction . . . . .	187
7.5.2	Inertial Tensor . . . . .	188
7.5.3	Halo Shape . . . . .	189
7.5.4	Halo Alignment . . . . .	190

7.5.5	Comparison with the observers approach. . . . .	191
7.5.6	Evolution of the Halo Shape . . . . .	193
7.5.7	Comparison With A Standard Disc Galaxy . . . . .	197
7.5.8	Conclusion . . . . .	197
7.6	Angular Momentum . . . . .	199
7.6.1	Introduction . . . . .	199
7.6.2	Evolution of the angular momentum of the gas, dark matter and stars . . . . .	200
7.7	Formation process . . . . .	204
7.7.1	Tracing gas . . . . .	204
7.7.2	Last major merger . . . . .	204
7.7.3	Angular momentum of the infalling gas . . . . .	206
7.8	Summary & Further Work . . . . .	210
<b>8</b>	<b>CONCLUSIONS</b>	<b>211</b>
<b>9</b>	<b>FUTURE WORK</b>	<b>218</b>
	<b>References</b>	<b>220</b>

# List of Tables

2.1	Summary of the SAM models and their basic differences . . . . .	59
2.2	The best fit polynomials for the changing spatial density of groups with linking length. . . . .	67
2.3	The number of galaxy groups in M_D06 and D_B06 and T10 as a function of linking length. The numbers in each column are for the different luminosity cuts. The order quoted is where the r-band magnitude is: $< -18$ , $< -19$ , $< -20$ , respectively. . . . .	69
2.4	The mean group richness for each model at the different linking lengths. The number in brackets indicates the variation in different subvolumes. The ‘*’ specifies that loose groups in Tago et al. (2010) corresponds to $l = 250h^{-1}\text{kpc}$ with a -18 mag cut instead of the number quoted in the first column. The T10 column also shows the mean number of galaxies per group at each linking length. Errors in the T10 column are of the form $\sigma/\sqrt{N}$ . . . . .	71
2.5	Best fit formulae for the correlation function shown in Fig. 2.5 . .	78
2.6	Best fit formulae for the correlation function shown in Fig. 2.5, with slope set to a canonical -1.8. . . . .	78
3.1	The median and standard deviation of the gapper and standard velocity dispersions for M_D06 and D_B06 at three linking lengths.	87

3.2	Proportion of galaxy group types where the first number is the proportion of inner, peripheral and distinct. <i>na</i> indicates where no data is provided. . . . .	92
3.3	The number of groups used to generate the plots in Fig. 3.5 . . . .	94
3.4	KS-tests where the null hypothesis is that the group shape and the random group shapes are not extracted from the same distribution.	101
3.5	The % of vCGs in a particular environment. The luminosity cut is -18 in the sdss r-band. . . . .	106
3.6	Averages and standard deviations for vCG environments. The number in brackets is the standard deviation, the other is the mean in 64 boxes. . . . .	106
3.7	<b>Top two rows:</b> The % of LGs containing more than 1 or 2 vCGs. <b>Lower two rows:</b> The % of vCGs occupying an LG containing more than 1 or 2 compact groups. . . . .	107
5.1	Proportion of galaxy group types, where the three numbers are the percentage of bright central, peripheral and dim central groups. . .	135
5.2	Best fit parameters for groups of galaxies. Schechter functions are fit to satellite galaxies in all three models and to D_B06 centrals. M_D06 and Be07 centrals are fit with Gaussian. This Table shows the parameters used in Fig. 5.3. For all satellite galaxy profiles the Schechter parameters, the position of the knee, the low luminosity slope and the normalisation. For the Gaussian centrals of M_D06 and M_B07 the parameters given are the position, deviation and height of the peak. . . . .	137

5.3	Best-fit parameters for the inferred conditional luminosity, plotted in Fig. 5.5. For all satellite galaxy profiles, the Schechter parameters, (the position of the knee, the low luminosity slope and the normalisation), are shown. For the Gaussian centrals of M_B07 and M_D06 the parameters given are the position, deviation and height of the Gaussian. . . . .	140
5.4	Percentage of groups with magnitude gap between first and second ranked galaxies greater than 2 magnitudes (top) and less than 0.5 magnitudes (bottom) . . . . .	149
6.1	The mean, median, standard deviation of the merged galaxy lifetime and number of galaxies for each model. . . . .	165
7.1	Comments on simulation outputs. 'o' shows important changes to the system and X is the primary output. . . . .	179

# List of Figures

2.1	The spatial density of groups according to the linking length (top panel), profile normalised by the number of LGs (second panel), and the spatial density distribution according to the density contour (bottom panel). The blue dashed, red, pale blue, green and black lines show the D_B06, M_D06, M_B07, D_F08 and N05 models respectively. . . . .	65
2.2	The profiles of the number of groups in the D_B06 and M_D06 models and T10 observations normalised to the total number of group galaxies. Corresponds to Table 2.3. Black is for the -20 magnitude cut, Green is the -19 magnitude cut and Blue is for the -18 magnitude cut. The solid lines show D_B06 groups and the dashed lines are for M_D06 groups, the dotted lines are for T10 observation groups. . . . .	69
2.3	Shows the distribution of mean group richness against linking length in the D_B06 (blue dashed line), D_F08 (green solid line), M_B07 (blue solid line), M_D06 (red solid line) and N05 (black solid line) datasets. The errors are $\sigma/\sqrt{N}$ , where $\sigma$ is the standard deviation and $n$ is the number of groups at that linking length. . . . .	70

2.4	The distribution of richness with the mean amount of mass per galaxy in a halo. This is a measure of galaxy density. M_D06, M_B07, D_B06 and D_F08 are the red, pale blue, dark blue and green symbols. Again we see that there are more galaxies in D_B06 groups and the amount of mass per galaxy converges for large objects, with greater scatter at low richness. . . . .	72
2.5	The correlation functions of LGs, CGs and vCGs for M_D06 and D_B06 models. LGs are shown by the solid block, CGs are vertical lines and diagonal lines are for vCGs. This thickness of the plots shows the error and the M_D06 model is red, the D_B06 model is dark blue. The units of R on the x-axis are $\log(h^{-1}\text{Mpc})$ . . . . .	77
3.1	The solid lines show the median group harmonic radius for a sub-volume for the N05 (black) M_D06 (red), M_B07 (pale blue), D_B06 (dark blue dashed) and D_F08 (green) models. The red, light blue, dark blue and green dotted lines show the harmonic radii for groups based on the dark matter distribution. The harmonic radii of T10 groups is shown in the purple dotted line. . . . .	83
3.2	Shows the distribution of group harmonic radius for different luminosity cuts in the D_B06 model. The red line shows the $M_r = -17$ luminosity cut, the blue line is for a $M_r = -20$ luminosity cut and the green line is the $M_r = -21$ cut. The width of the line indicates the Poisson error. . . . .	85
3.3	Shows the median group standard velocity dispersion, solid lines show the velocity dispersion for the N05 (black), M_D06 (red), M_B07 (pale blue), D_B06 (dark blue) and D_F08 (green) models. The dotted lines show the velocity dispersion for halo based groups.	88

3.4	The solid lines show the median group crossing time for a subvolume for the N05 (black), M_D06 (red), M_B07 (pale blue), D_B06 (dark blue) and D_F08 (green) models. The dotted/dashed lines show the crossing time for halo based groups. The dashed line shows the crossing time of Hickson et al. (1992) for Hickson compact groups. . . . .	91
3.5	Shows the luminosity against 1D velocity dispersion. The black contour shows the distribution of central groups, the red contour shows peripheral groups in the models. The dark blue points show T10 centrals and the red are T10 peripherals. The model and group catalogue is given in each panel. The numbers of points in each plot are given by Table 3.3 . . . . .	93
3.6	A plot of the position of the galaxy in the top 50 most massive clusters in the millimillennium simulation. The left panel shows the normalised number of galaxies against radius from the centre, the right panel shows the normalised number of galaxies against the radius scaled by the radius of the most distant cluster member. The dashed line is for D_B06 groups, the solid line is for M_D06 groups, and the red line is Y07 observations. Errors are poisson, i.e. $\sqrt{N}$ , where N is the number of galaxies in each radial bin. . .	95
3.7	The distribution of nearest neighbour pair separations for galaxies in LGs for the three models, the dotted line is M_B07, the dashed line is M_D06, and the thick line is D_B06. The plots shows that D_B06 galaxies tend to be closer together. . . . .	95

3.8	The distribution of group elliptical axial ratios for random groups (colours) and simulated groups (contours). The top row shows all groups in the group catalogue, the middle from those groups with more than 20 members and the bottom row those groups which have 4 members. LG, CG and vCG are from left to right. Panel a shows the axial ratios and Panel b shows the relationship between sphericity and triaxiality. . . . .	100
3.9	Shows the mean and standard deviation (error bars) for spherical groups against the number of members in the random catalogue. The black line shows results for spherical groups, the red line for a large N axial ratio of 1:15, green for ratio is 1:2 and blue is for 1:3. This is for 2D groups. . . . .	102
3.10	The 2D ellipticities of projected groups. The same groups are plotted at different inclinations and the different projected axial ratios are shown. . . . .	102
3.11	Plot of the profile of ellipticity against group membership. The dotted lines show the predicted mean ellipticities for 1000 random groups of ellipticity given in the figure. The solid line is for D06 vCGs and the error bars are the standard deviation of the distribution. The groups seem to converge to $b/a \sim 0.6 \pm 0.2$ , in keeping with Oleak et al. 1998. . . . .	103
3.12	Shows the ellipticity distribution of the projected group shape for groups with 4 galaxies. Within the error the M_D06 groups (red) are remarkably close to the observations, (Y08 is green, T08 is black), while some D_B06 (blue) groups tend to be more elliptical. Also shown are the trends for randomly filled spheres. . . . .	104

3.13	A cluster from T10 consisting of 86 galaxies and 6 compact regions. All cluster members are marked on the figure with circles. Those galaxies also members of vCGs are marked with white circles. This image is 512 pixels by 512 pixels and has 3" per pixel. . . . .	109
3.14	The ratio of group mass calculated from the virial approximation for CGs and their associated LG. The dotted line is the 1:1 ratio, the contours show the point density, the same for each plot, and the crosses show the mass calculated from the virial quantities of the LGs and CGs. . . . .	111
3.15	Shows the velocity dispersion and type of group in M_D06 and T10 groups for vCGs and LGs. The y axis shows the velocity dispersion of groups formed with a $250h^{-1}$ kpc linking length, and the x-axis vCGs. Red squares are peripheral M_D06 groups, dark blue squares are central M_D06 groups, yellow stars are peripheral T10 groups and blue stars are central T10 groups. We define central and peripheral to be the environment of the compact group. . . .	112
4.1	The distance from the cluster core against velocity offset from the cluster core for all subhaloes within $2.5 r_{vir}$ . . . . .	119
4.2	Mass of subhalo against distance from cluster centre. . . . .	119
4.3	Mass of subhalo against velocity offset from parent cluster. . . . .	120
4.4	<b>Top panel:</b> The distance from the cluster core against velocity offset for the 5 most massive subhaloes within $R_{vir}$ . <b>Bottom panel:</b> The distance from the cluster core against velocity offset for the 2 most massive subhaloes within $R_{vir}$ . Red points are for the BCGs, green points are for the second most massive subhalos and the blue points are for the second, third and fourth most massive subhalos. . . . .	121
4.5	3D velocity offsets for all haloes within the virial radius. . . . .	123

4.6	1D velocity offsets for all haloes within the virial radius. . . . .	123
4.7	Comparison between the velocity offsets of Andernach et al. (red) and our 2 most massive subhaloes, (black). The dotted lines are the median +/- the standard error on the median. . . . .	124
4.8	The distribution of BCGs in observations, (black solid lines), and N-body subhalos (red dashed lines). <b>Panel a:</b> projected separation and <b>panel b</b> velocity space separation. . . . .	127
5.1	Derived SDSS r-band luminosity functions for galaxy groups constructed with the SAMs described herein: “All” refers to the global galaxy luminosity function; “LG” to loose groups; “CG” to compact groups; “vCG” to very compact groups. The dashed/dotted/-solid lines refers to the M_B07/M_D06/D_B06 models, respectively.	130
5.2	Group luminosity functions for for the three primary SAMs under consideration (M_B07, M_D06, D_B06). In each panel, the dotted lines correspond to central galaxies and the dashed lines are for the satellites; the thick solid lines represent the group luminosity function and the thin solid line defines the global galaxy luminosity function for reference. The legend M_B07, M_D06, D_B06 refers to the model as defined above and the number in brackets refers to the linking length in $h^{-1}\text{kpc}$ . . . . .	132

5.3	The best fit lines for group luminosity functions for the three primary SAMs under consideration (M_B07, M_D06, D_B06). Labels as in Fig. 5.2. The thick dashed and dotted lines show the best fit functions for satellites and centrals respectively. The thin lines, solid for satellites, dashed for centrals. See Table 5.2 for best fit parameters, but best fit lines for LG centrals in the M_D06 (520) and M_B07 (520) are not shown because they show considerable deviation from a Schechter or Gaussian profile. . . . .	133
5.4	Luminosity function of all first ranked galaxies (thin solid line); distribution of bright central groups (thick solid line); the first ranked galaxies in peripheral groups (dotted line) and dim central groups (dashed line) . Labels as in Fig. 5.2. An excess of peripheral brightest group galaxies is apparent in the Munich models. . . . .	136
5.5	The conditional luminosity functions in three mass bins for halo-based groups for the three primary SAMs , at redshift $z=0$ . The top row shows the profiles of all halo members, the second row show central galaxies and the bottom row shows satellites. Three mass bins are used, roughly, clusters, large groups and small groups. The thin solid, dashed and thick solid lines are for the M_B07, M_D06 and D_B06 models respectively. The best fit Schechter and Gaussian profiles are shown in Table 5.3 . . . . .	139

- 5.6 The conditional luminosity function of the models, D\_B06 (solid black line) and M\_D06 (dashed line) plotted over the CLFs of Y08 (shown in red). The number quoted being the centre of each mass bin and the box width being  $\sim 0.31$  mag. In panel ‘a’ the top pair of lines are the  $10^{14.58}M_{\odot}$  cut, the next is the  $10^{13.94}M_{\odot}$  cut etc, down to  $10^{12.16}M_{\odot}$ . The numbers on the panels are the  $\log(\text{Mass})$  of the parent halo in solar masses. . . . . 142
- 5.7 Conditional (mass-dependent) magnitude gaps between first- and second-ranked galaxies for the SAMs included in this study. Thick solid, thin solid and dashed lines are for D\_B06, M\_B07 and M\_D06 groups respectively. Panels A-C are for halo-based groups subdivided by group mass, and panels G,K and P are for all FoF-groups regardless of mass. Panels D-G are for LGs, panels H-K are for CGs, and panels L-P are for vCGs. The vertical line shows the cut off for Fossil groups (Sales et al. 2007). The numbers in each panel give the percentage of groups which are fossil systems, and, in brackets, the total number of groups in each mass bin. The first number is for D\_B06, the second for M\_D06 and the third for M\_B07. 145

5.8	<p>Left column: Normalised counts of the magnitude gap between 1st and 2nd ranked galaxies. The thin solid, dashed and thick solid lines are for M_B07, M_D06, D_B06 models. The top left panel shows Tago et al. (2008) groups (dot-dashed line), Tucker et al. (2000) groups (blue dotted line) and Yang et al. (2008) groups (solid red line). The middle panel shows the results for CGs in SAMs, and the bottom left panel shows Allam and Tucker (2000) compact groups along with vCGs. Right column: The upper panel shows the second ranked luminosity function for LGs, and the lower panel shows the distribution of first ranked galaxies. Line styles are the same as for the right column. Data are limited to those groups with a first ranked to fourth ranked magnitude gap of 2 magnitudes, to mimic a survey dynamic range. . . . .</p>	148
5.9	<p>Lines as in Fig. 5.8 but with a first to fourth ranked magnitude gap of 3. Here the D_B06 model essentially matches the Y08 data.</p>	150
6.1	<p>The masses of the linked pairs of halos from the two models. The red line is the 1:1 line. . . . .</p>	161
6.2	<p>Shows the number of mergers in matched pairs of galaxies. Top panel: The number of satellite-central galaxy mergers. Bottom panel: The number of halo-cluster mergers. The blue dashed line is the 1:1 ratio. Red squares illustrate the effect of discarding clusters, wherein the D_B06 model central galaxy becomes a satellite for several time steps. . . . .</p>	163

6.3	Shows the number of mergers in each model (D_B06 are squares, M_D06 are stars). The top panel shows the number of satellite-central galaxy mergers, and the bottom panel shows halo-cluster mergers. Red symbols illustrate the effect of discarding clusters, wherein the D_B06 model central galaxy becomes a satellite for several time steps (approx 1 Gyr). . . . .	164
6.4	Shows the distribution of galaxy merging times normalised by the total number of galaxy mergers. The black line is the D_B06 model and error while the red dotted line is for the M_D06 model. Errors are Poisson. The number of merging galaxies in each model is quoted in the panel. . . . .	166
6.5	Shows the time of infall of galaxies into the cluster. <b>Panel A</b> shows the infall time of halos which merge with the central galaxy. <b>Panel B</b> shows the infall time of galaxies which do not merge. <b>Panel C</b> shows the sum of panel A and panel B. The x axis is the look back time. The solid black line shows the D_B06 result and the red dashed line is for the M_D06 model. . . . .	167
7.1	The distribution of dark matter particles at $z = 19$ . Dark blue particles are the lowest mass, and the red are the most massive particles. . . . .	175
7.2	The star formation rate of the polar disc galaxy along slits laid across the old (formed at 6.5-7.5 Gyr) stellar disc (black), and the young polar disc (red). The global star formation rate is also shown as the dashed line (but divided by 10.) . . . . .	180

7.3	Mass accretion of the various baryonic components in the galaxy. The cold gas is maintained by cooling hot gas, and star formation. The stellar component shows three eras of star formation, initial fast star formation before 4 Gyr, an intermediate period of moderate star formation and a time of slow star formation in the polar disc after 8 Gyr. . . . .	182
7.4	The mass accretion history of the dark matter halo (solid), and the Weschler best fit line (dashed) . . . . .	184
7.5	Metallicity profile of stars formed in the stellar disc (black line), and the polar disc cold gas (blue), along 1kpc thick slits. The stellar disc ends at $\sim 4$ kpc at which point the stars are in the galaxy halo. The polar disc ends at $\sim 9$ kpc. . . . .	185
7.6	The stellar age profile along the polar (black), and stellar disc(red), slits. $t_{form}$ is the mean formation time of stars at a given radius. The stellar disc ends at $\sim 4$ kpc, at which point the stars are part of the galaxy halo. The polar disc ends at $\sim 9$ kpc. . . . .	186
7.7	The radial profile of the halo shape shows a smooth distribution of the halo sphericity. The top panel shows the sphericity from the centre to the virial radius, using all particles within a distance $r$ . The low panel focuses on the inner region of the halo. The vertical dotted line is the radius of the stellar disc and dashed line is the radius of the polar disk. . . . .	190
7.8	For the $z=0.17$ output, the radial profile of the alignment of the dark matter halo shape. The black line shows the angle of the minor axis of the angular momentum with the z-axis, $\gamma$ , the red line shows the x-axis component of the halo shape and the blue line shows the profile of the y-axis. . . . .	191

7.9	<b>Panel A:</b> The line of sight velocity profile of the galaxy disks. The red line is the polar disk, the blue line is the stellar disc, based on the motion of the stars. The black line is the line-of-sight velocity of the cold gas along the polar disc slit. <b>Panel B:</b> the ratio of the masses calculated from the velocity profiles. These mass profiles are shown in <b>Panel B</b> with the same colours as in panel A . . . .	192
7.10	Evolution of the halo shape with time. The specific epoch of each panel is shown in the plot. . . . .	194
7.11	The time evolutions of the alignment profile of the minor halo axis with the three principle axes of the simulation. The black line is for z-axis, the red line is for x-axis and the blue line is for y-axis. The y axis of the plot is the arccosine of the modulus of the projection of the minor axis along each of the principle axes. The y axis is defined as the angle of the minor axis relative to the z axis of the angular momentum of the cold gas. . . . .	195
7.12	The evolution of angular alignment of the minor axis along the three principle axes. Black is the z axis alignment, red is the x-axis alignment and blue is the y axis alignment. The solid line shows the minor axis of the halo within the virial radius, while the dashed line is for the inner kpc of the halo. . . . .	196
7.13	A cartoon of halo orientation. . . . .	198

7.14	Shows the normalised angular momentum projected on the three principle axes of the simulation volume. Black shows the z axis, red the x axis, and blue the y axis. The top panel, labelled ‘halo’, is the angular momentum of the entire halo, the panel labelled ‘inner’ is the angular momentum of the inner kpc of the halo, the panel labelled ‘stars’ is the angular momentum evolution of old ( $t_{form} < 3$ Gyr) stars, and the panel labelled ‘cold’ shows the trend for the cold gas. The grey area is the time of the last major merger. . . . .	201
7.15	The variation of angle between the angular momenta of stars and cold gas with time. The dashed line shows the last major merger, and the dotted line indicated the beginning of star formation in the polar disk. . . . .	203
7.16	The projected schematic of the last major merger at $z=2$ , just before the stars merge. The black star is the central galaxy, while the red star is the galaxy which merges. The blue and green lines are the projected velocity vectors. Distances are in kpc. . . . .	205
7.17	Shows x-y projection of a 20 kpc slice around the merging event. The interacting galaxies are marked with circles, the angular momentum of the gas is marked with an orange line, the angular velocity of the interaction is marked with a blue line. . . . .	207
7.18	Shows x-z projection of a 20 kpc slice around the merging event. The interacting galaxies are marked with circles, the angular momentum of the gas is marked with an orange line, the angular velocity of the interaction is marked with a blue line. . . . .	208

7.19 Shows y-z projection of a 20 kpc slice around the merging event. The interacting galaxies are marked with circles, the angular momentum of the gas is marked with an orange line, the angular velocity of the interaction is marked with a blue line. . . . . 209

# Acknowledgements

Many thanks to my supervisor, Brad Gibson and to Chris Brook, Stéphanie Courty and Patricia Sánchez-Blázquez for supervision, advice and encouragement. I thank STFC for providing my studentship: PPA/S/S/2006/4526.

I also would like to thank Daisuke Kawata for supplying useful code and Hideki Yahagi for supplying the high resolution N-body data. I am grateful to Alexander Knebe excellent advice and for hosting me for a month at UAM. I am thankful to Laura Sales for an informative discussion and input into this project.

I also wish to thank my parents for their support and patience.

The Millennium Simulation databases used in this paper and the web application providing online access to them were constructed as part of the activities of the German Astrophysical Virtual Observatory.

Funding for the SDSS and SDSS-II has been provided by the Alfred P. Sloan Foundation, the Participating Institutions, the National Science Foundation, the U.S. Department of Energy, the National Aeronautics and Space Administration, the Japanese Monbukagakusho, the Max Planck Society, and the Higher Education Funding Council for England. The SDSS Web Site is <http://www.sdss.org/>.

# Chapter 1

## INTRODUCTION

The universe can be studied through either direct observation, or through simulation. There are distinct advantages and disadvantages in using simulations.

There are several basic tools available to simulate the universe, the simplest and best understood of which is the N-body dark matter simulation.

These models probe the structure of the dominant mass component of the universe, and so trace out the shape of the large scale structure. In order to compare simulations directly to observations, additional physics must be included. Most of our understanding of the universe comes from observing luminous matter, in the form of gas and stars. These forms of matter are, however, missing from the N-body simulations. Ideally, we would be able to follow the gas and stars using fully hydrodynamical simulations. Unfortunately, we are limited by available computational resources. In hydrodynamical simulations, which follow the gas explicitly, we are limited to relatively small volumes of the universe, even to individual galaxies. In order to explore the large-scale properties of the universe a “semi-analytic model”, or SAM, is required, e.g. Cole et al. (2000). These models use simplified physical prescriptions to explore the galaxy distribution. The techniques commonly used include the assumption of spherical symmetry when gas cools, and extremely simple models of star formation and feedback

## CHAPTER 1

processes (Baugh, 2006).

We use the results of various semi-analytical models, N-body and hydrodynamical simulations in this thesis. The results of semi-analytical models are used to explore the properties of groups of galaxies in a large region of the universe. We use the SAMs applied to the Millennium Run (Springel et al., 2005). This is because dense objects are rare objects, and so, in order to study the full range of galaxy environments, we need large statistical samples. We also use hydrodynamical simulations, which simulate individual galaxies, in order to explore the properties of a particular, exotic, type of galaxy called a “polar disc galaxy” (Whitmore et al., 1990).

Galaxies are not distributed randomly throughout space, but tend to cluster along filaments, and in clusters and groups. The early cluster catalogues were identified by visual inspection of galaxies, e.g. by Abell (1958). Since then, many more surveys have been produced, using a variety of approaches, and have become automated, e.g. Eke et al. (2004). The “preferred” environment of the average galaxy throughout the Universe is not that of the spectacular, rich, and dense, clusters, nor that of the isolated field; instead, galaxies prefer to be located within something of an intermediate “group” environment, including our own Milky Way.

In the simplest sense, groups can be categorised as being either “Loose” (Eke et al. 2004; Tago et al. 2008, 2010; Tucker et al. 2000; Yang et al. 2007, 2008 etc.) or “Compact” (Shakhbazyan 1973; Shakhbazyan and Petrosyan 1974; Hickson 1982; Barton et al. 1996; Focardi and Kelm 2002; Iovino et al. 1999). The classification of these group environments as being distinct populations from one another cannot be argued *a priori*. Instead, the combined use of spatial *and* redshift catalogues informed by numerical simulations can be used to explore the properties of galaxies in groups spanning a range of densities. In this thesis, we

## CHAPTER 1

use the Millennium Run SAMs and an N-body simulation to explore the continuum of galaxy densities between the two extremes. There is no discontinuity between loose and compact galaxy associations, despite the literature treating them as seemingly distinct entities. We will explore the properties of galaxies in groups over a full range of densities, from compact to loose groups, in order to try and resolve this false separation of the group population. Due to there being several different methods available to approximate galaxy formation physics in semi-analytic models, we will compare and contrast various models.

In the Introduction we will discuss the numerical methods used in the various simulations we have used. We will introduce the processes involved in generating dark matter and hydrodynamic simulations, and then discuss in detail the different physical approximations utilised in the semi-analytic models. Finally, we will introduce the observations used to compare our analysis to the real universe.

### 1.1 Description of content

This thesis is divided into three sections. The main bulk of the work deals with groups of galaxies in SAMs, mainly the models of De Lucia and Blaizot (2007), Bertone et al. (2007), Bower et al. (2006) and Font et al. (2008). We compare the results of our analysis of these models to the observational catalogues of Allam and Tucker (2000); Tago et al. (2010); Yang et al. (2007). This investigation deals with the spatial density of groups and richness of groups (Chapter 2), the dynamics and morphology of groups (Chapter 3), the luminosity profile of groups (Chapter 5) and the merging of galaxies (Chapter 6). These chapters compare the SAMs described above with one another and with the observational catalogues. Chapter 4 describes our investigation into brightest cluster galaxies. In this chapter we look for possible correspondences between the most massive subhalo of a cluster and the brightest cluster galaxy. We also investigate the behaviour of a galaxy

## CHAPTER 1

group as it falls into a cluster. Chapter 7 deals with a more detailed study of a single polar disc galaxy. This uses a cosmological simulation to investigate the dark matter, formation and metallicity profile of these very rare objects. Finally we provide a summary of our main findings and highlight possible future research directions.

### 1.2 Structure formation

The universe is composed of 73% dark energy, 23% dark matter and 4% baryons (Spergel et al., 2007). Dark energy is relevant only on the largest scales, and causes the Universe to accelerate its expansion. Dark energy only starts to dominate about 5 Gyrs after the Big Bang, before that the mass density is sufficient to overcome the effect of dark energy. Dark energy is usually parametrised as a ‘cosmological constant’ in the Friedmann equations (Friedman, 1999, 1922) describing basic cosmology.

The dominant matter component of the universe is dark matter. This form of matter does not interact with baryonic matter, except through gravity. However, because there is 5 times as much dark matter as ordinary matter it provides the gravitational framework on the large scale to which the baryonic matter we can observe responds. In other words, the baryonic matter traces out the potential field generated by the dark matter. This approximation only breaks down in the dense regions such as the baryon dominated centres of dark matter haloes.

On the largest scales, the universe consists of:

1. large filaments of overdense dark matter,
2. very dense, approximately spherical, dark matter haloes,
3. large underdense voids.

## CHAPTER 1

These are described by Gregory and Thompson (1978) among other authors. This structure is the natural result of the Gaussian initial conditions caused by minute quantum fluctuations during the inflationary era of the universe (Bardeen et al., 1986; Bond et al., 1996).

The current model of the formation of structure in the universe is hierarchical. Small dark matter haloes in the early universe merge over time to assemble large haloes at later times. This same process builds up large galaxies from smaller galaxies.

That said, not all mass in a galaxy is accreted from mergers. The gas in a massive galaxy at high  $z$  is now thought to be accreted mainly from filaments (Birnboim and Dekel, 2003; Weinberg et al., 2002). Gas flows along filaments and cools inside dark matter halos to form disc shaped structures. These gaseous discs form stars. It is a combination of these processes and mergers that give us the rich variety of galaxies we see today.

When several galaxies of significant size co-exist inside the same large dark matter halo we define the object as a galaxy group or cluster. Thus, it is possible to define a group or cluster in two ways. In a simulation a group is a halo of a certain mass which contains substructure. In observations, where the dark matter cannot be seen directly, a group is an overdensity of galaxies.

Galaxy groups and clusters were originally identified as overdensities of galaxies, e.g. Abell (1957). These structures appeared on the sky as dense systems of galaxies in projection. By assuming large clusters to be gravitationally bound structures it was possible to calculate, using the virial theorem, the cluster mass based on the position and velocities of the member galaxies (Zwicky, 1933, 1937). This was one of the early clues as to the existence of dark matter.

Clusters are thought to consist of large dark matter haloes of mass,  $M \sim 10^{14-15} M_{\odot}$  with virial radii up to a few Mpc, containing sub-haloes and galaxies.

## CHAPTER 1

These haloes can be seen in both simulations, e.g. Springel et al. (2005), and via gravitational lensing, e.g. Broadhurst et al. (2005). Groups are thought to be contained within lower mass dark matter haloes,  $M \sim 10^{13} M_{\odot}$ , with virial radii of about  $0.5h^{-1}$  Mpc, or consist of separate galaxy sized haloes,  $M < 10^{12} M_{\odot}$  (Dekel and Ostriker, 1999) that are simply close to one another.

Groups of galaxies do not only consist of dark matter and member galaxies. They possess a rich intergroup medium, composed of hot gas. The space between galaxies is filled with an energetic gas produced by gas falling into the group potential from large scale structure such as filaments. Alternatively the intergalactic gas in groups can be produced by energetic superwinds and retained by the group potential. As the gas falls into the halo it is heated during virialisation. The virial theorem is,

$$E_p = 2E_k, \quad (1.1)$$

where,  $E_p$  is the potential energy and  $E_k$  is the kinetic energy. During virialisation the additional energy,  $E_k$  goes into heating the gas to the virial temperature,  $T$ ,

$$T \sim \frac{GMm_p}{kR}, \quad (1.2)$$

where  $G$  is the gravitational constant,  $M$  is the halo mass,  $m_p$  is the mass of the average particles,  $k$  is Boltzmann constant and  $R$  is the halo radius. The excess energy is radiated away during the cooling process. This takes the form of Bremsstrahlung X-ray radiation and X-ray line emission. Ponman et al. (1996) found similar X-ray emission inside 75 % of Hickson Compact Groups (Hickson, 1982), indicating that these are real objects rather than chance projections. The dark matter component cannot radiate as it does not interact with light, thus it heats up and cannot collapse as far as an equivalent amount of gas. This collapsing gas can form new galaxies or can be added to already existing galaxies. If the

## CHAPTER 1

cooling time of gas is shorter than the dynamical time then the gas is assumed to cool quickly, while at longer cooling times, in more massive halos ( $M_{halo} > 1 \times 10^{11} M_{\odot}$ ) cooling occurs more gradually and the halo builds up a hot gas halo (Croton et al., 2006).

Galaxies can be ordered onto a sequence according to their morphology (Hubble, 1926). This sequence incorporates elliptical galaxies, irregulars, and spiral galaxies, both barred and unbarred. This split for spirals is why the sequence is often called the ‘Hubble Tuning Fork’. Galaxies in dense environments, such as groups, clusters and compact groups, tend to be redder than galaxies in the field (Oemler, 1974; Dressler, 1980), and this can be directly observed. This is due to a number of processes. Stars form as gas cools and becomes sufficiently dense (White and Rees, 1978). As a population of stars ages the bright blue stars quickly disappear leaving behind cooler, redder, long lived stars. This means that, in general, the redder a stellar population the older it is, thus, red galaxies have experienced little or no recent star formation.

Processes which reduce star formation exist in all galaxies, in all environments. Examples are supernova feedback, which reduces the amount of cold gas in small galaxies, e.g. (Croton et al., 2006) or AGN feedback, e.g. (Kauffmann and Haehnelt, 2000), which reduces the amount of gas in large galaxies. However, there are additional processes that are important in dense group and cluster environments. The most spectacular process in dense environments, which affects star formation and galaxy morphology, is galaxy merging (Hickson et al., 1977). There are two types of galaxy merger, the major merger, where galaxies are of comparable mass, and the minor merger where one galaxy is significantly smaller than the other. Major mergers have the effect of converting galaxies from discs to ellipticals, removing gas and triggering starbursts. In dense environments this is more effective because there are more galaxies within a given volume.

## CHAPTER 1

Other processes that remove gas include: ram-pressure stripping, e.g. Fujita and Nagashima (1999), where gas is removed from a galaxy by drag from the intercluster medium; strangulation, e.g. Larson et al. (1980), Balogh et al. (2000), where the interaction of the galaxy halo with the cluster potential reduces the amount of hot gas available to cool, depleting the amount of cold gas and thus star formation down the line; and galaxy harassment, where constant interactions change the morphology of a galaxy over time (Kawata and Mulchaey, 2008).

### 1.3 Numerical Methods

Simulations of the time evolution of structure throughout the Universe require appropriate initial conditions. The positions and velocities of the particles chosen to represent the density field of the early Universe are then allowed to evolve through time, with an adopted software package solving for the gravitational interactions between the particles. Below, we describe how such initial conditions are defined, as well as the time evolution of the spatio-kinetic properties of the dark matter particles involved. The final component of this work involves the analysis of the hydrodynamic properties of a simulated massive disc galaxy; as such, the relevant hydrodynamical physics is also described below.

#### 1.3.1 Initial Conditions

The initial density perturbation  $\delta(\mathbf{x})$  can be described, most generally, as,

$$\delta(\mathbf{x}) = \frac{\rho(\mathbf{x}) - \langle \rho \rangle}{\langle \rho \rangle}, \quad (1.3)$$

where  $\rho(\mathbf{x})$  is the density at position  $\mathbf{x}$  and  $\langle \rho \rangle$  is the mean density of the Universe. The initial density fluctuations in the early Universe are assumed to be Gaussian (Strauss and Willick, 1995; Doroshkevich, 1970) and can be described by a simple

## CHAPTER 1

power spectrum,

$$P(k) = Ak^n T_k^2, \quad (1.4)$$

where  $T_k$  is the transmission function,  $k$  is the wavenumber, the exponent  $n$  is assumed to be unity with equal power on all scales, and  $A$  is a constant, e.g. Baugh and Mordin (2000). This information is all that is required to generate the initial conditions for a cosmological simulation. Each particle in the simulation is placed on a regular grid and given a small displacement and peculiar velocity. The displacement and velocity are calculated according to the Zel'Dovich (1970) approximation,

$$\vec{r}(t) = a(t)[\vec{q} + D(t)\vec{f}(q)], \quad (1.5)$$

where  $\vec{r}$  is the physical coordinate of the particle,  $\vec{q}$  is the co-moving position,  $a(t)$  is the scale factor,  $D(t)$  is the linear evolution of the perturbation, and  $\vec{f}(q)$  is the time-dependant displacement field,

$$\vec{f}(q) = \nabla\phi(\vec{q}). \quad (1.6)$$

Here,  $\phi(\vec{q})$  is the gravitational field due to the density fluctuations, where these fluctuations are given by

$$\nabla^2\phi = \frac{\delta}{D}. \quad (1.7)$$

The corresponding velocity displacement is described as,

$$\vec{v} = \frac{d\vec{r}}{dt} - H\vec{r} = a\dot{D} \nabla\phi(q) \quad (1.8)$$

## CHAPTER 1

The initial conditions depend on the box size used to define the grid, the cosmology  $(\Omega_0, \Omega_\Lambda, \sigma_8, H_0)$ , and the total number of particles.

### 1.3.2 N-body Codes

An “N-body” scheme solves for the equations of motion governing an ensemble of “N” collisionless particles, using

$$\nabla_x \phi = 4\pi G \rho \tag{1.9}$$

and the standard equations linking potential and density to acceleration, velocity, and position via,

$$\frac{dv_i}{dt} = -\nabla_x \phi \tag{1.10}$$

$$\frac{dx_i}{dt} = v_i \tag{1.11}$$

where  $x_i$  and  $v_i$  are the position and velocity for each particle and  $\phi$  is the gravitational potential.

Here, the dark matter is modelled as a collisionless fluid, discretised and represented as particles. It has long been known that direct summation of the gravitational forces on a particle-by-particle basis becomes intractable for large  $N_p$ , (due to its  $N_p^2$  scaling, where  $N_p$  is the number of particles). We adopt standard approaches which mitigate the problems associated with direct summation - specifically, we adopt tree codes and grid codes. Tree codes scale as  $N_p \log(N_p)$ , while grid codes scale like  $N_g \log(N_g) + N_p$ , where  $N_g$  is the number of grid cells. These techniques are all that are required for modelling the spatio-kinetic properties of the dark matter.

## CHAPTER 1

### Tree code

The time evolution of the dark matter particle positions is handled via the use of an “hierarchical tree algorithm” in standard N-body tree codes, such as GADGET-II (Springel et al., 2005) or GASOLINE (Wadsley et al., 2004). In this technique, contributions to the force exerted on a particle,  $p_i$ , can come from individual particles, or from large groups of particles at greater distances from  $p_i$ . The simulation volume is decomposed into regions using the Barnes & Hut algorithm (Barnes and Hut, 1986). In this method the volume is divided into cubes, starting with the simulation box itself. This node is then split into eight subcells with half the linear dimensions. This process is carried out recursively until each particle is contained within its own cube. These cubes form the nodes of the ‘oct-tree’ structure and are arranged hierarchically. Each of these cells is henceforth referred to as a ‘node’.

The further a given node is from  $p_i$ , the less detail is required, and a larger node is used, to calculate the contribution to the gravitational potential at  $p_i$ . Close to  $p_i$  a smaller node is used. The more distant a node is from  $p_i$  the less accurately the force contribution needs to be. This means that when we wish to calculate the contributions of all particles, we do not need to sum the contributions of all particles individually.

Using the tree code approach we can lump particles together by only traversing part of the ‘oct-tree’. The contribution of the larger nodes is based on the average contribution of all particles in that node, so the further away we go from  $p_i$  the more particles are combined to make the average contribution. Whether a node is opened or not is controlled by an ‘opening angle’ which is the ratio of the node size to the distance from  $p_i$ . We recover the local potential of the particle in such a way that local information is more accurate than more distant parts of the simulation volume.

## CHAPTER 1

Tree codes also require gravitational softening to reduce two-body relaxation. This is the process by which the dark matter particles undergo a series of two-body interactions leading to the transfer of energy between particles. This is unrealistic as dark matter particles in the real universe are thought to be collisionless. During two-body relaxation particles come into close proximity with each other, and interact via gravity. This means that the particle trajectories will change. This effect is cumulative for each particle in the simulation volume, and a system undergoing two-body relaxation will see a significant re-distribution of energy. This process is a problem when modelling dark matter, because we are modelling a collisionless fluid, using discrete, massive, particles, which, without softening, are collisional. This means that the behaviour of the simulated dark matter will not be realistic. The gravitational force is “softened” via the use of a “kernel”, which in effect, weights the contribution of particle  $j$  on particle  $i$  based on  $j$ 's distance from  $i$ , according to an appropriately chosen function. In practise, this softening is limited to a certain maximum distance,  $h$ , called the ‘softening length’. This softening length can be adaptive and limits the spatial resolution of the simulation. The calculation of the gravitational force only becomes Newtonian at a distance greater than the softening length. This sets the force resolution of the simulation.

### **Grid code**

The grid code we have used utilises a Particle-Mesh technique to solve for gravity (Yahagi and Yoshii, 2001). A cloud-in-cell approach is implemented to assign the particle density to the nodes of the mesh. This means that a fraction of the mass of any given particle is assigned to the eight surrounding nodes, according to how close the particle is to a particular node. This produces a much smoother density field than simply assigning a particle to the nearest grid point. The result of this

## CHAPTER 1

creates a continuous background density field from which the potential is found via the Poisson equation. This technique utilises the fact that in Fourier space the Poisson equation is a simple algebraic expression,

$$\hat{\Phi} = 4\pi G \frac{\hat{\rho}}{k^2} \quad (1.12)$$

where  $\hat{\rho}$  is the density of the mesh points,  $G$  is Newton’s gravitational constant,  $k$  is the co-moving wavenumber, and  $\hat{\Phi}$  is the potential and “hats” indicate the associated Fourier transforms.

This equation is then used to calculate the force and hence the equations of motion for the particles. The spatial resolution is limited by the grid size, which is a severe short-coming of this method. In modern PM codes an adaptive mesh, usually based on ART (Adaptive Refinement Tree) (Kravtsov et al., 1997), is used. The ART code subdivides cells where higher resolution is required. The mesh cells are refined into eight smaller cells when the particle number is greater than a pre-set number. This, however, makes calculating the potential more difficult because the Fourier approach requires a regular grid. Thus, a multigrid approach (Press et al., 1992) is required for levels lower than the coarse (uppermost) grid. This ‘Adaptive Mesh Refinement’, or AMR, approach has the beneficial effect of concentrating the computational effort to where it is required.

### 1.3.3 Hydrodynamics with GASOLINE

In chapter 7 of this thesis, we use GASOLINE (Wadsley et al., 2004) to simulate the physics of a galaxy using collisionless dark matter, star particles and dissipative gas particles. GASOLINE uses a Smoothed Particle Hydrodynamical (SPH) approach to simulate the gas, and a tree N-body code (§1.3.2) to represent dark matter and stars. In such an approach, the particle number is the fundamental resolution element, as opposed to the grid cells in a mesh technique - e.g. Teyssier

## CHAPTER 1

(2002).

SPH smoothing is the hydrodynamical analogue of gravitational softening, where particles are used to sample the smoothly varying properties of a fluid. The kernel used in GASOLINE sets the resolution of the gas physics depending on the smoothing length. The particular implementation used in GASOLINE was defined by Hernquist and Katz (1989), as

$$W_{ij} = \frac{1}{2}w(|\vec{r}_i - \vec{r}_j|/h_i) + \frac{1}{2}w(|\vec{r}_i - \vec{r}_j|/h_j) \quad (1.13)$$

where  $W_{ij}$  is the kernel function,  $r_i$  and  $r_j$  are the positions of the particles,  $w(x)$  is the standard spline form (Monaghan, 1992) and  $h_i, h_j$  are the particle smoothing lengths. To model the gas physics of the simulation, the density, temperature, angular momentum, viscosity, pressure, energy, and entropy of the gas must be taken into account. A brief summary of the particular implementation of these quantities within GASOLINE is outlined below.

The density of the gas,  $\rho_i$ , is calculated from the sum of the local particle masses  $m_j$ , weighted by the kernel,

$$\rho_i = \sum_{j=1}^n m_j W_{ij}, \quad (1.14)$$

and the angular momentum is expressed as

$$M \frac{d\vec{v}_i}{dt} = - \sum_{j=1}^n m_j \left( \frac{P_i}{\rho_i^2} + \frac{P_j}{\rho_j^2} + \Pi_{i,j} \right) \nabla_i W_{ij} \quad (1.15)$$

where  $P_j$  is the pressure,  $\vec{v}_i$  is the velocity,  $M$  is the total mass, and  $\Pi_{ij}$  is the artificial viscosity, which is critical, to avoid the onset of unphysical oscillations. In the range of  $\vec{v}_{ij} \bullet \vec{r}_{i,j} < 0$ ,  $\Pi_{ij}$  is given by,

$$\Pi_{ij} = \frac{\alpha \frac{1}{2}(c_i + c_j)\mu_{ij} + \beta \mu_{ij}^2}{\frac{1}{2}(\rho_i + \rho_j)} \quad (1.16)$$

## CHAPTER 1

where,

$$\mu_{i,j} = \frac{h(\vec{v}_{ij}) \bullet \vec{r}_{ij}}{r_{i,j}^2 + 0.01(h_i + h_j)^2} \quad (1.17)$$

and  $r_{ij} = \vec{r}_i - \vec{r}_j$ ,  $v_{ij} = \vec{v}_i - \vec{v}_j$ , and  $c_j$  is the speed of sound. By construction,  $\alpha = 1$  and  $\beta = 2$  are coefficients chosen to represent shear and Von Neumann-Richtmyer viscosity, respectively. The Von Neumann-Richtmyer viscosity is a term modifying material compression. It is important in order to smooth shocks in the simulation (von Neumann and Richtmyer, 1950).

GASOLINE uses the thermal energy formalism described by Evrard (1988) and Benz et al. (1989) to derive energy (as the pressure-averaged energy equation can give rise to negative energy),

$$\frac{du_i}{dt} = \frac{P_i}{\rho_i^2} \sum_{j=1}^n m_j v_{ij} \bullet \nabla_i W_{ij} \quad (1.18)$$

where  $u_i$  is the internal energy of particle  $i$ . This formulation also closely conserves entropy.

In addition to the simple hydrodynamical quantities listed above, SPH (and grid-based) codes must take into account feedback, cooling, heating, and star formation, in order to correctly model galaxy formation.

The star-formation and supernova recipes employed are detailed in Stinson et al. (2006). For a gas particle to form a star, the local spatial density must be in excess of  $0.1 \text{ cm}^{-3}$ , in an overdense region ( $>55\rho/\bar{\rho}$ ), part of a convergent gas flow, and Jeans unstable,

$$\frac{h_i}{c_i} = \frac{1}{\sqrt{4\pi G \rho_i}}. \quad (1.19)$$

Star particles are formed from gas particles in a probabilistic manner, as discussed further in Ch 7.

### 1.3.4 Halo finding

Dark matter haloes and subhaloes are self-bound overdensities of particles in the simulation volume. In order to identify haloes a halo finder is required, but subhalo identification is more complex. A halo can be defined as a sphere, centred on an overdensity peak of average density greater than a given overdensity (Lacey and Cole, 1994) or a region enclosed by a specific overdensity contour (Davis et al., 1985). Subhalos, which are halos within halos, are not so easily defined and require more complex explorations of the particle distribution.

In order to identify self-bound overdensities of particles we make use of the AMIGA Halo Finder (AHF).<sup>1</sup> AMIGA is the successor to MLAPM, and AHF is an updated version of the MLAPM Halo Finder (MHF: Gill et al 2004). This finder makes use of the adaptive mesh grids of the MLAPM (Knebe et al., 2001) N-body code, and is essentially parameter free when used on AMIGA / MLAPM simulations. We apply AHF to our simulation outputs and set the refinement criteria such that the resolution of the grids is as close as possible to the resolution of the original (parent) simulation. Isolated areas of high refinement are used to identify potential halo centres. The program then constructs a grid tree, by looking at the hierarchy of adaptive grids, and collects particles together. It does this by looking for all particles within a certain isodensity contour and then iteratively checks to see which of those particles are bound to the potential halo centre. This process continues until no more particles are removed or there are too few bound particles for the object to be considered a halo. AHF then computes a host of halo properties, but in doing so rejects particles outside the virial radius. The virial radius is defined as the radius of a sphere, the mean density of which is  $\sim 340$  times the background density at  $z=0$ . This value of the virial overdensity is based on the dissipationless spherical top-hat collapse model (Gill et al., 2004;

---

<sup>1</sup>**AMIGA's-Halo-Finder**; AHF can be downloaded from <http://www.aip.de/People/aknebe/AMIGA>.

## CHAPTER 1

Knollmann and Knebe, 2009).

The AHF code is used to process the GASOLINE output, but the differences between an AMR and Tree code must be taken into account. The maximum refinement level of AHF must be set to the resolution of the GASOLINE gravitational softening, or the code will refine the grids in an unphysical manner. A Tree code approach to solving gravity allows the particles to bunch closer together than an AMR technique. We use a simple formula to specify the maximum refinement level used in AHF,

$$L_{max} = \frac{\log(B/s)}{\log(2)} \quad (1.20)$$

where  $L$  is the refinement level,  $B$  is the size of the simulation volume, and  $s$  is the gravitational softening length.

In comparison, the well-known Millennium Run uses an alternative halo finder, SUBFIND (Springel et al., 2001), which finds, as with AHF, locally dense self-bound objects using a two-pass approach. Initially, a Friends-of-Friends (FoF) algorithm (Geller and Huchra, 1983) is used to find local overdensities. The SUBFIND algorithm then finds the density of each particle via a smoothing kernel, and accepts particles with a density above a certain threshold. This procedure slowly decreases the density threshold for a particle to be accepted as potentially belonging to a halo. As the threshold falls, halos can blend together, forming subhalos. The particle velocities are then used to calculate whether the potential (sub)halo is a bound object.

There are subtleties to the halo finding procedures which are useful to outline here, starting with the three definitions of “halo” used in what follows (dubbed the Munich approach, the Durham approach, and the AHF approach, respectively). Although there is a halo identification number which includes halos and subhalos, in order to find an equivalent across all three approaches, we are forced to use only

## CHAPTER 1

the FoF halo identification number to decide if galaxies are in the same halo. FoF can spuriously add halos together, so the Durham group uses SUBFIND (Springel et al., 2001) to split the FoF halos. In the Durham model, joined parents are split if the centre of parent 1 is outside twice the half-mass radius of parent 2, and parent 1 has retained more than 75% of its original mass. Conversely, AHF defines a halo according to its virial radius, and a subhalo is simply an object which has its centre inside the virial radius of a higher mass object. The Munich approach is to use the output of SUBFIND. This algorithm, however, follows the density contour, producing an irregular shaped halo. Subhalos are defined as self-bound objects composed of particles associated with the host halo.

### 1.4 Semi-analytic Models

Semi-analytic models (SAMs) are phenomenological prescriptions of baryonic physics employed to model large samples of galaxies in such a manner as to allow ready comparisons with observations. These prescriptions are applied to dark matter halo merger trees, upon which the baryonic physics is assumed to depend.

#### 1.4.1 Merger Trees

Dark matter halos coalesce to form ever-larger halos, ultimately leading to the formation of groups and clusters. The tool which allows us to keep track of these processes is the “merger tree”. These trees allow us to identify which halos have merged, and give us the basis for understanding how interactions with the environment affect galaxy formation. Effectively a merger tree for a dark matter simulation involves identifying where the tracer particles belonging to a halo at time  $t$  are at time  $t + \Delta t$ . Once identified, a process called “walking the tree”

## CHAPTER 1

is used to follow an object through time. In the Millennium Run, a Depth-First search algorithm is employed in which an object is followed back in time to its formation before another branch of the tree is traversed.

### 1.4.2 Description of the Models

The SAMs used in our analysis employ the merger trees associated with the Millennium Simulation (Springel et al., 2005), a large N-body simulation corresponding to a significant volume of the visible Universe, and generated using the WMAP Year 1 cosmology (Spergel et al., 2003). The simulation used  $2160^3$  particles in a periodic box of length  $500h^{-1}$  Mpc, gravitational softening of  $5h^{-1}$  kpc, and individual particle masses of  $8.6 \times 10^8 M_{\odot}$ . 64 outputs exist within the Millennium database, ranging from redshift  $z=127$  to  $z=0$ . The simulation was post-processed using a Friends-of-Friends (FoF) algorithm (Geller and Huchra, 1983), in order to identify density peaks. Then SUBFIND (Springel et al., 2001) was employed to identify substructure and split spuriously joined halos. This information was then used to build merger trees for the dark matter halos, onto which the SAMs are “mapped”.

We will highlight the different ways in which the SAM codes create merger trees, the way in which galaxy positions are defined, the implementation of satellite disruption and accretion, and the way in which supernova and AGN feedback are implemented. This is critical, in order to interpret their predictions in light of the observational constraints described later.

When a halo first forms it is given a specific amount of hot gas, the upper limit for which is set by the baryonic mass fraction of the Universe, although in practise, this is reduced in smaller halos by the inclusion of a heating effect due to the ultraviolet background (Gnedin, 2000; Kravtsov et al., 2004). This gas is assumed to be heated to the virial temperature of the dark matter halo.

## CHAPTER 1

This hot gas is then allowed to cool. In large halos this occurs according to the cooling time, given by,

$$t_{cool} = \frac{3\bar{\mu}m_pkT_{vir}}{2\rho_g(r)\Lambda(T, Z)} \quad (1.21)$$

where  $t_{cool}$  is the time it takes for the hot gas to cool to a temperature where it is potentially starforming,  $\bar{\mu}m_p$  is the mean particle mass,  $k$  is Boltzmann's constant,  $T_{vir}$  is the halo virial temperature,  $\rho_g(r)$  is the hot gas density, and  $\Lambda(T, Z)$  is the plasma cooling function. The halo is assumed to be isothermal,

$$\rho_g(r) = \frac{m_{hot}}{4\pi R_{vir}r^2} \quad (1.22)$$

where  $m_{hot}$  is the hot gas mass of the halo,  $R_{vir}$  is the virial radius of the halo, and  $r$  is the radius. A cooling radius  $r_{cool}$  needs to be defined which is proportional to the age of the halo. In Croton et al. (2006) this is set to the radius at which  $t_{cool}$  is equal to the halo dynamical time. In small halos ( $< 3 \times 10^{11} M_\odot$ ) the cooling time is equal to the free-fall time. The cooling radius and density of the halo are then used to calculate the mass of hot gas which has cooled in that timestep and consequently increase the cold gas reservoir,

$$\dot{m}_{cool}\Delta t = 4\pi\rho_g(R_{cool})r_{cool}^2\dot{r}_{cool}\Delta t \quad (1.23)$$

where  $\dot{m}_{cool}\Delta t$  is the change in the hot gas mass and  $\dot{r}_{cool}$  is the velocity at which the cooling radius increases. As the hot gas cools, more hot gas falls into the halo from outside, proportionally to the increase in dark matter mass.

Merging dark matter halos result in satellite galaxies, starbursts, and other processes. When halos merge the galaxy of the larger halo is usually chosen to be the central galaxy of the new halo, and the secondary halo's galaxy becomes a satellite galaxy. This galaxy then loses its hot gas reservoir in order to mimic

## CHAPTER 1

the effect of ram-pressure stripping (McCarthy et al., 2008). A countdown then begins which describes the amount of time the satellite has until it is considered to merge with the central galaxy. Equation (1.24) below, is used by Croton et al. (2006), De Lucia and Blaizot (2007), Bertone et al. (2007), and Nagashima et al. (2005), after Binney and Tremaine (1987), where  $\ln(\Lambda)$  is the Coulomb logarithm. Lacey and Cole (1993) identified an alternative form for the dynamical friction of galaxies, shown in equation (1.25). These equations differ in that the satellite mass in equation (1.24) is the mass after stripping has taken place, (i.e., the last time the subhalo can be identified by the halo finder), while in equation (1.25) it is the mass *before* stripping.

$$\tau_{mrg} = 1.17 \frac{V_{vir} r_{sat}^2}{G m_{sat} \ln(\Lambda)} \quad (1.24)$$

$$\tau_{mrg} = f_{df} \Theta_{orbit} \tau_{dyn} \frac{0.3722 M_H}{\ln(\Lambda) M_{sat}} \quad (1.25)$$

where  $\Theta_{orbit}$  is a function of halo internal energy, angular momentum, orbital radius, and halo virial radius,  $M_H$  is the halo mass,  $M_{sat}$  is the mass of the satellite including dark matter,  $V_{vir}$  is the virial velocity, and  $f_{df}$  is a free parameter. The central assumptions in Eqn. 1.24 used in this expression are that all orbits are circular, galaxies are point masses, and galaxy mass is the total mass of stars plus the mass of the satellite halo the last time the halo was identified. The countdown to merging begins when the galaxy enters the parent of the merging dark matter haloes. The more massive galaxy becomes the new central galaxy (Cole et al., 2000), by construction.

Galaxy mergers are defined as one of two types - minor and major. A major merger is defined to be that between one galaxy and a second one whose mass is in excess of 30% of the former. A minor merger is assumed to have very little impact on the central galaxy while a major merger is assumed to induce a starburst.

## CHAPTER 1

Stars form from an associated cold gas disk, which corresponds to gas lying below a prescribed density threshold. This gas is assumed to be evenly distributed throughout the disk and hence a critical cold gas mass for star formation can be determined. For example, in the Croton et al. (2006) model this is given by

$$m_{crit} = 3.8 \times 10^9 \left( \frac{V_{vir}}{200 \text{ km s}^{-1}} \right) \left( \frac{3\lambda/\sqrt{2}R_{vir}}{10 \text{ kpc}} \right) M_{\odot} \quad (1.26)$$

from Kauffmann (1996) and Mo et al. (1998).  $\lambda$  is the spin parameter of the dark halo (Bullock et al., 2001). From this the star formation rate is

$$\dot{m}_* = \alpha_{SF} (m_{cold} - m_{crit}) V_{vir} / r_{disk} \quad (1.27)$$

Galaxy disks form via cold gas accretion, and bulges form from starbursts and disc buckling from unstable disks. Starbursts destroy galaxy disks in the simulations and a tunable fraction of the cold gas is turned into stars (Croton et al., 2006)

Feedback acts to regulate star formation. It is required because the luminosity function of groups is significantly different from the dark matter halo mass function. Supernova feedback is dominant in small halos. Supernova feedback, which comes from exploding stars, acts to heat the cold gas back into hot gas, or can eject gas from the halo. This provides an explanation for the observed absence of many small galaxies, such as the missing dwarf galaxies which, from the simulations, should orbit the Milky Way.

AGN feedback dominates in large halos and acts to heat the gas. This process is tied to the growth of supermassive black holes. Two approaches to AGN feedback are used in the models utilised in this thesis, both of which are described in the subsequent two subsections.

The final stage of any SAM is to convert from the mass regime, to observables

## CHAPTER 1

such as luminosity. This requires extensive knowledge of the merging history, metallicity, and stellar mass. Cole et al. (2000) and Kauffmann et al. (1999) describe two methods of achieving this, including their preferred methodology for taking into account the effects of dust extinction.

### **1.4.3 Durham Models: Bower et al. (2006; D\_B06); Font et al. (2008; D\_F08)**

In the so-called “Durham” models, merger trees are produced by linking together halos in different outputs, according to the specific halo at later times that contains the largest fraction of particles in a halo at an earlier time. The Durham models do not trace the actual dark matter subhalos. To position the galaxies within a parent halo, the Durham model assigns the galaxy to the most bound particle of the halo at the time of galaxy formation. The model constantly checks that the galaxy remains bound to the dark halo throughout the simulation, and if not the galaxy is reassigned to the most bound particle of the parent. The galaxy is said to have merged with the halo central galaxy according to the dynamical friction time-scale.

AGN feedback is modelled in such a way as to regulate the cooling of hot gas. If the cooling time for a particular dark halo exceeds a tunable fraction of the free-fall time, the AGN can have a significant effect on the galaxy luminosity. In large halos with large Eddington luminosities, the AGN feedback is assumed to balance heating and cooling. This truncates star formation and prevents the formation of overluminous galaxies. While feedback is active, the supermassive black hole is assumed to grow proportionally to the cooling luminosity and the gas accretion, due to disk instabilities. The model assumes quasi-hydrostatic cooling for AGN “active” galaxies. It has a strict transition between AGN “active” and “inactive” phases, with AGN feedback becoming efficient in galaxies of mass

## CHAPTER 1

$\sim 2 \times 10^{11} h^{-1} M_{\odot}$ .

For low mass galaxies, supernova feedback becomes an important mechanism by which galactic winds are driven and star formation is quenched, both of which lead to a reduction in the number of low luminosity galaxies. Bower et al. (2006) and Font et al. (2008) relate supernova reheating directly to the circular velocity of the galaxy disk according to Cole et al. (2000):

$$\dot{M}_{reheat} \propto \frac{1}{V_{disk}^2} \dot{M}_* \dot{M}_{eject} \propto V_{disk}^2 \dot{M}_* \quad (1.28)$$

where  $\dot{M}_{reheat}$  is the rate of change of mass of reheated gas,  $V_{disk}$  is the disk circular velocity,  $\dot{M}_*$  is the time derivative of stellar mass, and  $\dot{M}_{eject}$  is the change in the mass of ejected gas. In halos with a shallow potential this has the effect of reducing the amount of cold gas available to form stars by heating the gas back into the hot gas reservoir. The hot gas reservoir is dominated by (i) ejection from low mass halos, and by (ii) reheating, without ejection, from large halos.

The essential difference between the Bower et al. (2006) and Font et al. (2008) models is in the implementation of ram-pressure stripping of the hot gas. In the Bower et al. (2006) model, along with both Munich models described below, the hot gas is instantaneously stripped when it enters a halo already containing a central galaxy. In the Font et al. model, this process happens gradually and depends on the orbit of the galaxy. This has the beneficial effect of reducing the population of faint red galaxies, and more closely matching the observations.

### **1.4.4 Munich Models: De Lucia et al. (2006; M\_D06); Bertone et al. (2007; M\_B07)**

The so-called ‘‘Munich’’ model merger trees (Springel et al., 2005), used by De Lucia et al. (2006), De Lucia and Blaizot (2007) and Bertone et al. (2007), follow

## CHAPTER 1

the positions of subhalos for as long as they can be identified, according to the minimum number of particles set by SUBFIND. The trees are constructed by following the most bound halo particles and searching for the descendant halo in the next output.

The Munich models calculate galaxy position by assigning the galaxy to the most bound particle of a (sub)halo at each time step. This is done until the (sub)halo is no longer identifiable, whereupon the galaxy is assigned to the most bound particle of the (sub)halo, the last time the (sub)halo could be identified. The countdown to galaxy merging begins when the satellite subhalo can no longer be identified and resets if the parent halo undergoes a major merger.

The dynamical friction calculation in the Munich models is simpler than in the Durham models, but the semi-analytic countdown to merging is delayed compared to the Durham models. In De Lucia et al. (2006), De Lucia and Blaizot (2007) and Bertone et al. (2007), the lifetime of galaxies in groups depends on the amount of time the (sub)halo finder can identify the subhalo plus the analytic countdown given in Eqn. (1.24).

A two-mode formalism is adopted in the Munich models. Here, a high-energy or “quasar” mode occurs subsequent to mergers, along with a constant low-energy “radio” mode, which suppresses cooling flows (Croton et al., 2006). In the quasar mode, accretion of gas onto the black hole peaks at  $z \sim 3$ , while the radio mode reaches a plateau at  $z \sim 2$ . AGN feedback is assumed to be efficient only in massive halos, with supernova feedback being more dominant in lower-mass halos.

In De Lucia and Blaizot (2007), the amount of reheated (by supernovae) cold gas is proportional to the stellar mass, and the mass ejected from the halo is inversely proportional to the host halo’s circular velocity squared (Croton et al., 2006).

## CHAPTER 1

$$\dot{M}_{reheat} \propto \dot{M}_* \dot{M}_{eject} \propto V_{vir}^{-2} \dot{M}_* \quad (1.29)$$

As also occurs with the Durham models, some of the gas will be ejected from low mass halos.

Bertone et al. (2007) adopt a more sophisticated treatment of supernova feedback, while maintaining the same AGN feedback as in De Lucia et al. (2006). Rather than simply parametrising the effect of supernovae feedback, the Bertone et al. (2007) model follows the dynamical evolution of the wind as an adiabatic expansion followed by snowploughing. This implementation has the effect of increasing the luminosity of the brightest galaxies. The calculation of merger timescale in the De Lucia et al. (2006) model follows that of Croton et al. (2006) and is based on a similar equation to the Durham model and is given in eqn. 1.24.

The properties of groups in the De Lucia and Blaizot (2007) and Bertone et al. (2007) models are similar to one another, as are the properties of the two Durham models - Bower et al. (2006) and Font et al. (2008). Thus, in some of what follows, we just discuss the De Lucia and Blaizot (2007) and Bower et al. (2006) model predictions, as they are both excellent representatives of their models' lineage. We discuss the results based upon their descendants, Bertone et al. (2007) and Font et al. (2008), respectively, only when they show significantly different behaviour from De Lucia and Blaizot (2007) and Bower et al. (2006).

Another minor point to note is that these SAMs sometimes “double count” certain galaxies, in the sense that the same galaxy may be listed more than once, with a different ID and history, but the same particle position as another galaxy. This trend is slightly more common in the Durham models than in the Munich models. Thus a galaxy group may be formed of several galaxies in exactly the same place and so have zero galaxy separation. This is not a large effect, and

does not affect the results of the analysis which follows. This effect is  $\sim 1\%$  of all galaxies in the Bower model and far less in the Munich models.

## 1.5 N-body data

Using the same cosmology as the Millennium run we also used an N-body simulation by Nagashima et al. (2005), N05, although not the SAM also presented in the same paper. This simulation uses a  $70h^{-1}$  Mpc box, and  $512^3$  particles. This means that the mass and force resolution is much finer than in the Millennium run. We limit the mass to those (sub)halos with a mass greater than  $1.72 \times 10^{10} M_{\odot}$ . This corresponds to 80 particles in N05, (20 particles in the Millennium Run<sup>2</sup>). In order for the mass limits of the datasets to match, we should use a mass cut of almost 200 particles. However, subhalos rapidly loose up to 90% of their mass, due to stripping (Klypin et al., 1999; Diemand et al., 2007). This mass limit is also greater than the completeness limit of the simulation. The mass function of the simulation begins to turn over at 40 particles, such that there are more halos with 40 particles than with 20. This is clearly not correct for a  $\Lambda$ CDM cosmology which is expected to follow the Press-Schechter function, Press and Schechter (1974). Hence, we limit the size of the haloes we utilise in the N-body model exploration, and set a minimum luminosity for galaxies in the SAMs to -17 magnitudes in the r-band.

## 1.6 Types of Group & Observational Data.

We employ a wide range of observational data related to groups, to compare with the SAM predictions: these include the datasets of Tucker et al. (2000), Tago et al. (2008, 2010), Yang et al. (2007) along with those of Allam and Tucker

---

<sup>2</sup><http://galaxy-catalogue.dur.ac.uk:8080/Millennium/Help?page=simulation>

## CHAPTER 1

(2000), Barton et al. (1996), Hickson (1982), and Hickson et al. (1992). We include the Hickson Groups because they are the archetypical and best-studied sample of compact groups, and remain the primary source against which all newer catalogues are compared. Completion corrections for Malmquist bias in these magnitude-limited group catalogues are problematic; how each relevant observational dataset dealt with this bias is described below.

### 1.6.1 Loose groups

In a general (and ideal) sense, groups as a whole are virialised ensembles of galaxies orbiting a common centre, but without the richness possessed of more massive clusters. We use the word “ideal” to reflect the fact that many so-called groups are not bound physically, but instead have been categorised as groups based upon random projection effects. Although we can identify objects which are in close proximity in projection, it is not possible to be precise along the line of sight. For distant objects we must rely on the Hubble flow to identify where a galaxy lies, but this is complicated by the line-of-sight peculiar velocities of the galaxies; a peculiar velocity of 1000 km/s can result in an error in the distance derivation of  $\sim 10h^{-1}$  Mpc.

Ideally, the loose group identified in a redshift survey should correspond to actual bound objects, although this is not always the case because of the problems outlined above. Kim et al. (2002) and Nichol (2004) compared various methods - e.g. Adaptive Kernel, Voronoi Tessellation and Friends-of-Friends - of *cluster* identification but groups often have different properties. The most commonly used method (Eke et al., 2004; Tago et al., 2008; Huchra and Geller, 1982) is the Friends-of-Friends (FoF), see Chapter 2. In N-body simulations, a group is defined as a virialised region with mass greater than an individual galaxy and less than a cluster, usually taken to lie between  $5 \times 10^{11} M_{\odot}$  and  $5 \times 10^{13} M_{\odot}$ . In

## CHAPTER 1

redshift surveys, where the group-cluster division is done on the basis of galaxy numbers, a group has  $3 < N_{mem} < 30$  galaxies, where  $N_{mem}$  is the group richness, although this is again complicated by the aforementioned Malmquist bias plaguing magnitude-limited surveys. These divisions are not well-defined and vary between authors; this is a representative problem when comparing observational data with theoretical predictions - the former tend to prefer to work in “luminosity space”, while the latter tend to favour “mass space”.

### 1.6.2 Tucker et al. (2000)

This group catalogue was taken from the Las Campanas Redshift Survey (Schechter et al. 1996), an optically-selected redshift survey extending to  $z = 0.2$ . The sample of galaxies spans recession velocities of 7500 to 50000 km/s and luminosities between  $-22.5$  and  $-17.5$  in the R-band. Groups are selected to lie within the velocity range 10000 to 45000 km/s, to avoid incompleteness. Galaxies were assembled into groups via a Friends-of-Friends algorithm (Chapter 2). The linking length is adaptive, meaning the linking length increases with distance according to the galaxy sampling rate.

The linking lengths are given by

$$D_{ij} = 2D_{ave} \sin(\theta_{ij}/2) \leq D_L$$

$$V_{ij} = c \times |z_i z_j| \leq V_L$$

where  $D_{ij}$  is the projected linking length,  $D_{ave}$  is the average distance of galaxies  $i$  and  $j$ , and  $\theta_{ij}$  is the angular separation of galaxies  $i$  and  $j$ .  $D_L$  is the fiducial linking length,  $V_{ij}$  is the line of sight linking length,  $c$  is the speed of light,  $z_{i,j}$  is the redshift separation of galaxies  $i$  and  $j$ , and  $V_L$  is the fiducial line-of-sight

## CHAPTER 1

linking length.

These limits come from the choices of linking length which are  $0.715h^{-1}$  Mpc in projection and 500 km/s along the line-of-sight, so ten galaxies stretched out along the line-of-sight can exceed the velocity range of the survey. The projected linking length corresponds to a minimum density contour of 80 above background. One limitation of this survey is that each field is observed only once, so that close galaxies in groups can be split and group properties misrepresented.

The final catalogue contains 1495 groups which include 35% of the total number of galaxies in the sample. The group definition requires three galaxies to be linked in order to make a galaxy group.

### **1.6.3 Yang et al. (2007,2008)**

The next important compilation of groups is that of Yang et al. (2007, 2008), based upon the fourth data release of the Sloan Digital Sky Survey (Adelman-McCarthy et al. 2006; SDSS DR4), and in particular, the Sample II described therein.

The group finder (Yang et al., 2005) uses an FoF algorithm with a linking length of 0.3 times the mean galaxy-galaxy separation in projection, and 0.05 along the line-of-sight. From this, the geometric and luminosity weighted centres are identified. Each group is assigned a characteristic luminosity and the mass-to-light ratio and the mass of the parent dark halo is assumed. Galaxies are assigned to the halo and various group properties are calculated. The distance of each galaxy from the group centre is identified and a galaxy number density found. If this density is above a certain threshold then it is applied to the group. This process is iterated.

Yang et al. (2008) apply this catalogue to conditional luminosity functions, which we will use in a later chapter.

#### 1.6.4 Tago et al. (2008; T08); Tago et al. (2010; T10)

The T08 catalogue is based on SDSS DR5 (Adelman-McCarthy et al. 2007) using the FoF approach, with a scaling relation with distance of,

$$LL/LL_o = 1 + a \arctan(d/L) \quad (1.30)$$

where  $LL/LL_o$  is the scaling of the linking length,  $a$  is a constant,  $d$  is the comoving distance of the object and  $L$  is the fiducial distance (Tago et al., 2008). The justification for this approach is that this scaling procedure removes many of the systematic changes to the group with distance. An example is that in Eke et al. (2004) the size of a group increases steadily with distance. This catalogue uses a more traditional scaling procedure based on the selection function of the survey. This systematic bias is considerably reduced using the Tago et al. approach. Values of the parameters in Equation (1.30) are found by taking galaxy groups and shifting them to various distances and identifying how the changing luminosity cut affects the group size. Tago et al. (2008) fit  $a = 0.83$  and  $L = 169.8h^{-1}$  Mpc to Eqn. (1.30). The linking parameters in the line of sight are 250km/s and  $0.25h^{-1}$  Mpc, in projection. These choices avoid the inclusion of filament galaxies. Groups are produced using a fixed linking length, and are then translated to various distances, so much so that some galaxies become too dim to be identified. The groups are then examined using a minimal spanning tree in order to find the minimum linking length required to reassemble the group. The trend of this linking length with distance is used to identify Eqn. (1.30) and define the constants  $a$  and  $L$ .

Tago et al. (2010) apply the same method to SDSS DR7 Adelman-McCarthy et al. (2008), where  $a = 1$  and the scaling redshift is 0.05. However, they also apply FoF to a volume-limited sample with a minimum luminosity of  $-18$  mag. The linking length scaling is derived iteratively, using the mean redshift of the

## CHAPTER 1

group to set the distance scale. Also, no group is identified with  $> 100$  members, because the scaling law was found to break down at this point, resulting in unphysically large clusters.

### 1.6.5 Compact Groups

There are several definitions of compact groups in the literature. The original quantifiable definition was by Hickson (1982), who specified four criteria for defining compact groups:

1.  $N_{members} > 4$  (Richness)
2.  $\theta_N \geq 3\theta_G$  (Isolation)
3.  $\bar{\mu}_G < 26.0$  (Compactness)
4.  $m_{min} = m_{BGG} + 3$  (Luminosity)

where  $N$  is the number of galaxies,  $\theta_N$  is the angular separation of the group and the nearest non-group member,  $\theta_G$  is the angular diameter of the group, and  $\bar{\mu}_G$  is the group surface brightness,  $\bar{\mu}_G = m + 2.5\log(A)$ , where  $m$  is the total apparent magnitude of galaxies and  $A$  is the area in square arcseconds. An additional criterion is that the galaxies that are included are those which lie within three magnitudes of the brightest group galaxy (BGG).

There are certain limitations and justifications for each of these criteria. The magnitude restriction attempts to limit the redshift range of the galaxies assigned to a group. The isolation criterion excludes cluster cores and high density regions; the compactness criterion ensures that the group is compact in projection. The galaxies are separated by approximately their own diameter, and yet provide a large enough sample from the survey. The most complex of these rules is the isolation criterion which limits both the local density of the environment and

## CHAPTER 1

limits the size of the group. However, the isolation criterion fails in its objective to exclude objects which are subsets of larger systems because Tovmassian et al. (2006) found that many compact groups are the dense cores of loose groups. It also can exclude valid systems because of an interloping galaxy within the zone of exclusion. Other catalogues have been developed, based on Hickson's criteria, modified to take into account the specifics of a given survey - e.g. Iovino (2002) and Focardi and Kelm (2002).

Barton et al. (1996), however, implemented a friends-of-friends procedure to identify compact groups by taking advantage of the redshift information of the CfA Survey (Huchra et al., 1983). Galaxies are linked by their distance in projection, and by their redshift velocity along the line of sight. The search areas for neighbours are cylindrical, as opposed to our 3D spherical search area. Barton et al. (1996) settled on a linking length of 50 kpc in projection and a redshift velocity linking length of 1000 km/s. This line of sight linking length corresponds to  $10h^{-1}$  Mpc, to take into account the peculiar velocity of galaxies. They arrived at these values by exploring the parameter space, and chose the linking lengths which most closely matched Hickson's results.

Hickson's criteria, which are the basis for all compact group studies, are quite arbitrary; for example, the compactness criterion was given its particular value to ensure groups were compact, but also to simply ensure that there were sufficient groups in his catalogue.

### **1.6.6 Barton et al. (1996)**

Barton et al. (1996) were the first to identify compact groups using a FoF algorithm, the linking lengths for which were employed in the Allam and Tucker (2000) work described below. They use the CFA2 (Geller and Huchra, 1989; Huchra et al., 1990, 1995; Giovanelli and Haynes, 1985) survey containing 6500

## CHAPTER 1

+ 4283 galaxies along with the SSRS2 survey (da Costa et al., 1988) containing 3600 galaxies. These observations made use of photographic plates and avoided the fibre-induced errors faced by Tucker et al. (2000). Barton et al. (1996) use  $V_L = 1000$  km/s and  $D_L = 50$  kpc, chosen as noted earlier, to recover the trends defined by the Hickson compact groups.

### 1.6.7 Allam et al. (2002)

This catalogue of compact groups is the companion to Tucker et al. (2000). The survey limits are the same, both in luminosity and recession velocity. The principal difference is that the linking lengths in the FoF algorithm were modified. The projected linking length is  $50h^{-1}$  kpc and the line of sight linking length is 1000 km/s. The linking length again scales in the same way as before. Apart from the increased velocity space linking length, we would expect these galaxies to be a subset of the Tucker et al. groups. That the line-of-sight linking length differs makes direct comparison with the work outlined in subsequent chapters somewhat difficult. This catalogue contains a total of 76 groups, although this will not be a complete sample for the field because of the selection effects described in Tucker et al. (2000).

## Chapter 2

# DISTRIBUTION AND RICHNESS OF GROUPS

### 2.1 Introduction

We begin our examination of group properties by investigating group populations at  $z=0$ . We assemble groups using different linking lengths. This will give us an overview of how changing the linking length of the FoF algorithm, and therefore the galaxy density of groups, effects the spatial distribution of the objects identified. This is a logical first step in identifying any differences between the SAMs and the observations of Tago et al. (2010), between  $z=0$  and  $z=0.2$ . Within the Millennium Simulation at  $z=0$ , the four SAMs yield different numbers of galaxies, despite being built upon the same underlying dark matter distribution. It is useful to review the respective galaxy numbers, and distributions, for these models. A summary of the four SAMs used is shown in Table 2.1.

Table 2.1: Summary of the SAM models and their basic differences

Family	Model	Reference	Description
Munich	M_D06	De Lucia et al. (2006)	2 mode AGN
Munich	M_B07	Bertone et al. (2007)	Improved SN feedback
Durham	D_B06	Bower et al. (2006)	Single mode AGN
Durham	D_F08	Font et al. (2008)	More gradual ram-pressure stripping
N-body only	N05	Nagashima et al. (2005)	High resolution N-body

## 2.2 Group Finding Algorithm and the construction of group catalogues for the present work.

The Friends-of-Friends algorithm is one of the most popular methods of assembling galaxies into groups (Geller and Huchra, 1983). It links galaxies together based on spatial proximity. If we start at galaxy 1, we search for all galaxies within a distance  $l$  of that galaxy; then, for each of those galaxies, we search for all galaxies within  $l$  that have not already been assigned to a group. We continue this process until no more galaxies are added to the list. These linked galaxies are then a group. In a 3D simulation volume such as the Millennium Run and the Nagashima et al. (2005) simulation  $l = \sqrt{dx^2 + dy^2 + dz^2}$ , where  $l$  is the linking length,  $dx$  is the separation along the  $x$  axis,  $dy$  is the separation along the  $y$  axis, and  $dz$  is the separation along the  $z$  axis.

In observational catalogues this procedure becomes more complex, requiring separate linking lengths in projection (right ascension and declination) and along the line of sight. Typically the linking length needs to be much greater along the line of sight because distances are calculated from the Hubble flow, but are affected by the peculiar velocities of the galaxies. For example, in Barton et al. (1996), the projected linking length is  $50h^{-1}$  kpc in projection and 1000 km/s along the line of sight, which is equivalent to  $10000h^{-1}$  kpc - i.e., two orders of magnitude greater. Another problem, discussed in detail by Eke et al. (2006)

## CHAPTER 2

and Tago et al. (2008) is that a technique must be found for compensating for the fact that the observation threshold for galaxy absolute magnitudes increases with distance, so that at great distances only the very brightest objects can be seen. This typically results in more distant galaxies appearing more diffuse.

### 2.2.1 Synthetic group catalogues

In order to construct a statistically significant (and representative) galaxy group catalogue, we have worked with a sub-sample of the Millennium Simulation amounting to  $\sim 3\%$  of the available volume: specifically, 64 boxes of length  $125h^{-1}$  Mpc drawn from the database. Our results are robust to this choice, having been tested *a posteriori* on alternate  $125h^{-1}$  Mpc boxes. A luminosity limit of  $M_r = -17$  in the SDSS r-band was imposed. At lower luminosity the effect of the limited mass resolution of the N-body background affects the completeness of the sample. We identify galaxy groups as overdensities in the galaxy population using an FoF algorithm (Geller and Huchra, 1983). No maximum number of members is set but we require that at least four galaxies be linked in order to define a group. Although this removes groups such as the Local Group, it does adhere to Hickson’s (1982) definitions for compact groups.

We first construct a “loose group” (LG) catalogue using a linking length of 0.2 times the mean inter-particle separation. This linking length was chosen based on the assumption that the galaxy position distribution traces the dark matter exactly.

A linking length of 0.2 times the mean inter-particle separation corresponds to a co-moving linking length of  $\sim 500h^{-1}$  kpc. To further examine the effects of density we also define two “compact group” catalogues, Compact (CG) and Very Compact (vCG) Groups, using co-moving linking lengths of  $150h^{-1}$  kpc and  $50h^{-1}$  kpc, respectively. The vCG linking length is comparable to the projected

## CHAPTER 2

linking length used by Barton et al. (1996) and Allam and Tucker (2000) to identify groups. The value of  $50h^{-1}$  kpc is arrived at by calibrating to the Hickson (1992) catalogue using projected galaxy separations. The middle linking length of  $150h^{-1}$  kpc is similar to that advised by McConnachie et al. (2008), based upon their 3D linking length analysis of mock catalogues of Hickson compact groups based on the De Lucia et al. (2006) SAM.

Henceforth we refer to the SAMs as M\_B07, M\_D06, D\_B06, D\_F08 for the Bertone et al. (2007), De Lucia and Blaizot (2007), Bower et al. (2006) and Font et al. (2008) models, respectively. In selecting the galaxies we will use to assemble our groups we must bear in mind the limits of the Millennium Run. There is a completeness limit on the Millennium Run SAMs caused by the finite mass resolution. Galaxies with a luminosity less than -17 mag are incomplete because dark matter halos below a certain mass resolution are poorly detected.

Another catalogue, based on all galaxies that lie within the same dark matter halo, hereafter called the halo-based group catalogues, is also produced, as this is the natural unit of the SAMs. Each galaxy is assigned to a particular halo by SUBFIND based on whether a given halo contains the dark matter particle that is flagged to be a particular galaxy.

We also provide a small sample of compact groups from the Nagashima et al. (2005) N-body simulation, called N05.

Where possible, these synthetic group catalogues are compared directly with the empirical datasets of Tucker et al. (2000), Allam and Tucker (2000), and Tago et al. (2008); the former two datasets are particularly useful in this regard as they provide both loose and compact groups from the same underlying survey.

We also construct observational group catalogues based on the method of Tago et al. (2010), shown in section 1.6.4 of Chapter 1. We apply our FoF algorithm using the same parameters and linking lengths as Tago et al. (2010) and can

## CHAPTER 2

recover the same catalogue (volume limited;  $-18$  mag) to within 1% accuracy. We can then use this algorithm to produce a loose-compact group catalogue. The difference is due to the methods we use to calculate the velocity separation which has an effect on the projected separation as well.

We note that the CG galaxies are, by necessity of the group finding algorithm, subsets of the LG catalogue, in that every galaxy assembled into a group at short linking length must be part of a group with a larger linking length. Our catalogues also contain clusters and cluster cores, a point to which we return shortly. The physical interpretation of the linking length variation and its impact upon resulting galaxy distribution is non-trivial. The FoF algorithm essentially probes deeper into the potential well at shorter linking lengths, selecting galaxies closer to the cluster/group core. These galaxies are generally old, and have sunk deeper into the cluster potential, or they are galaxies near their respective orbital pericentre.

However, the algorithm also extracts galaxies in the cluster periphery that happen to be close to one another, either by chance or as an artifact of their infall history. These peripheral groups are a natural part of the analysis and can be considered as essentially cluster substructure. They represent a negligible proportion of LGs but can represent  $\sim 20\%$  of CGs and vCGs. Conversely, the adopted LGs linking length, while popular in the literature, usually associates galaxies from small separate halos and assigns them to the cluster/group when they are not within the cluster/group enveloping dark halo.

Groups can also be defined according to the position of galaxies in the host dark matter halo. There are slight differences in the definition of host halo in the Durham and Munich models. In the Durham models the hosts are based on FoF halos and a SUBFIND pass to identify those halos only connected spuriously. Munich groups are merely FoF groups.

## 2.3 Global properties

The spatial distribution and richness of groups is highly dependant on the luminosity limits of a particular dataset. For comparison with SDSS observations, we concentrate on luminosity cuts in the SDSS r-band. However, we also note certain properties of the Johnson R-band. The relationship between these two bands is fairly close: the best fit for M\_D06 is,

$$J = 0.94 \times S - 0.7, \quad (2.1)$$

where J is the Johnson R-band, and S is the SDSS r-band. D\_B06 shows a best fit line of:

$$J = S - 0.06, \quad (2.2)$$

There is very little scatter in these profiles. This means that there is only a small difference in the catalogues, regardless of bands chosen. This difference, though slight, is larger in the Munich models. The result of this is that we can use either the sdss-r and Johnson-R bands interchangeably.

### 2.3.1 Spatial Distribution

The starting point for any exploration of group properties has to be the background galaxy distribution. We show below the initial number of galaxies, or dark halos, in the datasets. We also provide the corresponding standard deviations for the SAMs. There is no standard deviation for the N05 model, because there is only one volume. For the -17 mag cut we find:

- $\Delta_{D\_B06} = 0.065 (0.006) h^3 \text{Mpc}^{-3}$
- $\Delta_{D\_F08} = 0.066 (0.009) h^3 \text{Mpc}^{-3}$
- $\Delta_{M\_D06} = 0.063 (0.006) h^3 \text{Mpc}^{-3}$

## CHAPTER 2

- $\Delta_{M\_B07} = 0.050$  (0.005)  $h^3\text{Mpc}^{-3}$
- $\Delta_{N05} = 0.12 h^3\text{Mpc}^{-3}$

where  $\Delta$  is the number of galaxies per cubic megaparsec. The first number is the mean spatial density in the 64 subvolumes, and the number in brackets is the standard deviation. We henceforth refer to  $\Delta$  as the “spatial density”.

The M\_B07 model has the fewest galaxies, while the other three SAMs have essentially the same number of galaxies per cubic megaparsec. This difference in galaxy number density is due to the different supernova feedback approach implemented in the M\_B07 model. This particular approach reduces the number of dim galaxies, while making the brightest galaxies unphysically brighter (Bertone et al., 2007).

Halo-based groups follow the general distribution of dark matter halos. These groups are assembled by grouping galaxies that lie within the same dark matter halo. For FoF groups, as the linking length decreases, so too does the number of galaxy groups. For each SAM, a box,  $125h^{-1}$  Mpc on the side, was extracted from the entire Millennium volume, and the group finder was run at various linking lengths. When linking lengths are referred to it is the FoF groups that are being discussed. The resulting distributions are shown in Fig. 2.1. Panel 1 shows that Durham models produce a higher number of groups than either Munich model. It also shows that D\_F08 produces the most groups at all linking lengths. This is a consequence of the ram pressure stripping procedure implemented in D\_F08, where the loss of hot gas from the galaxy is more gradual than in the other models.

Panel 1 clearly shows that the M\_B07 model produces the fewest groups overall. The two Munich models converge at short FoF linking lengths, but the trends begin to diverge at  $\sim 200h^{-1}$  kpc. This is because the M\_D06 model has a significantly steeper slope in the range,  $200 - 500h^{-1}$  kpc. The result of

## CHAPTER 2

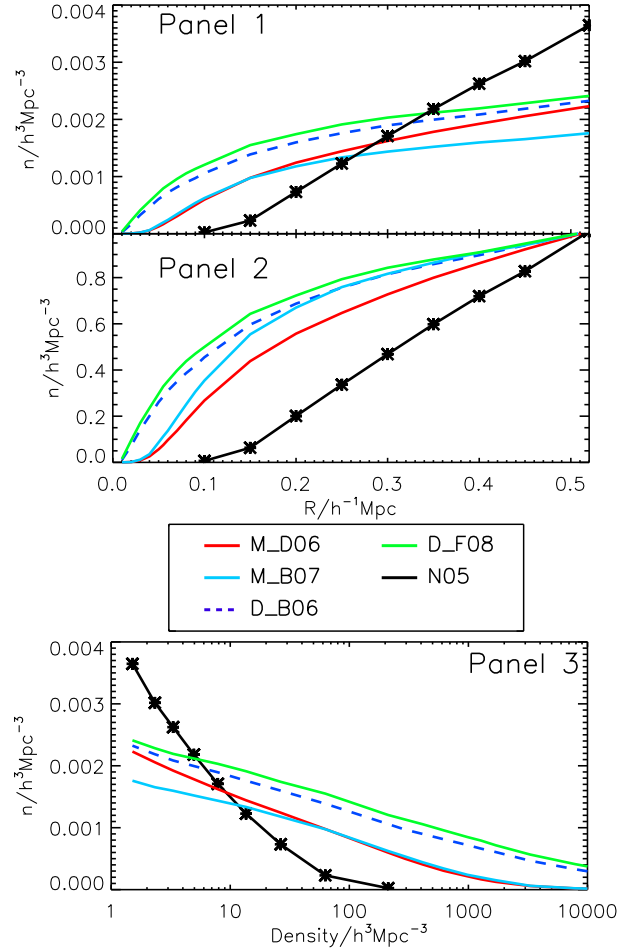


Figure 2.1: The spatial density of groups according to the linking length (top panel), profile normalised by the number of LGs (second panel), and the spatial density distribution according to the density contour (bottom panel). The blue dashed, red, pale blue, green and black lines show the D\_B06, M\_D06, M\_B07, D\_F08 and N05 models respectively.

this different gradient is that M\_B07 produces far fewer LGs. The Durham and Munich models show increasingly different group populations as the FoF galaxy group finer linking length *decreases*. Although the M\_B07 model produces far fewer loose groups, the profile has the same gradient as the Durham models, at longer linking lengths. The result of the supernova feedback process implemented in M\_B07 is to remove some of the galaxies close to the luminosity cut. This has the effect of reducing the number of groups with more than four galaxies of  $\text{mag} < -17$  in the r-band. The N05 catalogue, however, produces a significantly lower

## CHAPTER 2

compact group population than any of the SAMs.

The linking length of the FoF galaxy group finder can also be interpreted as a density threshold, in that we have two particles within a search radius  $l$ . Thus, the minimum density of objects in groups is given by

$$\rho = \left( \frac{3}{2\pi l^3} \right) \quad (2.3)$$

This is shown in Panel 3 of Fig. 2.1. Our vCGs, CGs and LGs have a galaxy density threshold of  $3.8 \times 10^3$ ,  $1.4 \times 10^2$  and 3.4 respectively, which corresponds to an overdensity of  $\sim 60000.0$ , 2000.0 and 52.0. The overdensity is  $\Delta = \rho/\bar{\rho}$ , where  $\rho$  is the density contour picked out by the FoF algorithm, and  $\bar{\rho}$  is the background galaxy density. This means we produce a density profile of galaxies in the simulation volume. We conclude that galaxies in the Durham models tend to occupy significantly denser regions than galaxies in the Munich models. The N05 N-body simulation produces a third as many CGs as in the M\_D06 model, while LGs are twice as common.

The most striking difference between the group populations in the SAMs, and in the N-body simulation, is that the spatial density/linking length gradient is much steeper in N05. The profile is practically linear for N-body and curved for the SAMs. We fit a polynomial to give a quantitative estimate of the difference between the models. The form we fit is,

$$y = (m \times l + c)^{\frac{1}{\alpha}} \quad (2.4)$$

where  $m, c$  and  $\alpha$  are constants, and  $l$  is the linking length. The slope of the distribution is much steeper for a low value of  $\alpha$ , as shown in Panel 2 of Fig. 2.1. Restricting the discussion to the relevant sampling criteria (i.e.,  $Mr < -17$ ), the M\_D06 & M\_B07, and D\_B06 & D\_F08 models have a galaxy number density given in Table 2.2.

## CHAPTER 2

Table 2.2: The best fit polynomials for the changing spatial density of groups with linking length.

Model	m	c	$\alpha$
B06	$6.1 \times 10^{-9}$	$-3.9 \times 10^{-10}$	3.24
D06	$6.4 \times 10^{-6}$	$-4.5 \times 10^{-7}$	2.09
B07	$1.4 \times 10^{-8}$	$-1.1 \times 10^{-9}$	2.98
F08	$2.5 \times 10^{-10}$	$-1.6 \times 10^{-11}$	3.79
N05	$6.1 \times 10^{-3}$	$-7.9 \times 10^{-4}$	1.08

The relative proportions of galaxies that are classified as being members of groups, along with the average group richness, are listed in Table 2.3. The percentage of galaxies associated with LGs is comparable in three of the four SAM variants. The M\_D06 model shows approximately 6 percent fewer groups than D\_B06 groups. The models diverge increasingly with decreasing linking length.

The difference in the proportion of galaxies in groups should provide a key diagnostic for comparing and discriminating between the four SAMs. Indeed, McConnachie et al. (2008, 2009) compared compact groups in mock redshift catalogues to SDSS DR6 observations, and concluded that the M\_D06 SAM overproduced compact groups by  $\sim 50\%$ . By extension, this means that the D\_B06 & D\_F08 models necessarily result in an even more dramatic “overproduction” of CGs (by an order of magnitude), suggesting that the Durham models provide a significantly worse fit to the empirical data.

The steepness of the N-body slope is, in part, due to overmerging. When halos fall into a larger halo they are tidally stripped. Nagashima et al. (2005) approximate the rate at which this occurs using

$$\frac{r_t}{r_s} = \frac{r_{peri}}{r_{apo}} \frac{M_h}{M_s} \left( \frac{V_{circ,s}}{V_{circ,h}} \right)^3, \quad (2.5)$$

where  $r_t$  is the stripped radius,  $r_s$  is the pre-stripped radius,  $r_{peri}$  and  $r_{apo}$  are the pericentric and apocentric radii,  $M_h$  is the host mass,  $M_s$  is the subhalo

## CHAPTER 2

mass and  $V_{circ,h}, V_{circ,s}$  are the circular velocities of host and satellite. For a given radial distribution, Eqn. 2.5 gives the mass stripped in one orbit. However, Klypin et al. (1999) discovered that the finite numerical resolution of simulations results in additional numerical stripping. Also, galaxies continue to exist after their dark matter (sub)halos have dropped below the identification threshold, as in Limousin et al. (2009). Dark matter halos extend far beyond the inner region that contains the galaxy, and so in close spatial proximity to group cores a halo finder has difficulty in identifying individual (sub)halos (Gill et al., 2004). At lower resolution, the subhalos can only be found within an unphysically brief amount of time. These considerations mean that we limit the minimum group finding linking length to  $150h^{-1}\text{kpc}$ . The fact that galaxies last longer than haloes is not entirely due to the numerical limitations of the simulation. The longer life of galaxies makes physical sense, because the baryons are at the bottom of the potential well, and subhalos are stripped from the outside in (Diemand et al., 2007).

We include the total number of galaxies in Table 2.3. We do this in order to make direct comparisons between the datasets, as it provides a method of normalisation.

Finally, we compare the D\_B06 and M\_D06 to T10 in Fig. 2.2. In one  $125h^{-1}$  Mpc box we find the total number of galaxies with a particular luminosity cut. We chose these to match the luminosity cuts of the Tago et al. (2010) volume limited catalogues, namely, -17,-18,-19 and -20 in the r-band

Figure 2.2 shows that there is a different trend in galaxy fraction in observations and SAMs. The gradients of the number of groups versus linking length in the three catalogues are different. The models show a decreasing gradient with linking length, while in the observations the gradient increases. In principle, this may be due to the 2D group finding method used in the observations, while the

CHAPTER 2

Table 2.3: The number of galaxy groups in M\_D06 and D\_B06 and T10 as a function of linking length. The numbers in each column are for the different luminosity cuts. The order quoted is where the r-band magnitude is:  $< -18$ ,  $< -19$ ,  $< -20$ , respectively.

ll	D_B06	M_D06	T10
all	(95000,53142,26247)	(94262,56986,27071)	(40665,94912,148195)
400	2643, 1453, 533	1847, 758, 235	-, -, 2771
350	2541, 1362, 507	1695, 693, 203	-, -, 2267
300	2384, 1269, 450	1522, 607, 186	-,2108, 1814
250	2212, 1182, 396	1363, 526, 151	996, 1687,1283
200	1994, 1022, 342	1126, 431, 122	786, 1254, 800
150	1681, 855, 275	822, 316, 89	521, 774, 413
100	1277, 640, 196	480, 171, 43	242, 297, 112
50	728, 310, 96	85, 35, 10	41, 21, 3

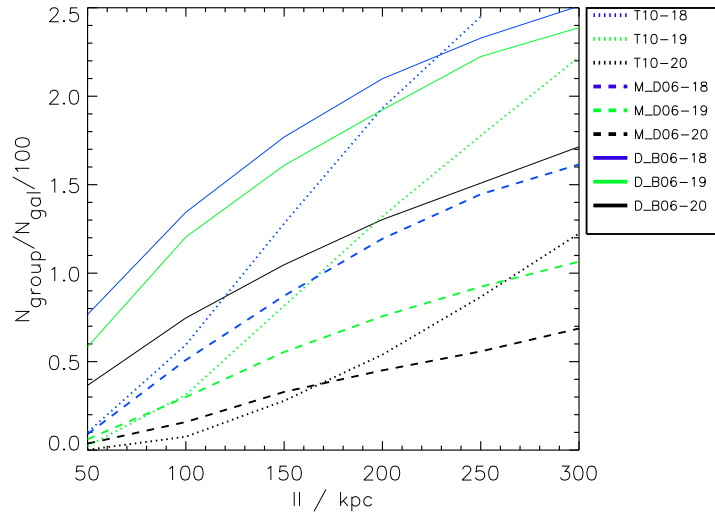


Figure 2.2: The profiles of the number of groups in the D\_B06 and M\_D06 models and T10 observations normalised to the total number of group galaxies. Corresponds to Table 2.3. Black is for the -20 magnitude cut, Green is the -19 magnitude cut and Blue is for the -18 magnitude cut. The solid lines show D\_B06 groups and the dashed lines are for M\_D06 groups, the dotted lines are for T10 observation groups.

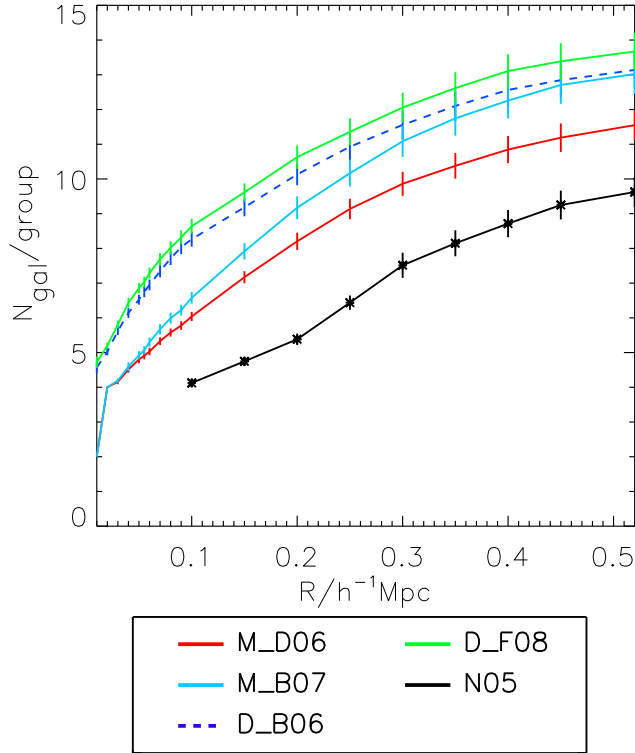


Figure 2.3: Shows the distribution of mean group richness against linking length in the D\_B06 (blue dashed line), D\_F08 (green solid line), M\_B07 (blue solid line), M\_D06 (red solid line) and N05 (black solid line) datasets. The errors are  $\sigma/\sqrt{N}$ , where  $\sigma$  is the standard deviation and  $n$  is the number of groups at that linking length.

models use a 3D linking length. Upon examination, however, we find this is not the case. In the D\_B06 model, which we use to test the above idea, we find that the gradient of the profile decreases with increasing linking length distance. This suggests that this trend is intrinsic to the SAM method of placing galaxies, which does not mimic the universe. The profiles with linking length depend on the placement of galaxies in groups, which is discussed in the next chapter.

### 2.3.2 Group Richness

The group richness is a measure of the number of galaxies present in a group at a given linking length. We see in Fig. 2.3 and Table 2.4 that there are obvious patterns in the richness profiles. Of the four SAMs, the M\_D06 model produces

## CHAPTER 2

Table 2.4: The mean group richness for each model at the different linking lengths. The number in brackets indicates the variation in different subvolumes. The ‘\*’ specifies that loose groups in Tago et al. (2010) corresponds to  $l = 250h^{-1}\text{kpc}$  with a -18 mag cut instead of the number quoted in the first column. The T10 column also shows the mean number of galaxies per group at each linking length. Errors in the T10 column are of the form  $\sigma/\sqrt{N}$

model	D_B06	M_D06	M_B07	D_F08	N05	T10
<i>halos</i>	14.9	13.3	14.6	15.2	11.4	
$l = 520h^{-1}\text{kpc}$	13.5 (0.1)	11.8 (0.07)	13.6 (0.1)	14.0 (0.1)	9.6	$6.5^* \pm 0.2$
$l = 150h^{-1}\text{kpc}$	9.4 (0.04)	7.5 (0.04)	8.4 (0.05)	9.7 (0.05)	4.7	$5.3 \pm 0.1$
$l = 50h^{-1}\text{kpc}$	6.6 (0.02)	4.7 (0.01)	4.9 (0.01)	6.7 (0.02)	N/A	$4.1 \pm 0.1$

groups with the lowest richness at all linking lengths.

N05 shows a lower richness than any of the SAMs. This is due to the issues described in the previous section. For comparison, Hickson (1982) finds an average richness of 4.2 in compact groups. The richness profile for the SAMs, Fig 2.1, reproduces the fact that there are two families of SAM. All four catalogues produce different profiles for CGs. The gradient of the Munich model profiles is slightly steeper, and produces a significantly lower numbers of large CGs. The N05 simulation has a shallower profile. However, the most striking difference is in vCGs. The Durham models have a similar trend to each other, and produce many times more groups at all richnesses. Munich models produce far fewer groups at all richnesses, as we have already shown in Fig. 2.1. We also present, in Table 2.4, the error on the mean of the 64 subvolumes, i.e.  $\sigma/\sqrt{N}$ , where  $\sigma$  is the standard deviation and  $N$  is 64. This gives us a measure of the variation in the different volumes. There is no error on the N05 sample because we only have a single volume. The way in which the group richness varies with mass is shown in Fig. 2.4.

From Yang et al. (2008), based on the integral of the luminosity functions provided in the paper, see §5.4, and the SAMs D\_B06 and M\_D06, we show the mean total number of galaxies in groups of various masses. In the list below the

## CHAPTER 2

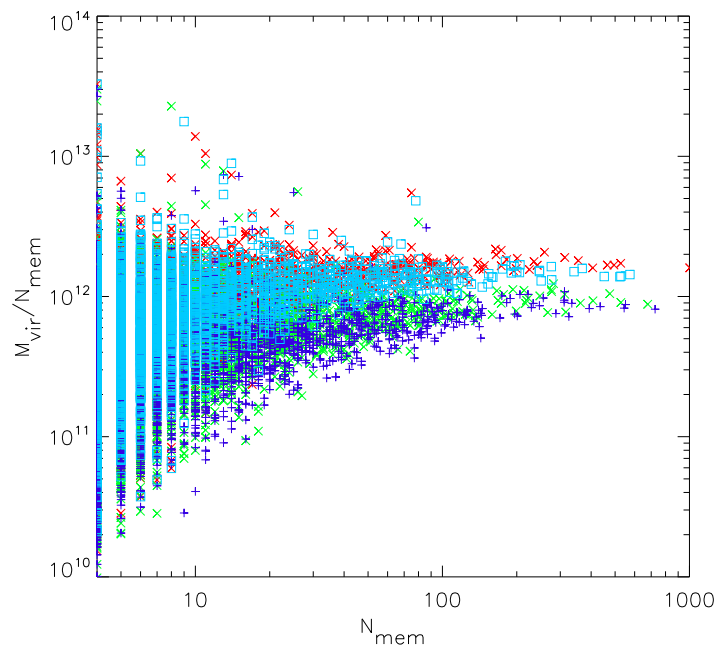


Figure 2.4: The distribution of richness with the mean amount of mass per galaxy in a halo. This is a measure of galaxy density. M\_D06, M\_B07, D\_B06 and D\_F08 are the red, pale blue, dark blue and green symbols. Again we see that there are more galaxies in D\_B06 groups and the amount of mass per galaxy converges for large objects, with greater scatter at low richness.

## CHAPTER 2

results are given in order, Y07, D\_B06 and M\_D06

- $10^{14.4} - 10^{15.0} M_{\odot}$  : 414.4, 366.012, 478.141
- $10^{14.1} - 10^{14.4} M_{\odot}$  : 126.2, 158.459, 215.551
- $10^{13.8} - 10^{14.1} M_{\odot}$  : 56.6, 80.9649, 109.507
- $10^{13.5} - 10^{13.8} M_{\odot}$  : 24.8, 41.4742, 55.2979
- $10^{13.2} - 10^{13.5} M_{\odot}$  : 11.96, 20.8117, 28.181
- $10^{12.9} - 10^{13.2} M_{\odot}$  : 6.57, 10.4643, 14.5028

Both SAMs show a higher group richness than the Yang et al. (2008) observations. It is interesting that the Munich values are higher than the Durham values, but this is based on halo based groups rather than FoF defined objects and is dependant on the mass of the host halo. The hosts in D\_B06 tend to be more massive than in M\_D06. The Yang et al. (2008) data are based on the integration of the luminosity function, which compensates for the selection effects of the survey.

## 2.4 Correlation Functions of Groups

The correlation function of galaxies is a commonly used measurement of the clustering of objects. The distributions of galaxy-galaxy separations are compared with a distribution of random points. The end result of this may be power function of the form

$$\zeta(r) = \left(\frac{r}{r_o}\right)^{\gamma}, \quad (2.6)$$

where  $r$  is the galaxy pair separation,  $r_o$  and  $\gamma$  are free parameters and  $\zeta(r)$  is the correlation function.  $r_o$  is a measure of the clustering distance of the

## CHAPTER 2

distribution and provides a scale for clustering.  $\gamma$  is the slope of the log of the correlation function. There are several forms for  $\zeta(r)$  presented in the literature: see especially Davis and Peebles (1983); Hewett (1982); Hamilton (1993); Landy and Szalay (1993).

The most basic form for the correlation function is

$$\zeta(r) = \left( \frac{DD}{RR} \right) - 1, \quad (2.7)$$

where  $DD$  is the normalised histogram of galaxy pair separations

$$DD = \sum_i \sum_j n(\delta r)_i n(\delta r)_j, \quad (2.8)$$

and  $RR$  is the histogram of random pair separations. However, there are several problems associated with this form, which has led to the development of several new forms. This technique was originally designed for large scale galaxy surveys, and is based on the angular and redshift space separations. The key problem with the above, so-called ‘natural’, form of the correlation function, is that the survey selection function declines with distance. The limits of the natural form led to the development of the Davis and Peebles (1983) estimator,

$$\zeta(r) = \left( \frac{DD}{DR} \right) - 1, \quad (2.9)$$

where  $DR$  is the cross correlation between galaxies and random points, with the same selection function. Other estimators, Hewett (1982)

$$\zeta(r) = \left( \frac{DD - DR}{RR} \right), \quad (2.10)$$

and Hamilton (1993),

## CHAPTER 2

$$\zeta(r) = \left( \frac{DD \cdot RR}{DR^2} \right) - 1, \quad (2.11)$$

attempted to refine this further. This method attempts to reduce selection effects, and decrease the error to approximately Poisson counting errors. Landy and Szalay (1993) presented an estimator where the error was approximately Poissonian,

$$\zeta(r) = \left( \frac{DD - 2DR + RR}{RR} \right), \quad (2.12)$$

The error on this estimator is:

$$\Delta\zeta(r) = \left( \Delta(GG) \frac{1}{RR} \right)^2 + \left( \Delta(CC) \frac{2}{RR} \right)^2 + \left( \Delta(RR) \frac{GG - 2CC}{RR^2} \right)^2, \quad (2.13)$$

where  $\Delta(GG)$ ,  $\Delta(RR)$  and  $\Delta(NN)$  are  $\sqrt{N_{GG}}/N_{g-g-pairs}$ ,  $\sqrt{N_{RR}}/N_{r-r-pairs}$  and  $\sqrt{N_{CC}}/N_{g-r-pairs}$  and  $N_{GG}$  is the number of galaxy-galaxy pairs in a bin and  $N_{g-g-pairs}$  is the total number of possible galaxy-galaxy pairs and  $\zeta(r)$  is the correlation function.

We select the Landy and Szalay (1993) estimator, which has the lowest error, and calculate the correlation function of LG, CG and vCGs. For large volumes we extract a random sample of galaxies. We take this selection because the calculation of the correlation function is an  $N^2$  algorithm, and so it is not feasible to calculate  $\zeta(r)$  for very large numbers of galaxies. We find the correlation function based on 20000 randomly selected groups from each catalogue.

Figure 2.5 shows the correlation function of vCGs and LGs for the M\_D06 and D\_B06 groups. There is a shorter clustering length for LGs than CG and vCGs. CGs have the steepest slope. The correlation length is always less than the mean galaxy-galaxy separation.

## CHAPTER 2

In log space, Eqn. 2.6 has the form,  $y = mx + c$ , where  $m$  is  $\alpha$  and  $c$  is  $-\alpha \log_{10} R_o$ . The power law form is only present in a certain range. At either end of the distribution the profile deviates, as can be seen in Fig. 2.5. We include the poisson error on the distribution.

In Fig. 2.5 we see that there is very little difference in the correlation lengths between groups of similar density in the M\_D06 and D\_B06 models. There is, however, a noticeable increase in the correlation length as the group intergalactic separation changes. This can also be seen in Tables 2.5 and 2.6. In Table 2.6 we have fixed the slope to -1.8 (Mo and White, 1996) in order to make comparisons in the correlation length,  $R$ .

As we increase the group density we see that the correlation length of the groups increases. This indicates that vCGs are more strongly clustered than loose groups. This trend is useful in identifying the properties of the environments of compact groups.

There is a considerable literature, e.g. Mo and White (2002), Mo and White (1996), Jing (1998), Sheth and Tormen (1999), Sheth et al. (2001) and Magliocchetti and Maddox (1999), on how the correlation length of halos is affected by the halo mass and the redshift of formation. For example, Merchán et al. (2000) find that for halos with mass cuts of  $5 \times 10^{12} < M < 4 \times 10^{14} M_{\odot}$ ,  $2 \times 10^{13} < M < 4 \times 10^{14} M_{\odot}$  and  $5 \times 10^{13} < M < 4 \times 10^{14} M_{\odot}$  the correlation lengths are, 9.5, 10.8 and 14.1  $h^{-1}$  Mpc respectively. Thus, the mean vCG appears to occupy a higher mass halo than the mean LG. Mo and White (2002) find that below  $M_*$  there is little dependency of clustering on halo mass, (not found by Jing (1998)), above  $M_*$  there is a strong dependence on mass. This is the regime we are exploring with groups.

At the low galaxy separation,  $R < 2^{-1}$  Mpc, there is a noticeable difference. Unfortunately, this region cannot be fitted with a power law and has large error

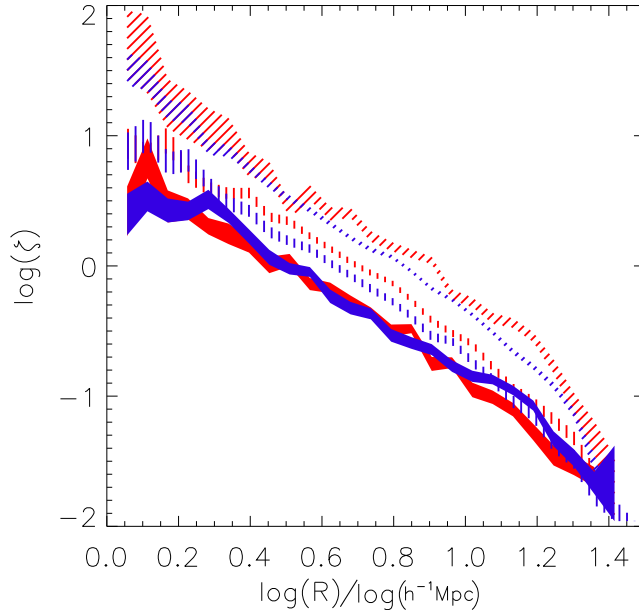


Figure 2.5: The correlation functions of LGs, CGs and vCGs for M\_D06 and D\_B06 models. LGs are shown by the solid block, CGs are vertical lines and diagonal lines are for vCGs. This thickness of the plots shows the error and the M\_D06 model is red, the D\_B06 model is dark blue. The units of  $R$  on the x-axis are  $\log(h^{-1}\text{Mpc})$ .

bars. In the region  $0.8h^{-1}\text{Mpc} \leq R < 2h^{-1}\text{Mpc}$  the M\_D06 and D\_B06 models have a distinctly different slope. The errors are too large to be certain of this difference.

Mo and White (2002), Mo and White (1996), Jing (1998), Sheth and Tormen (1999), Sheth et al. (2001) and Magliocchetti and Maddox (1999) show that haloes of a given mass actually become more strongly clustered with increasing redshift once the mass chosen exceeds  $M_*(z)$ , where  $M_*(z)$  is the knee of the galaxy mass function and is approximately the mass of the Milky Way galaxy. This suggests that vCGs and CGs occupy either more massive haloes or older haloes. The result for the halo mass is useful, because it implies that vCGs are predominantly inside massive halos, possibly meaning that a greater fraction of vCGs are inside clusters, or are cluster cores than CGs or LGs.

## CHAPTER 2

Table 2.5: Best fit formulae for the correlation function shown in Fig. 2.5

Model	vCG	CG	LG
D06	$(R/7.51)^{-1.75}$	$(R/4.92)^{-1.93}$	$(R/3.29)^{-1.78}$
B06	$(R/6.41)^{-1.89}$	$(R/4.27)^{-1.92}$	$(R/3.26)^{-1.64}$

Table 2.6: Best fit formulae for the correlation function shown in Fig. 2.5, with slope set to a canonical -1.8.

Model	vCG	CG	LG
D06	7.51	4.84	3.31
B06	6.63	4.17	3.48

## 2.5 Summary

We see a significantly different predicted compact group spatial density distribution in each of the SAM lineages. The trends are different from the observations, which we at first thought was due to the 2D implementation of the group finder, but later disproved. The two SAM lineages are clearly shown in the group spatial density and richness profiles. The population and richness of the Durham SAMs are considerably higher than in the Munich SAMs. We also tentatively conclude that the model groups are richer than indicated in the observations.

The N-body catalogue shows a significantly different trend in group population with increasing linking length. There are fewer dense N-body groups, and considerably more large groups in the SAMs. This is due to the difference in the samples and subhalo mass cuts in the SAMs and N-body simulation. In the SAMs we are able to cut according to the galaxy luminosity, while in the N-body simulation the cut as to be in the halo mass. The N-body groups show a lower richness, because of the stripping of subhalos, and the shortcomings of the halo finder.

The correlation function of the two different SAM lineages are the same. The correlation length increases with decreasing linking length indicating that denser objects exist in more massive groups and clusters than the average loose group.

## CHAPTER 2

Alternatively, the correlation length  $\xi$  can also increase according to the redshift of formation of the host halo. The slope of the log of the correlation function does not change significantly with group density and is fit by a canonical slope of 1.8.

# Chapter 3

## GROUP PROPERTIES

### 3.1 Introduction

Ribeiro et al. (1998) found that Hickson Compact Groups (Hickson, 1982), (HCGs), are not homogeneous from a dynamical point of view. We calculate the various properties of the groups from the SAMs and the N-body simulation. The properties of groups are difficult to recover with any precision, because of the small number of galaxies. However, the large numbers of groups in our catalogues allow us to arrive at certain conclusions about group properties.

We calculate the harmonic radius of groups, a property which is used as a proxy for the virial radius (Tucker et al., 2000). We also make comparisons with our sub-catalogues from the observational group catalogue of Tago et al. (2010), T10, and the observations of Yang et al. (2007), Y07. As Tucker et al. (2000) and Yang et al. (2007) are magnitude limited surveys, we ask whether a luminosity cut affects the physical properties of the group. From Tago et al. (2008) we know that Eke et al. (2006) groups, among others, show a noticeable trend in group size. These results show that groups have greater size at higher redshift. This suggests that the scaling relation for linking length, based on the survey selection function, introduces a systematic deviation. In other words, the dynamic linking

## CHAPTER 3

length does not merely compensate for the loss of galaxies which fall below the apparent magnitude limit of the survey. An alternative was presented by Tago et al. (2008, 2010), presented in Chapter 1. In the SDSS observations Tago et al. (2008, 2010) use the constants  $a = 1.0$  and  $z_0 = 0.05$ , (for  $n_{mem} \geq 2$ ). Using this method they find that the group size does not change with redshift.

It is a direct consequence of our group finding method that groups formed from smaller linking lengths are subsets of larger groups. This means that each compact group must be either a group in its own right, or it is a denser region inside a larger group. We can associate a compact group with a loose group using a variety of techniques.

Many of the methods used to identify group properties rely on the assumption of virialisation. This, however, is not necessarily true for many groups (Niemi et al., 2007), especially for more compact groups (McConnachie et al., 2008). We examine a variety of group properties, and compare how these vary with linking length. We also explore the associations between compact groups and their loose parents.

## 3.2 Group Properties

### 3.2.1 Harmonic Radius

The harmonic radius of a group is often used as a proxy for the virial radius (e.g. Tago et al. 2008), and, as such, is a very useful quantity to calculate. This quantity gives us access to the formulae for virialised structures. However, the harmonic radius is known to change with linking length.

In 3D we calculate the harmonic radius using

$$R_{harm} = \frac{2}{n(n-1)} \sum_{i=1}^{n-1} \sum_{j=i}^n \frac{1}{|\mathbf{x}_i - \mathbf{x}_j|} \quad (3.1)$$

## CHAPTER 3

where,  $n$  is the number of group members,  $|\mathbf{x}_{i,j}|$  is the  $i^{th}$  or  $j^{th}$  particle position.

The 2D equivalent, based on positions in  $ra$  and  $dec$ , is

$$R_{harm} = D \sin \left( \frac{N_{mem}(N_{mem} - 1)}{4} \left( \sum_i \sum_{j>i} \theta_{ij}^{-1} \right)^{-1} \right) \quad (3.2)$$

where,  $\theta_{ij}$  is the angular separation of galaxies  $i$  and  $j$ .

We apply Eqn. 3.1 and Eqn. 3.2 to the models, and the observations of T10 and Y08. Y08 is used only for LGs, because we have not applied *our* FoF algorithm to this dataset. These two sets of observations are described in Tago et al. (2010); Yang et al. (2007). T10 groups are defined using an FoF algorithm applied to a volume-limited sample which mimics the simulation boxes used in the models. These qualities enable us to use shorted linking lengths on the groups in order to compare to our model groups. The Y08 dataset uses a more complex technique, Yang et al. (2005), to assemble groups, based on a magnitude limited survey. For this reason we use only the loose group catalogues, as presented in Yang et al. (2007)

The harmonic radius of groups is tightly correlated with the maximum galaxy-galaxy separation, which is set by the linking length, the number of galaxies in a group, and the group shape. This is because a group stretched out along a line is going to have a larger harmonic radius than a spherical group.

Tucker et al. (2000) find a median harmonic radius of  $0.53h^{-1}Mpc$  for their 2D projected groups. These authors include a constant,  $\pi$ , in their 2D formulation, such that  $R_{harm}$  becomes  $\pi R_{harm}$ , which we neglect. If, however, we include  $\pi$  in Eqn. 3.1, the median harmonic radius of LGs in the Munich SAMs approaches this value. The N05 LG median harmonic radius exceeds their value, and the Durham group harmonic radius falls below it. This is shown in Fig. 3.1. The harmonic radius instantly shows a significant difference between M\_D06 and D\_B06 groups.

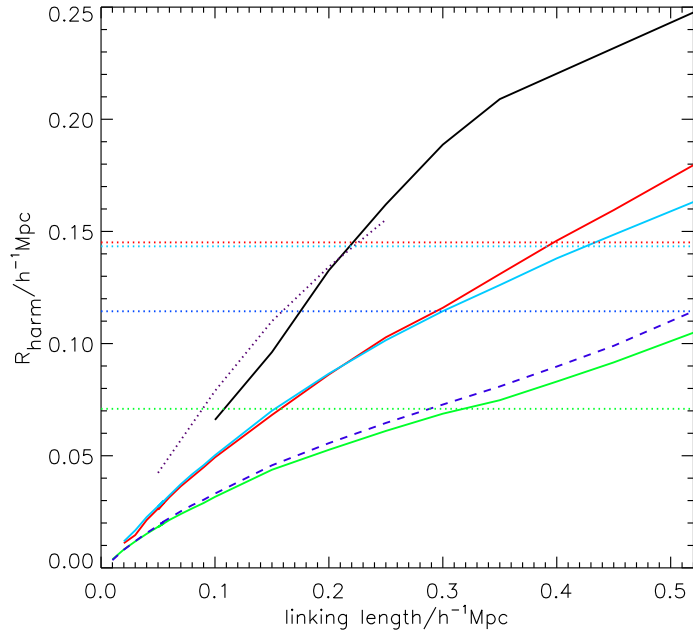


Figure 3.1: The solid lines show the median group harmonic radius for a sub-volume for the N05 (black) M\_D06 (red), M\_B07 (pale blue), D\_B06 (dark blue dashed) and D\_F08 (green) models. The red, light blue, dark blue and green dotted lines show the harmonic radii for groups based on the dark matter distribution. The harmonic radii of T10 groups is shown in the purple dotted line.

## CHAPTER 3

Allam and Tucker (2000) find that for their compact groups the mean harmonic radii is  $0.05h^{-1}Mpc$ , while Hickson found that  $\bar{R}_{harm} = 0.06h^{-1}Mpc$ . We find that for M\_D06, and D\_B06, groups, the harmonic radii is close to  $0.03h^{-1}Mpc$  for both models. As we find in the SAMs, the group catalogues of Allam and Tucker (2000), and Tucker et al. (2000), show the same strong dependence on linking length, i.e.  $0.05 \pm 0.002h^{-1}Mpc$  and  $0.58 \pm 0.1h^{-1}Mpc$ , where the difference in linking length is  $0.05h^{-1}Mpc$  against  $0.72h^{-1}Mpc$ .

$R_{harm}$  is often used to define the virial mass of a group. The sensitivity of this parameter to the linking length makes the virial approximations of group mass etc., more sensitive to the method used to identify groups, than the physics behind them.

We can see, in Fig. 3.2, that there is no significant difference in harmonic radius, as we change the luminosity cut. Thus, the luminosity cut does not have a large effect on the results. This makes comparison between the model datasets and the observations easier.

CHAPTER 3

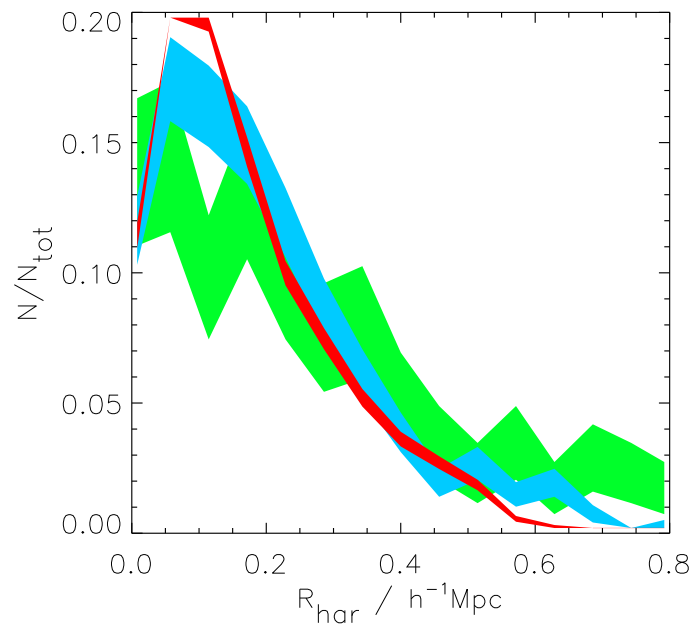


Figure 3.2: Shows the distribution of group harmonic radius for different luminosity cuts in the D\_B06 model. The red line shows the  $M_r = -17$  luminosity cut, the blue line is for a  $M_r = -20$  luminosity cut and the green line is the  $M_r = -21$  cut. The width of the line indicates the Poisson error.

### 3.3 Velocity Dispersion

The velocity dispersion of groups is traditionally, (Yahil and Vidal, 1977), given by,

$$\sigma_v = \sqrt{\sum_{i=1}^N (x - \bar{x})^2 \frac{1}{(N-1)}} \quad (3.3)$$

where  $\sigma_v$  is the velocity dispersion,  $x$  is the velocity along the x, y, z axes,  $\bar{x}$  is the mean of  $x$ , and  $N$  is the number of galaxies in the group.

Although Eqn. 3.3 is the traditional definition for velocity dispersion, it is not particularly robust. For low  $N_{mem}$  groups Beers et al. (1990) and Wainer and Thissen (1976), suggested the ‘gapper’ method. This involves arranging the galaxy velocities in descending order, and finding the separation between successive pairs,  $g_i$ ,

$$g_i = x_{i+1} - x_i, i = 1, \dots, n-1 \quad (3.4)$$

where  $x_i$  is the 1D velocity of galaxy,  $i$ . Each galaxy,  $i$ , is weighted by  $w_i$ ,

$$w_i = i(n-i) \quad (3.5)$$

where  $n$  is the number of galaxies in the group. The final form of the Beers estimator for the velocity dispersion is,

$$\sigma_v = \frac{\sqrt{\pi}}{(n-1)} \sum_{i=1}^{n-1} w_i g_i \quad (3.6)$$

Using these two estimators, we look at one  $125h^{-1}$  subsample, and compare the Beers and standard velocity dispersion. We choose vCGs because the gapper approach is designed for low richness groups, so we should see a greater difference in vCGs. Surprisingly, we find that there is very little scatter between the two

CHAPTER 3

Table 3.1: The median and standard deviation of the gapper and standard velocity dispersions for M\_D06 and D\_B06 at three linking lengths.

model	l/h <sup>-1</sup> Mpc	Gapper		Standard	
		median/kms <sup>-1</sup>	$\sigma$ /kms <sup>-1</sup>	median/kms <sup>-1</sup>	$\sigma$ /kms <sup>-1</sup>
M_D06	50	505.102	372.258	472.318	351.053
D_B06	50	356.100	237.458	339.851	234.068
M_D06	150	378.396	282.253	360.446	274.814
D_B06	150	308.443	240.065	295.438	236.793
M_D06	520	148.408	102.951	172.048	130.031
D_B06	520	145.932	98.8997	169.876	125.739

methods for any of the model. The difference between our models and observations, apart from our velocity dispersions being in 3D, is that the observations limit the maximum possible velocity dispersion, via the line of sight linking length.

The median and standard deviation of the velocity dispersion for our groups is shown in Table 3.1 and Fig. 3.3. Hickson et al. (1992) find a mean velocity dispersion of 300km/s for both compact groups and loose groups. We find that our compact sample has a significantly higher median velocity dispersion than loose groups. This suggests that the lack of Hickson’s isolation criterion means we are probing the bottom of deep potential wells, where Hickson does not. We also find that M\_D06 has a higher velocity dispersion than D\_B06 groups, despite having fewer members. This suggests that the distribution of groups by host mass is different, with more M\_D06 vCGs being contained within high mass halos. This result can also be inferred from the correlation function analysis in the previous chapter. Alternatively it could mean that more M\_D06 groups are unbound.

The mean and median values for Tucker et al. (2000) loose groups is 153 km/s. Tago et al. (2010) show a lower velocity dispersion of 89 km/s. Tago et al. (2010) note that their restrictive linking lengths bias velocity dispersions, but it is the choice they have made in order to remove potential filament galaxies from their

## CHAPTER 3

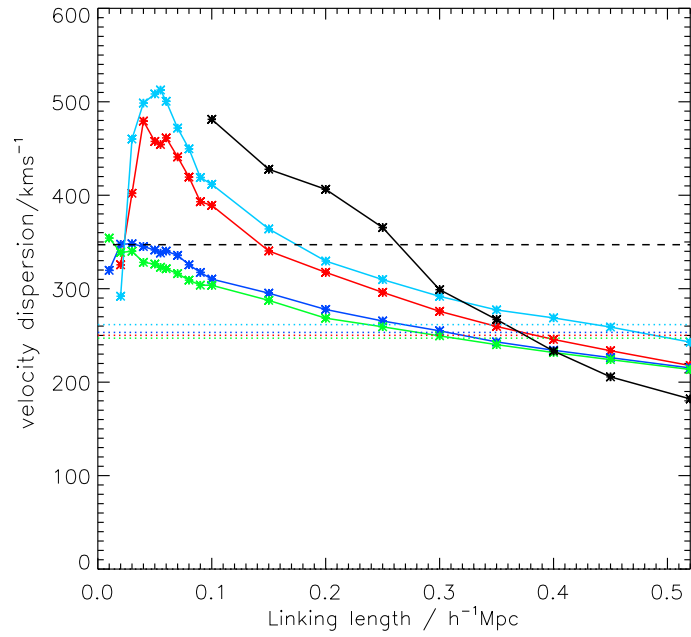


Figure 3.3: Shows the median group standard velocity dispersion, solid lines show the velocity dispersion for the N05 (black), M\_D06 (red), M\_B07 (pale blue), D\_B06 (dark blue) and D\_F08 (green) models. The dotted lines show the velocity dispersion for halo based groups.

samples.

### 3.4 Crossing time

Hickson et al. (1992) defined the dimensionless crossing time of groups,

$$t_{dyn} = \frac{r_{pair}}{\sigma_v} \quad (3.7)$$

as a measure of the level of dynamical evolution. This parameter measures the maximum number of times a galaxy could orbit the group since its formation. This is slightly different from the form implemented in Hickson et al. (1992), because we use the 3D harmonic radius, while Hickson uses the projected values. Assuming the group is spherical (which is not strictly true, §3.7) the difference between this and Hickson’s parameter is a factor of  $\sqrt{2}/\sqrt{3}$ . Hickson et al. (1992) give a median crossing time of  $0.016 H_o^{-1}$ .

We show the results from one subvolume, for a variety of linking lengths, and for halo based groups in Fig. 3.4. As Hickson interpreted the crossing time as a measure of dynamical evolution, we can state that D\_B06 and D\_F08 are more dynamically evolved systems than M\_D06 and M\_B07 groups, at all linking lengths greater than  $0.1h^{-1}Mpc$ . The reason for this probably lies in the form of the satellite lifetime, which must be longer in D\_B06 and D\_F08. The M\_D06 model is the least dynamically evolved of the SAMs. The difference in slope between M\_D06 and M\_B07 indicates that the supernovae feedback prescription has an effect on the apparent dynamical evolution of groups. This is an indirect effect, however. The supernova feedback in M\_B07 removes low luminosity galaxies from the sample and so we are left with fewer galaxies in groups. This lack of dim galaxies has an effect on the calculation of the crossing time. We also note that the crossing times of the FoF LGs are higher than the halo-based groups, due to the addition of galaxies/halos not contained within a parent halo. The crossing time of the SAMs is proportional to the linking length, such that we

## CHAPTER 3

can simply conclude that the larger the group the less dynamically evolved it is. The N05 groups, however, show a different trend, such that compact groups are dynamically evolved, while at longer linking lengths they are distinctly not. This links in with the distribution of galaxies in groups, shown below. The N05 groups have a much higher crossing time, which is not a straight line like the others. The reason for this is that the dark matter halos disintegrate quicker than the galaxies (Diemand et al., 2007). This is because the galaxy is in the centre of a dark matter halo, and thus protected from the effect of the gravity of the host halo, and baryonic matter in galaxies has a high density. The effect of numerical resolution also enhances the effect of halo stripping (Klypin et al., 1999). Alternatively, the old halos sink to the centre and can no longer be identified (Gill et al., 2004) as previously discussed. Thus, using dark matter halos we preferentially select new, dynamically younger objects, than in the SAMs.

Comparing our data to Hickson’s compact groups, we find that the crossing time of all groups are approximately the same at low linking length. This result is, however, 2.5 times too small, relative to Hickson. Tucker et al. (2000) found that his loose groups have a median crossing time of  $0.1H_o^{-1}$ , which is 1.5 times the value for D06 groups. D\_B06 loose groups are 2.5 times smaller than Tucker groups. Using the Tago catalogue we find a crossing time for compact groups to be  $0.015 H_o^{-1}$ , which is higher than the models. This difference between models and observations may be due to the different luminosity cuts in the models or the group finder itself. The luminosity cut is -17 throughout in the models, but varies significantly over the Hickson sample. We did, however, explore the effect of luminosity cuts on the harmonic radii of groups in a previous section and found the effect to be minimal. Tucker’s loose group show a much larger crossing time than Hickson or the model compact groups. This is because, as previously noted, the group radius is very sensitive to the galaxy separation. Hickson’s

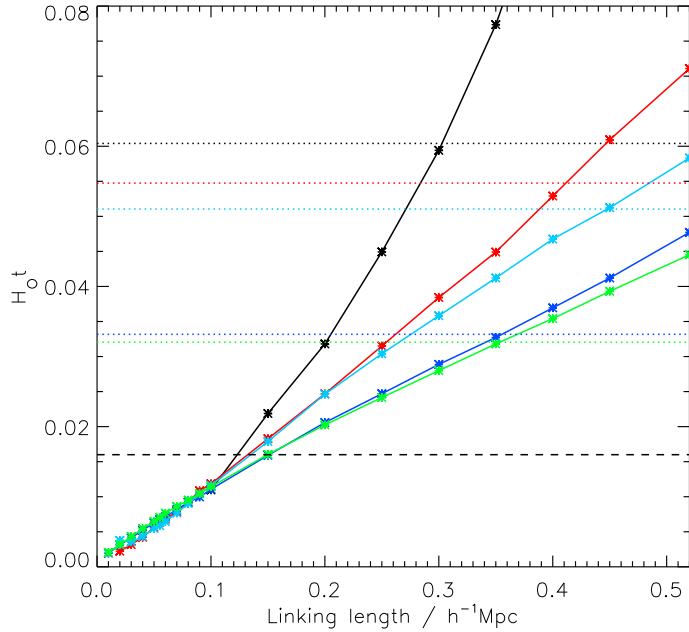


Figure 3.4: The solid lines show the median group crossing time for a subvolume for the N05 (black), M\_D06 (red), M\_B07 (pale blue), D\_B06 (dark blue) and D\_F08 (green) models. The dotted/dashed lines show the crossing time for halo based groups. The dashed line shows the crossing time of Hickson et al. (1992) for Hickson compact groups.

groups are a heterogeneous sample, with a wide variety of group sizes. This is because, in dense environments groups can be comparatively larger than in dense environments, while the FoF approach we use effectively limits the inter-galaxy separation. A combination of this, or the effect of selection effects from the observations versus the models, are potential explanations for the difference.

### 3.5 Group Types

We define several types of group based on various properties of groups. We define three types of group based on their dark matter distribution. Groups of galaxies can consist of galaxies in several situations in the SAMs. They can contain galaxies from a single host halo, or multiple halos. They can contain the central

## CHAPTER 3

Table 3.2: Proportion of galaxy group types where the first number is the proportion of inner, peripheral and distinct. *na* indicates where no data is provided.

Model	vCG	CG	LG
M_D06	80 / 19 / 0	78 / 22 / 0	35 / 1 / 64
M_B07	77 / 22 / 0	77 / 22 / 0	48 / 2 / 51
D_B06	83 / 14 / 2	83 / 12 / 5	20 / 0 / 80
D_F08	82 / 15 / 3	83 / 11 / 6	22 / 0 / 78
T10	39 / 60 / na	84 / 15 / na	na / na / na

galaxy of the host or not. These can be summarised as follows:

1. Inner(I) - The group lies in the bottom of the host potential, defined in the SAMs as containing the host central galaxy. In observations, we say that an inner group contains the brightest group galaxy of the parent. The central galaxy, and the brightest galaxy, are not necessarily the same in the SAMs, but this is a common approximation in observational catalogues, i.e. Yang et al. (2008)
2. Distinct(D) - The group consists of galaxies in separate dark halos, defined as containing at least 1/4 of galaxies from more than one host. We do not define this type for observations.
3. Peripheral(P) - The group consists of galaxies from a halo, but not the central galaxy. We also require that any galaxies from other halos are from halos with significantly smaller mass. If a group in observations in part of a parent, but does not contain the brightest group galaxy, it is peripheral.

Clearly, in the halo based group catalogues, groups are all type-I. Table 3.2 shows the proportions of group types as defined above.

An interesting observation that can help determine the difference between peripheral and central groups is the group luminosity and group velocity dispersion relation. If we calculate the total luminosity of groups and the mass, we can see a distinct population of dim, high velocity dispersion, high mass groups, Fig.

## CHAPTER 3

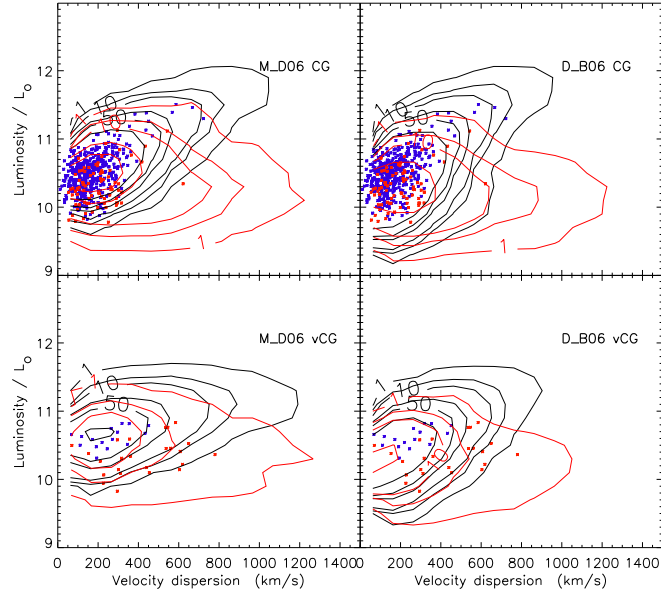


Figure 3.5: Shows the luminosity against 1D velocity dispersion. The black contour shows the distribution of central groups, the red contour shows peripheral groups in the models. The dark blue points show T10 centrals and the red are T10 peripherals. The model and group catalogue is given in each panel. The numbers of points in each plot are given by Table 3.3

3.5. Luminosity and mass is tightly correlated for central groups, but there is a subset of groups which are not correlated, and form a cloud of points. Observationally, this is a useful method for distinguishing peripheral from central groups. Peripheral groups tend to be the smallest in terms of the number of galaxies.

Table 3.3: The number of groups used to generate the plots in Fig. 3.5

Model	Total (vCG)	Total (CG)
M_D06	2311	4115
D_B06	6743	9610
T10	41	521

### 3.6 Galaxy distribution

In Fig. 3.6 we find that cluster galaxies in D\_B06 are more highly concentrated in the cluster centre, than in M\_D06, right panel. The results are similar when scaled. We compare, in the left panel, with the observations of Y07, in order to identify whether the flat or peaked form is replicated in the real universe. These plots are done using a face-on projection rather than the full 3D, because of the need for observational comparison. We see that the centre of the observational clusters show a fall in the number of galaxies.

Figure 3.7 shows the distances to the nearest neighbour galaxies in LGs. We find that the D\_F08 model is very similar to D\_B06, and is not included in the figure. It can be seen that the D\_B06 model, the nearest neighbour separation is slightly smaller than for the Munich models. The figure shows that the Durham models are denser than those in the Munich models. This may be indicative of *shorter merging times in the Munich models, than in the Durham approach*. The longer the galaxy survives, the deeper it sinks into the parent halo because of dynamical friction. It follows that the longer the average galaxy lifetime, the denser the resulting environment. This also explains the lower abundances of CGs and vCGs in the Munich models. The higher population of vCGs and CGs in the D\_B06 model, compared to the Munich models, may be traceable to the subhalo accretion prescriptions, (Li and Helmi, 2008; Berrier et al., 2009). A faster merging time in the Munich Models may result in smaller survival times

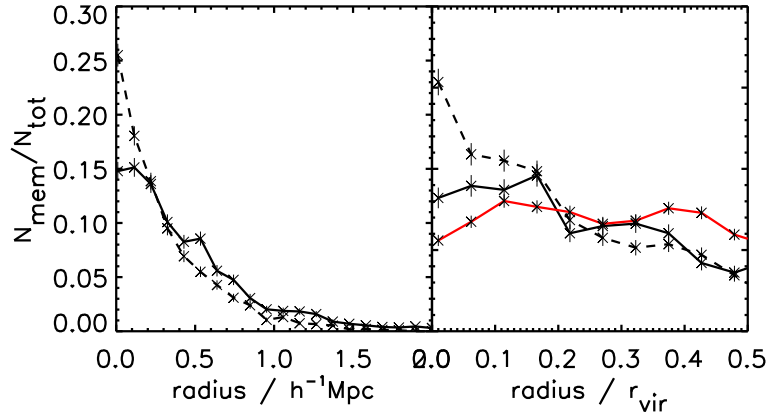


Figure 3.6: A plot of the position of the galaxy in the top 50 most massive clusters in the millimillennium simulation. The left panel shows the normalised number of galaxies against radius from the centre, the right panel shows the normalised number of galaxies against the radius scaled by the radius of the most distant cluster member. The dashed line is for D\_B06 groups, the solid line is for M\_D06 groups, and the red line is Y07 observations. Errors are poisson, i.e.  $\sqrt{N}$ , where  $N$  is the number of galaxies in each radial bin.

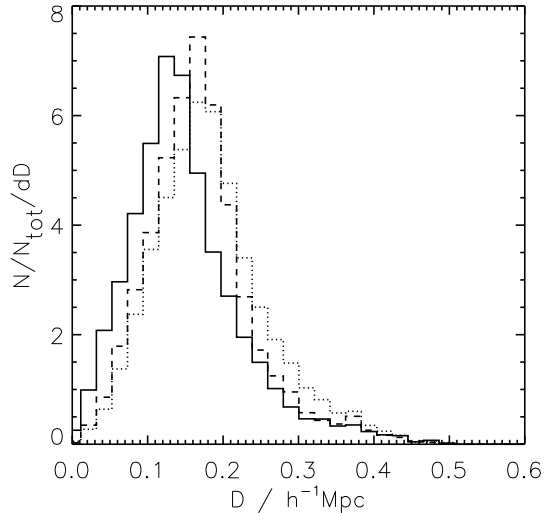


Figure 3.7: The distribution of nearest neighbour pair separations for galaxies in LGs for the three models, the dotted line is M\_B07, the dashed line is M\_D06, and the thick line is D\_B06. The plots shows that D\_B06 galaxies tend to be closer together.

## CHAPTER 3

for non-central galaxies. This explains the lower abundances of CGs and vCGs in the Munich models.

The shallower profile in the observations goes some way to explain why the profile of the number of groups against linking length is so different in the observations. The galaxy distribution in the real universe is less concentrated than in SAMs so a longer linking length is required to assemble more groups.

### 3.7 Group Shape

A number of authors have looked at the shape of groups and clusters: e.g. Robotham et al. (2008); Paz et al. (2006); Plionis et al. (2004); Orlov et al. (2001). Other authors have studied the shape of Compact groups e.g. Oleak et al. (1998). Our advantage is that we have 3D group information and environmental information as well as comparatively large (Hickson, 1982; Allam and Tucker, 2000; Barton et al., 1996) sample sizes. Tovmassian et al. (2006) found evidence that Compact groups are the elongated cores of loose groups, and we can look at these ideas in detail. We examine the shape of groups, at different linking lengths, and compare with observations. However, the groups have low richness, and so has large uncertainties when the group shape is calculated.

In order to calculate the shape of groups we calculate the inertial tensor of the group and derive the eigenvalues. This method is favoured by most authors, e.g. Paz et al. (2006); Plionis et al. (2004). We calculate the geometric centre of the group, and shift the group into that reference frame. Next we calculate the inertial tensor.

CHAPTER 3

$$I = \frac{1}{N} \begin{pmatrix} \sum_{n=1}^N (x_n x_n) & \sum_{n=1}^N (x_n y_n) & \sum_{n=1}^N (x_n z_n) \\ \sum_{n=1}^N (y_n x_n) & \sum_{n=1}^N (y_n y_n) & \sum_{n=1}^N (y_n z_n) \\ \sum_{n=1}^N (z_n x_n) & \sum_{n=1}^N (z_n y_n) & \sum_{n=1}^N (z_n z_n) \end{pmatrix} \quad (3.8)$$

where  $N$  is the number of particles,  $x_n$  is the  $x$  position of the  $n$ th particle,  $y_n$  is the  $y$  position of the  $n$ th particle and  $z_n$  is the  $z$  position of the  $n$ th particle. The diagonal elements are the moments of inertia of the particle ensemble.

The inertial tensor is derived from the angular momentum of a set of particles. The angular momentum,  $\mathbf{L}$ , is written as :

$$\mathbf{L} = \sum_{i=1}^N m_i (\mathbf{r}_i \times \mathbf{v}_i) = \sum_{i=1}^N m_i \mathbf{r}_i (\boldsymbol{\omega}_i \times \mathbf{r}_i) \quad (3.9)$$

where  $N$  is the number of particles,  $\mathbf{r}_i$  is the position of the  $i$ th particle,  $\mathbf{v}_i$  is the velocity of the  $i$ th particle,  $m_i$  is the mass of the  $i$ th particle and  $\boldsymbol{\omega}_i$  is the angular velocity of the  $i$ th particle. This can be rewritten as

$$\mathbf{L} = \mathbf{I}\boldsymbol{\omega} \quad (3.10)$$

where,  $\boldsymbol{\omega}$  is the angular momentum vector and  $\mathbf{I}$  is the inertial tensor.  $\mathbf{I}$  then takes the form of

$$\mathbf{I} = \sum_{i=1}^N m_i \begin{pmatrix} \left[ \begin{array}{ccc} y_i^2 + z_i^2 & -x_i y_i & -x_i z_i \\ -y_i x_i & x_i^2 + z_i^2 & -y_i z_i \\ -z_i x_i & -y_i z_i & x_i^2 + y_i^2 \end{array} \right] \end{pmatrix} \quad (3.11)$$

This can then be rewritten as

## CHAPTER 3

$$\mathbf{I} = \sum_{i=1}^N m_i \left( \begin{bmatrix} r_i^2 & 0 & 0 \\ 0 & r_i^2 & 0 \\ 0 & 0 & r_i^2 \end{bmatrix} - \begin{bmatrix} x_i^2 & x_i y_i & x_i z_i \\ y_i x_i & y_i^2 & y_i z_i \\ z_i x_i & z_i y_i & z_i^2 \end{bmatrix} \right) \quad (3.12)$$

Usually only the second term of Eqn. 3.12 is commonly used in deriving the shape of halos or groups, e.g. Knebe et al. (2010).

We extract the eigenvalues of the above matrix,  $\lambda_a, \lambda_b, \lambda_c$  and, where  $(a, b, c) = \sqrt{\lambda_a, \lambda_b, \lambda_c}$ , and define the axes such that  $a > b > c$ .  $a, b$  and  $c$  are the axial ratios of the shape ellipse. The moments of inertia are the diagonal elements of  $\mathbf{I}$ .

We also calculate the sphericity, the measure of how spherical the group is:

$$S = \frac{c}{a} \quad (3.13)$$

and the triaxiality, (Franx et al., 1991), which measures how oblate, ( $T=0$ ), or prolate, ( $T=1$ ), the group is:

$$T = \frac{a^2 - b^2}{a^2 - c^2} \quad (3.14)$$

The 2D equivalent of sphericity is eccentricity, or

$$E = \frac{b}{a} \quad (3.15)$$

Paz et al. (2006) discover that the shape of subsamples of galaxies from rich groups are indistinguishable from the shape of poor groups. They find that groups with a small number of members produce extended non-spherical distributions, simply due to the small numbers. As many of the groups have very few members, there is a large degree of error in calculating the group shape. In order to make any definitive conclusions we create a monte-carlo catalogue of spherical groups.

## CHAPTER 3

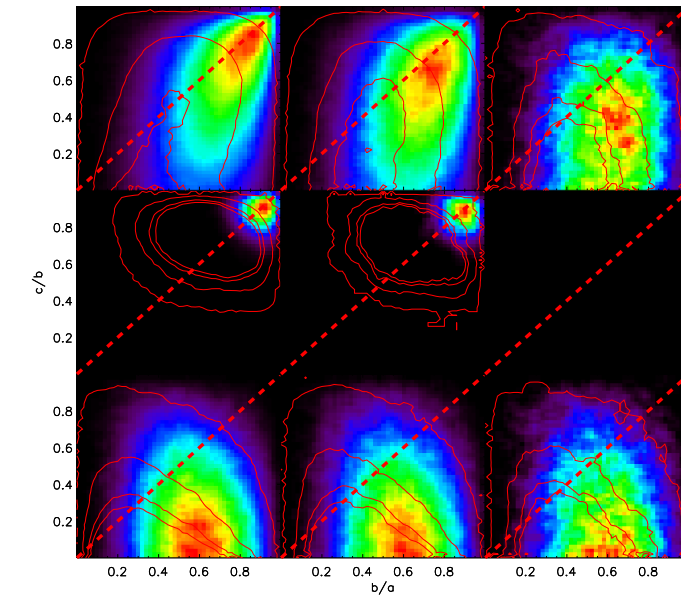
We construct our mock catalogues to have the same richness function as the groups. For each group in the catalogue about group shape we find the number of members,  $N_{mem}$ . We then generate random positions, and remove all points outside a sphere. We then select the first  $N_{mem}$  points from this list. The mock and group catalogues are then fed into Eqn. 3.8. The placement of the mock galaxies is such that for large N the group would be spherical. Any deviation from the sphere is only due to small number sampling. We then run KS tests of the result. If the FoF groups are spherical, we expect the distributions to lie on top of one another. By comparing groups to the random catalogue we can see whether groups tend towards prolate ( $a > b = c$ ), oblate ( $a = b > c$ ), spherical ( $a = b = c$ ) or triaxial ( $a \neq b \neq c$ ) forms.

Fig. 3.8 demonstrates the distribution of  $b/a$  against  $c/b$ . Where  $c/b = 1$  the group is prolate, while  $b/a = 1$  groups are oblate. Where both  $c/b = 1$  and  $b/a = 1$  the group is spherical. The diagonal line is the 1:1 ratio. It is instantly obvious that the shape of the SAM groups is not spherical, and that they tend towards being prolate. This is most clear in clusters, which appear more prolate than the random data. Smaller groups are more triaxial and scattered, as expected. There appears to be no significant difference in the plots as the linking length is altered. In order to test this statement, we perform KS tests on the data, Table 3.4.

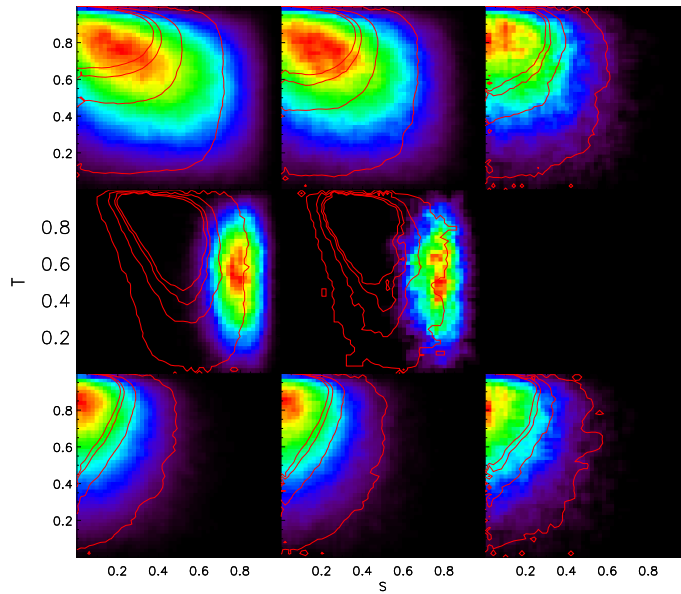
Paz et al. (2006) identify the 3D shapes of groups in 2PIGG, SDSS-DR3GC and a GALFORM mock 2PIGG catalogue (Cole et al., 2000). They conclude that small numbers produce less spherical and more prolate objects, than high richness objects. This can be inferred from our Figs. 3.8(a) & 3.8(b). Figure 3.9 shows that groups tend to be less spherical than the random catalogue.

The elongated shapes of compact groups have important implications for Hickson's groups. He requires that the group fit into a circle of radius R, and be

CHAPTER 3



(a)  $b/a$  v.  $c/b$



(b)  $S$  v.  $T$

Figure 3.8: The distribution of group elliptical axial ratios for random groups (colours) and simulated groups (contours). The top row shows all groups in the group catalogue, the middle from those groups with more than 20 members and the bottom row those groups which have 4 members. LG, CG and vCG are from left to right. Panel a shows the axial ratios and Panel b shows the relationship between sphericity and triaxiality.

CHAPTER 3

Table 3.4: KS-tests where the null hypothesis is that the group shape and the random group shapes are not extracted from the same distribution.

	$D_{b/a}$	$D_{c/a}$	$D_{c/b}$	$D_T$	$p_{b/a}$	$p_{c/a}$	$p_{c/b}$	$p_T$
LG								
all	0.267	0.293	0.200	0.213	0.008	0.003	0.090	0.059
= 4	0.160	0.200	0.200	0.253	0.275	0.090	0.090	0.014
< 30	0.453	0.280	0.280	0.213	0.000	0.005	0.005	0.059
CG								
all	0.227	0.267	0.347	0.227	0.038	0.008	0.000	0.038
= 4	0.160	0.200	0.200	0.213	0.275	0.090	0.090	0.059
< 30	0.413	0.267	0.293	0.160	0.000	0.008	0.003	0.275
vCG								
all	0.120	0.200	0.347	0.200	0.633	0.090	0.000	0.090
= 4	0.093	0.160	0.147	0.187	0.889	0.275	0.376	0.135

isolated by a radius  $3R$ . However, because the groups tend to be elongated structures, this preferred circular geometry does not follow from these results, or the observations, i.e. Tovmassian et al. (2006); Oleak et al. (1998). These groups have a lower richness limit of 5 galaxies, so we remove all CGs with  $N < 5$  from our sample. The distribution of shape is affected by the number of members in 2D as well as 3D. They also find that this is even slower in 3D than in 2D. Using 2D coordinates introduces an additional problem; the measured shape depends on the inclination of the group, Fig. 3.10. If we produce a new sample of random catalogues containing groups of different axial ratios, (Oleak et al., 1998), and over plot the results for groups, we find that, in general, groups of galaxies have an ellipticity of  $0.6 \pm 0.2$ , Fig 3.11.

We compare the results of the SAMS to the galaxy groups of Yang et al. (2008), based on the SDSS DR4. We convert between the right ascension,  $\alpha$ , and declination,  $\delta$  and Cartesian  $x$  and  $y$ , using,

## CHAPTER 3

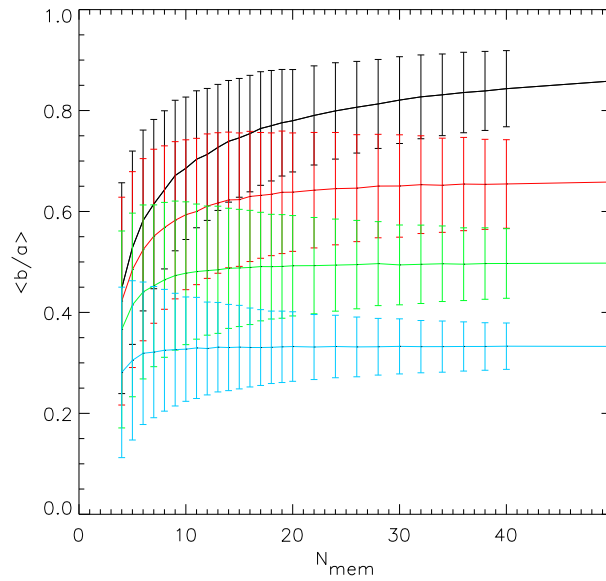


Figure 3.9: Shows the mean and standard deviation (error bars) for spherical groups against the number of members in the random catalogue. The black line shows results for spherical groups, the red line for a large  $N$  axial ratio of 1:15, green for ratio is 1:2 and blue is for 1:3. This is for 2D groups.

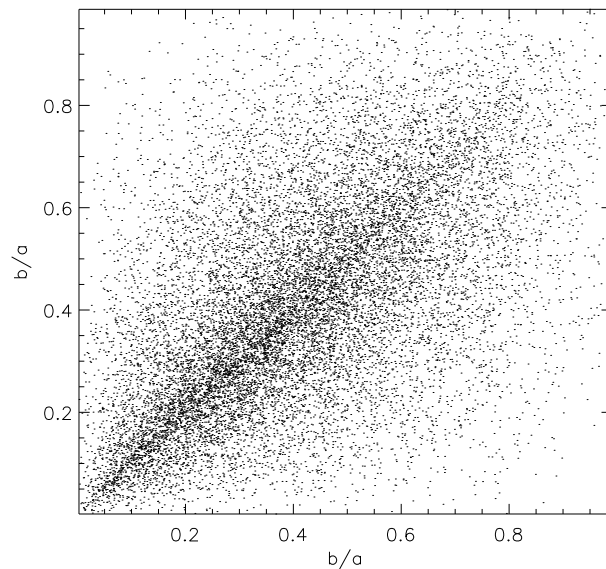


Figure 3.10: The 2D ellipticities of projected groups. The same groups are plotted at different inclinations and the different projected axial ratios are shown.

## CHAPTER 3

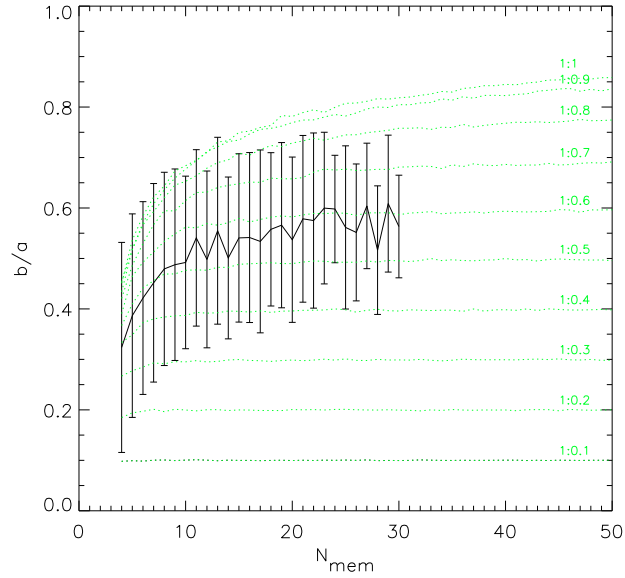


Figure 3.11: Plot of the profile of ellipticity against group membership. The dotted lines show the predicted mean ellipticities for 1000 random groups of ellipticity given in the figure. The solid line is for D06 vCGs and the error bars are the standard deviation of the distribution. The groups seem to converge to  $b/a \sim 0.6 \pm 0.2$ , in keeping with Oleak et al. 1998.

$$x = (\alpha - \langle \alpha \rangle) \cos(\langle \delta \rangle)$$

$$y = (\delta - \langle \delta \rangle)$$

where,  $\langle \alpha \rangle$  is the group luminosity weighted mean right ascension, and  $\langle \delta \rangle$  is the group luminosity weighted mean declination. We apply this to the inertial tensor, Eqn. 3.8, setting  $z_i = 0.0$ . There are several issues with comparing the observations to the models, because more distant groups lack the low luminosity galaxies present in closer groups. However, the overriding problem for shape finding is, yet again, the low richness of some groups. Nevertheless, we also run our spherical group random sample to compare our group shapes with it, and can use this to gain insight into the shape of groups.

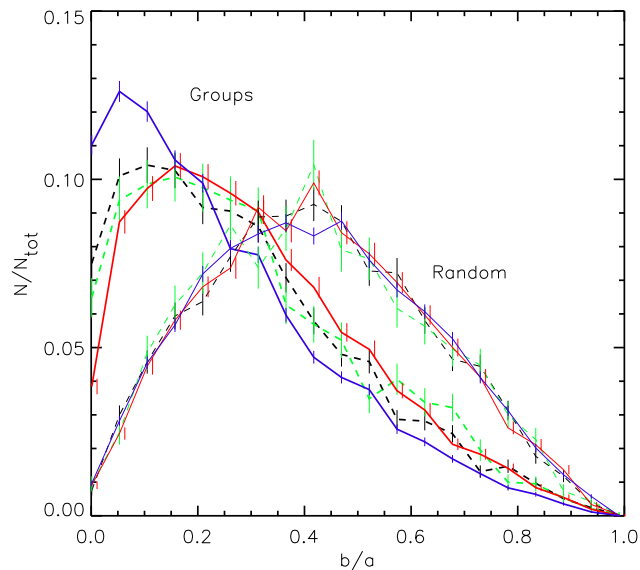


Figure 3.12: Shows the ellipticity distribution of the projected group shape for groups with 4 galaxies. Within the error the M\_D06 groups (red) are remarkably close to the observations, (Y08 is green, T08 is black), while some D\_B06 (blue) groups tend to be more elliptical. Also shown are the trends for randomly filled spheres.

Both the models and the observations show that groups tend to be significantly more elliptical than the random spheres, Fig. 3.12. The SAMs show group shape to be relatively insensitive to linking length. D\_B06 groups, show a higher proportion of triaxial groups than the observations, making the Munich groups a better fit.

### 3.8 Environment of Groups

Although we have removed the isolation criterion from our group finding analysis, we explore the local environment of our groups. Barton et al. (1996) searched their galaxy catalogue for the closest galaxies around compact groups. They identify which groups exist in a dense environment and which do not. One drawback of their method is that the single closest galaxy may be spurious, a galaxy that just

## CHAPTER 3

by chance happens to be close to the group in an otherwise diffuse environment. They define the environment of their compact groups using the parameter,

$$\Upsilon = R_{iso}/R_{group} \quad (3.16)$$

where  $R_{iso}$  is the isolation radius and  $R_{group}$  is the group size. If  $\Upsilon > 3$  then the group is isolated in a manner kin to Hickson's isolation criterion. Our choice of group finding approach allows us more sophistication. All compact groups found using our method are a subset of the loose group catalogue. This comes from the fact that galaxies linked by a shorter linking length, must be linked by a longer linking length. This means each vCG has an associated CG and LG. Thus, we can specify that compact groups are part of either,

1. a cluster - where the galaxy population of the LG is  $N > 30$
2. a rich group - where the galaxy population of the LG is  $10 > N \leq 30$
3. a poor group - where the galaxy population of the LG is  $5 > N \leq 10$
4. isolated - where the LG contains no additional galaxies

These definitions are based on pairing a particular compact group with a particular loose group. Occasionally, the largest clusters contain more than one compact group. Additional definitions are required to identify whether a group is truly isolated, or whether it is part of a group or a cluster core. The spirit of Hickson's definition, (Hickson 1982), suggests that isolated or peripheral compact groups are what he originally had in mind. Tovmassian et al. (2001) identified that many Hickson Compact groups (HCGs) are the cores of loose groups.

The procedure used to identify these correspondences is the same as used in a simple merger tree algorithm. The particle id number of galaxies in compact groups, and identify which loose group it lies within. This is repeated for all

CHAPTER 3

Table 3.5: The % of vCGs in a particular environment. The luminosity cut is -18 in the sdss r-band.

Environment	M_D06	D_B06
Isolated	7.1%	3%
Poor	28.2%	19%
rich	36.5%	41%
Clusters	28.2%	36%

Table 3.6: Averages and standard deviations for vCG environments. The number in brackets is the standard deviation, the other is the mean in 64 boxes.

Environment	M_D06	D_B06
Isolated	6.38(2.6)	30.66(6.5)
Poor	46.03(7.2)	201.08(20.0)
Rich	74.59(11.4)	363.61(34.2)
Clusters	108.08(21.5)	468.55( 87.8)
Total	235.08(30.7)	1063.89(131.3)

galaxies in compact groups. Technically, we require only that one galaxy per compact group is traced, because all compact group galaxies must lie within the same loose group, as explained above.

Table 3.5 shows the number of groups in a particular environment for a single  $125h^{-1}Mpc$  volume. When we take the mean and standard deviation of all 64 volumes we find similar results, Table 3.6, but with considerable variation between subvolumes.

Thus, in both models, 3%-7% of very compact groups are what Hickson originally had in mind when he defined compact groups, in that they are not part of a larger system. We find a total of 2000 true compact groups in the entire Millennium volume in the Bower model, and 408 for the De Lucia model, making these extremely rare objects.

We can identify potentially peripheral compact groups, most of which are in

## CHAPTER 3

Table 3.7: **Top two rows:** The % of LGs containing more than 1 or 2 vCGs. **Lower two rows:** The % of vCGs occupying an LG containing more than 1 or 2 compact groups.

		D_B06	M_D06
LGs	> 1	0.9+/-0.2	0.1+/-0.04
LGs	> 2	3.5+/-0.7	1.2+/-0.7
vCGs in LG	> 1	10.7+/-1.0	5.8+/-1.4
vCGs in LG	> 2	2.8+/-0.3	0.3+/-0.1

clusters, or rich groups, and compare their dynamics to cluster/rich group cores. Over a quarter of compact groups that lie within clusters are peripherals, i.e. not part of the cluster core. Most loose groups do not contain a very compact region. On the other hand, Table 3.7 shows that 10% of very compact groups exist in loose groups which contain more than one compact region. Between 2 and 4% lie in loose groups contain more than 2 compact groups. The cluster with the largest number of compact regions contains 41 compact groups, including the cluster core. Alternatively, we can say that 2-3% of all loose groups contain more than one compact region in the D\_B06 model. We repeat this analysis for the M\_D06 model, shown in Table 3.7. This difference in substructure is most probably due to the higher number of galaxies in LGs in the D\_B06 model compared to the M\_D06 model. D\_B06 model LGs have closer together galaxies, thus more potential vCGs. This table also suggests that part of the vCG population in D\_B06 models is directly due to the richer haloes in the Durham models because a greater percentage of vCGs lie inside large LGs.

The limited number of compact groups in M\_D06 makes a telling difference in this analysis. If we look at clusters (> 30 galaxies) the difference is most drastic. 31% D\_B06 and 5% M\_D06 clusters contain more than one compact group. This difference should help provide a refinement to the SAMs, and provide a diagnostic

## CHAPTER 3

for observational comparison. Comparing cluster substructure to observations will provide a good diagnostic between the merging timescales in SAMs, and whether reality is more closely mimicked by M\_D06 and D\_B06.

### 3.8.1 Observations

In our T10 sample we identify 41 vCGs. We find that most of them are the only one in a given LG, 24 are alone in their loose group and the remaining 17 are divided up in 7 clusters. 2 vCGs are isolated, 7 are in poor groups, 15 are in rich groups and 17 are in clusters. Proportionally this is, 5%, 17%, 37% and 41% in each environment, which is not too dissimilar to the models. Unfortunately we do not have enough objects to distinguish which model fits best. We show an example of a cluster with multiple compact objects, extracted from the SDSS DR7, Fig. 3.13.

The figures show that compact galaxy associations are real and can be a considerable fraction of cluster galaxies. In this case, the cluster contains 86 galaxies, 29 of which are in compact associations. In this case one of the compact groups contains the brightest cluster galaxy, despite being off centre.

### 3.8.2 Correspondences

We can compare the correspondences of compact groups properties to their host loose groups. In this way we can calculate the effectiveness of finding group properties from the vCG sample. Thus, we effectively measure the validity of using compact group parameters, such as the crossing time estimator, Eqn. 3.7, to measure the group characteristics. This is important, because groups should really be virialised, bound, structures.

We compare the predicted halo mass calculated using,

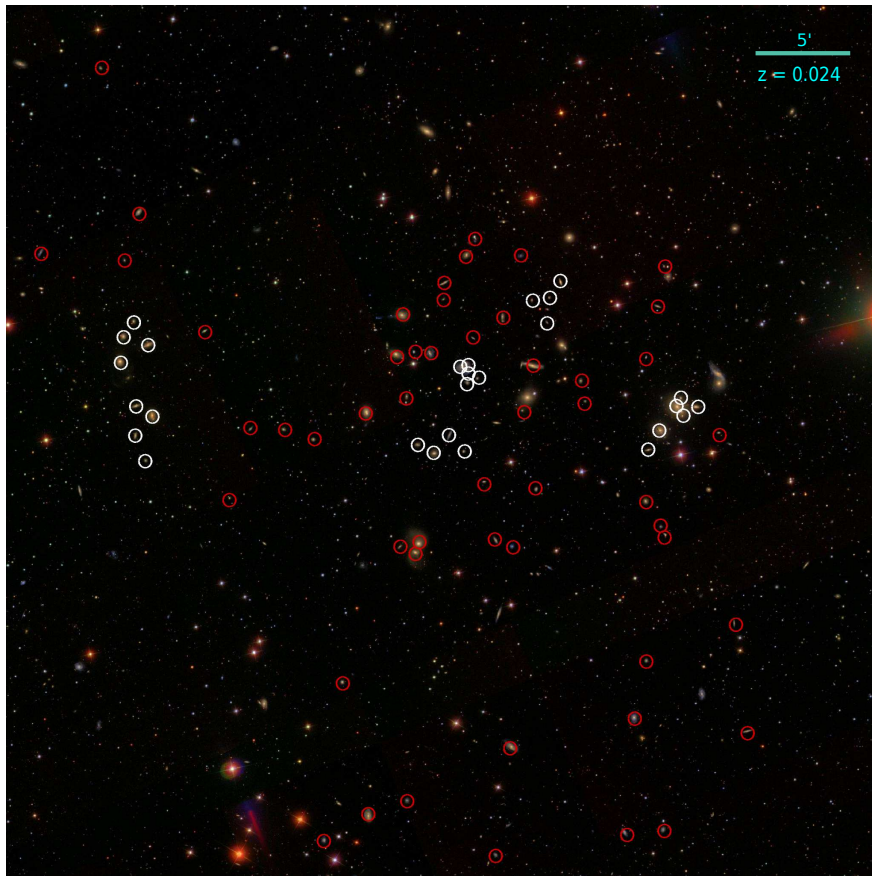


Figure 3.13: A cluster from T10 consisting of 86 galaxies and 6 compact regions. All cluster members are marked on the figure with circles. Those galaxies also members of vCGs are marked with white circles. This image is 512 pixels by 512 pixels and has  $3''$  per pixel.

## CHAPTER 3

$$M_{vir} = \frac{\sigma^2 r_{vir}}{G} \quad (3.17)$$

where  $\sigma$  is the velocity dispersion, and  $r_{vir}$  is the virial radius or harmonic radius. There is some correlation between vCGs and LGs, Fig. 3.14, but the result is highly scattered, making conclusions difficult from these plots alone.

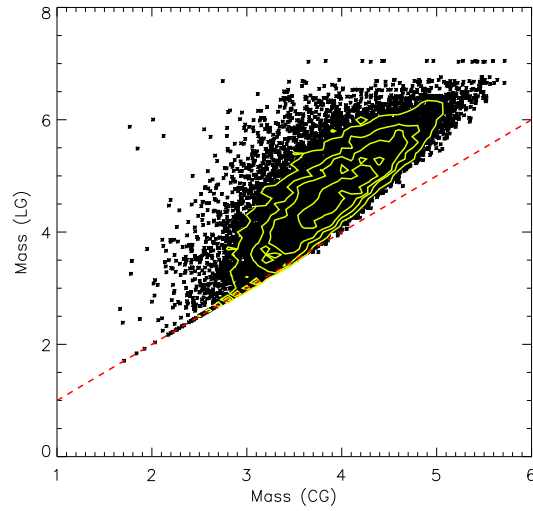
In the observations, we see something similar, although we can only use the 2D projection. We must multiply our harmonic radius by  $\sqrt{3/2}$  and our velocity dispersion by  $\sqrt{3}$ , thus Eqn. 3.17 becomes,

$$M_{vir} = \frac{3^{3/2} \sigma^2 r_{vir}}{G\sqrt{3}} \quad (3.18)$$

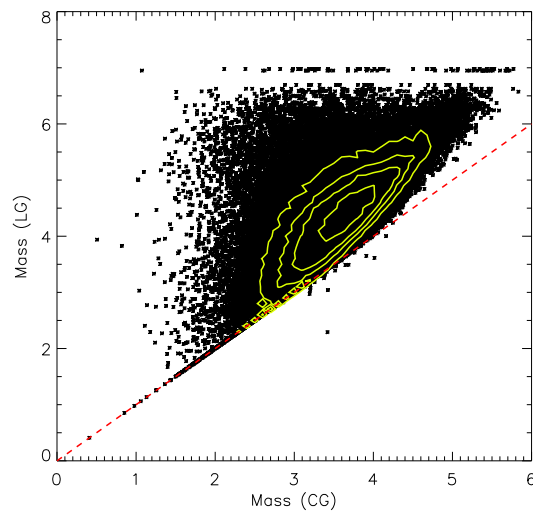
Again, we find a large scatter in the results. Instead of using two derived quantities, harmonic radius and velocity dispersion, we examine the correlation in velocity dispersion alone, in an attempt to reduce the scatter in the system.

The comparison of velocity dispersion in our T10 catalogues shows a tight correlation between vCGs and LGs, especially for central vCGs. Fig. 3.15 shows that the behaviour of observations, and the SAMs are reasonably close. Except that T10 groups peripherals dominate at the high velocity dispersion, more than in the model. This is due to the different luminosity cut meaning more groups are central. However, applying a KS test to Fig. 3.15 we find that the samples of peripherals and central groups are members of the same distribution to a probability of 0.34 for peripherals and 0.35 for centrals. However, the accuracy of the k-s test is limited by the small number of galaxies in the subsamples. There are only 246 M.D06 galaxies used in Fig. 3.15 and 41 T10 galaxies. If we apply the same tests to the distributions as a whole we find that there is only a probability of 0.02 that they are of the same distribution. These values are however, substantially higher than two utterly dissimilar distributions. We concluded, tentatively, that these distributions are the same and the models match the data well.

## CHAPTER 3



(a) M.D06



(b) D.B06

Figure 3.14: The ratio of group mass calculated from the virial approximation for CGs and their associated LG. The dotted line is the 1:1 ratio, the contours show the point density, the same for each plot, and the crosses show the mass calculated from the virial quantities of the LGs and CGs.

CHAPTER 3

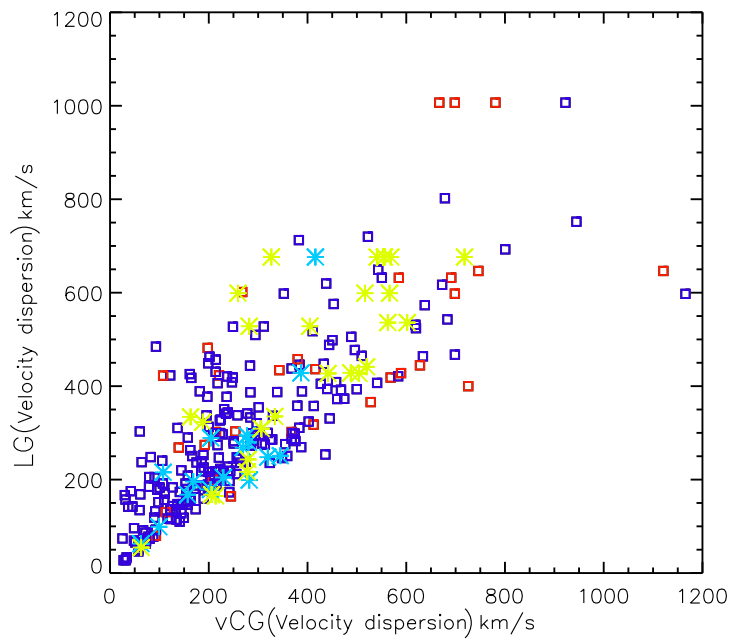


Figure 3.15: Shows the velocity dispersion and type of group in M\_D06 and T10 groups for vCGs and LGs. The y axis shows the velocity dispersion of groups formed with a  $250h^{-1}$  kpc linking length, and the x-axis vCGs. Red squares are peripheral M\_D06 groups, dark blue squares are central M\_D06 groups, yellow stars are peripheral T10 groups and blue stars are central T10 groups. We define central and peripheral to be the environment of the compact group.

## CHAPTER 3

This close relationship between the velocity dispersions of LGs and vCGs means that the mass calculation using the assumption of virial equilibrium is dependant on the harmonic radius. Similarly for the crossing time. There is no reason to assume that the crossing time of compact groups in Hickson (1982), is useful if the group is part of a larger structure. The radius used in the calculation of the crossing time should be the radius of the parent object not just the compact group within the loose group.

### 3.9 Conclusion

We find notable differences between the predictions made by the two SAMs, the N-body simulation, and the observations. However, what we have seen suggests an alternative method of identifying compact groups. Hickson (1982) devised his criteria for identifying compact groups before automatic group finding algorithms were widely available. He used a preferential geometry, using a minimum enclosing circle approach for identifying potential group members, and a larger circle defining the degree of isolation. We have found, however, that most compact groups are elongated filamentary structures which sit within relatively non-spherical structures. A more natural approach to group finding would be to identify loose groups using FoF, and then use smaller linking lengths to identify dense knots of galaxies. Once this has been done the criteria of isolating or surface brightness etc. can be applied to match the author's requirements. Our method allows the author to naturally study the environment of compact groups, and provides a more systematic way of studying the behaviour of galaxies in dense environments.

# Chapter 4

## BRIGHTEST CLUSTER GALAXIES

### 4.1 Introduction

Brightest cluster galaxies, or BCGs, are giant, extremely luminous giant elliptical galaxies. These objects are the most massive, and luminous, galaxies in the universe. BCGs can be divided into 3 classes, cD, D and gE galaxies. A cD or D galaxy differs from a standard giant elliptical, because its luminosity profile is shallower than de Vaucouleurs' law <sup>1</sup> (Schombert, 1987). Additionally, a cD galaxy lies within a diffuse stellar halo. Most BCGs are elliptical galaxies, and so it is common to compare these objects with standard ellipticals. Various authors have discovered, both in observations (Schombert, 1987; Hoessel et al., 1987; Lauer and Postman, 1992), and semi-analytic simulations, such as von der Linden et al. (2007), that BCGs are 'special'. These differences are thought to be due to the high density environment in which these objects reside.

There has been considerable debate over the origins of BCG's, and cD galaxies

---

<sup>1</sup> $I(R) = I_0 \exp(-kR^{0.25})$ , where  $I$  is the surface brightness,  $I_0$  and  $k$  are constants and  $R$  is the distance from the centre.

## CHAPTER 4

in particular. One model, based on ‘Galactic Cannibalism’, suggests that large galaxies in the cluster cores merge to form the cD or D galaxy. This galaxy then grows via further mergers, (Hausman and Ostriker, 1978; Ostriker and Tremaine, 1975). This scenario has been shown to be insufficient for the formation of large  $10L^*$  galaxies, (Lauer, 1988). The favoured scenario is that cD and D galaxies form via mergers inside groups of galaxies, whereupon the group falls into a cluster. The lower velocities of galaxies in groups means that the galaxy merger efficiency is greater, (Zabludoff and Mulchaey, 1998). This model would explain the existence of cD galaxies in poor clusters. It is the favoured model, if BCGs with high velocity offsets are identified, (Oegerle and Hill, 2001).

It was long believed that BCGs exist at the bottom of the cluster potential, consistent with the position of the X-ray peak (Jones et al., 1979). BCGs, therefore, would be expected to exist in the cluster core, and move with a velocity equal to the cluster average. In fact, it is frequently assumed that the BCG is the central galaxy in a cluster, and no further thought is given to the matter. A number of investigations, using small samples of clusters, Zabludoff et al. (1993), Laine et al. (2003), Kriessler and Beers (1997) and Beers and Geller (1983), for example, have shown that this is not the case.

Andernach et al. (2007) took a large sample of DSS images, and derived the line of sight velocity offsets of the BCGs for 326 clusters, resulting in a sample of 385 BCGs. The clusters used in this sample contain cD galaxies, or galaxies which are Bautz-Morgan Type I-II. Type I clusters have a very bright cD galaxy, Type III clusters contains a BCG that is not significantly brighter than average, and Type II clusters are intermediate between Type I and III.

Andernach et al. (2007) discovered that 50 per cent of BCGs had a velocity offset greater than  $0.37\sigma_v$ . They concluded that this result is consistent with the seeds of BCGs being collapsed compact or loose groups. Additionally, Beers &

## CHAPTER 4

Geller and Krissler & Beers noted that D and cD galaxies occupy *local* density maxima, rather than the cluster potential minimum.

Gravitational effects are dominated by the dark matter distribution of the cluster. Each galaxy rests at the bottom of a local potential well, which is produced by a dark matter subhalo. This subhalo is itself embedded inside the dark matter halo of the cluster. There is a well known relationship between galaxy dark halo mass and galaxy luminosity, (Vale and Ostriker, 2006, 2008). This relationship allows us to model the properties of the BCG in dark matter only simulations. Henceforth, in this Chapter we use the most massive cluster subhalo, MCS, as a proxy for the Brightest Cluster Member. We are able to identify massive subhaloes that should correspond to particularly luminous galaxies. This means our sample is only comparable to BCGs in general, and not specific classes of brightest galaxy i.e. cD galaxies.

The reason for this work was the paper by Andernach et al. (2007). They suggested that their high proportion of velocity offsets  $> 0.37\sigma_v$  is evidence that BCGs emerge from infalling galaxy groups.

## 4.2 Method

We use two sets of previously published simulations to model 48 clusters with a mass range between  $3.6 \times 10^{14}h^{-1}M_{\odot}$  and  $4.2 \times 10^{14}h^{-1}M_{\odot}$ . In each case we use the same cosmological parameters,  $\Omega_m = 0.3, \Omega_{\Lambda} = 0.7, \Omega_b = 0.048, h = 0.7, \sigma_8 = 0.9$ , from the WMAP 1-Year results (Spergel et al., 2003).

The first dataset was presented in Nagashima et al. (2005), N05, using  $512^3$  particles in a  $70h^{-1}Mpc$  box.

The second data set was presented by Gill et al. (2004, 2005); Warnick et al. (2008). They presented a sample of 8 clusters, generated using a re-simulation

## CHAPTER 4

technique. This simulation uses a  $64h^{-1}\text{Mpc}$  box and  $512^3$  particles. It is simulated using the MLAPM, (Knebe et al., 2001), a cosmological AMR code. The force resolution is  $\sim 2h^{-1}\text{kpc}$  and a mass resolution of  $1.6 \times 10^8 h^{-1} M_{\odot}$  is attained.

The force resolution of the Warnick et al. (2008) simulation is twice as fine as N05. This means that these subhaloes will suffer less from numerical effects, (Klypin et al., 1999).

We look at the 3D and 2D separations of the subhaloes from the cluster density maxima, and potential energy centres. We then scale the data with the virial radius of the parent cluster. This is done so that clusters of different masses can be compared easily. The velocity offsets of the subhalos of each cluster are found in both 3D and 1D. These offsets are scaled by the cluster velocity dispersions.

$$\frac{\bar{V}_{off}}{\sigma_v} = \frac{\bar{V}_{SH} - \bar{V}_{clus}}{\sigma_v} \quad (4.1)$$

where  $V_{off}$  is the 3D velocity offset,  $V_{clus}$  is the velocity of the cluster dark matter halo,  $V_{SH}$  is the subhalo velocity and  $\sigma_v$  is the velocity dispersion of the cluster. We can do this because there is only a small difference between the velocity dispersion of the dark matter in a halo, and the velocity dispersion of the subhaloes, e.g. Gill et al. (2004).

For our 1D results we use:

$$\frac{v_{off}}{\sigma_{v,1D}} = \frac{v_{SH} - v_{clus}}{\sigma_{v,1D}} \quad (4.2)$$

$$\frac{d}{R_{vir}} = \frac{\sqrt{(X_{SH} - X_{clus})^2 + (Y_{SH} - Y_{clus})^2}}{R_{vir}} \quad (4.3)$$

where  $v$  is the velocity along the line of sight, and X and Y is the 2D position of the object on the sky.

For the observational case of Y07 we use the distance equation of

$$\frac{d}{R_{vir}} = 2 \frac{D_L}{R_{har}} \sin\left(\frac{\Theta_{ij}}{2}\right) \quad (4.4)$$

and,

$$\frac{v_{off}}{\sigma_{v,1D}} = c \frac{z_{SH} - z_{clus}}{\sigma_{v,1D}} \quad (4.5)$$

for the velocity offset.

We use the Yang et al. (2007) dataset because this catalogue includes clusters, while Tago et al. (2010) does not include groups with a richness  $> 80$  because of subtleties in their group finding method.

## 4.3 Results

### 4.3.1 Identifying clusters

AHF, the (sub)halo identification algorithm we applied to the simulation (Gill et al., 2004), returns haloes from the simulation in order of mass, so it is relatively simple to extract the most massive objects. We require that the cluster halo is not a subhalo of another, more massive, cluster. We also require that the cluster contains more than 25 subhaloes within its virial radius. Using these criteria we select the 40 most massive clusters from N05. The number of subhaloes in our clusters ranges from 201 to 26 with a median of 48 for the Nagashima run. The clusters in the Warnick & Knebe simulation contain 78 to 388 haloes within the same mass range.

### 4.3.2 Subhalo

In Fig. 4.1, we plot the subhalo velocity offset against its distance from the dark matter density maximum. These values are then scaled by the halo velocity

CHAPTER 4

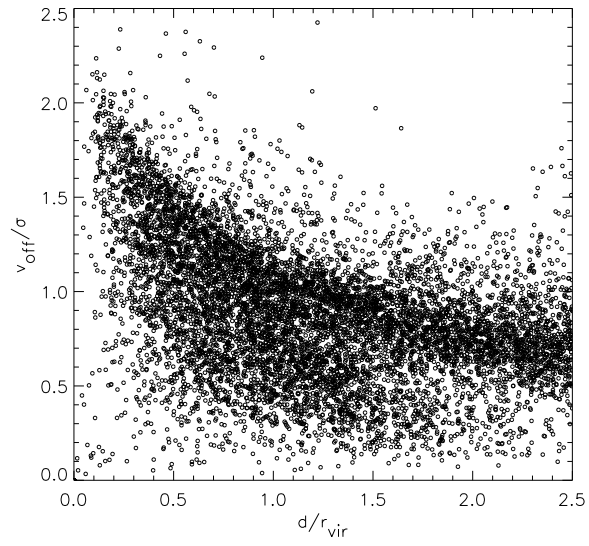


Figure 4.1: The distance from the cluster core against velocity offset from the cluster core for all subhaloes within  $2.5 r_{vir}$

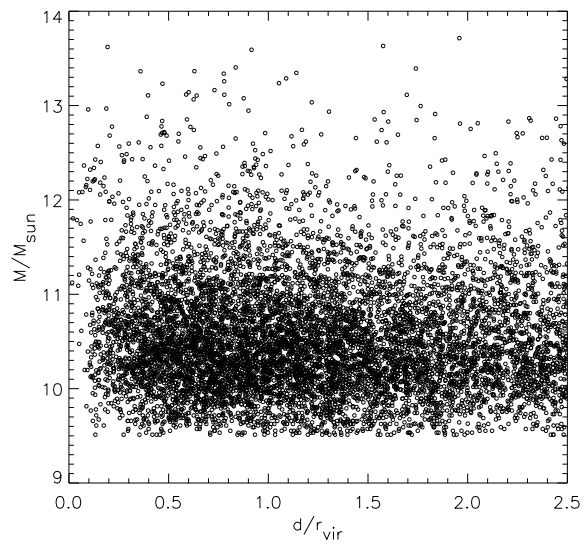


Figure 4.2: Mass of subhalo against distance from cluster centre.

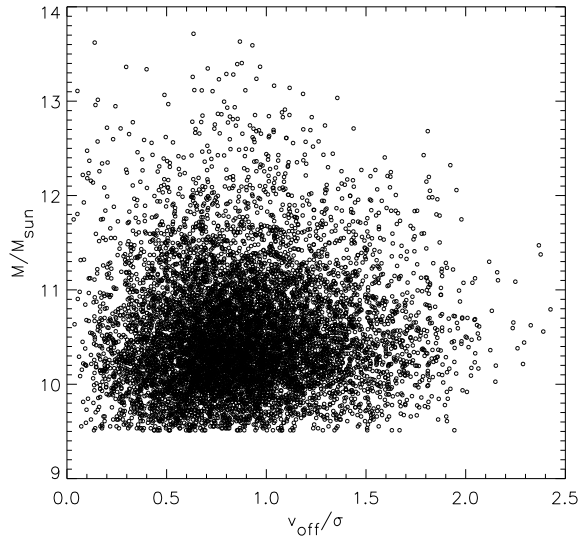


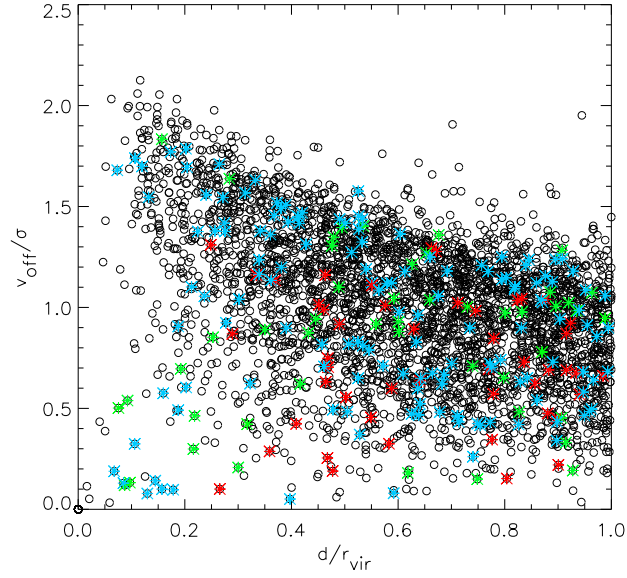
Figure 4.3: Mass of subhalo against velocity offset from parent cluster.

dispersion, and halo virial radius respectively. Also shown is the relationship between each parameter and the subhalo mass, Fig. 4.2 and Fig. 4.3.

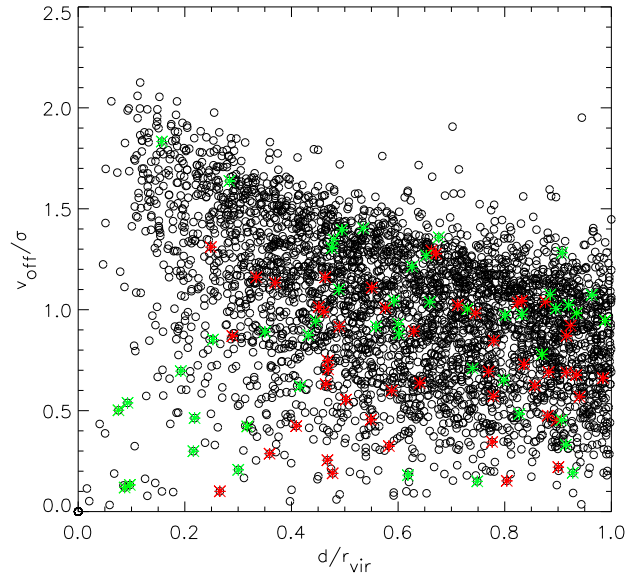
In Fig. 4.1 we can see a number of features. The first is that the velocity offset of dark matter haloes is greater towards the centre of each cluster. This is unsurprising, as it is due to basic orbital mechanics. We can also see the effects of the ‘backsplash population’. These subhalos are those galaxies that have passed through the cluster at least once, and are falling in a second time. The high speed tail shows the population of infalling haloes, and the low speed population are the backsplash galaxies (Gill et al., 2005; Knebe et al., 2008). In Fig. 4.2 we see that the distribution of subhalo mass with distance from the cluster centre is essentially uniform. High mass haloes are found at all distances from the centre. This is consistent with constant infall onto the cluster. On the other hand, the subhalo velocity offsets have a median of  $0.86\sigma_v$ , suggestive of an offset between the dark matter, and average subhalo velocity.

We can repeat this process for 1D velocity offsets, and 2D separations, in order to model what can be observed. We take 3 projections, along the x,y and z axes

CHAPTER 4



(a) The top two most massive halos



(b) The top five most massive halos

Figure 4.4: **Top panel:** The distance from the cluster core against velocity offset for the 5 most massive subhaloes within  $R_{vir}$ . **Bottom panel:** The distance from the cluster core against velocity offset for the 2 most massive subhaloes within  $R_{vir}$ . Red points are for the BCGs, green points are for the second most massive subhalos and the blue points are for the second, third and fourth most massive subhalos.

## CHAPTER 4

and use  $\sigma_{1D} = \sqrt{3}\sigma_{3D}$ , assuming that the cluster is approximately virialised. For each projection, we take the velocity offset projected along the line of sight, and the separation of the subhalo from the cluster density maximum, projected onto the plane perpendicular to the line of sight. These are then stacked to increase the statistical significance of our results. We lose the clear trend between distance and velocity offset in projection.

### 4.3.3 Most Massive Cluster Members

We repeat the analysis above for the 5 most massive subhaloes in each cluster. The most noticeable thing is that there is a greater proportion of high mass subhaloes in the low  $V_{off}/dist$  region of the parameter space. By the time the 6 to 10th most massive subhaloes are plotted, they are essentially indistinguishable from the general distribution in 3 dimensions.

Taking the same plot as Fig. 4.4(a), but only using the 2 most massive subhaloes in each cluster, we show in Fig. 4.4(b) that the low velocity offset population appears to be more dominant.

Compiling the velocity offset information, we recover the histograms produced by Andernach et al. (2007) in both 3D and 1D. Fig. 4.5 shows the 3D velocity offsets for all subhaloes within the cluster virial radius. The subhalo velocity offset peaks at around  $1.1 \sigma_v$ , suggesting a slight antibias between the dark matter velocity distribution, and the subhalo velocities. Figure 4.6 shows the 1D equivalent.

We compare the histograms of the velocity offset of the 2 most massive subhaloes with the histogram by Andernach et al. (2007), Fig. 4.7. Our histogram is significantly less steep than the one produced by Andernach et al. We put this down to their sample being of cD galaxies, and very luminous galaxies, and our being unable to distinguish between galaxy types.

CHAPTER 4

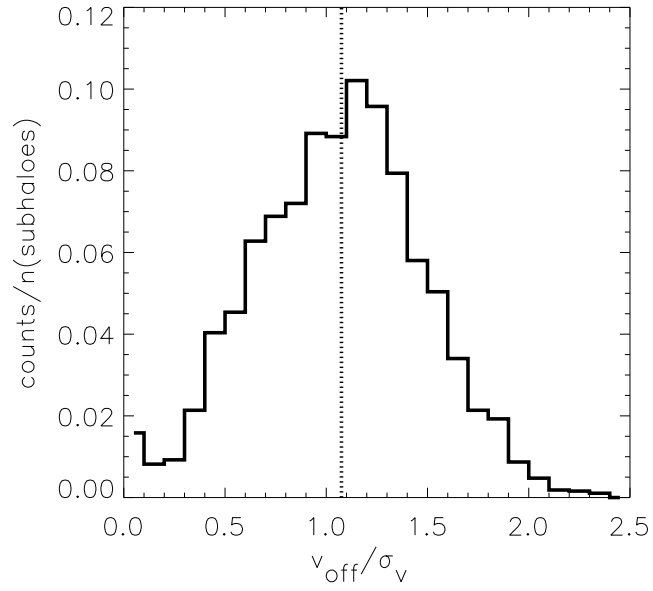


Figure 4.5: 3D velocity offsets for all haloes within the virial radius.

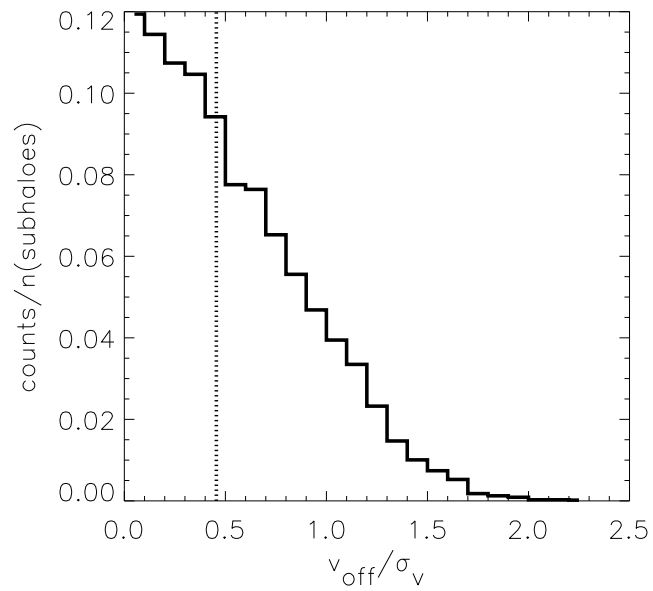


Figure 4.6: 1D velocity offsets for all haloes within the virial radius.

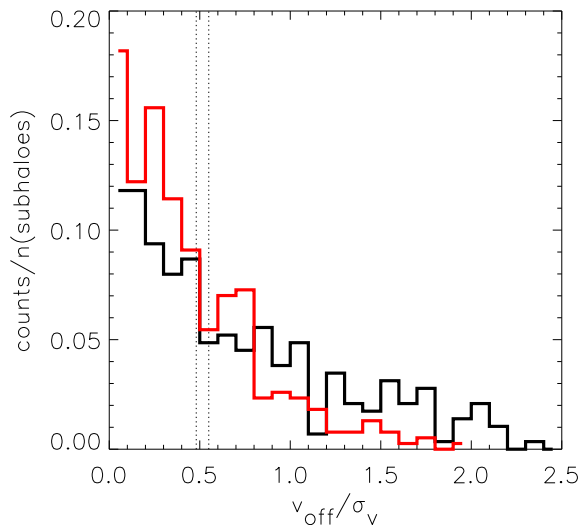


Figure 4.7: Comparison between the velocity offsets of Andernach et al. (red) and our 2 most massive subhaloes, (black). The dotted lines are the median  $\pm$  the standard error on the median.

## 4.4 In the SDSS survey

Using the Yang et al. (2008) catalogue, we compare the position of the most luminous galaxy with the geometric and luminosity weighted cluster centre. We then compare this with a set of randomly selected galaxies from within the clusters. In this catalogue we define a cluster as containing more than 30 galaxies with a luminosity within 3 magnitudes of the BCG. A similar project was recently carried out by Skibba et al. (2011). They make comparisons to SAMs (MORGANA; Monaco et al. (2007), the model of Croton et al. (2006)) and halo occupation functions. Here, we compare the N-body results with the observations, Figs. 4.8(a) & 4.8(b). We centre the cluster on the luminosity weighted mean, in order to provide equivalence between the models and observations. We chose this measure of the cluster centre because the centre of a cluster is an ill-defined concept without dark matter information, or X-ray observations. We see that the BCG in Yang et al. is much more centrally concentrated than the most

massive subhalo. This indicates that the most massive subhalos are not a good match for the spatial distribution of brightest cluster galaxies in projection, but are a better match in redshift space.

## 4.5 Discussion & Conclusion

It has been noted that clusters of galaxies have, in general, very bright galaxies near their centre. This is not always the case, but is true in a majority of cases. We examined whether we could find the same trend using high resolution N-body only simulations and found that, although there was a noticeable correspondence using the velocity offset of clusters in dark matter simulations and observations, we did not see any correspondence between the trends in projected spatial offset. This could be because limitations in the model. These limitations are:

1. The tidal stripping of the dark matter subhalo rapidly reduces its mass before it reaches close proximity with the centre, e.g. Klypin et al. (1999). This is because the halo loses mass because of gravitational interactions. This happens in nature, but is enhanced by the limited resolution of the simulation.
2. The halo that close to the bottom of the potential cannot easily be identified by the halo finder (Gill et al., 2004). This is because the density contrast between the halo centre and the cluster centre is insufficient for the subhalo to be identified.
3. The BCG has been at the centre of the cluster for some time and has built up in-situ and is therefore indistinguishable from the cluster halo itself. This is because the cluster centre and the centre of the BCG are the same so the halo finder cannot untangle them.

## CHAPTER 4

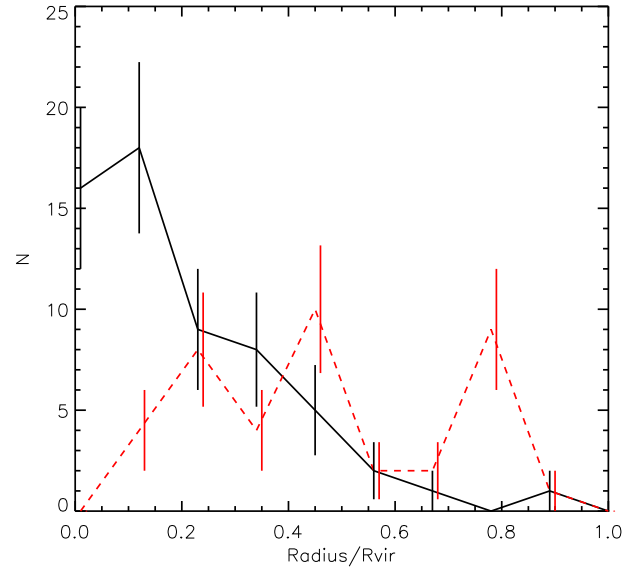
Further investigation is required, of both the BCGs in observations and the mass history of the infalling objects, before the particular reason for this difference can be identified.

We note that when groups fall into clusters, the subhalos are stripped rapidly from the group parent, after one orbit of the cluster centre, although the core of the group remains. This suggests that if the brightest galaxy in the group is offset from the centre of the group then it will be found in the cluster periphery.

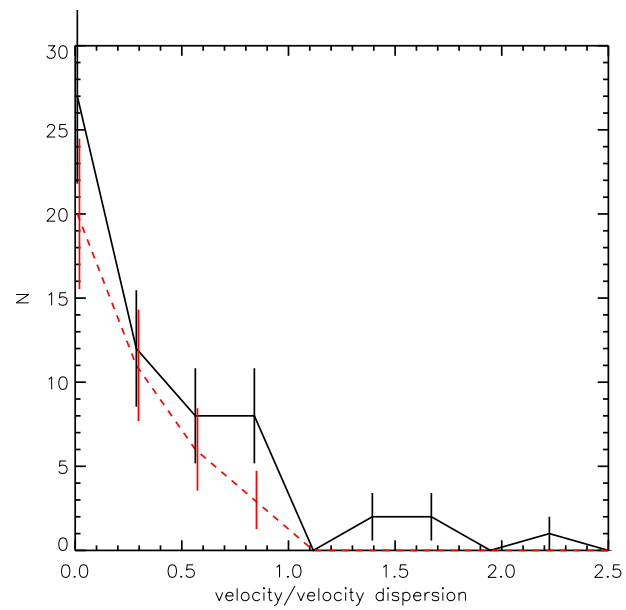
There is also the issue of bias from the numerical approach that must be considered. The halo finding procedure uses density contrast to define potential halos, and the density profile to define subhalo radius. As this radius is tied to the mass proximity to the cluster centre the halo finder can reduce the subhalo size artificially. The halos are stripped rapidly, yet the galaxy should be unaffected for far longer than the halo because of its privileged location in the centre of the subhalo potential well, (Diemand et al., 2007).

An infalling group falls into the cluster as a local density maximum. The bright central galaxy of that group may outshine the cluster central galaxy. We see this effect in the Millennium Run SAMs (see the following chapter for details). Tracking groups into the cluster we find that subhalos and galaxies are rapidly stripped from the group, within  $\sim 1$  orbit. This suggests that a bright group central galaxy should not be within a density maximum for more than one orbit. Bertone and Conselice (2009) find that more massive galaxies merge more rapidly with the cluster central galaxy. This provides a potential explanation of the BCG position. When the brightest group galaxy first falls into the cluster it is in the local density maximum of the galaxies bound to the group halo. After one orbit the other group galaxies have been dispersed, but the massive group brightest galaxy will rapidly merge with the BCG. More work is required to explore this scenario.

## CHAPTER 4



(a) Spatial separation



(b) Velocity space

Figure 4.8: The distribution of BCGs in observations, (black solid lines), and N-body subhalos (red dashed lines). **Panel a:** projected separation and **panel b** velocity space separation.

# Chapter 5

## LUMINOSITY FUNCTIONS

### 5.1 Introduction

It is in the examination of the luminous properties of galaxies that SAMs must be carefully constructed and tuned. Many physical processes are required to correctly model the luminosity distribution of galaxies. The physical prescriptions discussed in the Introduction to this thesis are all required, including supernova feedback, gas infall, radiative cooling, dust etc. Along with prescriptions to change these parameters into observables by modelling spectrophotometry etc. Particularly important for modelling galaxies are AGN and supernova feedback effects which reduce the luminosity of the brightest and dimmest galaxies respectively. When galaxies merge with a parent halo all the hot gas of those galaxies is added to the central galaxy of the halo which is assumed to lie in the halo centre.

We now examine the luminosity function of FoF groups in the semi-analytical models at  $z=0$ . The global luminosity function is usually fit with a Schechter function, (Schechter, 1976),

$$\Phi(M) = \phi_* \left( \frac{M}{M_*} \right)^\alpha \exp \left[ - \left( \frac{M}{M_*} \right) \right], \quad (5.1)$$

## CHAPTER 5

where  $M$  is the absolute magnitude of the galaxy,  $\alpha$  defines the low end slope,  $\phi_*$  is the function normalisation and  $M_*$  is the position of the knee in the distribution. This can be used straightforwardly for the SAMs. In order to produce a luminosity function for redshift survey data, Yang et al. (2008) use the stepwise maximum-likelihood method, Efstathiou et al. (1988). The profile from the redshift survey ‘as-is’ is not appropriate without modification because the dimmest galaxies are removed from a sample as the survey distance increases. In order to compensate for this effect an estimator must be used. The stepwise maximum-likelihood method assumes that the luminosity function can be parametrised as a set of  $N_p$  step functions of width  $\Delta M$ , such that  $\phi(M) = \phi_k$  and the best fit weights of  $\phi_k$  identified via a minimum likelihood approach.

We used the luminosity distribution to explore the properties of groups at different linking lengths because it draws in all the SAM physics, and compare to the observations of Yang et al. (2008) among others. We also study the magnitude gap profile and how this is affected by linking length.

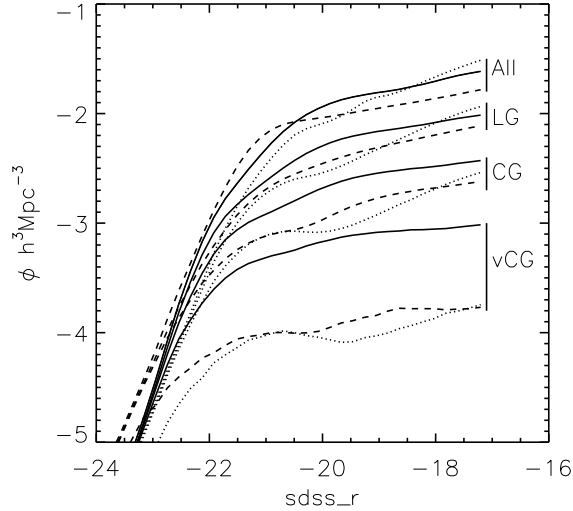


Figure 5.1: Derived SDSS r-band luminosity functions for galaxy groups constructed with the SAMs described herein: “All” refers to the global galaxy luminosity function; “LG” to loose groups; “CG” to compact groups; “vCG” to very compact groups. The dashed/dotted/solid lines refers to the M\_B07/M\_D06/D\_B06 models, respectively.

## 5.2 Luminosity Function of FoF Groups

Fig. 5.1 shows how the luminosity function changes with FoF linking length for different SAM prescription. It is unsurprising that the global luminosity functions of all the models are similar because the semi-analytic models are designed to replicate the same observational luminosity function of Blanton et al. (2003) so it is expected that the models are similar in this regime. At smaller linking lengths (moving from top to bottom in the figure) there are a decreasing number of galaxies, in all SAMs, a fact which is more dramatic in the “Munich” variants (M\_D06; M\_B07), as noted in § 4. This suggests that the “Durham” model galaxies are more centrally concentrated than those of the “Munich” variants, discussed in detail Chapter 3.

The second, and perhaps more striking, feature of Fig. 5.1 is the relative dearth of intermediate luminosity ( $-21 \leq M_r \leq -18$ ) galaxies in the M\_D06

## CHAPTER 5

catalogues (in relation to a simple Schechter (1976) function). This is manifest in the “wobble” or “dip” seen in the M\_D06 group luminosity function that is not present in the other models. This wobble becomes more apparent at shorter linking lengths (i.e., CGs and vCGs).

The M\_B07 SAM, which employs the same AGN feedback prescription as that of M\_D06, shows no such feature in the luminosity function. Weinmann et al. (2006; fig 3) show a similar wobble in the luminosity function of groups in particular mass bins, known as the conditional luminosity function, using the Croton et al. (2006) SAM (a close “cousin” to the M\_D06 SAM employed here).

Luminosity function, the magnitude gap, relative populations of vCGs etc. all suggest that Durham models are more centrally concentrated. A possible reason for this higher central concentration is largely due to the accretion prescriptions. If the subhalos in the Munich models accreted on shorter timescales, then once they reach the central region they are rapidly accreted, whereas in D\_B06 the galaxies remain present in the central regions over a longer time, hence those groups tend to be more concentrated. This potential difference in satellite lifetime is down to the different techniques the two models use to follow satellites. The Munich models follow subhaloes until they can no longer be identified, before initialising an analytical countdown. The Durham models, however, do not follow subhaloes, and use a different technique to calculate the satellite merging time. This will be discussed in further detail in the next chapter.

Fig. 5.2 shows the luminosity functions of the three primary SAMs (M\_D06, D\_B06, M\_B07) and the three primary linking lengths (LG, CG, vCG) under consideration here, decomposed into centrals and satellites. Fig. 5.3 shows the best fit profiles to the plots. The M\_D06 and M\_B07 centrals are fit by a Gaussian, while the D\_B06 model centrals are fit with Schechter functions. All satellites are fit by Schechter functions. The characteristic shape of the centrals has been

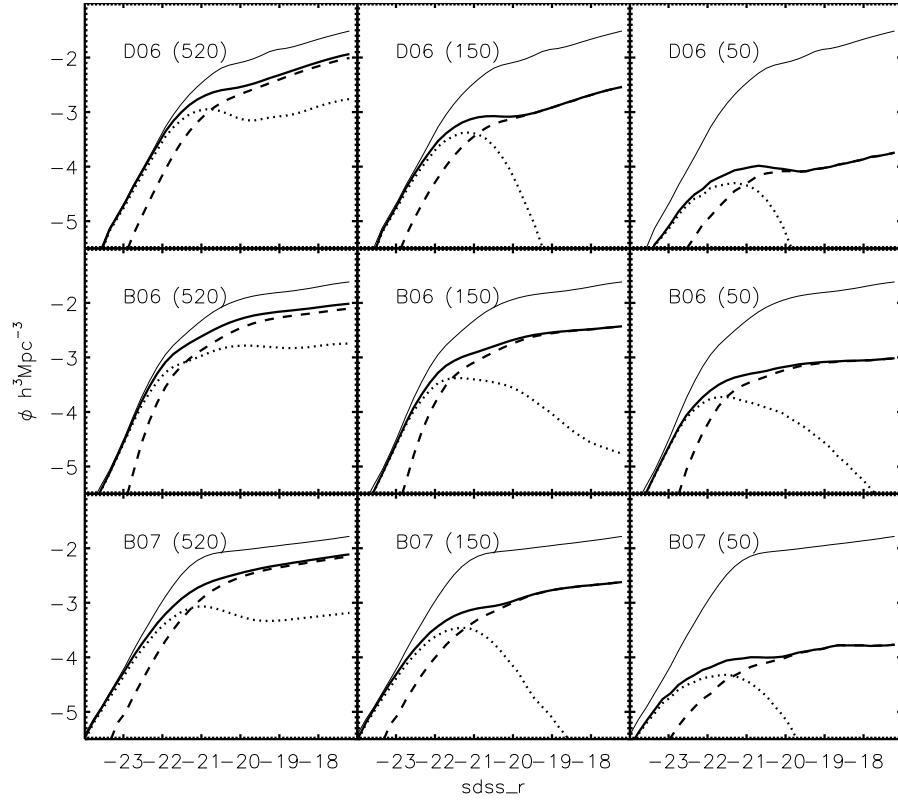


Figure 5.2: Group luminosity functions for for the three primary SAMs under consideration (M\_B07, M\_D06, D\_B06). In each panel, the dotted lines correspond to central galaxies and the dashed lines are for the satellites; the thick solid lines represent the group luminosity function and the thin solid line defines the global galaxy luminosity function for reference. The legend M\_B07, M\_D06, D\_B06 refers to the model as defined above and the number in brackets refers to the linking length in  $h^{-1}\text{kpc}$ .

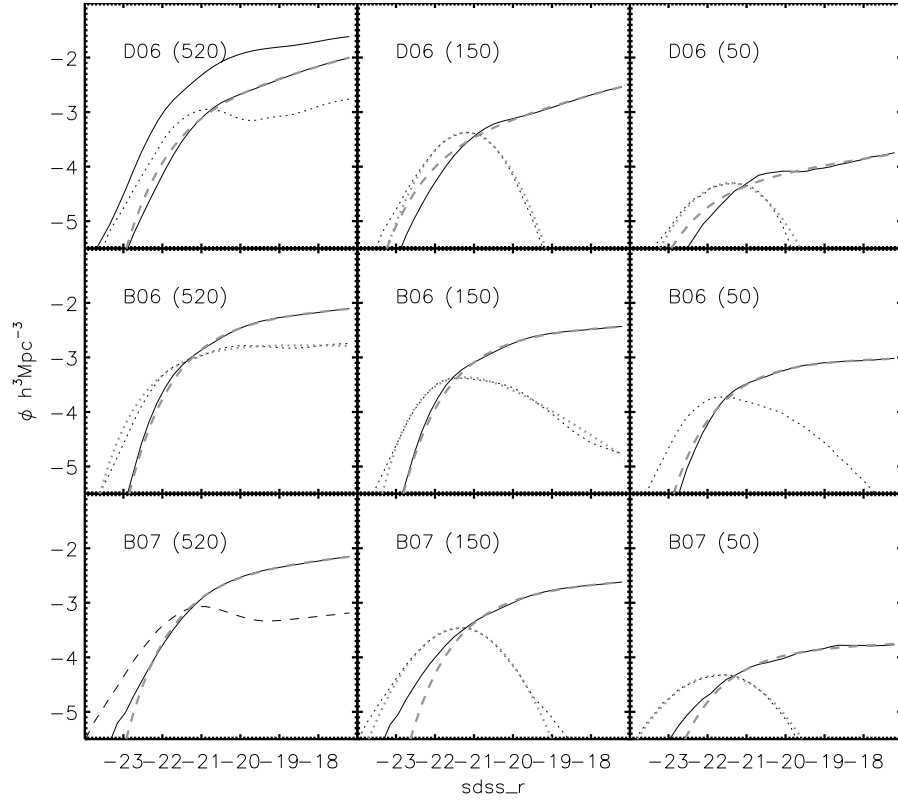


Figure 5.3: The best fit lines for group luminosity functions for the three primary SAMs under consideration (M\_B07, M\_D06, D\_B06). Labels as in Fig. 5.2. The thick dashed and dotted lines show the best fit functions for satellites and centrals respectively. The thin lines, solid for satellites, dashed for centrals. See Table 5.2 for best fit parameters, but best fit lines for LG centrals in the M\_D06 (520) and M\_B07 (520) are not shown because they show considerable deviation from a Schechter or Gaussian profile.

## CHAPTER 5

suppressed in the LGs due to the contamination of central galaxies with centrals of low mass haloes surrounding the main group halo. This is because LGs include centrals from small mass haloes outside the main group halo.

The luminosity function for CGs, however, shows the aforementioned Gaussian central + Schechter function satellite two-component structure, when decomposed. The best fit parameters are shown in Table 5.2. The aforementioned wiggle in the M\_D06 luminosity function is apparently due to the combined effect of (i) a general lack of satellites, and (ii) the sharpness (or “peakiness”) of the central galaxy luminosity distribution. Relative to the D\_B06 SAM prediction, this central distribution is very narrow, without the low-luminosity tail associated with the D\_B06 model. Further, the satellite galaxy luminosity function is much steeper in the M\_D06 model than in either those of D\_B06 or M\_B07. The third panel in the first row of Fig. 5.2 clearly illustrates the signature of the deficit of intermediate luminosity galaxies in the M\_D06 SAM. The third row of Fig.5.2 shows that this effect remains at the shortest linking lengths (and the difference in the absolute number of vCGs is also clear).

The contrast between the M\_D06 and M\_B07 models is of particular interest because they use the same AGN feedback implementation, but differ in their choice of supernovae feedback. This has the effect of reducing the number of low-luminosity galaxies, whilst simultaneously making the most massive (luminous) galaxies “over-luminous” (Bertone et al., 2007). Although not clear from 5.2 the M\_B07 treatment of supernovae feedback also leads to a more significant population of intermediate-luminosity satellites and a shallower luminosity function, thus smoothing out the “wiggle”.

Table 5.1: Proportion of galaxy group types, where the three numbers are the percentage of bright central, peripheral and dim central groups.

Model	LG	CG	vCG
B07	82/02/16	70/22/08	71/23/06
D06	90/01/09	74/21/05	75/20/05
B06	79/00/21	63/12/25	64/15/21

### 5.3 In SAMs

We define three types of identified groups. The first type, Bright central groups, are those where the brightest galaxy is also the central; the second type, Peripheral groups are those without a central galaxy and, therefore, the central galaxy is a satellite. The third type of group, dim centrals are those where the central galaxy is not the brightest. The relative number of groups with each type is shown in Table 5.1. Except in the F08 model, the central galaxy is the only one with hot gas and it acquires all the hot gas from infalling satellites. The central galaxy is also the only galaxy that experiences mergers and grows hierarchically.

There is a striking difference between the three main models for LGs and a noticeable difference between the Munich and Durham models at shorter linking lengths. B06 groups show a significant under-abundance of Brightest Group Galaxy (BGG) centrals compared to D06 groups, while B07 sit between the two extremes for LGs and is more similar to D06 for denser groups. There is a significant proportion of peripheral CGs and vCGs, but very few peripheral LGs. Many LGs consist of galaxies in a large group halo and galaxies in smaller halos around it.

In Fig. 5.4 the luminosity functions of the first ranked galaxies of our groups have been decomposed by group type. It can be seen that, in the Munich SAM, for the denser groups, there is a large difference between the shape of the LF of central and peripheral groups. The difference is most extreme for the D06 model, where the low magnitude tail is due, almost entirely, to peripheral groups. On the

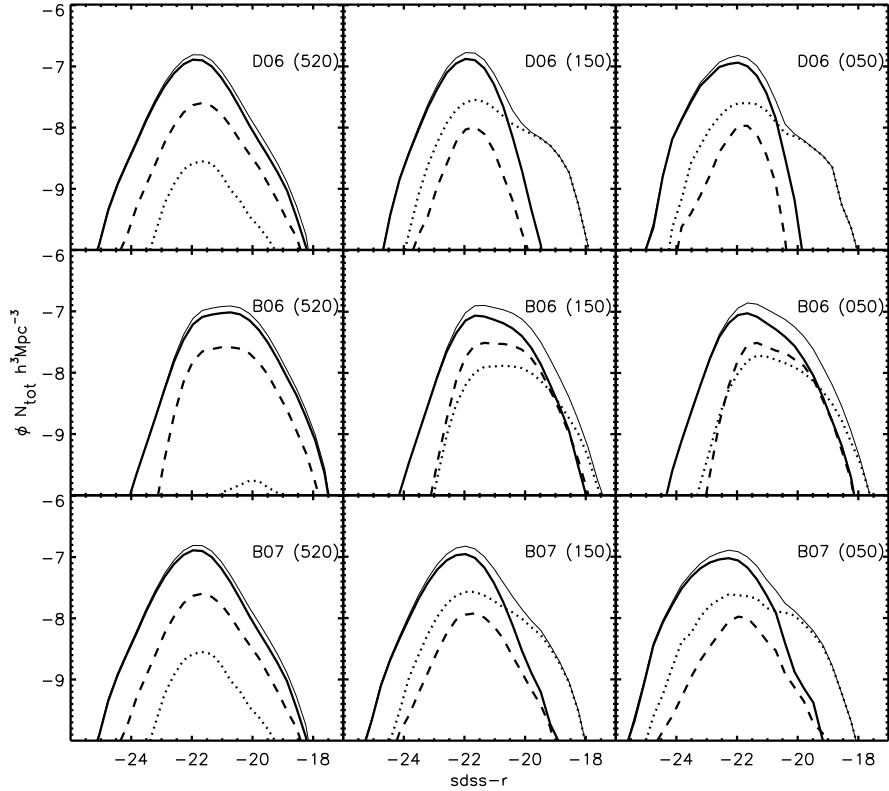


Figure 5.4: Luminosity function of all first ranked galaxies (thin solid line); distribution of bright central groups (thick solid line); the first ranked galaxies in peripheral groups (dotted line) and dim central groups (dashed line). Labels as in Fig. 5.2. An excess of peripheral brightest group galaxies is apparent in the Munich models.

contrary, in the B06 model the distribution of groups is not particularly different for the different group types.

## 5.4 Conditional Luminosity Function

We now examine the conditional luminosity functions in four different mass bins for the D\_B06, M\_D06, and M\_B07, SAMs. In this section groups consist of galaxies within the same dark matter halo. The limit on the minimum number of members still applies. Even for LGs there is not a one-to-one correspondence between halo groups and FoF groups.

CHAPTER 5

Table 5.2: Best fit parameters for groups of galaxies. Schechter functions are fit to satellite galaxies in all three models and to D\_B06 centrals. M\_D06 and Be07 centrals are fit with Gaussian. This Table shows the parameters used in Fig. 5.3. For all satellite galaxy profiles the Schechter parameters, the position of the knee, the low luminosity slope and the normalisation. For the Gaussian centrals of M\_D06 and M\_B07 the parameters given are the position, deviation and height of the peak.

	linking length	Centrals			Satellites		
		$\bar{M}$	$\sigma$	$H$	$M_*$	$\alpha$	$\phi$
M_B07	LG	N/A	N/A	N/A	-21.1	-1.47	0.0021
	CG	-21.20	0.65	0.0004	-21.7	-1.47	0.0005
	VCG	-21.42	0.77	5.03e-05	-21.9	-1.26	6.064e-05
M_D06	LG	N/A	N/A	N/A	-20.1	-1.18	0.0043
	CG	-21.35	0.75	0.0003	-20.7	-1.12	0.0018
	VCG	-21.69	0.91	4.77e-5	-21.1	-1.06	0.0002
		$M_*$	$\alpha$	$\phi_*$	$M_*$	$\alpha$	$\phi$
D_B06	LG	-21.56	-0.95	0.0022	-20.7	-1.13	0.0057
	CG	-21.03	0.20	0.0013	-20.8	-1.09	0.0031
	vCG	-21.20	0.33	0.0005	-21.0	-1.04	0.0009

We calculate groups based on those galaxies which lie in the same dark matter halo and subdivide by mass. We plot these mass-dependent luminosity functions in Fig. 5.5, and present the corresponding best-fit Gaussian and Schechter functions in Table 5.3. The  $10^{13-14}M_\odot$  mass bin shows little evidence for the “wiggle” (for any of the SAMs) alluded to earlier, whereas the  $10^{14-15}M_\odot$  and  $10^{12-13}M_\odot$  bins show “peaks” in the Munich (M\_D06, M\_B07) models, but not in the Durham (D\_B06) model. As the satellite luminosity functions are essentially the same here, the difference is necessarily due to the shape of the central galaxy luminosity function which is widest for the D\_B06 SAM, and narrowest for the M\_D06 models. The “wiggle” in the M\_D06 model is particularly prominent in the lowest mass bin (top right panel), where a number of physical processes become relevant. Bower et al. (2006) points out that at  $\sim 2 \times 10^{11}M_\odot$  the cooling rate exceeds the free-fall rate and the halo is no longer in hydrostatic equilibrium. This has repercussions for the effectiveness of feedback from the central source,

## CHAPTER 5

(Binney 2004), and is used in the Durham paper to explain the break in the luminosity function. Our results indicate that in the Munich models this may have other repercussions.

For the highest mass bin we can see that the satellite luminosity function is steepest for the M\_D06 SAM and shallowest for the D\_B06 model. The characteristic luminosity at the “knee” of the Schechter function, ( $M_*$ ), is lowest for the D\_B06 model. However, this bin has only a small effect on our groups because the FoF group luminosity function “wiggle” occurs at lower luminosity than the wiggle seen in this particular mass bin. The wiggle seen in the group luminosity function can be traced primarily to the luminosity function in the  $10^{12-13}M_\odot$  bin. In this mass range, the satellite distribution is fairly steep and the central galaxy luminosity function relatively narrow and bright.

In contrast with the M\_D06 SAM, the wiggle in the luminosity function does not occur with the D\_B06 model due to the latter’s much broader central galaxy luminosity function, a breadth which tends to produce significantly more low-luminosity centrals compared to M\_D06. The wiggle is most clear in the  $10^{12-13}M_\odot$  mass bin where the width of the Gaussians are,  $\sigma_{D\_B06} \approx 1.64\sigma_{M\_D06}$ , and  $\sigma_{M\_B07} \approx 1.35\sigma_{M\_D06}$ . Below this mass, the centrals dominate over satellites and the wiggle is not apparent because more haloes contain simply one galaxy. The group galaxy luminosity decreases with halo mass in both centrals and satellites, although more for centrals, which causes the wiggle to shift to lower luminosity.

Using galaxies in dark haloes compared to galaxies identified using a particular FoF algorithm it is found that the FoF method produces a narrower central galaxy profile than the halo method. This does not affect our model-model comparison but is important when comparing directly with observations. In figure 3

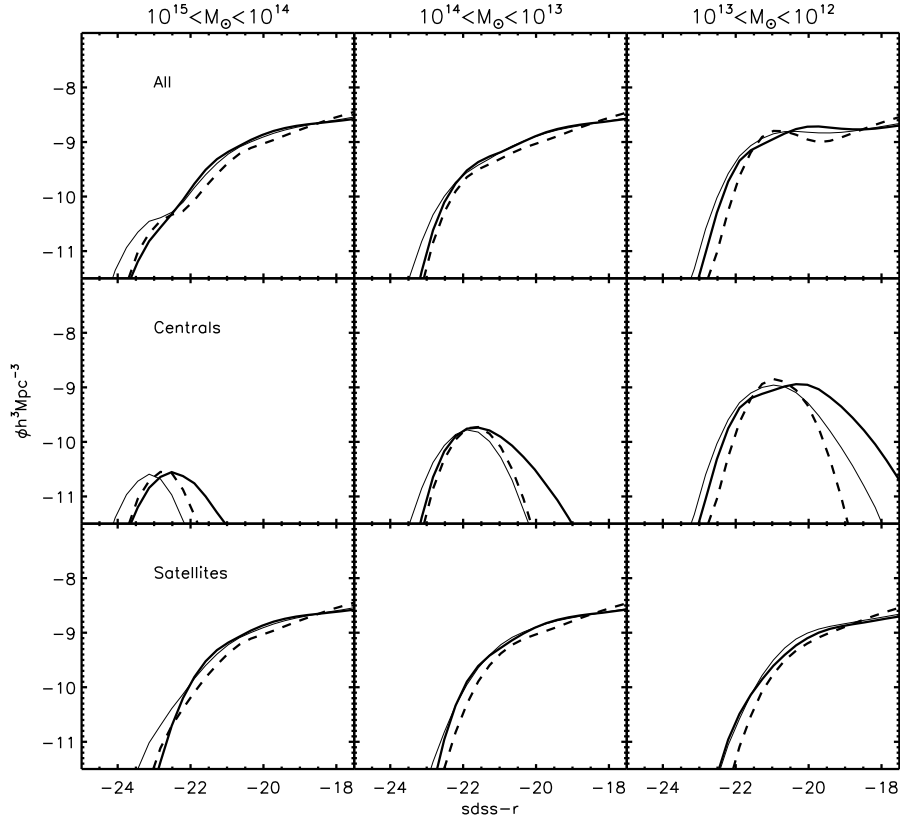


Figure 5.5: The conditional luminosity functions in three mass bins for halo-based groups for the three primary SAMs, at redshift  $z=0$ . The top row shows the profiles of all halo members, the second row shows central galaxies and the bottom row shows satellites. Three mass bins are used, roughly, clusters, large groups and small groups. The thin solid, dashed and thick solid lines are for the M\_B07, M\_D06 and D\_B06 models respectively. The best fit Schechter and Gaussian profiles are shown in Table 5.3

of Weinmann et al. (2006), also Yang et al. (2008), we can see that the conditional luminosity function of groups depends on the method used to identify group members and the method used to define group masses.

The luminosity and mass distributions of central galaxies are similar for both Munich (M\_D06, M\_B07) models, and significantly wider for the Durham (D\_B06) SAM, but the M\_D06 SAM leads to a much lower luminosity and stellar mass Schechter function normalisation ( $\phi$ ) than either of the M\_B07 or D\_B06 models. While the turnover in the satellite distributions occurs at approximately the same

CHAPTER 5

Table 5.3: Best-fit parameters for the inferred conditional luminosity, plotted in Fig. 5.5. For all satellite galaxy profiles, the Schechter parameters, (the position of the knee, the low luminosity slope and the normalisation), are shown. For the Gaussian centrals of M\_B07 and M\_D06 the parameters given are the position, deviation and height of the Gaussian.

	$\log(M)$	Centrals			Satellites		
		$M_*$	$\alpha$	$\phi$	$M_*$	$\alpha$	$\phi$
		$M$	$\sigma$	$H$	$M_*$	$\alpha$	$\phi$
M_B07	14 – 15	-23.12	0.47	0.00001	-21.03	-1.210	0.00083
	13 – 14	-21.85	0.58	0.00018	-20.90	-1.150	0.00208
	12 – 13	-20.94	0.76	0.00124	-20.41	-1.042	0.00230
M_D06	14 – 15	-22.74	0.44	0.00001	-21.48	-1.50	0.00031
	13 – 14	-21.67	0.52	0.00020	-21.36	-1.47	0.00078
	12 – 13	-20.88	0.55	0.00171	-20.67	-1.45	0.00106
D_B06	14 – 15	-21.2	2.33	0.00001	-20.84	-1.089	0.00160
	13 – 14	-20.7	1.47	0.00033	-20.66	-1.093	0.00289
	12 – 13	-20.3	0.36	0.00419	-20.26	-1.047	0.00254

position in each of the SAMs, the low-mass end slope is steepest for the M\_D06 SAM and, as noted previously, the M\_D06 centrals' distribution is roughly two-thirds the width of that of the M\_B07 and D\_B06 SAMs. This suggests that, as with our FoF groups, the peak is due to a relatively sharp central peak and a dearth of intermediate satellites. The behaviour of the stellar mass function essentially echoes that of the luminosity function and Munich groups tend to have thinner profiles, except for peripherals compared to D\_B06.

The Munich galaxy types are decomposed into those galaxies in the centre of subhalos and those where the galaxies subhalos are unresolved. The steepness of the low luminosity end of the luminosity profile is due to an excess of satellites in unresolved subhalos. Additionally the stellar mass of galaxies in Munich models is not reduced by stripping. Maybe a fraction of low luminosity satellites would fall below the  $M_r = -17$  limit we imposed once this effect is taken into account. Should this effect be included the distribution may flatten, but fewer vCGs would be found.

Y08 shows the CLFs for SDSS groups. The luminosity functions are produced

## CHAPTER 5

using the Y08 study of the conditional luminosity function of SDSS DR4 galaxies. They are fit modified Schechter and Gaussian functions to the satellite and central galaxy luminosity distributions. The functional forms are,

$$\Phi_{cen}(L|M) = \frac{1}{\sqrt{2\pi}\sigma_c} \exp\left[-\frac{(\log L - \log L_c)^2}{2\sigma_c^2}\right], \quad (5.2)$$

$$\Phi_{sat}(L|M) = \phi_s^* \left(\frac{L}{L_s^*}\right)^{(\alpha_s^*+1)} \exp\left[-\left(\frac{L}{L_s^*}\right)^2\right], \quad (5.3)$$

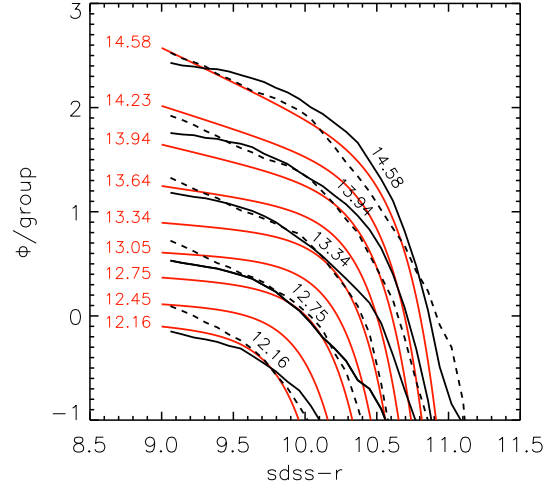
where,  $L$  is the luminosity,  $L_c$  is the mean position of the Gaussian,  $\sigma_c$  is the width of the Gaussian,  $\phi_s^*$  is the normalisation of the modified Schechter function,  $\alpha_s^*$  is the low mass slope and  $\log(L_s^*) = \log(L_c^*) - 0.25$  and is the position of the knee of the modified Schechter function.

Y08 provide the best fit parameters, which we compare to the M\_D06 and D\_B06 models using the same mass cuts as Y08. In Fig. 5.6(a) and Fig. 5.6(b) we show the model and Y08 group luminosity functions. Each model diverges quite noticeably from the observations. These plots show the luminosity functions of all galaxies which are members of groups within a specific mass range divided by the total number of groups in that mass range.

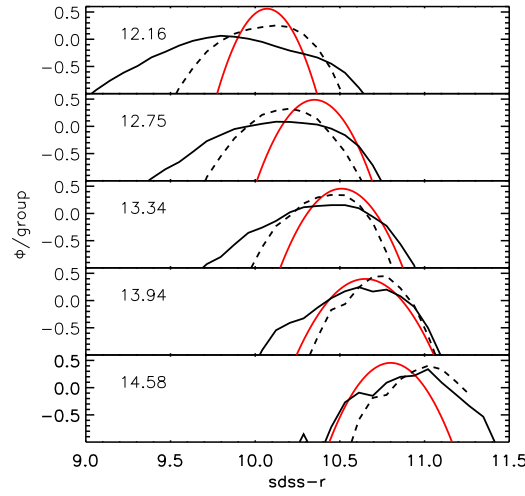
We show the entire observational mass range in each plot because the different methods of identifying mass in the model and the observations may include a systematic difference.

The best fit curves presented in table 1 of Y08 are compared with luminosity functions of the D\_B06 and M\_D06 models. The resulting plots are shown in Fig. 5.6(b). The normalisation of the plots is the number of galaxies per luminosity per group. That is the standard luminosity function divided by the number of groups. Panel ‘a’ shows the satellite galaxy distribution. It appears that the luminosity function of galaxies in each mass bin correspond best to Y08 luminosity function of the same mass bin.

CHAPTER 5



(a) Satellite galaxies



(b) Central Galaxies

Figure 5.6: The conditional luminosity function of the models, D\_B06 (solid black line) and M\_D06 (dashed line) plotted over the CLFs of Y08 (shown in red). The number quoted being the centre of each mass bin and the box width being  $\sim 0.31$  mag. In panel ‘a’ the top pair of lines are the  $10^{14.58} M_{\odot}$  cut, the next is the  $10^{13.94} M_{\odot}$  cut etc, down to  $10^{12.16} M_{\odot}$ . The numbers on the panels are the  $\log(\text{Mass})$  of the parent halo in solar masses.

## CHAPTER 5

The shape of the profiles are considerably different for the CLFs are previously mentioned. For low mass groups there are far fewer satellites than in the observations, although the M\_D06 model has more galaxies in the halo. The  $10^{12.75}M_{\odot}$  groups show that M\_D06 groups produce more low mass galaxies. The mass given by Y08 seems to be closer to 2.24 times larger than the closest equivalent in the Millennium Run, given the scaling of the luminosity functions. In general the number of galaxies per group with low luminosity is higher in the M\_D06 model than in the D\_B06 model for satellites, although the D\_B06 model has more bright galaxies. There is some evidence of the dearth of intermediate luminosity galaxies in M\_D06 at the high mass end.

Weinmann et al. (2006) note that the method used by Y08, presented in Yang et al. (2005), artificially narrows the central galaxy luminosity function. This is because their iterative technique uses the brightest galaxy luminosity in the derivation of the group halo mass, while in the models there is no such direct linking of mass and luminosity. However, even taking this into account, there are significant differences between the models and the observations. The M\_D06 model shows that the low mass group centrals peak in the same place at the observations while the others are somewhat displaced. However, the D\_B06 groups are even wider than the M\_D06 groups.

However, the D\_B06 groups still look like Gaussians, while for FoF groups they look like Schechter function. This, we conclude, therefore, is the result of the higher proportion on non-central BCGs in this model. As the observed groups use the same criterion (the central is the BCG) we can state that the D\_B06 model is less true to the observations than the M\_D06 model in this respect. There is most divergence in the three data sets for low mass halos, particularly for the lowest mass satellites.

We note that the majority of group halo hosts in the models lie in the upper

centre region of the distribution. The median vCG has a mass of  $1.7 \times 10^{13} M_{\odot}$  for both M\_D06 and D\_B06, but with considerable variation in each case. This means that the profiles closest to this value are more important to the analysis of vCGs than further away. In Fig. 5.4 we see that the models are reasonably similar at this point, although the peak in the central luminosity function is greater in the Munich variant.

This also suggests that the relative lack of vCGs in M\_D06 compared to D\_B06 is due to the ‘placement’ of galaxies in groups rather than the absolute numbers. In the following section we examine the possible reasons for the dearth of galaxies in CGs and vCGs.

## 5.5 Magnitude Gap

The magnitude “gap” between the first- and second-ranked (and, indeed, lower-ranked) galaxies within a group can be used as a fair predictor of the group (or halo) age (von Benda-Beckmann et al., 2008), as the central galaxy tends to grow unceasingly with time via satellite accretion/stripping. This process inevitably increases the magnitude gap. This process is controlled by feedback processes in the central galaxy (Section 2) and by infalling galaxies. Taken to its extreme, such an effect gives rise to the so-called “fossil groups”, which are groups with a huge magnitude gap most likely caused by a lack of recent galaxy infall onto the group (D’Onghia et al., 2005; Milosavljević et al., 2006; Sommer-Larsen, 2006; Dariush et al., 2007; Sales et al., 2007; van den Bosch et al., 2007; Díaz-Giménez and Mamon, 2010; Jones et al., 2000, 2003; Mendes de Oliveira et al., 2006; Cypriano et al., 2006; Santos et al., 2007; Vikhlinin et al., 1999). However, Zibetti et al. (2009) contradict the above papers, showing that although there is a high magnitude gap in these objects, there is no apparent lack of substructure.

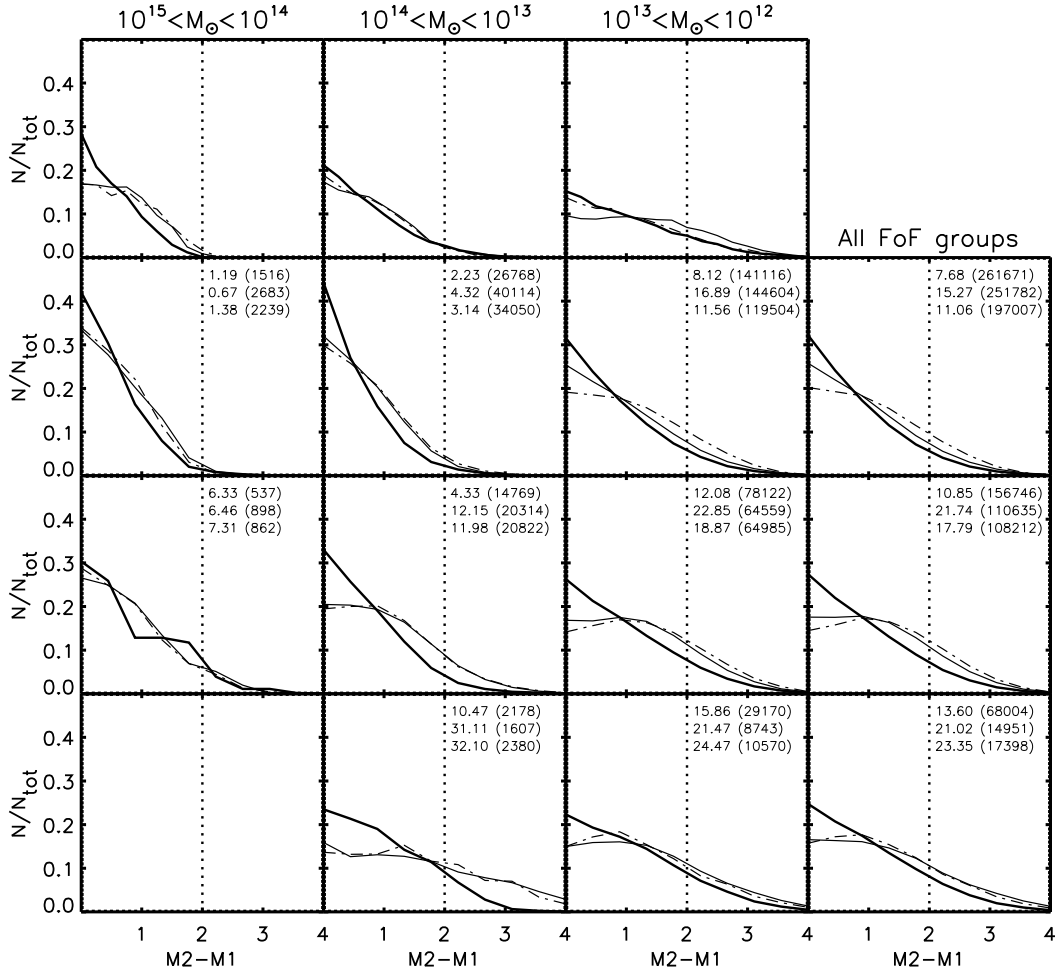


Figure 5.7: Conditional (mass-dependent) magnitude gaps between first- and second-ranked galaxies for the SAMs included in this study. Thick solid, thin solid and dashed lines are for D\_B06, M\_B07 and M\_D06 groups respectively. Panels A-C are for halo-based groups subdivided by group mass, and panels G,K and P are for all FoF-groups regardless of mass. Panels D-G are for LGs, panels H-K are for CGs, and panels L-P are for vCGs. The vertical line shows the cut off for Fossil groups (Sales et al. 2007). The numbers in each panel give the percentage of groups which are fossil systems, and, in brackets, the total number of groups in each mass bin. The first number is for D\_B06, the second for M\_D06 and the third for M\_B07.

## CHAPTER 5

In Fig. 5.7, far right column, we compare the magnitude gap distribution between first and second ranked group galaxies in both the suite of SAMs employed here and the observations (both in the SDSS r-band). Both the Durham and Munich SAMs appear to provide only limited matches. The M\_D06 model (and to a lesser extent, that of M\_B07) shows a preferred magnitude gap of  $\sim 1$  mag between the two most-luminous galaxies in the model groups (particularly in the CGs and vCGs), while the D\_B06 SAM predicts more equal luminosity first- and second-ranked group galaxies. On the other hand if we compare to the results of van den Bosch et al. (2007) we find that we have far fewer fossils (LGs) in the highest two mass bins for all three models but more for M\_D06 groups in the lowest mass bin.

A fairer comparison of the model predictions with the observations must take into account the selection effects inherent within the data. Specifically, the data upon which these results are based have (i) a limited dynamic range of  $\sim 2$  mag, Lin et al. (1996) which is driven by minimum signal-to-noise requirements, and (ii) discard groups that contain fewer than four galaxies within  $\sim 2$  mag of the first-ranked galaxy. We have imposed comparable selection effects upon the models, and the impact upon the luminosity functions of the first- and second-ranked CG galaxies is shown in the right hand panels of Fig. 5.8. The figure shows that the turnover in the Munich models is no longer shown in the heavily selected data. The entire range of the profile is curtailed and the models and data now lie closer to one another. However, the models produce a significant shortage of pairs with low magnitude gaps for LGs and a higher population of groups with a magnitude gap of 1. This effect is more extreme in the Munich models but is still present in D\_B06.

When implementing this limiting criterion the left hand column of Fig. 5.8 demonstrates that the models appear to match with observations in this case,

## CHAPTER 5

most significantly in the bottom panel, showing vCGs. In the LG catalogue (Top left panel), the models suggest that the magnitude difference between the brightest and second brightest galaxies is slightly too large. A possible interpretation of this is that real groups are accreting large galaxies on their peripheries (which are not found in the vCG catalogue because it probes the centres of groups), thus producing the broader profile. These infalling galaxies are rapidly stripped in the models resulting in the convergence between model and observation with decreasing linking length. Fig. 5.7 however, shows that the unrestricted magnitude gap profile widens slightly with density suggesting that there is a population of bright infalling galaxies where the infalling galaxy is also the brightest in the group. This seems contradictory but Fig. 5.8 shows a similar broadening in the observations. The small sample size of observed compact group catalogues means that care should be taken before drawing firm conclusions from this trend and that larger samples are required to test this hypothesis.

The central galaxy of a group in M\_D06 is too bright compared to the brightest satellite. This may be because the central galaxy is so privileged in that only it undergoes merging and hot gas accretion. The D\_B06 model is closer to the magnitude gap distribution of the observations, possibly due to the higher population of none central brightest group galaxies. The SAMs define the central in each output to have the properties of the central of the largest progenitor halo in the previous output, but if both halos are similar in mass there is no physical justification for this extremal strict difference. Also, because only the central galaxy merges there can be no satellites which grow while in the group environment, favouring the central still further.

When the dynamic range is increased to 3 mag the models begin to diverge clearly, with the M\_D06 model both “broadening” and shifting to lower luminosity, relative to the distributions, based upon the M\_B07 and D\_B06 SAMs

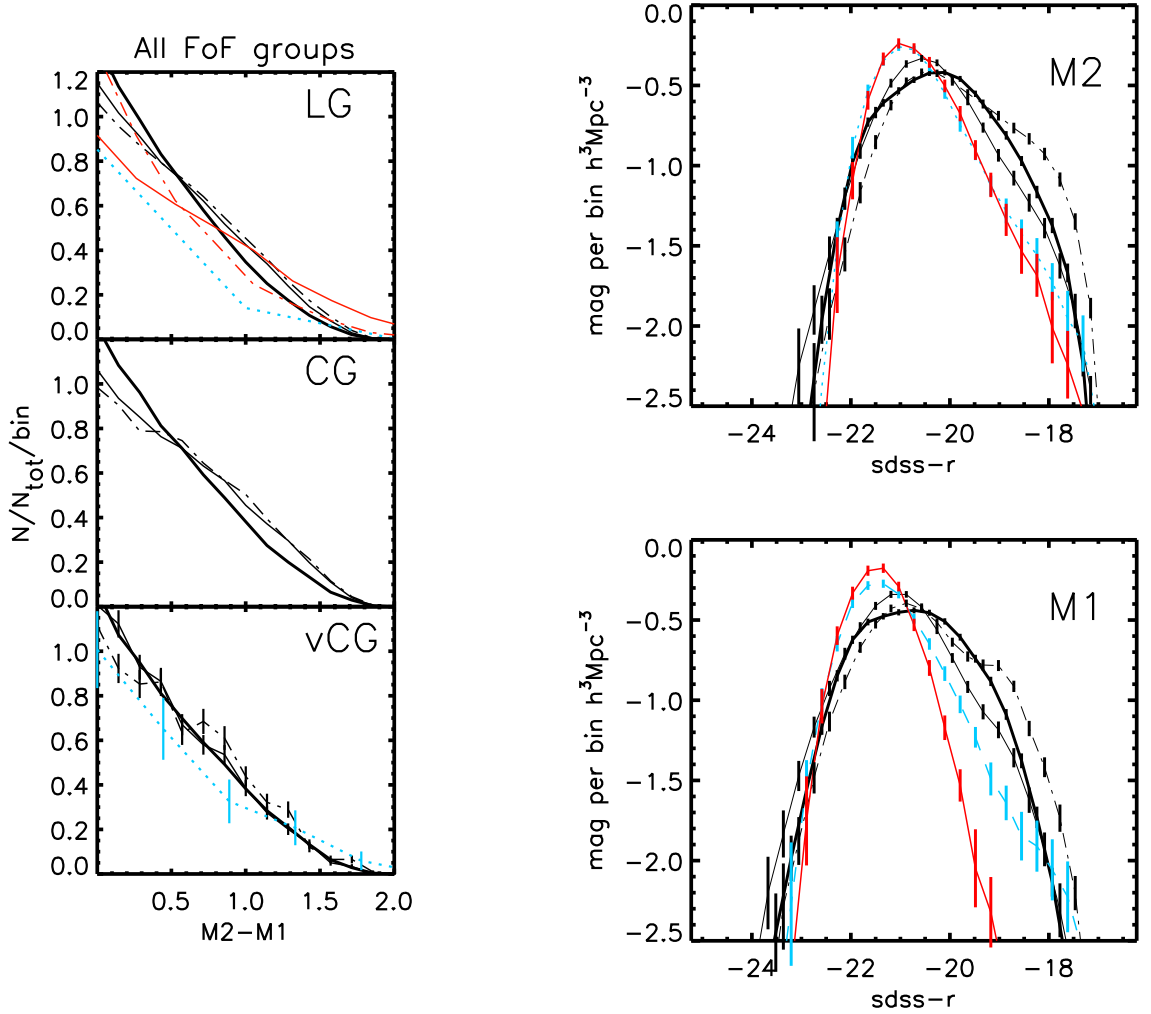


Figure 5.8: Left column: Normalised counts of the magnitude gap between 1st and 2nd ranked galaxies. The thin solid, dashed and thick solid lines are for M\_B07, M\_D06, D\_B06 models. The top left panel shows Tago et al. (2008) groups (dot-dashed line), Tucker et al. (2000) groups (blue dotted line) and Yang et al. (2008) groups (solid red line). The middle panel shows the results for CGs in SAMs, and the bottom left panel shows Allam and Tucker (2000) compact groups along with vCGs. Right column: The upper panel shows the second ranked luminosity function for LGs, and the lower panel shows the distribution of first ranked galaxies. Line styles are the same as for the right column. Data are limited to those groups with a first ranked to fourth ranked magnitude gap of 2 magnitudes, to mimic a survey dynamic range.

CHAPTER 5

Table 5.4: Percentage of groups with magnitude gap between first and second ranked galaxies greater than 2 magnitudes (top) and less than 0.5 magnitudes (bottom)

	gap	M_B07	M_D06	D_B06
LG	> 2	15.2	20.6	10.8
CG	> 2	23.8	28.4	14.9
vCG	> 2	29.8	27.5	18.2
LG	< 0.5	28.7	22.7	35.6
CG	< 0.5	19.7	16.4	30.4
vCG	< 0.5	18.7	17.8	27.5

(right most column of Fig. 5.7). The turnover in the profiles becomes distinct at this dynamical range, whereas before it was not possible to easily distinguish the two models. Table 5.4 shows the populations of groups in the two extreme cases of small and large magnitude gap. The differences are very large between the Durham and Munich models. We also note that the profile in Yang et al. (2008) is distinctly wider than the profile for Tago et al. 2010, suggesting that Yang et al. has a higher dynamic range than Tago et al. groups. At a dynamic range of 4 magnitudes the three models shown are distinctly different and Yang et al. closely matches the D\_B06 model with no sign of the turn over, as noted by Dariush et al. (2010).

Although the global luminosity function of galaxies is well matched by observations the profiles for the first and second ranked galaxies shown in Fig.5.8 tend to be dimmer and wider than observations. Notable is the second peak in the luminosity function of the M\_D06 model caused by an excess of dim first and second ranked galaxies although this may be due to the specifics of the group finder.

We next analysed the magnitude gap statistic for the conditional halo based groups. What is readily apparent is that the “Munich” (M\_D06; M\_B07) models are both “flatter” (in the sense of showing little preference for either equal-luminosity first- and second-ranked group members (0 mag gap), or 1 mag gaps

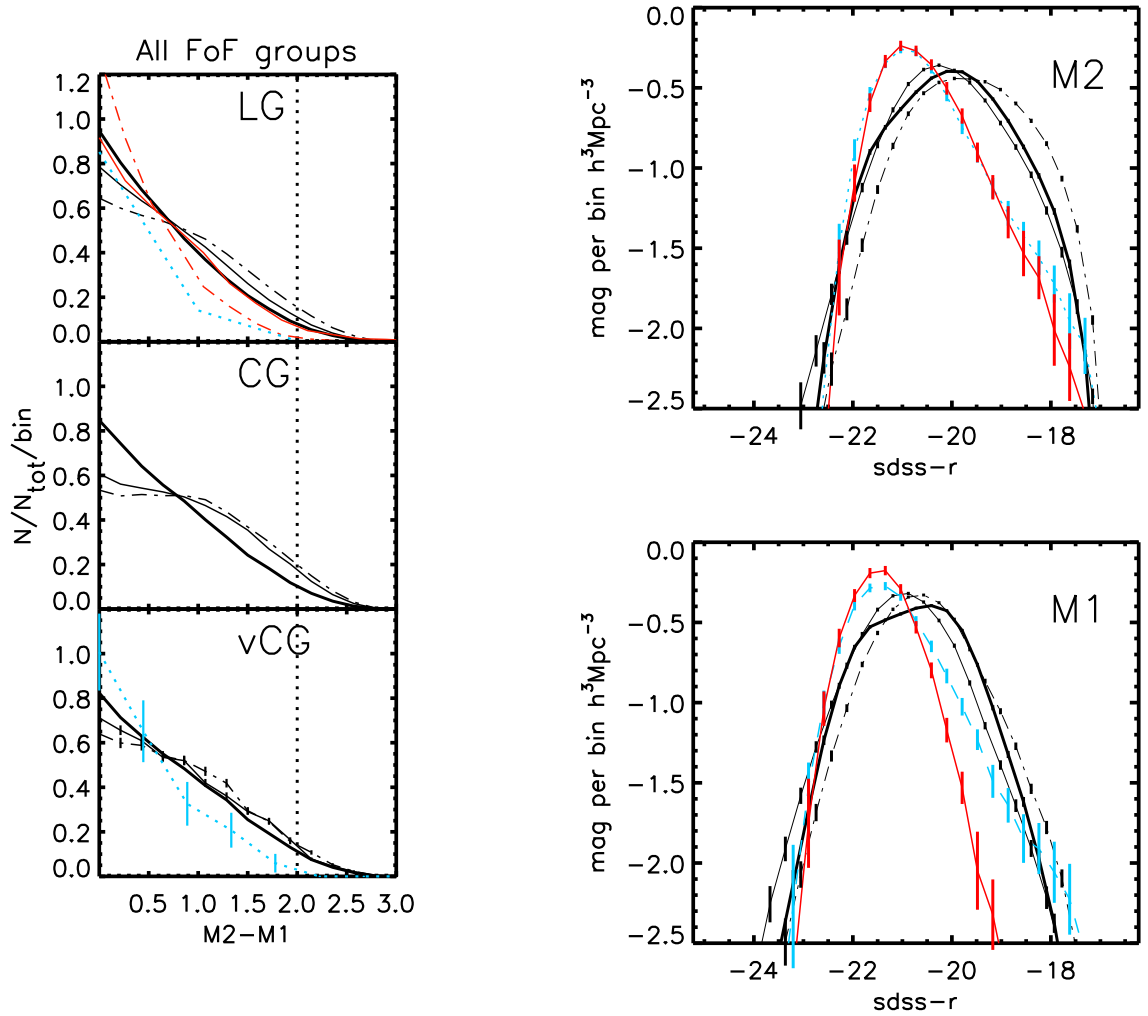


Figure 5.9: Lines as in Fig. 5.8 but with a first to fourth ranked magnitude gap of 3. Here the D\_B06 model essentially matches the Y08 data.

## CHAPTER 5

between the same) and “broader” than the “Durham” (D\_B06) models, but they trace each other reasonably well in the two highest mass bins; the Munich models only diverge in the lowest mass bin, as noted earlier in Fig. 5.5. This is where the M\_D06 model “turns over” and possesses its most obvious “peak”, while the D\_B06 and M\_B07 models appear most similar. We conclude therefore that this turnover in the Munich models’ luminosity functions can be traced to the “peak” in the lower mass bin of the associated conditional luminosity function.

Dariush et al. (2007); fig 4a, Smith et al. (2010), show a comparable representation of the top-left panel of our Fig. 5.7, employing the Croton et al. (2006) SAM as applied to the Millennium Simulation (in the  $R$ -band, and for a slightly different mass range, but effectively similar to what we have shown.) Dariush et al. (2007) point out that the magnitude gap profile of LGs in Croton et al. (2006) model is similar to  $\ln \Lambda=2$  theoretical model of Milosavljević et al. (2006), where  $\ln \Lambda$  is the Coulomb logarithm that controls the merger rate. When the Croton et al. (2006) SAM is compared with the SDSS C4 catalogue (Miller et al., 2005), as is done in fig. 4c of Dariush et al. (2007) the apparent mis-match at small first- and second-ranked magnitude differences between the Munich SAM and the data become apparent - i.e., the SDSS C4 catalogue shows a magnitude difference distribution which prefers approximately equal luminosity first- and second-ranked galaxies in groups and clusters, consistent with the Durham SAM predictions.

The proportion of first-ranked (by luminosity) galaxies being centrals is sufficiently high to make the transition from the theoretical definitions of “central” and “satellite” galaxies into the observational regime of “brightest” and “second brightest” group galaxies - i.e., we can associate the brightest group galaxy with a central, and the second-brightest galaxy with a satellite. This then allows us to

## CHAPTER 5

plot the luminosity function of first- (M1) and second-ranked (M2) group galaxies, as shown in Fig.5.8, and associate the distribution in M1 with model centrals, and the distribution in M2 with model (brightest) satellites.

In Fig. 5.8, top right panel we can see that the first-ranked galaxy luminosity function of D\_B06 is broader and flatter than those of the two Munich SAM variants; as expected, the M\_B07 model galaxies are on average more luminous. For the distribution of second-ranked galaxies, the M\_D06 galaxies are on average  $\sim 1$  mag less luminous than the Durham model galaxies, and the distribution is broader, peaking at approximately 3.7 rather than 4.1, (Fig. 5.8) which is as expected from the steep luminosity function slope for satellites. When we apply a pseudo-empirical dynamic range limitation of 2 mag to the Tucker et al. (2000) and Allam and Tucker (2000) data sets, the differences between the various SAMs become less apparent. The galaxy luminosity functions are broadened as a whole, with peaks in the distributions which are comparable with each other (Fig.5.8,bottom right panel).

Milosavljević et al. (2006) however, note that the r-band luminosity gap distribution of 730 galaxies from SDSS C4, (Miller et al., 2005), shows some degree of flattening / turnover. This effect is not as significant as for the M\_D06 model, above, but suggests that the turnover is a property of *clusters* rather than all groups.

### 5.6 Satellite-Satellite Mergers

One theory advanced in the above sections is that the shape of the magnitude gap is in part due to the lack of satellite-satellite merging. The Mitaka code by Nagashima and Yoshii (2004) has the option of implementing or not implementing this process.

The galaxies which have merged with the halo but not yet merged with the

central galaxy are assumed to merge at a rate governed by,

$$\tau_{col} = 1.48 \times 10^8 \frac{M^3 \left(\frac{V_c}{V_g}\right)^4}{V_c^3 M^2 n_g} \quad (5.4)$$

where  $M$  is the progenitor mass,  $V_c$  is the circular velocity of the halo,  $V_g$  is the circular velocity of the galaxy,  $n_g$  is the number of galaxies in the halo. We run the code to produce 1000 clusters of  $M = 1 \times 10^{14} M_\odot$  with a minimum progenitor mass of  $1.8 \times 10^{10} M_\odot$ . When the satellite-satellite merging is switched on the galaxy-galaxy richness falls by  $\sim 10\%$ , but there is no difference between the M1-M2 magnitude gap profile. This suggests that the presence of no satellite-satellite merging is a possible explanation of the higher compact group density identified by McConnachie et al. (2008), although not sufficient alone.

## 5.7 Conclusions

By constructing luminosity functions of galaxy groups (ranging from loose to very compact) using variants of several leading SAMs as applied to the Millennium Simulation, we have explored an astrophysical regime in which the SAMs have not previously been inter-compared in great detail.

Several obvious differences between the M\_D06 and D\_B06 (i.e., loosely speaking, the Munich and Durham variants, respectively) became apparent, including an intermediate luminosity “wobble” in the M\_D06 group luminosity functions not readily apparent when using the D\_B06 SAM. We trace the origin of this wiggle to two competing effects resulting from the underlying physics within the M\_D06 SAM - a steeper faint-end slope to the satellite luminosity function and a narrower distribution to the central galaxies’ luminosity function. This is most likely due to the lack of mass stripping in satellite galaxies without enveloping subhalos, type 2 groups, and the particular formulation of AGN in the Munich

## CHAPTER 5

models. A systematic exploration of parameter space in the respective SAM may however, be required to further isolate the cause of the difference.

Observations conducted by Weinmann et al. (2006) suggest that such a wiggle in the group luminosity function might exist, similar to that seen when applying the M\_D06 SAM. However, these same observations tend to show a steeper magnitude gap profile, between first and second ranked galaxies, than can be seen in any of the SAMs. We also see significant “flattening” in the M\_D06 gap distribution (i.e., a comparable likelihood for first- and second-ranked galaxies to be of equal luminosity, as to have a one magnitude luminosity difference), a feature that is not consistent with the data sets described by Miller et al. (2005) or Dariush et al. (2007).

The models applied to the Millennium simulation produce noticeably different galaxy group properties. The group luminosity functions diverge with increasing galaxy density. This means that, for example, the cores of clusters in the various models have different properties, while the properties of the entire cluster will be more similar. As the same dark matter background was used in the three models there are similar numbers of groups and clusters in the models, but according to our definitions, the denser structures are several times more common in the D\_B06 model. The M\_D06 model luminosity function shows a peak for the brightest galaxies that does not appear in the Durham models and is less evident in M\_B07. The magnitude gap profiles of the models also differ between the Munich and Durham models, demonstrating a different profile at the small gap part of the distribution. All models show a shallower, wider magnitude gap profile than the observations. This suggests that modellers need to improve how the central / bright satellite luminosities are calculated. The designation of a single central galaxy which is modelled in a manner that is different to that for the other group members is a simplification which will may need to be improved upon.

## CHAPTER 5

The existence of more, denser, CG and vCG groups in the Durham models compared to the Munich sample suggests that the different merging time-scales and implementations of satellite accretion can have noticeable effects on the predictions of the models. Similarly the fact that the Durham models show a shorter mean galaxy-galaxy separation, indicates that these groups are denser. This suggests that merging time-scales are longer in the Durham groups. This is backed up by the luminosity function of groups because the evident 'wiggle' in the M\_D06 groups appears to be due to a smaller population of satellites and brighter centrals, which is a direct result of the rate at which satellite galaxies are accreted onto the central galaxy. However, while observations show a similar 'wiggle' in group luminosity functions, suggesting the shorter merging time is more physical, McConnachie et al. (2008) find fewer compact groups in their field than in the SAMs, suggesting the merging time-scale should be even shorter. The limited magnitude gap profile indicates that the gap between central and satellite galaxies should be smaller, which may be due to additional physics that is not yet implemented in the models.

# Chapter 6

## MERGER TREES

### 6.1 Introduction

In the previous chapters we noted that the Durham models produce a higher number of vCGs compared to the Munich models. We suggested that this difference is due to different satellite galaxy lifetimes. We hypothesised that satellite merging times are shorter in the Munich models. This is needed in order to remove galaxies from groups and clusters. When a galaxy falls into a group or cluster its orbit decreases due to dynamical friction. This means that older galaxies are expected to lie closer to the centre of the cluster. If satellite galaxies last longer, we would expect clusters to be more centrally concentrated, thus producing more vCGs, etc. The Durham and Munich models use very different techniques to calculate the merging times of satellites.

Binney and Tremaine (2008) relate the merging rate of a satellite galaxy to the mass and circular velocity of the host halo, the mass of the satellite and the radius of the satellite from the cluster centre. This simple model has been frequently tested by comparison to numerical simulations (Conselice, 2006). Bertone and Conselice (2009) calculates the lifetimes of satellite galaxies according to satellite galaxy mass rather than cluster mass but find that between  $z=3$  and  $z=1$  a

## CHAPTER 6

significant decrease in galaxy lifetimes can be seen.

In this Chapter we will expand on our description of the merger trees presented in Chapter 1, and examine the merging times of galaxies in clusters. We will then attempt to explain the different vCG and CG populations.

### 6.2 Calculating Merging times

The Millennium Run produces 64 outputs spaced in time according to,

$$\log(1 + z_n) = n(n + 35)/4200, \quad (6.1)$$

where  $z$  is the redshift and  $n$  is the output number. These are then used to build up the merger trees in each model.

Haloes are assembled using an FoF algorithm (Huchra and Geller, 1982), forming haloes with a mean overdensity of 200, which is the same as a virialized group.

#### 6.2.1 Munich

The Munich model, (Croton et al., 2006), uses SUBFIND, (Springel et al., 2001), to compute the dark matter density field of each FoF halo and identifies subhalos. These subhaloes are extracted from the parent halo during the unbinding procedure, effectively lowering the mass by  $\sim 10\%$ . This means that halos in the Durham models are  $\sim 10\%$  more massive than Munich halos. The spherical overdensity approach is then used to define the virial mass of the halo. The centre of the group is the minimum of the gravitational potential. The sphere is then expanded until the mean overdensity is 200 times the critical density of the universe.

The merger trees used in the Munich models are described in Springel et al.

## CHAPTER 6

(2005). Halos are tracked by following particles from one output to the next, weighted by binding energy. The halo with the highest number of weighted particles is defined as the descendant halo. For each (sub)halo a unique descendant is known, and the merger tree contains a list of halo progenitors. There is no one-to-one correspondence between halos and FoF groups, because not all FoF groups contain bound structures. Halos are arranged by progenitor mass. The central galaxies of halos or subhalos can merge, but satellites without a subhalo can only merge with a galaxy at the centre of a halo or subhalo.

### 6.2.2 Durham

The Durham model merger trees are described by Harker et al. (2006) and Helly et al. (2003). SUBFIND is applied but subhalos are not followed by the merger trees. Satellite galaxies can only merge with the group central galaxy. One problem comparing the two sets of merger trees involves the slightly different methods used to assemble them. The Durham approach produces galaxies that first appear in the catalogue as a satellite, without a central phase. Occasionally main branch galaxies can have satellite status for several outputs. This does not occur in the Munich model.

## 6.3 Dynamical Friction Time

### 6.3.1 Munich

Substructure is followed until it can no-longer be identified, (Croton et al., 2006). This occurs when its mass falls below  $1.7 \times 10^{10} h^1 M_\odot$ . At this point the merging time is given by the equation of Binney & Tremaine (1987),

$$\tau_{friction} = 1.17 \frac{V_{vir} r_{sat}^2}{G m_{sat} \ln(\Lambda)} \quad (6.2)$$

## CHAPTER 6

where  $m_{sat}$  is the mass of the satellite orbiting in an isothermal halo of virial velocity  $V_{vir} = (GM_{vir}/r_{vir})^{1/2}$  and  $\Lambda = 1 + M_{vir}/m_{sat}$  where  $M_{vir}$  is the virial mass and  $r_{sat}$  is the distance of the satellite from the cluster centre.  $r_{sat}$  and  $m_{sat}$  are taken from the last time the subhalo could be identified. The merging time depends on the mass and radius of the cluster, the mass of the satellite and the distance of the satellite from the cluster centre. The countdown is reset when the parent halo merges with an even larger halo. The outcome of the galaxy-galaxy merger will depend on the baryonic mass ratio of the progenitors. The main progenitor will have the larger mass and the stars and gas of the lower mass galaxy will merge with this progenitor.

### 6.3.2 Durham

The dynamical friction timescale in this model is similar to the approach of Cole et al. (2000). However, the actual implementation comes from Benson et al. (2002), which is considerably more complex, but provides similar results as the Cole et al. equations according to Benson et al. (2002). Cole et al. define the merging timescale as:

$$\tau_{friction} = f_{df} \Theta_{orbit} \frac{0.3722\pi r_{vir} M_{vir}}{V_{vir} m_{sat} \ln \Lambda}, \quad (6.3)$$

where  $f_{df}$  is a tunable parameter, given to be 1.5,  $\Lambda = M_{vir}/m_{sat}$  and  $\Theta_{orbit}$  is,

$$\Theta_{orbit} = \left( \frac{J}{J_c(E)} \right)^{0.78} \left( \frac{r_c(E)}{r_{vir}} \right)^2, \quad (6.4)$$

where  $E$  and  $J$  are the initial energy and angular momentum of the satellite's orbit and  $r_c(E)$  and  $J_c(E)$  are the energy and angular momentum of a circular orbit of the same energy.

## CHAPTER 6

In the Benson et al. (2002) approach the orbit of the satellite galaxy is followed more closely. The initial orbital energy and angular momentum of the satellite upon merging is calculated. Two important parameters are defined,  $r_c(E)/R_{vir}$  which parametrises the median binding energy of the halo, and  $J/J_c$  which measures the orbital ellipticity.  $r_c(E)/R_{vir}$  is chosen to be constant, with a value of 0.5 and  $J/J_c$  can vary between 0.1 and 1.0 at random. Given these parameters, the apocentric distance of the satellite's orbit is found, and the orbit equations are integrated. The code keeps track of tidal stripping to remove mass from the satellite. The new mass is then used for the next iteration of the orbit equations. The equations of motion are integrated until it is terminated by one of three conditions:

1. The simulation reached  $z=0$ .
2. The host halo merges with a larger halo.
3. The satellite galaxy merges with the group central galaxy.

Satellite-central merging takes place when the orbital radius calculated from the orbital equations of Benson et al. (2002) falls below  $R_{merge}$ .  $R_{merge}$  is the sum of the half mass radius of the central and satellite galaxies. This method the satellite galaxy can also loose baryonic mass.

The effect of this is that although these merging times match Cole et al. (2000) generally, some satellites have very long merging times as they loose a great deal of mass through tidal stripping.

### 6.4 Method

Merger trees are supplied for both the Durham and Munich SAMs. In order to test the lifetimes of satellites in galaxies we explore the merger trees for both galaxies and halos.

## CHAPTER 6

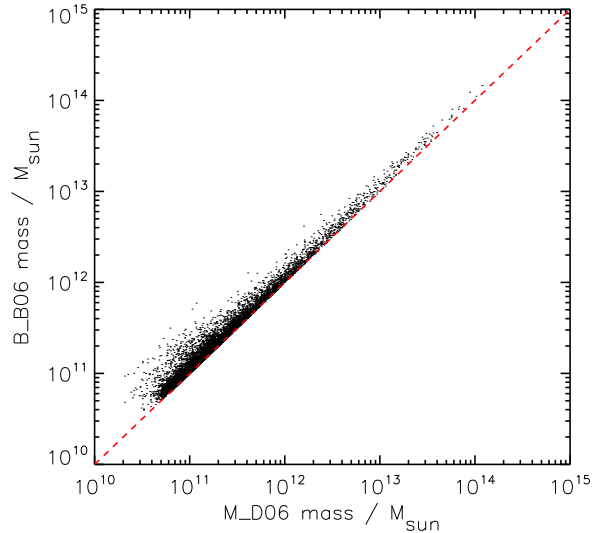


Figure 6.1: The masses of the linked pairs of halos from the two models. The red line is the 1:1 line.

We identify like pairs of the most massive clusters in both the D\_B06 and M\_D06. We do not use the full Millennium Run but use the models applied to the millimillennium simulation <sup>1</sup>. The cluster pairs are matched according to the position of the most bound particle of the cluster halo. The main systematic difference in the two sets of clusters is that D\_B06 clusters are, on average, 10% more massive than their fellows in M\_D06. Figure 6.1 does not simply apply to the clusters but all matched pairs of halos over the entire mass range.

Firstly, we extract the merger trees for halos in each model and follow the main branch of the merger tree. This lets us follow the main branch of the cluster back in time. The main branch is the track of the most massive progenitor of the cluster.

We decided to trace like clusters, and found the main branch of each. However the main branches of the M\_D06 and D\_B06 clusters are not necessarily the same. Where the main branches of the matched clusters different we discard

<sup>1</sup>This uses the same cosmology and resolution as the main Millennium Run but the box size is only  $64.5h^{-1}Mpc$

## CHAPTER 6

those clusters from our sample. If the D\_B06 main branch galaxy is found to be a satellite at any point we also discard that cluster pair. Of our 50 clusters, the first cut leaves 33 clusters with the same main branch, after the second cut we are left with 19 objects. This means that any scatter in the results of the matched pairs is due to differences in dark halo identification technique and the SAM implementation.

In each time step we look for galaxies which merge with the central galaxy of the cluster. We then identify the merging history of these galaxies. To do this we used exactly the same procedure on haloes which merge with the clusters.

Figure 6.2 shows that the D\_B06 model experiences more cluster-halo mergers than the M\_D06 model. If we take the smallest subsample of 19 clusters we can see a very tight correlation between halo infall. This difference is due to the larger volume of D\_B06 clusters and the additional time M\_D06 halos exist as subhalos. M\_D06 shows considerably more merging galaxies with the central, indicative of a faster merging rate. Figure 6.3 shows that for each cluster the merging rate of halos is similar and tightly correlated with halo mass and that D\_B06 galaxies have a lower number of mergers.

For our subsample of 19 clusters we follow those galaxies which merge with the cluster central galaxy back in time, and we can identify when that galaxy enters the cluster. We then calculate the time elapsed between the galaxy entering the cluster and it merging with the central galaxy, Fig. 6.4. We also identify satellite galaxies at  $z=0$  and identify when they enter the host cluster. We plot this in Fig. 6.5.

CHAPTER 6

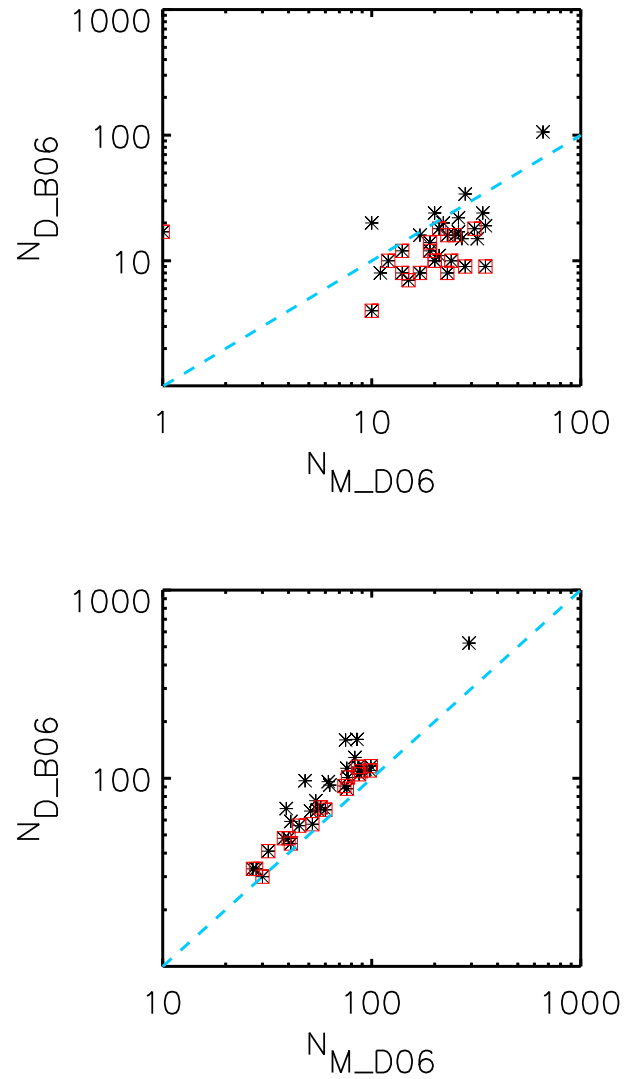


Figure 6.2: Shows the number of mergers in matched pairs of galaxies. Top panel: The number of satellite-central galaxy mergers. Bottom panel: The number of halo-cluster mergers. The blue dashed line is the 1:1 ratio. Red squares illustrate the effect of discarding clusters, wherein the D\_B06 model central galaxy becomes a satellite for several time steps.

CHAPTER 6

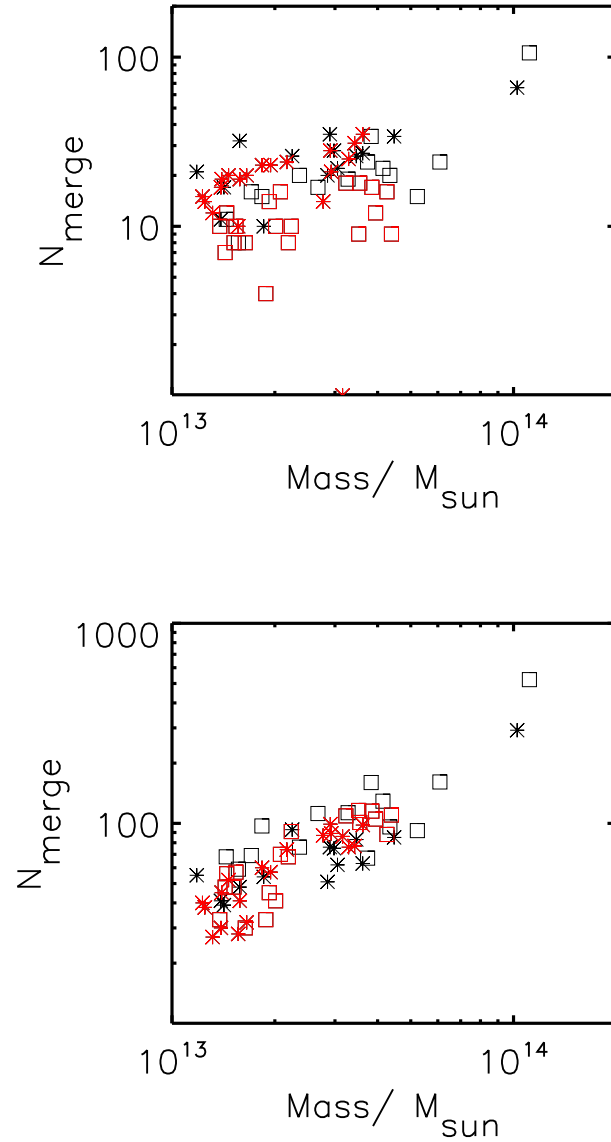


Figure 6.3: Shows the number of mergers in each model (D\_B06 are squares, M\_D06 are stars). The top panel shows the number of satellite-central galaxy mergers, and the bottom panel shows halo-cluster mergers. Red symbols illustrate the effect of discarding clusters, wherein the D\_B06 model central galaxy becomes a satellite for several time steps (approx 1 Gyr).

## 6.5 Merging times

We have described two sets of data in the previous section:

1. Galaxies which merge with the cluster central
2. Those which are cluster satellite galaxies at  $z=0$ .

### 6.5.1 Merged galaxies

Figure 6.4 shows the distribution of merging times in our cluster sample. We see that more galaxies merge rapidly in both models and the distributions are the same within the error, Table 6.1. Figure 6.4 shows that the trends in merging time are essentially the same. We do, however, see a difference in panel ‘A’ of Fig. 6.5. In this plot we can see that the additional galaxies which merge in the M\_D06 model fell in at very early times compared to the D\_B06 model. At more recent times the two models show no significant differences. Bertone and Conselice (2009) note that there is an additional 1 Gyr in the Munich models when the galaxy lies within the subhalo of a cluster, which may account for the difference in galaxy lifetime.

### 6.5.2 Satellite galaxies

Figure 6.5 panel ‘B’ shows the time at which each satellite galaxy enters the cluster. There is a population of satellites with early infall times in the B\_D06 model that is not present in M\_D06. If we add together the infall times of unmerged

Table 6.1: The mean, median, standard deviation of the merged galaxy lifetime and number of galaxies for each model.

Model	$\bar{x}$	$\tilde{x}$	$\sigma_x$	$n$
D_B06	2.22	1.40	2.33	183
M_D06	2.85	1.87	2.69	339

CHAPTER 6

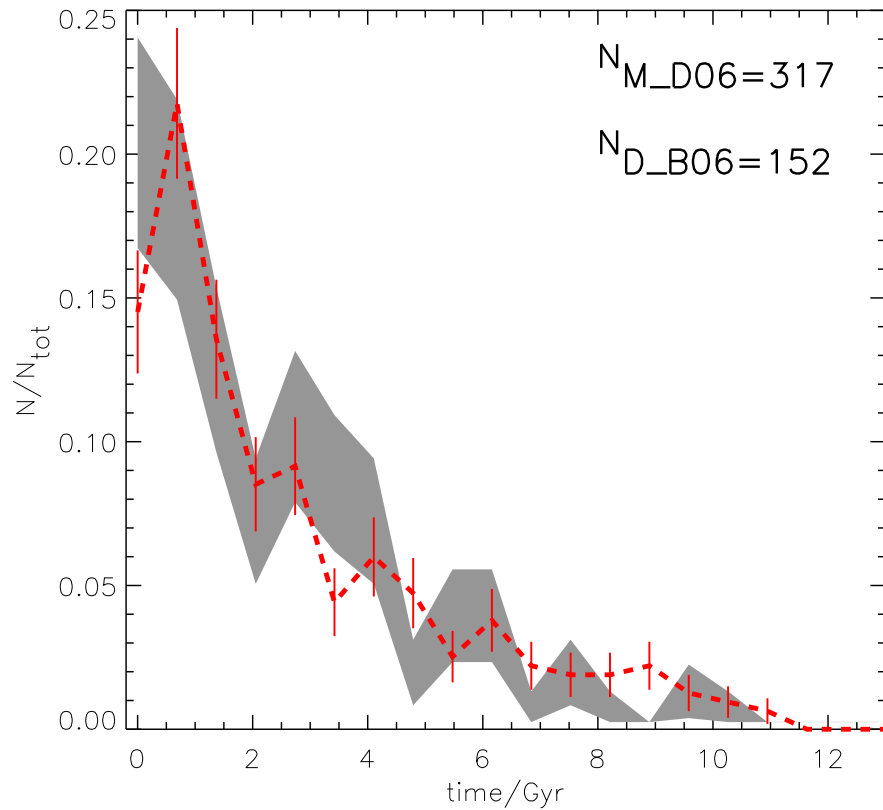


Figure 6.4: Shows the distribution of galaxy merging times normalised by the total number of galaxy mergers. The black line is the D\_B06 model and error while the red dotted line is for the M\_D06 model. Errors are Poisson. The number of merging galaxies in each model is quoted in the panel.

satellites and merged galaxies we can see that these early galaxies are the same as those which cause the merging excess in panel ‘A’.

Despite the short merging time of galaxies which do eventually merge there are far more galaxies in both models which never merge. We can set the upper limit of galaxy ages in M\_D06 to be  $\sim 10$  Gyr, but in the D\_B06 model we can have satellites with potential ages greater than the Hubble time.

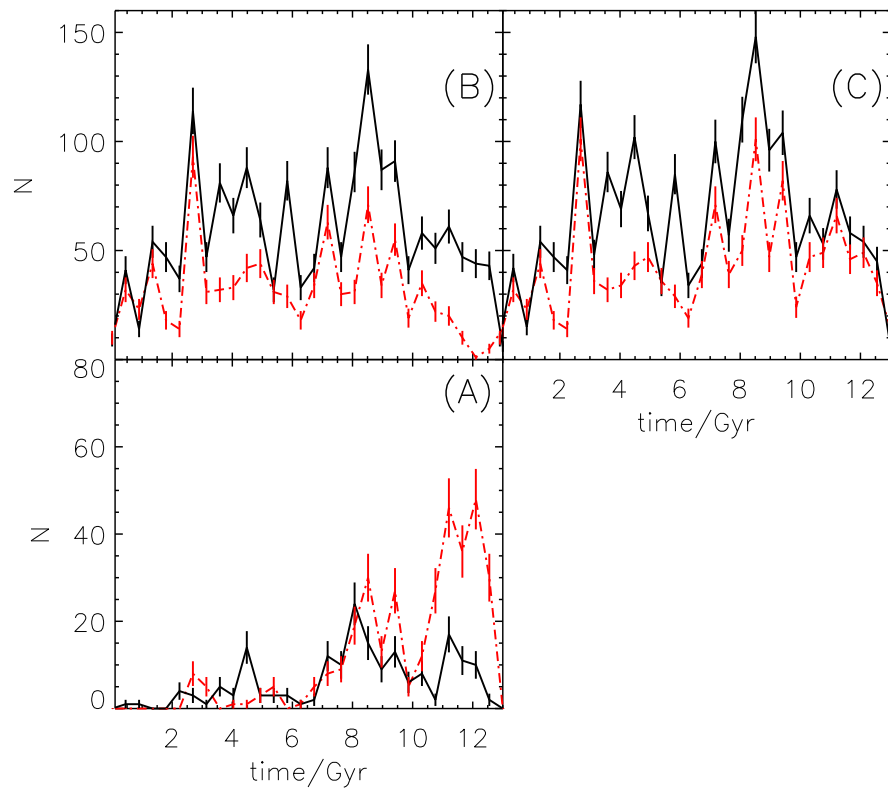


Figure 6.5: Shows the time of infall of galaxies into the cluster. **Panel A** shows the infall time of halos which merge with the central galaxy. **Panel B** shows the infall time of galaxies which do not merge. **Panel C** shows the sum of panel A and panel B. The x axis is the look back time. The solid black line shows the D\_B06 result and the red dashed line is for the M\_D06 model.

## 6.6 Conclusion

In this chapter we examined the lifetime of satellite galaxies in the different models, in an effort to reconcile the different population of vCGs. We found, however, that measuring the time between a galaxy entering the parent halo and merging is essentially the same in each model (D\_B06 galaxies take only 400 Myr more). We note that far fewer of the galaxies which enter a group halo merge in the D\_B06 model. However, there are similar numbers of galaxies entering a given halo in each model. This can be reconciled by the existence of a considerable population of galaxies which merge in the M\_D06 model and do not merge in the D\_B06 model. Thus, the Durham model produces a bimodal satellite population. A significant number of galaxies merge in a timescale comparable to the timescale of merging in the M\_D06 model, another population merges in a time longer than the age of the universe. This second population was alluded to in Benson et al. (2002), which first presented the merging timescale method used in the D\_B06 and D\_F08 models. Before 10 Gyr almost all galaxies in M\_D06 will merge, in D\_B06 this is only 20%. Thus we have a population of galaxies which merge relatively quickly, another which merges over periods greater than the Hubble time on D\_B06 and a population in M\_D06 which lasts 10 Gyr.

Thus, this explains the richer groups and clusters in the Durham models, and why Durham groups and clusters appear more centrally concentrated. The relative lack of mergers in the Durham models may also explain the relative brightness of the first ranked galaxies in the Munich models. More mergers mean that the brightest group galaxies are fed more gas and stars than other galaxies, especially at early times. This has the effect of increasing the magnitude gap and preventing the formation of the dim central galaxies seen in the D\_B06 groups.

# Chapter 7

## POLAR DISC GALAXY

### 7.1 Introduction

One of the original reasons for postulating the existence of dark matter was the flatness of the rotation curve of disc galaxies. The circular velocity of gas in galaxy discs was found to be non-keplerian far beyond the edge of the stellar disc, suggesting an invisible mass distribution surrounding the galaxies. From these observations the spherical density distribution of the inner region of the dark halo could be calculated. A polar disc galaxy (Whitmore et al., 1990), originally called a ‘multispin’ galaxy by Rubin (1994), is characterised as having two orthogonal discs. This characteristic of polar disc galaxies makes them useful in finding the shape of the dark matter halo. Using the orthogonal line-of-sight velocity profiles, it is possible to probe the shape of the inner region of the dark matter halo (Casertano and van Gorkom, 1991; Schweizer et al., 1983; Sackett et al., 1994; Iodice et al., 2006). Bailin et al. (2005) show that galaxy discs are normally aligned to the minor axis of the dark halo in the inner region, and then diverge at greater distances.

Polar disc galaxies are usually of type S0, surrounded by an orthogonal disc of gas and stars. Less than 1% of S0 galaxies have been found to contain polar

## CHAPTER 7

discs (Macciò et al., 2006). This, however, is a lower limit, because the polar disc tends to be diffuse relative to the old stellar disc, and can only be seen edge on. To identify polar discs at other inclinations, detailed kinematics are required (e.g. Chilingarian et al. (2009), Reshetnikov (2004)). Most polar disc galaxies commonly share various properties including: extended ring structure, (van Gorkom et al., 1987; van Driel et al., 1995, 2000; Arnaboldi et al., 1997; Iodice et al., 2002); young stellar populations (Gallagher et al., 2002; Karataeva et al., 2004; Cox et al., 2006); spiral arms (Arnaboldi, 1995; Iodice et al., 2004; Cox et al., 2006) and continuous, as opposed to bursty, star formation (Reshetnikov et al., 2002; Karataeva et al., 2004).

The literature presents several scenarios for the formation of a polar disc galaxy:

1. Head-on wet mergers with low initial angular momentum (Bekki, 1998).
2. Accretion of a gas-rich galaxy that is disrupted in a ring around the host (Schweizer et al., 1983; Reshetnikov and Sotnikova, 1997; Bekki, 1998; Tremaine and Yu, 2000; Sparke and Cox, 2000; Bournaud and Combes, 2003).
3. Cold gas accretion along filaments (Macciò et al., 2006).

Neither of the former two scenarios account for the high mass of the polar structure, its extended structure, or the lack of induced starbursts. These scenarios also suggest that polar discs should preferentially lie in high density regions, yet this is not observed (Brocca et al., 1997). Cold accretion, however, puts no limit on the mass of the polar disc and studies have shown (Macciò et al., 2006; Connors et al., 2006) it is possible for gas to flow into a galaxy perpendicular to the disc.

Macciò et al. (2006) identify a polar ring galaxy in their simulations, and

## CHAPTER 7

attribute the formation to gas flowing in from extended filaments. The gas flows into the galaxy along preferential directions, and is braked by ram-pressure. The gas collides with both halo gas, and gas from a second filament. The small impact parameter is sufficient to allow the gas to retain angular momentum, and rotate at  $\sim 15\text{kpc}$ . By measuring the shape of the dark matter halo directly in the simulation, they find that the halo is closely spherical, and the potential is oblate. This means that inflowing gas not directly perpendicular to the disc is quickly brought into the plane of the disk. Macciò et al. (2006) find that the polar disc exists for 1.6 Gyr when in-falling satellites, which disrupt the polar disc, are removed from the simulation.

Brook et al. (2008) also find a polar disc formed through accretion. This exists for 3 Gyr, with new gas falling onto the polar disc only from  $z=0.5$  onwards. This is backed up by observations of NGC 4650A (Whitmore et al., 1990), which has a star-forming polar disc for at least 1 Gyr (Iodice et al., 2002). Brook et al. indicate that the latter part of the lifetime of the polar disc is unstable, with some coupling between the polar disc and the central disc. They suggest that the polar disc forms as a result of the last major merger changing the angular momentum of the stars and gas of the central disc. Subsequent gas falls in along the old trajectory.

### 7.1.1 Motivation

We examine how precisely the dark matter halo aligns with the orthogonal discs, and exactly how or why the cold flows become so extremely disoriented with respect to the inner disc. These extreme objects are excellent test beds for studying the role of gas infall, and merging, in the universe. We expand on the precise reason a polar disc galaxy should form. If a polar disc galaxy forms by cold accretion of gas, we examine the mechanism which causes the polar structure to

## CHAPTER 7

develop, as opposed to simply adding gas to the old disc. We also try to identify whether a polar disc is a ‘special’ object, or if it is merely an extreme example of a more common effect, such as a warp. We identify what event causes the galaxy to take on the polar disc structure.

We align the particle positions to the polar disc and measure the angle and axial ratios of the dark matter halo, and how these properties vary with radius. We compare these results with the angular momentum of the dark halo at various radii. We also examine how this varies with time: for example, how the shape and angular momentum of the dark halo influences, or is influenced by, the polar disc.

The shape of dark matter haloes is a prediction of  $\Lambda$ CDM cosmology. One way to measure the shape of dark matter haloes in real galaxies has been to use polar disc galaxies. Having two orthogonal discs provides an unparalleled opportunity to study the shape of dark matter haloes observationally (Casertano and van Gorkom, 1991; Schweizer et al., 1983; Sackett et al., 1994; Iodice et al., 2006), because the circular velocity of the gas and stars is dependant on the mass distribution, which is influenced by the dark matter distribution.

We use the simulations to test whether such methods are valid. We are able to measure the shape of the dark matter halo using methods which mimic observations, and compare them with the actual shape of the dark matter halo.

### 7.1.2 Simulation

The polar disc studied in this chapter forms through cold accretion, and is taken from Brook et al (2008). It was modelled using GASOLINE, (Wadsley et al., 2004). GASOLINE is used to compute the collisionless dark matter background, the gas and the stars, using self-consistent cosmological initial conditions. The simulation was carried out using the San Diego Supercomputing Facility, for a

## CHAPTER 7

total of 500000 CPU hours. The CMBFAST code was used to generate the transfer functions, and initial power spectrum.

The size of the simulation volume is 28.5 Mpc, which is large enough to provide realistic tidal torques from the large-scale structure. The force resolution of the simulation is defined by the smoothing length of 0.15 kpc. The simulation is run from  $z = 100$  until  $z = 0$ . The cosmology is  $\Omega_0 = 0.3, \Omega_\Lambda = 0.7, \sigma_8 = 0.9, H_0 = 70.0$ , where  $\Omega_0$  is the matter density,  $\Omega_\Lambda$  is the cosmological constant,  $h$  is Hubble's constant and  $\sigma_8$  is the rms fluctuation of the power spectrum at the 8 Mpc scale.

Re-simulation is the only way to simulate both a large enough volume to achieve a realistic merging history, and detailed galaxy properties. There are several steps in running a re-simulation. In this case, the technique of Katz and White (1993) was used. Trying to simulate the entire volume at high enough resolution, with gas physics included, is prohibitive, because computational power is wasted modeling regions that are simply not of interest. We cannot simply extract the object of interest, and run it in isolation, because filaments and neighbouring haloes influence the evolution of the object. Initially, a dark matter only simulation was run to  $z=0$ , and a relevant dark matter halo was selected. It is then this region which was re-simulated at higher resolution. The simulation employs periodic boundary conditions, so it is elementary to recentre the volume on the object of interest. Higher resolution particles are then added, such that the particle masses increase with distance from the centre of the volume. Six generations of particle are used, each decreasing in mass by a factor of eight, ( $9.50 \times 10^4 M_\odot$ ,  $8.86 \times 10^5 M_\odot$ ,  $7.09 \times 10^6 M_\odot$ ,  $4.54 \times 10^8 M_\odot$ ,  $3.63 \times 10^9$ ,  $2.905 \times 10^{10} M_\odot$ ), their effective spatial proximity accordingly decreasing by two. Gas particles are added in the inner region, and are assumed to follow the dark matter initially. The high resolution initial conditions ('ICs') can be achieved by interpolating new spatial

## CHAPTER 7

and velocity offsets from the original grid. The end result is shown in Fig. 7.1, which shows the dark matter particle distribution at  $z = 18.7$ . It is vital that the region of interest is not contaminated by higher mass particles. Gas is only followed within the high density region. The mass of the initial gas particles is  $1.6 \times 10^4 M_\odot$  and the mass of star particles is  $3.3 \times 10^3 M_\odot$ . Gas particles can transform into up to three star particles. Gas particles with a mass  $< 20\%$  of the original mass are removed from the simulation, and the mass is redistributed to nearby gas particles. Star particles lose mass due to supernovae and stellar winds, and the mass is redistributed to nearby gas particles. In comparison, in the polar disc simulated by Macciò et al. (2006) the dark matter particles are  $4.90 \times 10^4 M_\odot$ , whilst gas particles have mass  $9.75 \times 10^4 M_\odot$ , with a gravitational softening of 100 kpc.

Star formation, as defined by Stinson et al. (2006), requires various conditions to be present. The temperature of the gas  $< 15000\text{K}$ , and must be in a virialised region. Additionally, the gas must have a minimum density of  $0.1\text{cm}^{-3}$ , and be in a convergent flow. The star formation efficiency is set to 0.05. When the stars reach the end of their life, they release  $10^{50}$  ergs of energy back into the ISM. These parameters were defined using an isolated Milky Way sized galaxy.

### 7.1.3 Orientation of the disc

We calculate the angular momentum of the disc and re-orientate the simulation volume so that the polar disc of the galaxy is aligned to the z-axis. The particle positions and velocities are used to calculate  $\mathbf{L}$ , the angular velocity,

## CHAPTER 7

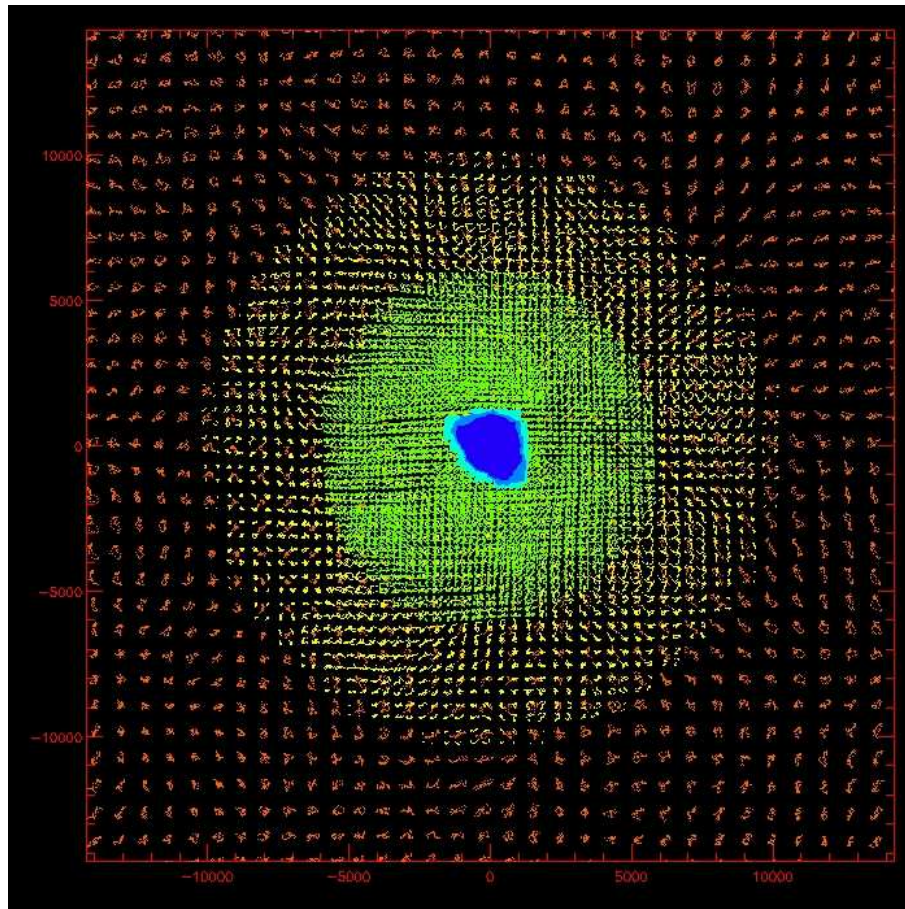


Figure 7.1: The distribution of dark matter particles at  $z = 19$ . Dark blue particles are the lowest mass, and the red are the most massive particles.

$$L_x = m(r_y v_z - r_z v_y) \quad (7.1)$$

$$L_y = m(r_z v_x - r_x v_z) \quad (7.2)$$

$$L_z = m(r_x v_y - r_y v_x) \quad (7.3)$$

$$\mathbf{L} = \sqrt{L_x^2 + L_y^2 + L_z^2} \quad (7.4)$$

where  $L_{x,y,z}$  is the angular momentum component in the x, y z direction,  $r_{x,y,z}$  is the position and  $v_{x,y,z}$  is the velocity component. We align the simulation volume such that the cold gas of the polar disc at  $z = 0.15$  is aligned with the z-axis. The cold gas in the polar disc is defined as those gas particles with a temperature  $< 40000\text{K}$ , and a distance from the centre of the galaxy of 15 kpc in physical units. This is used for all other outputs, so that the other outputs are aligned according to the polar disc cold gas at  $z = 0.15$ . We do, however, allow the centre of the volume to change, so that the origin is centred on the most bound particle of the dark matter halo in each output, and it is this point about which we rotate the volume.

## 7.2 Polar disc galaxy

AHF (Gill et al., 2004) was used to identify dark matter haloes, and merger trees were calculated using the algorithm included in the AHF package. When tracing the galaxy halo through time, we used the halo merger trees to follow the parent dark matter halo. We find that the largest galaxy halo is first identified at  $z = 7.9$ , and remains the halo with the largest number of particles from then onwards. At  $z=0.15$ , when the stellar and polar discs are at their maximum angle, the masses of the three components in this galaxy are:  $M_{stars} = 1.01 \times 10^{10}M_{\odot}$ ,  $M_{gas} = 7.63 \times 10^9 M_{\odot}$  and  $M_{dark} = 1.08 \times 10^{11}M_{\odot}$ .

## CHAPTER 7

We define the polar disc as those stars formed after 8 Gyr (see §7.4 for details). The stellar disc is defined by those stars formed between 4 and 7 Gyr. We also define a halo, which is comprised of stars which formed before 4 Gyr. The last major merger occurs at  $\sim 4$  Gyr, and the polar disc begins to appear at 7 Gyr. The times defined above are markers of important moments in the lifetime of the galaxy. According to these definitions, the polar disc has a stellar mass of  $1.3 \times 10^9 M_\odot$ , the stellar disc has a stellar mass of  $3.0 \times 10^9 M_\odot$ , and the halo has a mass of  $4.8 \times 10^9 M_\odot$ . Of the three components, the halo is by far the most massive, and the polar disc the least massive. However, both stellar discs have a higher density than the galaxy halo, and the baryons are dynamically dominant in the inner region. This differs slightly from the numbers quoted in Brook et al. (2008), but that is due to the specific definition of the three components. Our polar disc has a mass 2 times less than the stellar disc, similar to that found by Brook et al. (2008).

The virial radius of the halo is  $R_{vir} = 132 \text{ kpc}$ , and the cold gas mass is  $M_{cool} = 1.24 \times 10^9 M_\odot$ , where the cold gas is gas with a temperature below 40,000 K. The scale lengths of the two discs are 3.4 and 0.95 kpc for polar and stellar discs. The approximate edges of the polar and stellar discs are 5 and 9 kpc from the centre respectively, as determined by eye. At maximum inclination the discs are at an angle of 84 degrees. The Macciò et al. (2006) polar disc galaxy has a similar extent and mass. However, our polar disc galaxy, called the PDG henceforth, lasts longer than Macciò et al's galaxy, which only endures for 1.6 Gyr, while our polar disc exists for  $\sim 4$  Gyr. The Macciò et al. (2006) polar disc has a total baryonic mass of  $6.75 \times 10^9 M_\odot$  within a virial radius of 98 kpc. We also note that the formation time of the Brook et al. (2008) galaxy corresponds to the time of the last major merger.

### 7.3 Evolution of discs

The events described above form a narrative of galaxy formation. The galaxy disc first forms at  $z = 3.29$  whereupon the disc is face on in the  $y$ - $z$  plane. At  $z = 2$  the last major merger takes place, and the gas disc becomes a great deal more compact although the stellar disc takes on an elliptical shape, and a tidal tail is visible until  $z = 1.6$ . The disc is still face on in the  $y$ - $z$  plane defined by the  $z = 0.15$  polar disc. This interaction begins at  $z = 2.27$ , and lasts for 1 Gyr, with a merging mass ratio of 0.2. This merger causes the galaxy to become elliptical, throwing stars into the stellar halo. At  $z = 0.94$  a large knot of gas is accreted to the central galaxy, whereupon the polar disc starts to develop, and both the gas and stars begin to rotate around to their later orientation. By  $z = 0.8$  the polar disc consists of a diffuse cloud of gas surrounding a denser disc of gas, which is orientated with the stars. In the previous simulation output there are hints of the forming disc, and a large arc of cold gas can be seen back to  $z = 1.0$ . This arc is of insufficient mass to form the polar disc, discounting the first two formation scenarios outlined in the section 7.1. This inner gas has been completely ejected or has formed stars by  $z = 0.42$ , leaving only the polar disc with any cold gas.

We take  $z = 0.17$  as the main simulation output for the investigation and discussion because the polar disc is fully established, and this output shows very little disturbance. The last 4 Gyr of the simulation shows an essentially passive evolution.

The output-by-output description of the simulation found by looking at images of the galaxy's cold gas is shown in Table 7.1. This table shows various key events in the formation of the polar disc, and marks them with a 'o', but the principal output at  $z = 0.17$  is marked with an 'X'. By  $z = 0$  the polar structure has become unstable and can no longer be found. The polar disc is a stable structure for over 3 Gyr, showing evidence of spiral arms and warps.

## CHAPTER 7

Table 7.1: Comments on simulation outputs. 'o' shows important changes to the system and X is the primary output.

#	aexp	z	time	dT	Notes	tick
10	0.14	5.94	0.93	0	Galaxy gas disk forms	o
18	0.31	2.27	2.85	0.47	Disrupted gas Core remains intact, last major merger	o
21	0.37	1.68	3.79	0.47	Disk reforms, major merger complete, Tidal tail?	o
24	0.44	1.30	4.74	0.47		o
26	0.50	1.02	5.69	0.47	Disk shrinks, density increases Evidence of infalling gas	o
29	0.54	0.87	6.32	0.32	More polar disk diffuse gas visible	
30	0.56	0.80	6.63	0.32	Wispy polar disk appears	
31	0.57	0.75	6.90	0.26		o
32	0.57	0.74	6.95	0.05	Polar disc has empty inner region	
34	0.61	0.63	7.58	0.32	Polar ring thins, xy, definate ring Peak Sphericity moves inwards	
36	0.67	0.50	8.45	0.55	Very thin polar disk now, dense core, diffuse polar disk	o
38	0.70	0.42	9.00	0.47	Polar disk formed, no more core	o
47	0.86	0.17	11.36	0.32		X
48	0.88	0.14	11.68	0.32	Bar in polar disk?	
49-55	0.89	0.12	11.89	0.21	Bar grows passively	

## 7.4 Star formation

### 7.4.1 SFR

The star formation rate (SFR) of the galaxy is calculated along two slits and globally, for the whole galaxy. The slits are placed over each disc, and have a width of 2 kpc. The inner 1 kpc of the galaxy is excluded from the slit, because the two discs overlap in this region and become confused. Slit 'a' is placed over the stellar disc, defined to be stars formed between 6 and 6.5 Gyr. Slit 'b' is placed over the cold gas disc, where the cold gas has a temperature  $< 40000\text{K}$ . The global SFR is found simply by identifying the number of stars formed in the interval  $dt$ . The SFR is shown in Fig. 7.2, where the global SFR is divided by 10, so it can be shown on the same plot as the SFR along the slits.

The last major merger takes place between 2.8 and 3.8 Gyr, and is visible as a peak in the SFR of the stellar disc. Early stars, formed before the last major

## CHAPTER 7

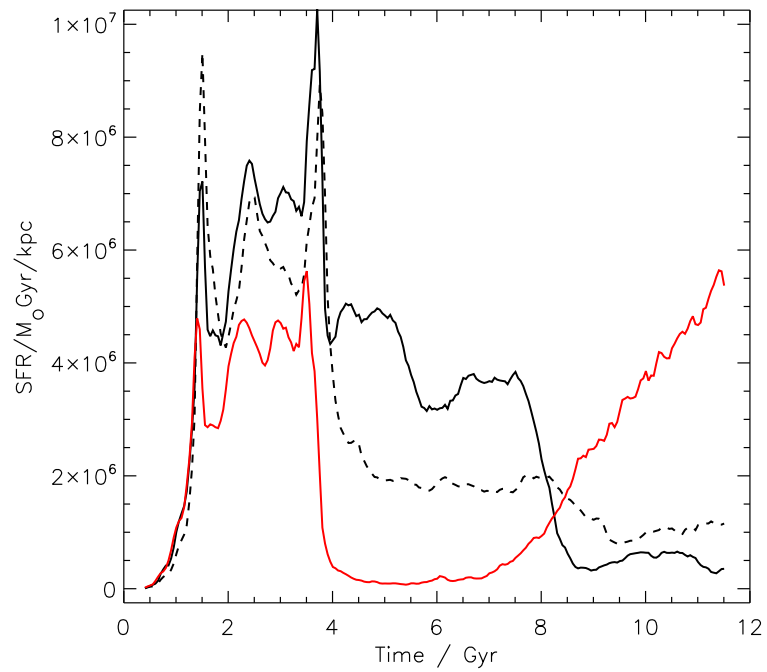


Figure 7.2: The star formation rate of the polar disc galaxy along slits laid across the old (formed at 6.5-7.5 Gyr) stellar disc (black), and the young polar disc (red). The global star formation rate is also shown as the dashed line (but divided by 10.)

## CHAPTER 7

merger can be seen along both slits, suggesting they are part of the stellar halo of the galaxy. Then, between 4-7 Gyr the SFR along the polar slit falls to zero and stars are formed in the central disc. After 7 Gyr the star formation along the polar slit increases consistently and the SFR in the stellar disk is negligible after 9 Gyrs when it uses up the inner gas. In the region between 4-7 Gyr there are two eras of increased star formation with a brief intermission, which is seen neither in the global or polar SFRs.

It is also clear that there are three distinct eras of star formation after 3 Gyrs, shown in Fig. 7.2 and Fig. 7.3. The first is between 3-4 Gyr where the mass of stars increases rapidly due to interactions with the merging halo. This is followed by a shallower rate of stellar mass increase between 4-8 Gyr, where stars form in the central disc. Finally there is an even shallower SFR when the polar disc is forming, from 8 Gyr onwards. The polar disc has a lower star formation rate, for  $t > 8\text{Gyr}$ , than the older stellar disc, due to the polar disc being more diffuse than the early gas disc.

The SFR for our polar disc has an average of  $0.06M_{\odot}\text{yr}^{-1}$ . There are some differences in the precise form of our PDG and, for example, NGC 4650A, one of the observed polar disc galaxies. The star formation rate of the polar disc galaxy NGC 4650A was studied by Spavone et al. (2010). This galaxy shows a low metallicity of  $0.2 Z_{\odot}$  with a negligible metallicity gradient. Spavone et al. (2010) find that the polar disc is approximately 1 Gyr old and the galaxy experienced a last starburst between 3-5 Gyr ago. Our PDG has an old polar disc, which lasts several Gyr, and the polar disc becomes important after a delay of several Gyr between the development of the polar disc and the last starburst. We also see that the star formation rate in the polar disc is smoothly increasing without significant starbursts.

We also find that the amount of cold gas (Temperature  $< 40000\text{K}$ ) in the inner

## CHAPTER 7

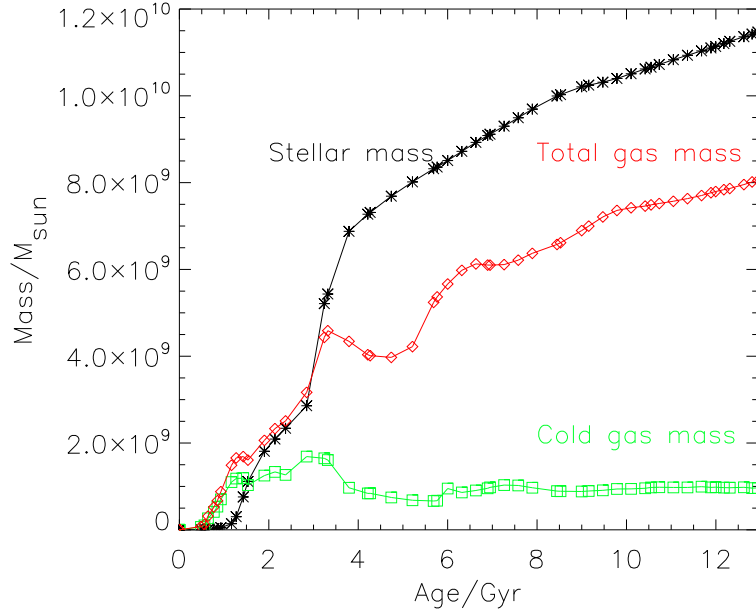


Figure 7.3: Mass accretion of the various baryonic components in the galaxy. The cold gas is maintained by cooling hot gas, and star formation. The stellar component shows three eras of star formation, initial fast star formation before 4 Gyr, an intermediate period of moderate star formation and a time of slow star formation in the polar disc after 8 Gyr.

15kpc of the galaxy remains basically constant (Fig. 7.3) in the range  $8.6\text{--}10.3 \times 10^8 M_{\odot}$ , between 6 and 13.2 Gyr. The fraction of cold gas experiences a peak as the polar disc begins to form. The following trough coincides with a peak in the SFR (Fig. 7.2). The rapid star formation then depletes the cold gas reservoir. As the polar disc becomes the dominant star forming region the mass of cold gas grows, only to turn over at 12Gyr and begin to decrease as the polar disc starts to become unstable. This corresponds to a slight decrease in the fraction of cold gas.

An analysis along these lines has previously been carried out in Brook et al. (2008) who use it to identify the changing location of star formation from the central disc to the polar disc at between 7 and 8 Gyr.

### Possible correlation with mass growth

Figure 7.4 shows the accretion of mass to the dark halo. The accretion and loss of mass is a natural feature of these simulations due to the methods used to define the virial mass of the halo (Gill et al., 2004). However, it is interesting to observe that the SFR peaks, in Fig. 7.2, correspond to a temporary increase in the host halo mass; in other words a trough in the halo mass corresponds to an increase in star formation. To improve the clarity of this result we fit a Wechsler profile (Wechsler et al., 2002), using a non-linear least squares fitting procedure:

$$M(a) = M_o \exp\left(-2a_c \left(\frac{a_o}{a} - 1\right)\right) \quad (7.5)$$

where  $a_c$  is the free parameter,  $a_o$  is the observation time,  $M_o$  is the mass at the observation time and  $M(a)$  is the halo mass at a given time. The actual values of  $a_o$  are irrelevant for this work but the line does prove a useful guide to identify the oscillation on halo mass. Some of the variation away from smoothly increasing mass is due to clumpy accretion, and this is partially responsible for deviations from the Wechsler curve. Measuring the subhalo mass fraction and subtracting it from this mass accretion does not remove the oscillation. This suggests that the peaks in the SFR after  $z=2$  are not caused by minor merger events. The mass accretion profile is not in itself interesting, because the variation is within the expected variation of the halo finder (Knebe et al. private communication). However, the correlation of this oscillation with the star formation rate might indicate some additional physical process.

### 7.4.2 Metallicity

The metallicity of the stars in the polar disc is found using the same slit method used for the SFR. We take stars from two different eras, 5.0–5.5 Gyr and 9.5–11.5

## CHAPTER 7

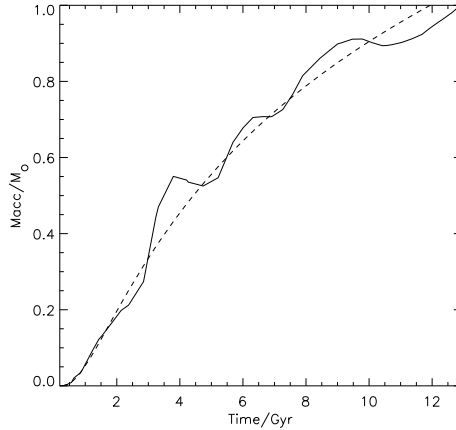


Figure 7.4: The mass accretion history of the dark matter halo (solid), and the Weschler best fit line (dashed)

Gyr. In each case, the metallicity is much higher in the central disc. We also note that the stellar disc is much more metal rich than the polar disc (see Fig.7.5). The metallicity of the stellar disc shows a much steeper profile than the polar disc in Fig. 7.5. The central disc of the galaxy ends at 4 kpc in this output ( $z = 0.17$ ). In the extremity of the central disc, the metallicity of the two discs is the same. The polar disc gas is more primordial and with a metallicity of  $0.34Z_{\odot}$ , compared to  $0.44Z_{\odot}$  in the central disc (where  $Z_{\odot} = 0.016$ ) consistent with Iodice (2010) for NGC4650A. This supports the suggestions of Macciò et al. (2006), Brook et al. (2008) and Iodice (2010), that the polar disc is formed from newly inflowing gas. In a subsequent section we will see this explicitly.

Buttiglione et al. (2006) found that polar structures have a decreasing metallicity with radius. This is also apparent in our simulation and characterises a polar disc being built up over time (Matteucci and Francois, 1989; Matteucci et al., 1989; Boissier and Prantzos, 1999). Spavone et al. (2010) find no such gradient in NGC 4650A. The polar disc in NGC 4650A is thought to be only  $\sim 1$  Gyr old and so the gradient may not have had time to build up.

The gradient of the metallicity with radius profile is shown in Fig. 7.5. We follow the gas metallicity of the galaxy though time and note that the global

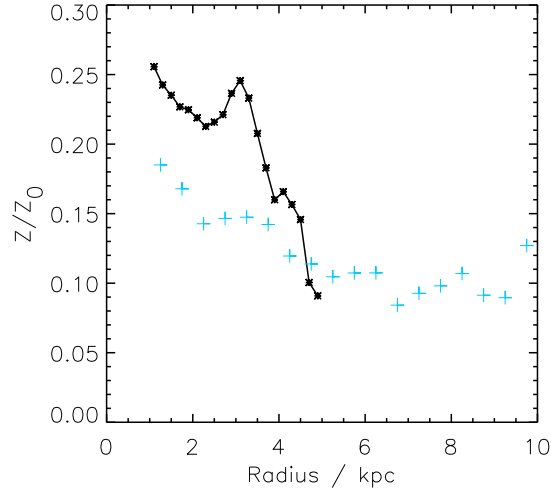


Figure 7.5: Metallicity profile of stars formed in the stellar disc (black line), and the polar disc cold gas (blue), along 1kpc thick slits. The stellar disc ends at  $\sim 4$  kpc at which point the stars are in the galaxy halo. The polar disc ends at  $\sim 9$  kpc.

metallicity of the cold gas in the halo increases with time. The slope of the normalised metallicity profile of the polar disc does not.

### 7.4.3 Stellar Age

Complementary to the metallicity profiles we next examine the stellar age along the slits (see Fig. 7.6). The age profile of the stellar disc is quite flat near the centre, dropping in the periphery of the disc. This plot is made by constructing a histogram of points along each slit and finding the mean age of all stars within a given bin. The range of stellar age is much greater along the polar disc slit. The stellar disc shows a relatively flat stellar age until a radius of 3.5 kpc when only older stars are present. The gradient of the stellar formation time profile is much steeper in the polar disc, where stellar formation times range from 3.9 Gyr to  $\sim 9$  Gyr. It is at this point the polar disc gives way to the pressure-supported stellar halo. The stars in the polar disc get younger up until a radius of about 5

## CHAPTER 7

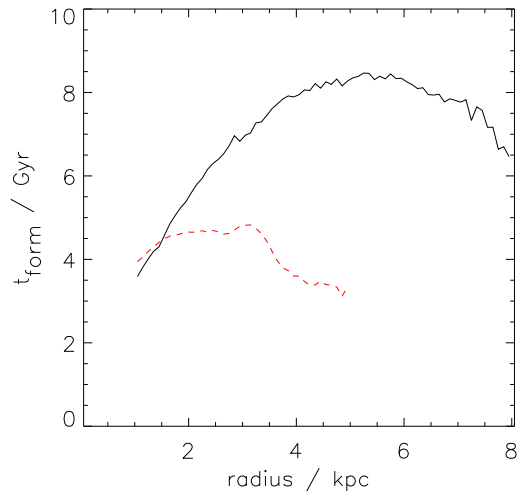


Figure 7.6: The stellar age profile along the polar (black), and stellar disc (red), slits.  $t_{form}$  is the mean formation time of stars at a given radius. The stellar disc ends at  $\sim 4$  kpc, at which point the stars are part of the galaxy halo. The polar disc ends at  $\sim 9$  kpc.

kpc, and the profile turns over in the outer region. This suggests that the polar disc forms from the inside out up until the turn over point.

By a radius of about 12 kpc the stellar ages are approximately the same and we have moved beyond the edge of the disc.

### 7.4.4 Summary

The Brook et al. (2008) simulated polar disc galaxy matches with many of the observations presented in the literature (Spavone et al., 2010; Iodice et al., 2002), but diverges in others. This may, however, simply be due to a small sample size. Based on the work in the above section we can re-emphasise the following points of interest:

- The polar disc structure in our simulation is older than NGC 4650A but has a similar mean metallicity.
- Our stellar disc is substantially more metal rich than the younger polar

## CHAPTER 7

disc.

- The polar disc has a steeper metallicity profile than NGC 4650A which is presented in Spavone et al. (2010).
- We find, however, that the polar disc does not produce substantial stars until 3-4 Gyr after the last major merger, due to the time required for the polar disc structure to build up sufficient cold gas. This is more like UGC 9796 (Cox et al., 2006).
- The stellar age profile shows a peak along the polar disc at 5.5 Gyr although this may be due to contamination from the stellar halo and the galaxy bulge.

## 7.5 Halo Shape

### 7.5.1 Introduction

Dark matter haloes are often approximated as spheres, but they are in actual fact triaxial. In dark matter only simulations, (e.g. Knebe et al. (2004)). Bailin et al. (2005), who included baryons, found that galaxy disks align with the inner region of dark matter haloes. It has also been shown that the spin axis (Flin and Godlowski, 1986; Navarro et al., 2004; Lee and Erdogdu, 2007), are aligned with the intermediate principle axes of local tidal tensors provided by the surrounding structure. The angular alignment and shape of the dark matter halo is free to change throughout the structure, e.g. Hayashi et al. (2007), Bailin et al. (2005). We explore the shape and orientation of the dark matter halo as a function of distance from the centre. The shape is a measurement of how spherical the halo is, and the orientation is the alignment between the halo shape, and the principle axes of the cold gas angular momentum. Once we measure the shape, we can compare this to the shape inferred from measuring the rotation curves of the

## CHAPTER 7

perpendicular discs, and the observations of Iodice et al. (2003). Iodice et al. (2003) finds that the polar disc halo must be oblate based on observations of the polar disc.

m

### 7.5.2 Inertial Tensor

We can find the shape of the dark matter halo using the inertial tensor approach. We follow the approach of Knebe et al. (2010) who find that using a simple spherical radial bin as opposed to ellipsoids does not affect the orientation of the axes, and that using elliptical shells instead of concentric spheres does not result in significantly different eigenvectors and eigenvalues that differ in an easily parametrised way. To find the true axial ratios of the triaxial halo, which is distorted by the use of spherical shells, the parameters must be adjusted by  $S = S_{spherical}^{\sqrt{3}}$  to match the shapes found by following the shape of the potential more closely. They discard the reduced inertial tensor, favouring the standard moment of inertia because the reduced approach gives greater weight to the centre of the halo and biases the result to higher sphericity.

The eigenvalues  $(a, b, c)$  of the inertial tensor define the shape of the halo. The radius of the stellar disc is  $\sim 5\text{kpc}$  and the polar disc extends out to  $\sim 10\text{kpc}$ . For our calculation we can use the tensors:

$$I_{i,j}^{std} = \sum_n m_n x_{i,n} x_{j,n}, \quad (7.6)$$

$$I_{i,j}^{red} = \sum_n m_n x_{i,n} x_{j,n} / r_n^2, \quad (7.7)$$

where  $I_{i,j}^{std}$  is the standard inertial tensor and  $I_{i,j}^{red}$  is the reduced inertial tensor.  $n$  is the particle id and  $i$  and  $j$  is the  $x,y,z$  component of position vector  $\mathbf{x}$ . The

## CHAPTER 7

axial ratios are  $(a, b, c) = (\sqrt{\lambda_a}, \sqrt{\lambda_b}, \sqrt{\lambda_c})$ . Here, ‘a’ is the major axis, ‘b’ is the intermediate axis and ‘c’ is the minor axis. This was presented by Bailin and Steinmetz (2005). These authors plot the shape defined by the reduced inertial tensor using spherical shells against the shape defined by the inertial tensor found using elliptical shells and find very little scatter.

### 7.5.3 Halo Shape

The sphericity of a halo is the ratio of the longest and shortest axes of the best fit ellipse and measures how spherical a halo is. If sphericity,  $S = c/a$ , is  $\sim 1$  then the halo is a sphere, if  $S \sim 0$  then the halo is extremely elongated. This is often paired with the triaxiality,  $T = (1 - (b/a)^2)/(1 - (c/a)^2)$ , of a halo which measures how oblate or prolate it is. The values of  $T$  and  $S$  define two axes of halo shape, the triaxiality-sphericity of the halo and how prolate-oblate the disc appears. We use the bootstrapping technique to work out errors, Heyl et al. (1994), and find they are negligible for this analysis.

The shape profile is extremely smooth and converges to a sphericity of 0.65 in the outer region of the halo, Fig. 7.7. The most interesting feature is in the inner region, between 0 to 3 kpc. The halo is most spherical at the edge of the stellar disk, which extends to  $\sim 4$  kpc and then falls again to 0.65 for larger radii. We also see that the halo is distinctly oblate, ( $T = 0$ ), except in the inner region near the stellar disc where it is prolate, ( $T = 1$ ). The polar disc is in the oblate region of the dark halo. This is different to the result of Macciò et al. (2006) where the peak of the sphericity is at 2 times the disc radius and is slightly less spherical than our result, with a sphericity of 0.5 at a radius of 48 kpc.

## CHAPTER 7

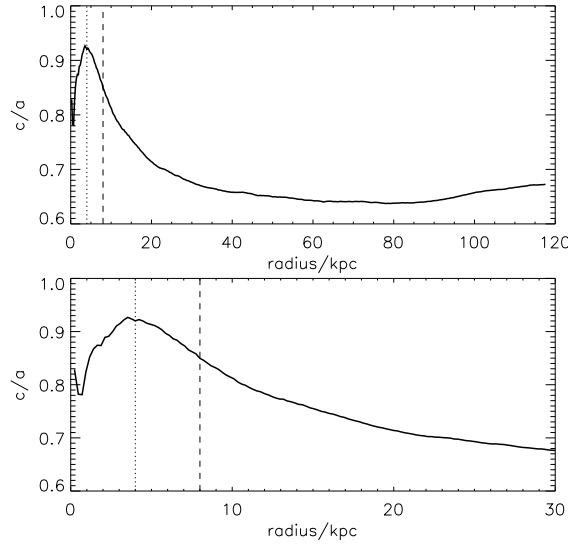


Figure 7.7: The radial profile of the halo shape shows a smooth distribution of the halo sphericity. The top panel shows the sphericity from the centre to the virial radius, using all particles within a distance  $r$ . The low panel focuses on the inner region of the halo. The vertical dotted line is the radius of the stellar disc and dashed line is the radius of the polar disk.

### 7.5.4 Halo Alignment

To determine the inner shape of the dark halo using the the two orthogonal disks, we rotate the volume such that the total angular momentum of the polar disc is aligned in the x-y plane and take the dot product of the eigenvector of the minor axis with the z axis. Because the algorithm we have used treats the positive and negative direction of the eigenvectors as interchangeable, we have chosen to select the absolute value of the vector in each case, i.e. the z-component of the eigenvector is always positive. This is shown in the Fig. 7.8. At  $z=0.17$  the stellar disk is approximately aligned to the y-axis, of the volume and the stellar disk has a radius of 3 kpc. It is striking that, up until the edge of the stellar disk, the minor axis of the halo is aligned approximately with the y-axis (green line in the figure) and then rapidly becomes orthogonal to it. The dark halo minor axis is henceforth aligned to the angular momentum vector of the polar disk.

This sudden shift suggests that the use of the orthogonal circular velocities is

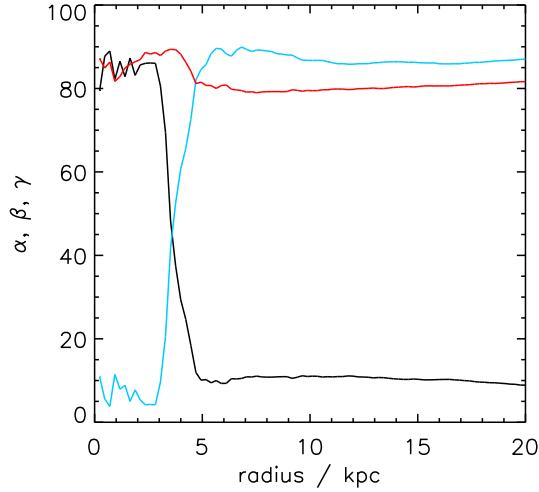


Figure 7.8: For the  $z=0.17$  output, the radial profile of the alignment of the dark matter halo shape. The black line shows the angle of the minor axis of the angular momentum with the  $z$ -axis,  $\gamma$ , the red line shows the  $x$ -axis component of the halo shape and the blue line shows the profile of the  $y$ -axis.

not an accurate guide to the shape of the halo even a small distance beyond the edge of the discs. The flip is consistent with the increased sphericity at the edge of the stellar disc.

### 7.5.5 Comparison with the observers approach.

The discovery of the tight correlation between the direction of the polar and stellar discs and the principle axes of the dark matter halo simplifies the observational comparison.

Using the orthogonal circular velocities to probe the disc assumes that the circular velocity is governed by the mass within a given radius,  $r$ . A flattened halo will contain more matter within a distance  $r$  aligned to the minor axis of the halo. We compare to our measurements of the circular velocity of of the two disk components in our primary output. Although the disks are inclined at 84 degrees we assume the angle is 90 degrees to make the calculation easier. Fig 7.9 shows

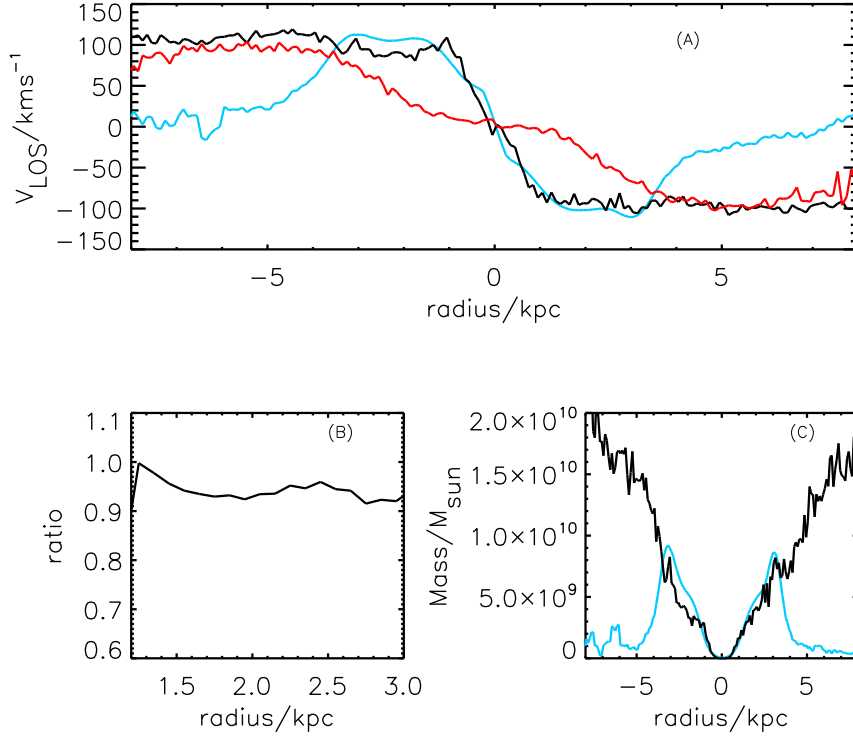


Figure 7.9: **Panel A:** The line of sight velocity profile of the galaxy disks. The red line is the polar disk, the blue line is the stellar disc, based on the motion of the stars. The black line is the line-of-sight velocity of the cold gas along the polar disc slit. **Panel B:** the ratio of the masses calculated from the velocity profiles. These mass profiles are shown in **Panel C** with the same colours as in panel A

the line-of-sight velocity distribution along each disk. We see that the stellar disc velocity increases more rapidly with radius than the polar disc. Thus, the gravitational potential must increase more rapidly along the central disc, (Iodice et al., 2002). Thus the short axis of the halo is aligned to the equatorial plane of the polar disc, (Iodice et al., 2003).

From the values of the rotational velocity in Fig. 7.9, we can calculate the mass within a given radius. The stellar disc peaks at 3 kpc, with a line-of-sight velocity of approximately 90 km/s. The polar disc has a similar velocity peak of 90 km/s, but at a radius of 6 km/s. The higher circular velocity of the stellar

## CHAPTER 7

disc does suggest a flattening of the halo in that direction because increased mass within a distance  $r$  produces a higher circular velocity according to  $M = v^2 r / G$ , where  $r$  is the radius,  $v$  is the circular velocity and  $G$  is the gravitational constant, but this is only true within the radius of the disc. Both the central disc stars and the polar gas have similar circular velocity profiles. This suggests that the halo is close to spherical at small radii. The mass ratios shown in the figure show that for a radius of 3 kpc the axial ratios are 0.9, which matches with the result of the inertial tensor method.

### 7.5.6 Evolution of the Halo Shape

By measuring the sphericity through time we can test to see when the observed properties of the halo shape are established. It is clear that the shape of the dark halo in the inner region is established early, (centre panel, left column of Fig. 7.10) before the polar disc starts forming stars or is even beginning to build up (which occurs  $\sim 2$  Gyr earlier). The  $z = 1.68$  panel in the figure shows the halo shape just after the last major merger dark halo can no longer be identified.

The evolution of the angular profile of the minor axis against the three principle axes of the simulation volume shows a particular evolution of halo orientation particularly in the inner region of the disc. The minor axis of the inner region of the dark matter halo is originally aligned to the x-axis, but evolves between  $z=1.3$  and 0.42 to be aligned to the y-axis. This highlights that the galaxy's potential is dominated by the stars in the inner region. Although the dark matter is the dominant mass component in the halo overall the mass of stars dominates in the inner region, thus the matter responds most to the potential of the stars. The dark matter particles move within the potential created by these stars in the inner region and so move in a potential which favours the direction of the disk. Outside this region, dark matter dominates the potential and the angle of the

## CHAPTER 7

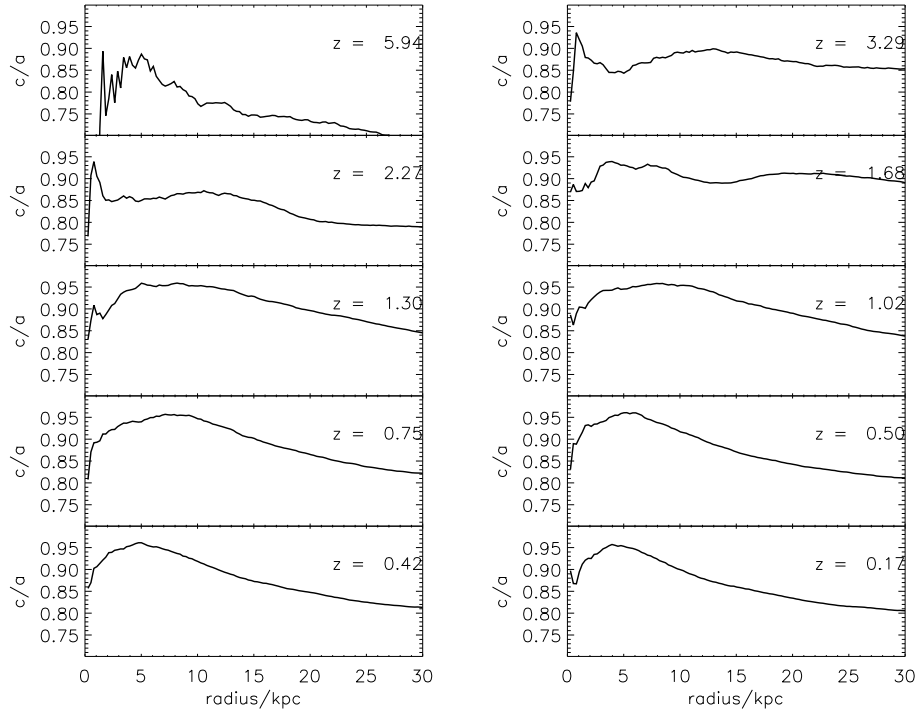


Figure 7.10: Evolution of the halo shape with time. The specific epoch of each panel is shown in the plot.

halo remains essentially constant. This suggests that the stellar disk is out of alignment due to a collision, as suggested in Brook et al. (2008). It also suggests that the infall of gas into the polar disc, having only 10% of the total baryonic mass, does not have a significant effect on the dark matter and that the old stars have a predominant influence on the inner dark matter shape.

A shift in the angle of the minor axis is apparent between the inner and outer regions of the halo. This shift appears to evolve through time, Fig. 7.11. Fig. 7.12 shows the evolution of the shape in the inner 1kpc and at the edge of the halo respectively. It presents the angle between the minor axis of the dark halo for the inner kpc and the entire halo against the x,y and z axes. The inner region still contains sufficient particles so the calculation of the shape remains robust. The  $1\sigma$  error derived from 100 bootstrap samples is sufficiently small to be neglected. Fig. 7.12 shows that the halo in the outer region is established early, at  $\sim 3$

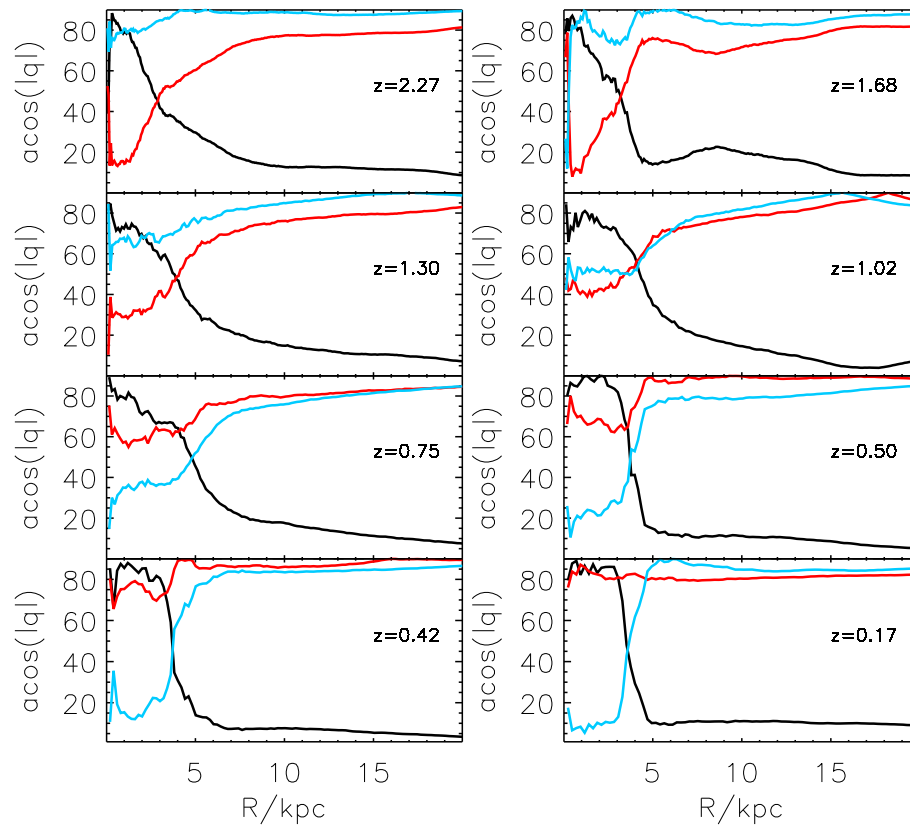


Figure 7.11: The time evolutions of the alignment profile of the minor halo axis with the three principle axes of the simulation. The black line is for z-axis, the red line is for x-axis and the blue line is for y-axis. The y axis of the plot is the arccosine of the modulus of the projection of the minor axis along each of the principle axes. The y axis is defined as the angle of the minor axis relative to the z axis of the angular momentum of the cold gas.

## CHAPTER 7

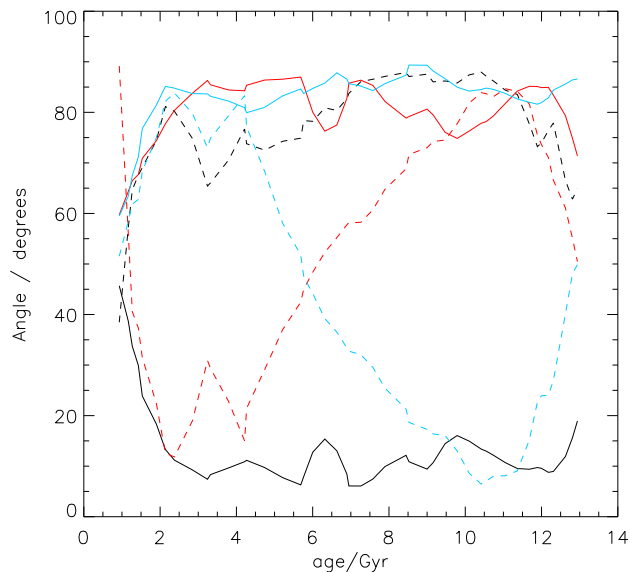


Figure 7.12: The evolution of angular alignment of the minor axis along the three principle axes. Black is the z axis alignment, red is the x-axis alignment and blue is the y axis alignment. The solid line shows the minor axis of the halo within the virial radius, while the dashed line is for the inner kpc of the halo.

Gyr, which is the start of the last major merging event, and remains essentially constant henceforth. The effect of the major merger on the entire system will be examined in more detail in §7.6. The inner region, containing the galaxy disc, is much more dynamic. The inner region is primarily aligned along the x-axis at earlier times but becomes increasingly angled towards the y axis, while the polar disc axis has minimal impact on the potential of the inner region. There is also a smooth rotation of the inner region minor axis towards being primarily aligned to the y axis from  $\sim 4$  Gyr until a maximum y-alignment at  $\sim 7$  Gyr. This time period corresponds to a slight reorientation of the gas disc which precedes the formation of the polar disc. This suggests that the last major merger is critical in forming a polar disc galaxy.

The high density of baryonic matter in the form of stars appears to be the most important factor in the inner system. The sheer mass of stars in the inner region appears to influence the shape of the halo.

## CHAPTER 7

We note that the shape and orientation of the halo has changed between measurements of the stellar and the outer region of the polar disc and so the two discs probe what are essentially two different haloes. A schematic of the shapes of the dark halo inside and outside the stellar disc are shown in Fig. 7.13

### 7.5.7 Comparison With A Standard Disc Galaxy

We examine how discs align with dark matter haloes in a comparable simulation of a normal disc galaxy. A standard galaxy has very different properties to the polar disk, as one would expect given the exotic nature of the polar disk. The normal disc in our standard disc galaxy shows that star formation falls to a relatively low level after 5 Gyr. This is a similar time to the polar disk galaxy. Critically, there is no long term ‘twist’ in the dark halo shape in this normal galaxy and the disc is consistently aligned with the galaxy disc in the inner region of the halo. The halo of this galaxy has a sphericity of 0.8 in the outer region and a peak of sphericity, 0.91 at 8 kpc, but the profile is not as smooth or as strongly peaked as in the polar disc. However, we do notice a brief, temporary ‘twist’ in the inner region. This occurs before 6 Gyrs when the galaxy is undergoing rapid merging. In the quiet era the minor axis of the dark halo is aligned with the x-axis and there is no long term twist in the inner region, although one is sometimes evident while rapid merging occurs. This also suggests that the dark matter responds to the stars in the inner region rather than the reverse.

### 7.5.8 Conclusion

In this section we studied the properties of the shape of the galaxy halo and identified several critical things that have direct impact on galaxy halo structure. Various authors, i.e. Iodice (2010), have used circular velocity estimates to measure the inner structure of the dark matter halo. We have found that the inner

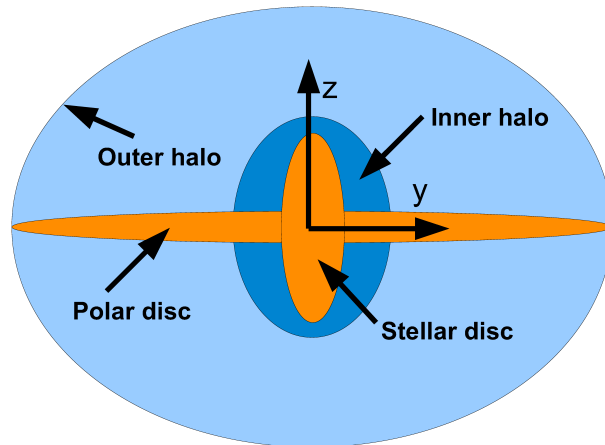


Figure 7.13: A cartoon of halo orientation.

structure probed by the orthogonal discs can vary greatly from the shape of the halo at only slightly greater distances from the galaxy due to the dominance of the baryonic matter on the gravitational potential in this region. The difference in shape is shown in Fig. 7.13. This affect is strong within the radius of the stellar disc. We also find that the  $z$  axis aligns throughout to the minor axis most of the halo beyond the galaxy itself. This is different to the findings of Bailin et al. (2005) who find that the correlation between galaxy disc and dark halo is poor at the virial radius of the halo. We find that the shape of the halo has changed at the edge of the stellar disc so the two discs probe different environments.

The twist in halo orientation is not evident in the ordinary galaxy we studied for more than brief intervals after a merger. This twist may be a characteristic of polar disc galaxies, but, without a larger sample size it is impossible to say for certain.

## 7.6 Angular Momentum

### 7.6.1 Introduction

A polar disc galaxy is a very rare object, and so must have an uncommon formation history. Birnboim and Dekel (2003); Katz and White (1993) and Weinberg et al. (2002) show cold accretion along filaments is the dominant mode of galaxy formation. Gas flows down filaments into the dark matter halo of the galaxy. The other way a galaxy accretes mass is due to galaxy mergers. Brook et al. (2008) theorised that the polar disc galaxy used here forms as a result of the last major merger. Alternatively the filament could change direction and gas will fall in along a new direction. We test the suggestion that the last major merger disrupts the gas and stars of the galaxy, and changes the angular momentum of the stars relative to the infalling gas. This pushes the stellar disc out of alignment with the filament, so that when new gas falls into the halo it falls in along the old direction, thus building up the polar disc.

The angular momentum of the dark matter, gas and stars is tied into the formation of the galaxy, the environment and mergers. Naively, one assumes that gas and dark matter fall into the galaxy from a filament with the same angular momentum. The gas sinks to the centre of the potential, conserving angular momentum as so producing the galaxy gas disc. The cold gas forms stars with the same angular momentum. Thus all the different components are aligned. The dark halo is an oblate structure, compressed along the  $z$  axis of the angular momentum vector because of the rotation. Reality is far more complex.

By studying the angular momentum of the different components of the galaxy and the evolution of the galaxy through time we expand on the proposal of Brook et al. (2008), that polar disc galaxies are formed due to the inflow of cold gas and the effect of the last major merger.

## 7.6.2 Evolution of the angular momentum of the gas, dark matter and stars

It is a characteristic of polar disc galaxies that the two discs have very different angular momenta. In the reference frame of the cold gas at  $z = 0.17$  the gas is, by necessity, aligned with the z-axis, while the angular momenta of the stars is free. Taking stars formed in the period 4-6.5 Gyr the inclination between stars and cold gas is 86 degrees while for old stars formed before the last major merger the angle is 90.3 degrees. The direction of the angular momenta for dark matter, old stars ( $t_{form} < 3$  Gyr), cold gas and the dark matter of the inner halo is shown in Fig. 7.14. Before the last major merger the different components are aligned to one another, but afterwards the inner and outer dark haloes, along with the gas and stars, become increasingly misaligned.

From this figure we can see that the inner region of the dark halo and the stars are locked together as the stars dominate the potential in this region. There is a suggestion in Fig. 7.14 that the inner dark halo responds to the stars. A peak is evident in the z axis of the stellar angular momentum which falls, reducing the final stellar angular momentum z axis to almost zero for the duration of the simulation. The inner dark halo also shows this, but perhaps at a slightly delayed time. Having said this, the output cadence of the simulation is insufficient to be sure that this has occurred in this way.

The angular momentum of the dark halo entire does not change significantly with time, apart from some evidence of tumbling, (the oscillation). There is some evidence in the plot that the first peak and trough in the angular momentum of the halo entire is echoed in the cold gas and stars, although with a slight delay.

The old stars show a peak in the profile around the time of the last major merger but it appears a temporary feature without long term effects. However, at this point the x and y axis components begin to twist towards their final state.

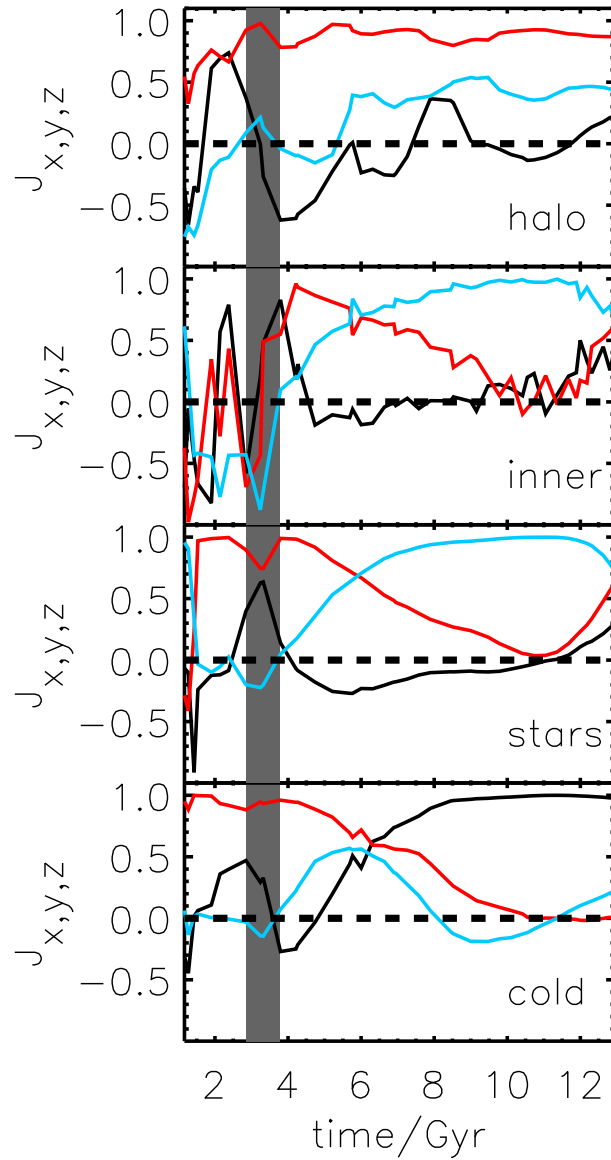


Figure 7.14: Shows the normalised angular momentum projected on the three principle axes of the simulation volume. Black shows the z axis, red the x axis, and blue the y axis. The top panel, labelled ‘halo’, is the angular momentum of the entire halo, the panel labelled ‘inner’ is the angular momentum of the inner kpc of the halo, the panel labelled ‘stars’ is the angular momentum evolution of old ( $t_{form} < 3$  Gyr) stars, and the panel labelled ‘cold’ shows the trend for the cold gas. The grey area is the time of the last major merger.

## CHAPTER 7

The inner region, however, shows some significant evolution. The x-axis of the angular momentum of the inner dark halo becomes highly positive just before the polar disk is established. The effect of the major merger on the total dark halo is temporary in the inner region, except, possibly in the x-axis, where the angular momentum gradually falls. There is a suggestion that the dark matter halo z axis becomes more negative due to this collision, but this does not carry through to the central region of the halo, where the dark matter angular momentum seems closely correlated. If we include subhaloes, a rapid, temporary, change of the x-axis can be seen caused by a small fast moving halo passing through the parent. This occurs at the time the polar disc begins to form, but this object has no contribution to the cold gas, stars or the angular momentum of the inner halo.

The old stars show a short term increase in the z-component of the angular momentum. The x-component then hovers around zero for the rest of the simulation. The angular momentum changes from being aligned to the x-axis to being aligned along the y-axis. This process begins at the last major merger, (age = 3 Gyr), but takes until 7 Gyr to be completely aligned to the y-axis. It is interesting to note the complementary change to the cold gas. As the stars align to the y axis, the gas aligns to the z axis, such that, as shown in Fig. 7.15. This change does not begin until 4.5 Gyr, 1.5 Gyr after the last major merger. This suggests that there is not simply one event which gives rise to the polar disk, but that it an effect of the environment. The inner/outer dark matter halo aligns show a large continuous change over time

The old stars change their angular momentum with time and this must be due to interactions with the environment, and note that the stars and gas appear to roll together with time. The angle between cold gas and old stars takes 4 Gyr to become orthogonal, Fig. 7.15. This suggests that the mechanism that forms the polar disc is a continuing process. It was noted by Bailin and Steinmetz (2005)

## CHAPTER 7

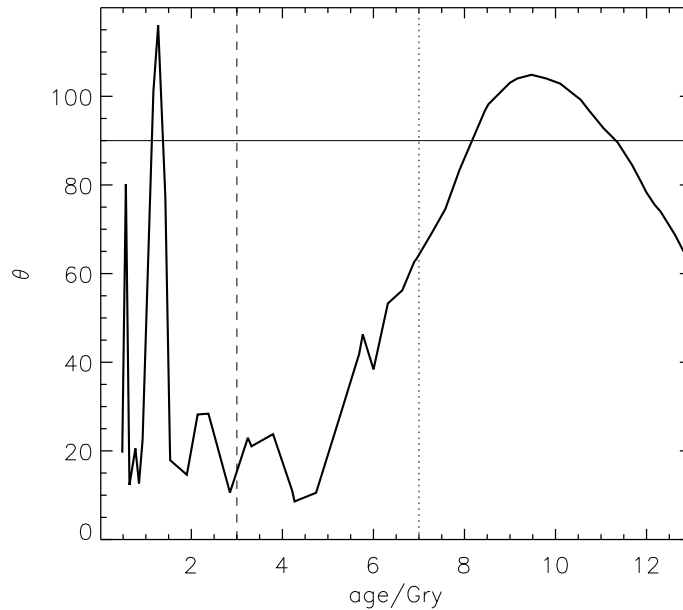


Figure 7.15: The variation of angle between the angular momenta of stars and cold gas with time. The dashed line shows the last major merger, and the dotted line indicated the beginning of star formation in the polar disk.

that as the disc accretes angular momentum its orientation changes and that this may be the cause of warps.

Finally, the stars, cold gas and halo entire are essentially correlated, pre-merger, then the stars and cold gas remain lock-step in the x axis angular momentum component, while the y and z axis components change with time. The primary difference is in the y and z axes. There is an oscillation in the y axis of the cold gas in Fig. 7.14, but the y axis of the cold gas seems to follow the z-axis of the stars. These trends seem amazingly close in the polar disc region to maintain the polar disc structure, almost as if the two structures are interacting to maintain the structure.

We also note that the intermediate axis of the halo shape is aligned to the the angular momentum of the halo.

## 7.7 Formation process

### 7.7.1 Tracing gas

We studied the inflow of gas into the galaxy in an attempt to find the origin of the polar structure. We have seen that the cold gas angular momentum is inclined to the stars and dark matter halo and becomes more misaligned with time. Macciò et al. (2006) points out that unless the infall of gas is along the polar axis of the potential it will be dragged to align with the disc potential. When gas collapses it maintains its angular momentum, thus, we should be able to see whether the gas which made up stars in stellar disc has a different origin to the gas that makes up the polar disc in the  $z=0.15$  output.

We identify the gas that comprises polar ring structure at  $z=0.15$  as all gas cooler than 12000K within the inner 10 kpc of the polar disc galaxy. We track these gas particles back in time to just before the last major merger and calculate the angular momentum of this gas at  $z=2$ . This is then used to align the simulation volume such that the angular momentum of the gas which makes up the polar disc at  $z=0.15$  is aligned to the  $z$  axis of the volume.

When we plot the orientation of the polar disc at  $z=0.15$  we find that the angular momentum of the infalling has hardly changed between  $z=2$  and  $z=0.15$ .

### 7.7.2 Last major merger

We measure the angular momentum of the last major merger in order to identify whether the angle of the interaction is sufficient to cause the polar disc structure. The co-incidence of the last major merger with the beginning of the changes to the galaxy angular momentum and shape shown in the previous sections suggests that it plays a major roll in the formation of the structure.

We concentrate on the stars of the galaxies during the interaction because it

CHAPTER 7

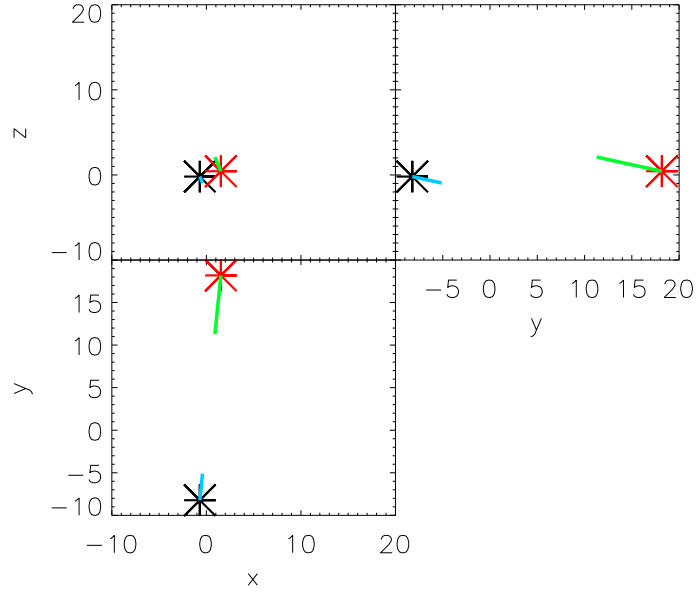


Figure 7.16: The projected schematic of the last major merger at  $z=2$ , just before the stars merge. The black star is the central galaxy, while the red star is the galaxy which merges. The blue and green lines are the projected velocity vectors. Distances are in kpc.

is the behaviour of this component which seems to give rise to the polar disc. The mass of stars in the polar disc galaxy at  $z=2$  is  $3.2 \times 10^9 M_{\odot}$  and the merging satellite is  $1.5 \times 10^9 M_{\odot}$ , a ratio of 11:2 as noted by Brook et al. (2008). The merging galaxy moves down the filament, rather than at an angle to it as we would have originally expected if it was the cause of the polar disc structure.

We calculate the angular momentum of the interaction treating each galaxy as a point sitting in free space in the reference frame of the infalling gas. The collision is shown in Fig. 7.16. The alignment in the  $y$  and  $z$  direction is very close and the relative tangential motion of the collision is anticlockwise.

Most of the angular momentum of the interaction is stored in the bulk motion of the galaxies rather than in the internal motions of the stars, where the angular momentum of the interaction, central and satellite galaxies are a ratio of 2.3, 1 and 1.5 respectively. We also note that the direction of the angular momentum of the stars of the satellite is in the same direction as the merger and the angle

## CHAPTER 7

of angular moment of the central galaxy is in the x-z plane.

The resulting angular momentum of this collision is along the x axis, orthogonal to the filament. As the angular momentum of the system must be conserved we suggest that this provides the initial kick which reorientates the central disc away from the orientation of the polar disc. The orientation of angular momentum of the stars within each galaxy is in the x axis direction for the infalling satellite and at an inclination in the x-z plane for the central galaxy, which a greater component along the z direction. Thus the total angular momentum of all the interacting components is highly orientated in the x direction.

An illustration of the gas filament and the angle of the collision is shown in Figs. 7.17, 7.18, 7.19

### 7.7.3 Angular momentum of the infalling gas

We take the gas from the three epochs, 3.3-3.5 Gyr, 6.3-6.5 Gyr and  $> 9$  Gyr and calculate the change in angular momentum through time. The angular momentum of the infalling gas changes as it falls into the polar disc galaxy. The gas which forms the polar disc aligns with the  $z=0.17$  polar disc angular momentum just after the major merger and is very close to it even before this. This gas does experience a massive disruption just after the major merger which drives it to the final angular momentum. This suggests that the major merger causes a significant contribution to the final angular momentum of the polar gas. This effect is not as noticeable in the gas distribution for older stars. This suggests that the large scale infall of gas is the critical cause of the polar disc galaxy. Initially, at  $z = 6$ , the angular momentum vectors of the gas are different, and the subsequent evolution increases this difference. The direction of the angular momentum of the infalling polar disk gas is aligned to the direction of the minor axis of the dark halo. We find that the total angular momentum of the cold gas

## CHAPTER 7

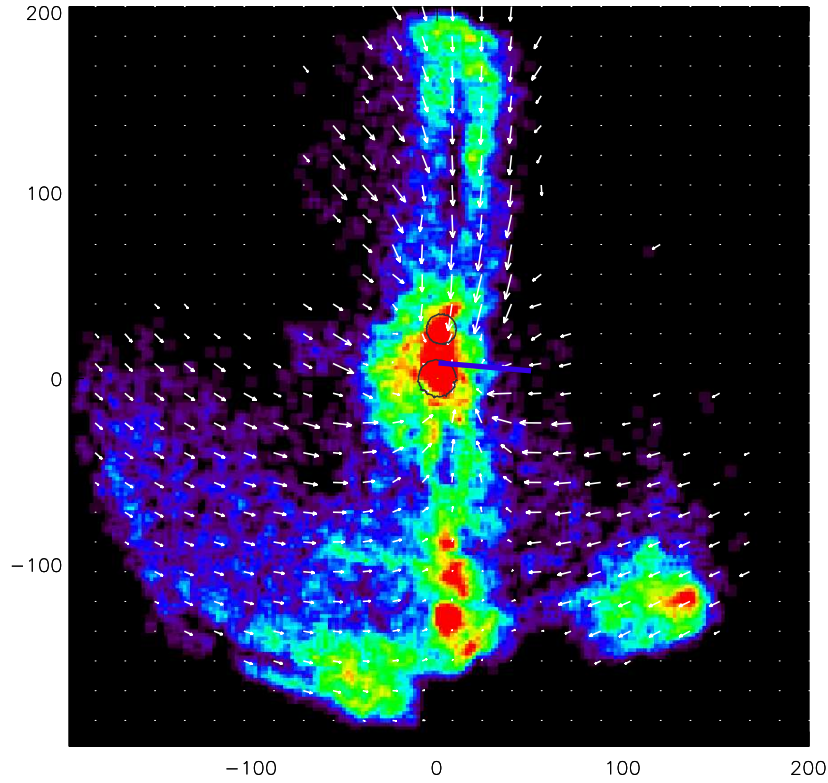


Figure 7.17: Shows x-y projection of a 20 kpc slice around the merging event. The interacting galaxies are marked with circles, the angular momentum of the gas is marked with an orange line, the angular velocity of the interaction is marked with a blue line.

converges towards the major axis of the dark halo shape. The gas which produces stars in the other two epochs is not aligned to the halo shape. They do, however, conform to the minor axis in the inner region of the halo as opposed to the outer edge.

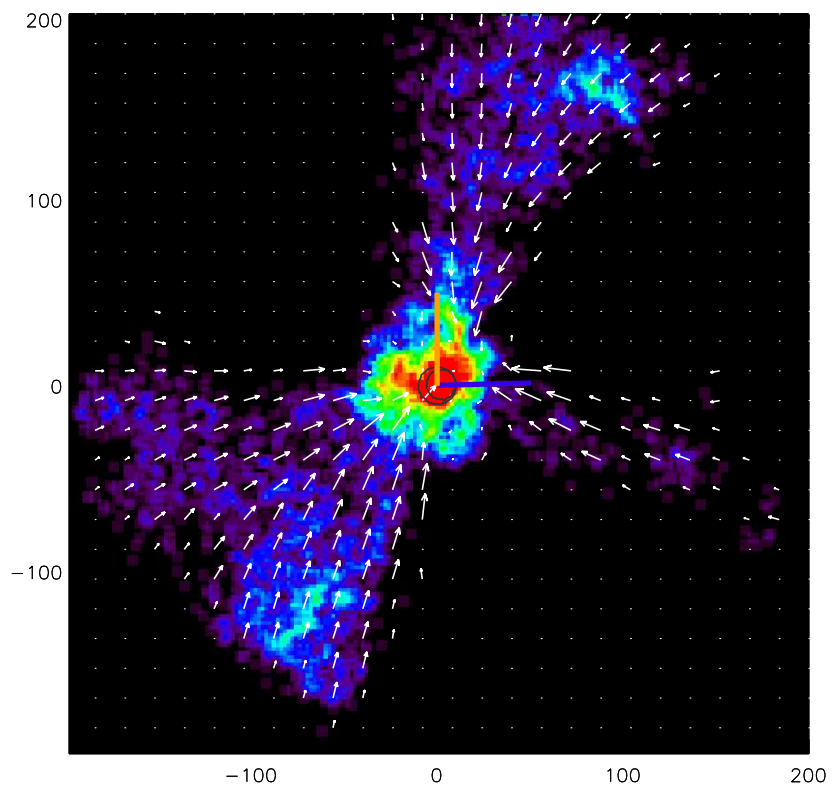


Figure 7.18: Shows x-z projection of a 20 kpc slice around the merging event. The interacting galaxies are marked with circles, the angular momentum of the gas is marked with an orange line, the angular velocity of the interaction is marked with a blue line.

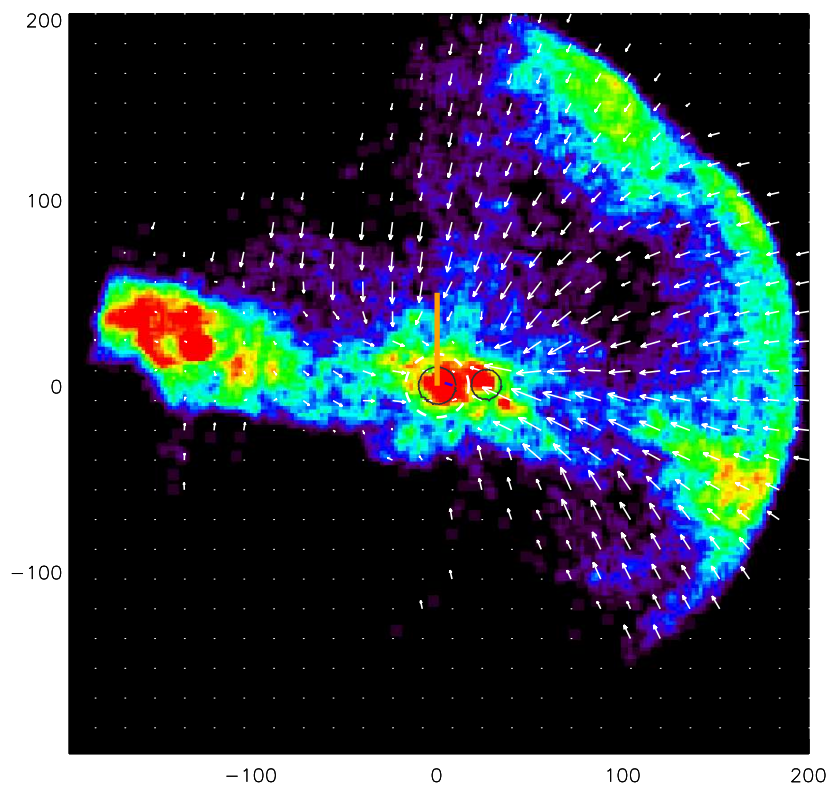


Figure 7.19: Shows y-z projection of a 20 kpc slice around the merging event. The interacting galaxies are marked with circles, the angular momentum of the gas is marked with an orange line, the angular velocity of the interaction is marked with a blue line.

## 7.8 Summary & Further Work

We will continue our examination of this structure. We have found that the polar disc shown here is not caused directly by a merger, or stripping. There is no merging halo that contains enough gas to form the massive polar disc. Thus, the polar disc must form due to inflowing cold gas. We attempted to identify the mechanism by which cold flows give rise to a polar structure. The structure of the polar disc seems to be a result of the direction of gas infall from the filament. We have shown that there is not a single moment when the polar disc forms but there is a constant evolution of the angular momentum of infalling gas and stars. The angular momentum of the last major merger is almost exactly orthogonal to the filament and we feel that this is the most likely origin of the polar disc structure. This major merger effects the stars most strongly without any significant influence on the dark halo. Subsequent to the major merger there is further evolution in the orientation of the central disc, presumably due to tumbling or torques from the halo. The magnitude and direction of the major merger interaction seems to begin this process.

We must also compare the polar disc galaxy to “normal” disc galaxies to identify what precisely results in the extreme behaviour of the polar disc. Clearly any conclusions for the formation of polar discs based on a single galaxy are tentative at best. We need to repeat this analysis on a larger sample of several polar disc galaxies.

# Chapter 8

## CONCLUSIONS

The primary conclusions of this thesis are drawn from an analysis of galaxy groups spanning a range of local density and environment, using a range of semi-analytical models (SAMs) applied to large-scale cosmological N-body simulations. While concurrent work has explored the properties of high-density compact groups within the Millennium Simulation (eg. McConnachie et al. 2008,2009; Diaz-Gimenez & Mamon 2008) using the classical Hickson (1982) criteria, our unique contribution provides a systematic exploration of the evolution of groups as a function of density, environment, and underlying baryonic physics prescription.

Mamon (2008) raises concerns regarding the misidentification of chance-aligned (in projected line-of-sight) galaxies in his earlier work (Mamon 1989) when employing these traditional Hickson (1982) criteria. Our approach in using a three-dimensional linking length within the SAMs avoids such projection effects. In redshift surveys, one identifies groups based upon projected spatial and redshift information, rather than 3d coordinates. Galaxies move with the Hubble flow, but also have local peculiar velocities. This means that, even when we have redshift information, groups can be greatly extended along the line-of-sight; this

## CHAPTER 8

phenomenon is known as the “Finger of God” effect. In our work, we have studied a number of properties of groups in SAMs, as applied to cosmological N-body simulations, and confronted the predicted characteristics with observations.

In Chapters 2 and 3, we explored the spatial distribution, richness, dynamical properties, and morphologies of groups, using a range of Friends-of-Friends (FoF) linking lengths. This allowed us to study the effect of spatial density on galaxy group properties, using data extracted from SAMs applied to the Millennium Run (Springel et al. 2005; De Lucia et al. 2006; Bower et al. 2006; Bertone et al. 2007; Font et al. 2008). In Chapter 4, we studied the behaviour of brightest cluster galaxies in a set of simulated, high-resolution, dissipationless, clusters, and compared our results with the catalogue of Yang et al. (2007). Chapter 5 presented a thorough analysis of the luminosity distribution of galaxy groups derived from various SAMs employing a range of baryonic physics to represent observed galaxy properties, and how this varies with FoF linking length. In Chapter 6, we examined the merger trees of galaxies in clusters employing the De Lucia et al. (2006) and Bower et al. (2006) SAMs.

Our main results can be summarised as follows:

- N-body only cosmological simulations do not adequately capture the properties of extremely dense groups. This is because of the methods used to identify haloes (Gill et al. 2004; Springel et al. 2001). In order to identify even moderately compact groups, in a representative volume of the Universe, we require very high spatial resolution. This is due to the “numerical stripping” (Klypin et al. 1999) which impacts upon lower resolution simulations.
- M.D06 and both Durham models produce similar numbers of Loose Groups (LGs). M.B07 results in overall lower group densities, with a significantly flatter relationship between spatial density and linking length. However,

## CHAPTER 8

the Durham models produce a significantly greater population of compact groups than the Munich models; the Durham groups are significantly richer than the Munich groups. In terms of the spatial density of groups, we find that  $D\_F08 > D\_B06 > M\_D06 > M\_B07$ , at all linking lengths.

- The richness of SAM groups is lowest using the M\_D06 model. Again, groups generated using the Durham-based SAMs are significantly richer. At short linking lengths, M\_B07 has a lower mean richness, but at long linking lengths it produces groups with the same population as D\_B06. This is because galaxies in the Durham SAMs are closer together. The results from observational catalogues show a different spatial density radial profile, presumably due to the 2D linking length used in our group finder. More research is required to identify the exact cause of this difference. However, the differences between the SAMs suggests a significant difference in galaxy formation history is a non-negligible contributor.
- As with previous authors (e.g. Berlind et al. 2006), we find that the group size is tightly correlated with the FoF linking length. This is worrying, as the group radius is an integral part of the derivation of many other group properties, such as group mass and crossing time. Each author who presents a group redshift survey uses their own linking length. For example, Tucker et al. (2000) use a linking length of 750 kpc in order to catch all potential group members, but Tago et al. (2008, 2010) use 250 kpc to avoid including filament galaxies. This difference can be traced to the galaxies being more concentrated towards the central region of groups based upon the D\_B06 SAM.
- We confirm, not surprisingly, that group shape varies with richness (Tovmassian et al. 2006). We found, however, that there are more elongated

## CHAPTER 8

groups in the D\_B06 model, as viewed in projection, than in either the Munich models or observations.

- The above analysis shows considerable differences between the models. In many ways the extent of the differences in the morphology and dynamical properties of groups is surprising, considering each model traces the most bound particles of infalling halos using a similar technique. All other things being equal, the dynamics and shape of the groups should be similar. Two things dominate the choice of which galaxies are included in our catalogues: the luminosity cut of galaxies, which we select based on the limitations of the Millennium Run mass resolution, and the lifetime of galaxies hardwired into the SAM codes. The effect of the luminosity cut was studied in Chapter 3 and was found to have only a small effect on group properties.
- We find further differences between the SAMs when compared with observations of the luminosity functions and magnitude gap (between first- and second-ranked group galaxies) profiles of groups. In the Munich models, we see a characteristic “wobble”, where the luminosity function of galaxy groups changes from being dominated by satellite galaxies to being dominated by central galaxies. This is not present in the Durham models, and is most significant in the M\_D06 model. This effect can be seen in the conditional luminosity functions of Yang et al. (2008) and Weinmann et al. (2006). This is due to the narrowness of the central galaxy profile in the Munich SAMs (M\_D06, in particular) and the smaller population of satellites in the Munich models compared to the Durham models. This effect is larger in compact groups (relative to loose groups), because of the greater ratio of centrals-to-satellites in less rich groups. The same feature is visible in lower-mass SAM groups, most pronounced for intermediate-mass groups, and hardly present in more massive groups. Suggested reasons for

## CHAPTER 8

the existence of the ‘wiggle’ in one set of SAMs, but not the other, include the effect of two-mode versus one-mode AGN feedback, the particular implementation of supernova feedback, and the different lifetimes for group satellite galaxies.

- The magnitude gap between the brightest and second-brightest group galaxy “turns over” in the Munich models (Dariush et al. 2010; Smith et al. 2010). Over a small survey dynamic range in luminosity, this feature cannot be identified, so observations used to examine this property must have a dynamic range  $> 3$  mags. This property of groups may be due to the aforementioned “wiggle”, because the magnitudes of the central and the closest satellites is wider in the M\_D06 model. This is particularly significant because the turnover is strongest in M\_D06, which is the model where the wiggle is most pronounced. Milosavljević et al. (2006) shows that the turnover is a property of clusters, one that is not modelled by D\_B06. Observations (Weinmann et al. 2006; Tago et al. 2010) tend to show a steeper behaviour in magnitude gap vs luminosity than in any of the SAMs.
- In order to resolve the problem of the larger population of very compact groups (vCGs) generated with the Durham models, as evidenced by their smaller mean galaxy-galaxy separations, and their greater central concentration (in the D\_B06 groups), we examined the satellite galaxy merger trees. We found that those galaxies which merge with cluster centrals in both the Munich and Durham models take a similar length of time to merge. However, most galaxies which fall in never merge with the central galaxy. In the M\_D06 model, all galaxies that fell in before a lookback time of 10 Gyr have merged, but this is not the case in the D\_B06 model. Therefore, there is a larger population of galaxies in the Durham models which never merge, relative to the M\_D06 model. This analysis was limited to clusters and

## CHAPTER 8

further investigation is required to cover the full mass range applicable to groups as well. The presence of the “wobble” in the M\_D06 group luminosity functions, and the greater similarity of the M\_D06 cluster galaxy radial distribution to observations, suggest that the merging times of this model may be more representative of reality. Conversely though, the worse fit to the relationship between first- and second-ranked galaxy magnitude and galaxy luminosity suggests this conclusion is not as straightforward as it might seem.

In Chapter 4, we explored the properties of infalling subhalos. In the first section, we attempted to show a relationship between the spatial and velocity offsets of the most massive cluster subhalo for 48 clusters and the offsets of brightest cluster galaxies in observations. Due to our small sample size we have difficulty coming to any significant conclusions. However, we do see that the spatial offsets from the cluster centre of the most massive satellite is greater than for brightest cluster galaxies. This is due to the effect of stripping of subhalos in the simulation. In the second section, we explored the infall of a group into a cluster and found that group galaxies are rapidly dispersed throughout the cluster. Overdensities seen in the cluster galaxy distribution caused by infalling groups suggest that they are being observed during their first orbit, prior to dispersal by the cluster tidal field.

Chapter 7 investigates the properties of a simulated polar disc galaxy. We expanded on the analysis of Brook et al. (2008) in order to explore the shape of the dark matter halo and formation history of this unusual object.

- We find a much stronger metallicity profile in our simulation than can be seen in similar observations of polar disc galaxies.
- There is a noticeable and long term “twist” in the shape of the inner region of the dark matter halo. This feature is not present in traditional disc

## CHAPTER 8

galaxy simulations (Bailin et al. 2005). The halo is aligned such that the halo minor axis is along the z-axis of the angular momentum of the polar disc. Unlike in Bailin et al. (2005) we see no significant deviation from this in the outer region.

- Despite the twist, the circular velocity profiles of the perpendicular discs appear to probe the shape of the outer regions of the halo. This confirms the suggestion of Iodice et al. (2006) that the perpendicular discs can be used to study the dark matter halo shape and alignment.
- The principal cause of the polar disc shape is strong inflows of gas along the same direction throughout cosmic time. The polar disc forms due to a major merger along the filament with an angular momentum perpendicular to the infall direction. This changes the angular momentum of the system and inspires formation of the polar disc.

# Chapter 9

## FUTURE WORK

Further examination of the effect of the different implementations of AGN and supernova feedback is required. Indeed, the treatment of energy feedback within hydrodynamical, semi-analytical, and purely analytical models remains perhaps the single-most important uncertainty governing the formation and evolution of galaxies. The development of an “open source” SAM code would provide the community with a “test-bed” for such exploration; this is the approach we have initiated in collaboration with Prof Masahiro Nagashima (Kyoto) using the Mitaka SAM (Nagashima & Yoshii 2004) as the base upon which to build a modular feedback framework, including both the Croton et al. (2006) and Bower et al. (2006) formalisms. A more direct “hands-on” approach should allow us to determine definitively the origin of the “wobble” seen in the galaxy group luminosity function.

We will also test the effect of galaxy-galaxy merging rates on the luminosity function. This will allow us to “tune” a SAM specifically to the group / cluster environment instead of the global luminosity function and improve modeling in this environment. Additional study of groups using full hydrodynamical simulations will of course provide unique insights into the formation of groups which are

## CHAPTER 9

beyond the reach of SAMs (including spatially-resolved baryonic physics and kinematics), and we are on the cusp of being able to generate the requisite statistical sample of said groups (to date, such work has been restricted to high-resolution dissipationless simulations of groups only).

As the different SAMs track satellites within their hosts in quite different manners, we feel that a more clinical examination of the satellite “lifetimes” is required, in particular the role played by the host halo mass on this lifetime. We have identified in a qualitative sense that this is an important source of the differences between the Durham and Munich models, but this needs to be re-examined more quantitatively.

An important next step in our polar disc analysis will be the extension to a statistical sample of comparable galaxies. We need to assess whether the physical model suggested here is applicable to the general case. A closer analysis of the physical state of the system prior to the last major merger will allow us to state definitively whether or not this is an integral part of the evolutionary process. With a statistical sample of polar disc simulations, we will also be able to determine whether or not the same physical processes which give rise to warps in standard discs are ultimately responsible for polar structures. Similarly, a larger suite of simulations will quantify the diversity of structure and lifetimes of polar rings, which ultimately will inform observational estimates of polar ring galaxy counts as a function of redshift and environment.

# Bibliography

Abell, G. O. (1957). The distribution of rich clusters of galaxies. *AJ* 62, 2–+.

Abell, G. O. (1958, May). The Distribution of Rich Clusters of Galaxies. *ApJS* 3, 211.

Adelman-McCarthy, J. K., M. A. Agüeros, S. S. Allam, C. Allende Prieto, K. S. J. Anderson, S. F. Anderson, J. Annis, N. A. Bahcall, C. A. L. Bailer-Jones, I. K. Baldry, J. C. Barentine, B. A. Bassett, A. C. Becker, T. C. Beers, E. F. Bell, A. A. Berlind, M. Bernardi, M. R. Blanton, J. J. Bochanski, W. N. Boroski, J. Brinchmann, J. Brinkmann, R. J. Brunner, T. Budavári, S. Carliles, M. A. Carr, F. J. Castander, D. Cinabro, R. J. Cool, K. R. Covey, I. Csabai, C. E. Cunha, J. R. A. Davenport, B. Dilday, M. Doi, D. J. Eisenstein, M. L. Evans, X. Fan, D. P. Finkbeiner, S. D. Friedman, J. A. Frieman, M. Fukugita, B. T. Gänsicke, E. Gates, B. Gillespie, K. Glazebrook, J. Gray, E. K. Grebel, J. E. Gunn, V. K. Gurbani, P. B. Hall, P. Harding, M. Harvanek, S. L. Hawley, J. Hayes, T. M. Heckman, J. S. Hendry, R. B. Hindsley, C. M. Hirata, C. J. Hogan, D. W. Hogg, J. B. Hyde, S. Ichikawa, Ž. Ivezić, S. Jester, J. A. Johnson, A. M. Jorgensen, M. Jurić, S. M. Kent, R. Kessler, S. J. Kleinman, G. R. Knapp, R. G. Kron, J. Krzesinski, N. Kuropatkin, D. Q. Lamb, H. Lampeitl, S. Lebedeva, Y. S. Lee, R. F. Leger, S. Lépine, M. Lima, H. Lin, D. C. Long, C. P. Loomis, J. Loveday, R. H. Lupton, O. Malanushenko, V. Malanushenko,

R. Mandelbaum, B. Margon, J. P. Marriner, D. Martínez-Delgado, T. Matsubara, P. M. McGehee, T. A. McKay, A. Meiksin, H. L. Morrison, J. A. Munn, R. Nakajima, E. H. Neilsen, Jr., H. J. Newberg, R. C. Nichol, T. Nicinski, M. Nieto-Santisteban, A. Nitta, S. Okamura, R. Owen, H. Oyaizu, N. Padmanabhan, K. Pan, C. Park, J. Peoples, Jr., J. R. Pier, A. C. Pope, N. Purger, M. J. Raddick, P. Re Fiorentin, G. T. Richards, M. W. Richmond, A. G. Riess, H. Rix, C. M. Rockosi, M. Sako, D. J. Schlegel, D. P. Schneider, M. R. Schreiber, A. D. Schwope, U. Seljak, B. Sesar, E. Sheldon, K. Shimasaku, T. Sivarani, J. A. Smith, S. A. Snedden, M. Steinmetz, M. A. Strauss, M. SubbaRao, Y. Suto, A. S. Szalay, I. Szapudi, P. Szkody, M. Tegmark, A. R. Thakar, C. A. Tremonti, D. L. Tucker, A. Uomoto, D. E. Vanden Berk, J. Vandenberg, S. Vidrih, M. S. Vogeley, W. Voges, N. P. Vogt, Y. Wadadekar, D. H. Weinberg, A. A. West, S. D. M. White, B. C. Wilhite, B. Yanny, D. R. Yocum, D. G. York, I. Zehavi, and D. B. Zucker (2008, April). The Sixth Data Release of the Sloan Digital Sky Survey. *ApJS* 175, 297–313.

Adelman-McCarthy, J. K., M. A. Agüeros, S. S. Allam, K. S. J. Anderson, S. F. Anderson, J. Annis, N. A. Bahcall, C. A. L. Bailer-Jones, I. K. Baldry, J. C. Barentine, T. C. Beers, V. Belokurov, A. Berlind, M. Bernardi, M. R. Blanton, J. J. Bochanski, W. N. Boroski, D. M. Bramich, H. J. Brewington, J. Brinchmann, J. Brinkmann, R. J. Brunner, T. Budavári, L. N. Carey, S. Carliles, M. A. Carr, F. J. Castander, A. J. Connolly, R. J. Cool, C. E. Cunha, I. Csabai, J. J. Dalcanton, M. Doi, D. J. Eisenstein, M. L. Evans, N. W. Evans, X. Fan, D. P. Finkbeiner, S. D. Friedman, J. A. Frieman, M. Fukugita, B. Gillespie, G. Gilmore, K. Glazebrook, J. Gray, E. K. Grebel, J. E. Gunn, E. de Haas, P. B. Hall, M. Harvanek, S. L. Hawley, J. Hayes, T. M. Heckman, J. S. Hendry, G. S. Hennessy, R. B. Hindsley, C. M. Hirata, C. J. Hogan, D. W. Hogg, J. A. Holtzman, S. Ichikawa, T. Ichikawa, Ž. Ivezić, S. Jester, D. E. Johnston, A. M.

Jorgensen, M. Jurić, G. Kauffmann, S. M. Kent, S. J. Kleinman, G. R. Knapp, A. Y. Kniazev, R. G. Kron, J. Krzesinski, N. Kuropatkin, D. Q. Lamb, H. Lampeitl, B. C. Lee, R. F. Leger, M. Lima, H. Lin, D. C. Long, J. Loveday, R. H. Lupton, R. Mandelbaum, B. Margon, D. Martínez-Delgado, T. Matsubara, P. M. McGehee, T. A. McKay, A. Meiksin, J. A. Munn, R. Nakajima, T. Nash, E. H. Neilsen, Jr., H. J. Newberg, R. C. Nichol, M. Nieto-Santisteban, A. Nitta, H. Oyaizu, S. Okamura, J. P. Ostriker, N. Padmanabhan, C. Park, J. Peoples, Jr., J. R. Pier, A. C. Pope, D. Pourbaix, T. R. Quinn, M. J. Raddick, P. Re Fiorentin, G. T. Richards, M. W. Richmond, H. Rix, C. M. Rockosi, D. J. Schlegel, D. P. Schneider, R. Scranton, U. Seljak, E. Sheldon, K. Shimasaku, N. M. Silvestri, J. A. Smith, V. Smolčić, S. A. Snedden, A. Stebbins, C. Stoughton, M. A. Strauss, M. SubbaRao, Y. Suto, A. S. Szalay, I. Szapudi, P. Szkody, M. Tegmark, A. R. Thakar, C. A. Tremonti, D. L. Tucker, A. Uomoto, D. E. Vanden Berk, J. Vandenberg, S. Vidrih, M. S. Vogeley, W. Voges, N. P. Vogt, D. H. Weinberg, A. A. West, S. D. M. White, B. Wilhite, B. Yanny, D. R. Yocum, D. G. York, I. Zehavi, S. Zibetti, and D. B. Zucker (2007, October). The Fifth Data Release of the Sloan Digital Sky Survey. *ApJS* 172, 634–644.

Adelman-McCarthy, J. K., M. A. Agüeros, S. S. Allam, K. S. J. Anderson, S. F. Anderson, J. Annis, N. A. Bahcall, I. K. Baldry, J. C. Barentine, A. Berlind, M. Bernardi, M. R. Blanton, W. N. Boroski, H. J. Brewington, J. Brinchmann, J. Brinkmann, R. J. Brunner, T. Budavári, L. N. Carey, M. A. Carr, F. J. Castander, A. J. Connolly, I. Csabai, P. C. Czarapata, J. J. Dalcanton, M. Doi, F. Dong, D. J. Eisenstein, M. L. Evans, X. Fan, D. P. Finkbeiner, S. D. Friedman, J. A. Frieman, M. Fukugita, B. Gillespie, K. Glazebrook, J. Gray, E. K. Grebel, J. E. Gunn, V. K. Gurbani, E. de Haas, P. B. Hall,

F. H. Harris, M. Harvanek, S. L. Hawley, J. Hayes, J. S. Hendry, G. S. Hennesy, R. B. Hindsley, C. M. Hirata, C. J. Hogan, D. W. Hogg, D. J. Holmgren, J. A. Holtzman, S. Ichikawa, Ž. Ivezić, S. Jester, D. E. Johnston, A. M. Jorgensen, M. Jurić, S. M. Kent, S. J. Kleinman, G. R. Knapp, A. Y. Kniazev, R. G. Kron, J. Krzesinski, N. Kuropatkin, D. Q. Lamb, H. Lampeitl, B. C. Lee, R. F. Leger, H. Lin, D. C. Long, J. Loveday, R. H. Lupton, B. Margon, D. Martínez-Delgado, R. Mandelbaum, T. Matsubara, P. M. McGehee, T. A. McKay, A. Meiksin, J. A. Munn, R. Nakajima, T. Nash, E. H. Neilsen, Jr., H. J. Newberg, P. R. Newman, R. C. Nichol, T. Nicinski, M. Nieto-Santisteban, A. Nitta, W. O’Mullane, S. Okamura, R. Owen, N. Padmanabhan, G. Pauls, J. Peoples, Jr., J. R. Pier, A. C. Pope, D. Pourbaix, T. R. Quinn, G. T. Richards, M. W. Richmond, C. M. Rockosi, D. J. Schlegel, D. P. Schneider, J. Schroeder, R. Scranton, U. Seljak, E. Sheldon, K. Shimasaku, J. A. Smith, V. Smolčić, S. A. Snedden, C. Stoughton, M. A. Strauss, M. SubbaRao, A. S. Szalay, I. Szapudi, P. Szkody, M. Tegmark, A. R. Thakar, D. L. Tucker, A. Uomoto, D. E. Vanden Berk, J. Vandenberg, M. S. Vogeley, W. Voges, N. P. Vogt, L. M. Walkowicz, D. H. Weinberg, A. A. West, S. D. M. White, Y. Xu, B. Yanny, D. R. Yocum, D. G. York, I. Zehavi, S. Zibetti, and D. B. Zucker (2006, January). The Fourth Data Release of the Sloan Digital Sky Survey. *ApJS* 162, 38–48.

Allam, S. S. and D. L. Tucker (2000). Compact Groups of Galaxies in the Las Campanas Redshift Survey. *Astronomische Nachrichten* 321, 101–114.

Andernach, H., K. Alamo-Martínez, R. Coziol, and E. Tago (2007). Dynamics and Shape of Brightest Cluster Galaxies. In I. Saviane, V. D. Ivanov, & J. Borissova (Ed.), *Groups of Galaxies in the Nearby Universe*, pp. 395–+.

Arnaboldi, M. (1995, August). Polar rings as probes of the intrinsic shape of dark

- matter halos. *PASA* 12, 134–134.
- Arnaboldi, M., T. Oosterloo, F. Combes, K. C. Freeman, and B. Koribalski (1997, February). New H I Observations of the Prototype Polar Ring Galaxy NGC 4650A. *AJ* 113, 585–598.
- Bailin, J., D. Kawata, B. K. Gibson, M. Steinmetz, J. F. Navarro, C. B. Brook, S. P. D. Gill, R. A. Ibata, A. Knebe, G. F. Lewis, and T. Okamoto (2005, July). Internal Alignment of the Halos of Disk Galaxies in Cosmological Hydrodynamic Simulations. *ApJL* 627, L17–L20.
- Bailin, J. and M. Steinmetz (2005, July). Internal and External Alignment of the Shapes and Angular Momenta of  $\Lambda$ CDM Halos. *ApJ* 627, 647–665.
- Balogh, M. L., J. F. Navarro, and S. L. Morris (2000, September). The Origin of Star Formation Gradients in Rich Galaxy Clusters. *ApJ* 540, 113–121.
- Bardeen, J. M., J. R. Bond, N. Kaiser, and A. S. Szalay (1986, May). The statistics of peaks of Gaussian random fields. *ApJ* 304, 15–61.
- Barnes, J. and P. Hut (1986, December). A hierarchical  $O(N \log N)$  force-calculation algorithm. *NATURE* 324, 446–449.
- Barton, E., M. Geller, M. Ramella, R. O. Marzke, and L. N. da Costa (1996, September). Compact Group selection From Redshift Surveys. *AJ* 112, 871–+.
- Baugh, C. and P. Murlin (2000, November). *Correlation Function and Power Spectra in Cosmology*.
- Baugh, C. M. (2006, December). A primer on hierarchical galaxy formation: the semi-analytical approach. *Reports on Progress in Physics* 69, 3101–3156.

- Beers, T. C., K. Flynn, and K. Gebhardt (1990, July). Measures of location and scale for velocities in clusters of galaxies - A robust approach. *AJ* 100, 32–46.
- Beers, T. C. and M. J. Geller (1983, November). The environment of D and cD galaxies. *ApJ* 274, 491–501.
- Bekki, K. (1998, May). Formation of a Polar Ring Galaxy in a Galaxy Merger. *ApJ* 499, 635–+.
- Benson, A. J., C. G. Lacey, C. M. Baugh, S. Cole, and C. S. Frenk (2002, June). The effects of photoionization on galaxy formation - I. Model and results at  $z=0$ . *MNRAS* 333, 156–176.
- Benz, W., F. Thielemann, and J. G. Hills (1989, July). Three-dimensional hydrodynamical simulations of stellar collisions. II - White dwarfs. *ApJ* 342, 986–998.
- Berrier, J. C., K. R. Stewart, J. S. Bullock, C. W. Purcell, E. J. Barton, and R. H. Wechsler (2009, January). The Assembly of Galaxy Clusters. *ApJ* 690, 1292–1302.
- Bertone, S. and C. J. Conselice (2009, July). A comparison of galaxy merger history observations and predictions from semi-analytic models. *MNRAS* 396, 2345–2358.
- Bertone, S., G. De Lucia, and P. A. Thomas (2007, August). The recycling of gas and metals in galaxy formation: predictions of a dynamical feedback model. *MNRAS* 379, 1143–1154.
- Binney, J. and S. Tremaine (1987). *Galactic dynamics*. Princeton, NJ, Princeton University Press.

- Binney, J. and S. Tremaine (2008). *Galactic Dynamics: Second Edition*. Princeton University Press.
- Birnboim, Y. and A. Dekel (2003, October). Virial shocks in galactic haloes? *MNRAS* *345*, 349–364.
- Blanton, M. R., D. W. Hogg, N. A. Bahcall, J. Brinkmann, M. Britton, A. J. Connolly, I. Csabai, M. Fukugita, J. Loveday, A. Meiksin, J. A. Munn, R. C. Nichol, S. Okamura, T. Quinn, D. P. Schneider, K. Shimasaku, M. A. Strauss, M. Tegmark, M. S. Vogeley, and D. H. Weinberg (2003, August). The Galaxy Luminosity Function and Luminosity Density at Redshift  $z = 0.1$ . *ApJ* *592*, 819–838.
- Boissier, S. and N. Prantzos (1999, August). Chemo-spectrophotometric evolution of spiral galaxies - I. The model and the Milky Way. *MNRAS* *307*, 857–876.
- Bond, J. R., L. Kofman, and D. Pogosyan (1996, April). How filaments of galaxies are woven into the cosmic web. *NATURE* *380*, 603–606.
- Bournaud, F. and F. Combes (2003, April). Formation of polar ring galaxies. *A&A* *401*, 817–833.
- Bower, R. G., A. J. Benson, R. Malbon, J. C. Helly, C. S. Frenk, C. M. Baugh, S. Cole, and C. G. Lacey (2006, August). Breaking the hierarchy of galaxy formation. *MNRAS* *370*, 645–655.
- Broadhurst, T., N. Benítez, D. Coe, K. Sharon, K. Zekser, R. White, H. Ford, R. Bouwens, J. Blakeslee, M. Clampin, N. Cross, M. Franx, B. Frye, G. Hartig, G. Illingworth, L. Infante, F. Menanteau, G. Meurer, M. Postman, D. R. Ardila, F. Bartko, R. A. Brown, C. J. Burrows, E. S. Cheng, P. D. Feldman, D. A. Golimowski, T. Goto, C. Gronwall, D. Herranz, B. Holden, N. Homeier, J. E. Krist, M. P. Lesser, A. R. Martel, G. K. Miley, P. Rosati, M. Sirianni,

- W. B. Sparks, S. Steindling, H. D. Tran, Z. I. Tsvetanov, and W. Zheng (2005, March). Strong-Lensing Analysis of A1689 from Deep Advanced Camera Images. *ApJ* 621, 53–88.
- Brocca, C., D. Bettoni, and G. Galletta (1997, October). The visible environment of polar ring galaxies. *A&A* 326, 907–914.
- Brook, C. B., F. Governato, T. Quinn, J. Wadsley, A. M. Brooks, B. Willman, A. Stilp, and P. Jonsson (2008, December). The Formation of Polar Disk Galaxies. *ApJ* 689, 678–686.
- Bullock, J. S., A. Dekel, T. S. Kolatt, A. V. Kravtsov, A. A. Klypin, C. Porciani, and J. R. Primack (2001, July). A Universal Angular Momentum Profile for Galactic Halos. *ApJ* 555, 240–257.
- Buttiglione, S., M. Arnaboldi, and E. Iodice (2006). Chemical abundance in the Polar Ring Galaxy NGC 4650A. *Memorie della Societa Astronomica Italiana Supplementi* 9, 317–+.
- Casertano, S. and J. H. van Gorkom (1991, April). Declining rotation curves - The end of a conspiracy? *AJ* 101, 1231–1241.
- Chilingarian, I. V., A. P. Novikova, V. Cayatte, F. Combes, P. Di Matteo, and A. V. Zasov (2009, September). NGC 6340: an old S0 galaxy with a young polar disc. Clues from morphology, internal kinematics, and stellar populations. *A&A* 504, 389–400.
- Cole, S., C. G. Lacey, C. M. Baugh, and C. S. Frenk (2000, November). Hierarchical galaxy formation. *MNRAS* 319, 168–204.
- Connors, T. W., D. Kawata, J. Bailin, J. Tumlinson, and B. K. Gibson (2006, July). On the Origin of Anomalous Velocity Clouds in the Milky Way. *ApJL* 646, L53–L56.

- Conselice, C. J. (2006, February). Early and Rapid Merging as a Formation Mechanism of Massive Galaxies: Empirical Constraints. *ApJ* 638, 686–702.
- Cox, A. L., L. S. Sparke, and G. van Moorsel (2006, February). Neutral Hydrogen in the Polar Ring Galaxy UGC 9796. *AJ* 131, 828–836.
- Croton, D. J., V. Springel, S. D. M. White, G. De Lucia, C. S. Frenk, L. Gao, A. Jenkins, G. Kauffmann, J. F. Navarro, and N. Yoshida (2006, January). The many lives of active galactic nuclei: cooling flows, black holes and the luminosities and colours of galaxies. *MNRAS* 365, 11–28.
- Cypriano, E. S., C. L. Mendes de Oliveira, and L. Sodré, Jr. (2006, August). Velocity Dispersion, Mass, and the Luminosity Function of the Fossil Cluster RX J1416.4+2315. *AJ* 132, 514–520.
- da Costa, L. N., P. S. Pellegrini, W. L. W. Sargent, J. Tonry, M. Davis, A. Meiksin, D. W. Latham, J. W. Menzies, and I. A. Coulson (1988, April). The Southern Sky Redshift Survey. *ApJ* 327, 544–560.
- Dariush, A., H. G. Khosroshahi, T. J. Ponman, F. Pearce, S. Raychaudhury, and W. Hartley (2007, November). The mass assembly of fossil groups of galaxies in the Millennium simulation. *MNRAS* 382, 433–442.
- Dariush, A. A., S. Raychaudhury, T. J. Ponman, H. G. Khosroshahi, A. J. Benson, R. G. Bower, and F. Pearce (2010, July). The mass assembly of galaxy groups and the evolution of the magnitude gap. *MNRAS* 405, 1873–1887.
- Davis, M., G. Efstathiou, C. S. Frenk, and S. D. M. White (1985, May). The evolution of large-scale structure in a universe dominated by cold dark matter. *ApJ* 292, 371–394.
- Davis, M. and P. J. E. Peebles (1983, April). A survey of galaxy redshifts. V - The two-point position and velocity correlations. *ApJ* 267, 465–482.

- De Lucia, G. and J. Blaizot (2007, February). The hierarchical formation of the brightest cluster galaxies. *MNRAS* 375, 2–14.
- De Lucia, G., V. Springel, S. D. M. White, D. Croton, and G. Kauffmann (2006, February). The formation history of elliptical galaxies. *MNRAS* 366, 499–509.
- Dekel, A. and J. P. Ostriker (1999, October). Book Review: Formation of structure in the universe / Cambridge U Press, 1999. *The Observatory* 119, 292–+.
- Díaz-Giménez, E. and G. A. Mamon (2010, December). Compact groups from the Millennium Simulations - I. Their nature and the completeness of the Hickson sample. *MNRAS* 409, 1227–1243.
- Diemand, J., M. Kuhlen, and P. Madau (2007, October). Formation and Evolution of Galaxy Dark Matter Halos and Their Substructure. *ApJ* 667, 859–877.
- D’Onghia, E., J. Sommer-Larsen, A. D. Romeo, A. Burkert, K. Pedersen, L. Portinari, and J. Rasmussen (2005, September). The Formation of Fossil Galaxy Groups in the Hierarchical Universe. *ApJL* 630, L109–L112.
- Doroshkevich, A. G. (1970, October). Spatial structure of perturbations and origin of galactic rotation in fluctuation theory. *Astrophysics* 6, 320–330.
- Dressler, A. (1980, March). Galaxy morphology in rich clusters - Implications for the formation and evolution of galaxies. *ApJ* 236, 351–365.
- Efstathiou, G., R. S. Ellis, and B. A. Peterson (1988, May). Analysis of a complete galaxy redshift survey. II - The field-galaxy luminosity function. *MNRAS* 232, 431–461.
- Eke, V. R., C. M. Baugh, S. Cole, C. S. Frenk, and J. F. Navarro (2006, August). Galaxy groups in the 2dF Galaxy Redshift Survey: the number density of groups. *MNRAS* 370, 1147–1158.

- Eke, V. R., C. M. Baugh, S. Cole, C. S. Frenk, P. Norberg, J. A. Peacock, I. K. Baldry, J. Bland-Hawthorn, T. Bridges, R. Cannon, M. Colless, C. Collins, W. Couch, G. Dalton, R. de Propris, S. P. Driver, G. Efstathiou, R. S. Ellis, K. Glazebrook, C. Jackson, O. Lahav, I. Lewis, S. Lumsden, S. Maddox, D. Madgwick, B. A. Peterson, W. Sutherland, and K. Taylor (2004, March). Galaxy groups in the 2dFGRS: the group-finding algorithm and the 2PIGG catalogue. *MNRAS* *348*, 866–878.
- Evrard, A. E. (1988, December). Beyond N-body - 3D cosmological gas dynamics. *MNRAS* *235*, 911–934.
- Flin, P. and W. Godlowski (1986, October). The orientation of galaxies in the Local Supercluster. *MNRAS* *222*, 525–541.
- Focardi, P. and B. Kelm (2002, August). Compact groups in the UZC galaxy sample. *A&A* *391*, 35–46.
- Font, A. S., R. G. Bower, I. G. McCarthy, A. J. Benson, C. S. Frenk, J. C. Helly, C. G. Lacey, C. M. Baugh, and S. Cole (2008, October). The colours of satellite galaxies in groups and clusters. *MNRAS* *389*, 1619–1629.
- Franx, M., G. Illingworth, and T. de Zeeuw (1991, December). The ordered nature of elliptical galaxies - Implications for their intrinsic angular momenta and shapes. *ApJ* *383*, 112–134.
- Friedman, A. (1922, December). Über die Krümmung des Raumes. *Zeitschrift für Physik* *10*, 377–386.
- Friedman, A. (1999, December). On the Curvature of Space. *General Relativity and Gravitation* *31*, 1991–+.

- Fujita, Y. and M. Nagashima (1999, May). Effects of Ram Pressure from the Intracluster Medium on the Star Formation Rate of Disk Galaxies in Clusters of Galaxies. *ApJ* 516, 619–625.
- Gallagher, J. S., L. S. Sparke, L. D. Matthews, L. M. Frattare, J. English, A. L. Kinney, E. Iodice, and M. Arnaboldi (2002, March). Wide Field Planetary Camera 2 Observations of the Polar Ring Galaxy NGC 4650A. *ApJ* 568, 199–209.
- Geller, M. J. and J. P. Huchra (1983, June). Groups of galaxies. III - The CfA survey. *ApJS* 52, 61–87.
- Geller, M. J. and J. P. Huchra (1989). The Center for Astrophysics Redshift Survey - Recent results. In M. Mezzetti, G. Giuricin, F. Mardirossian, & M. Ramella (Ed.), *Large Scale Structure and Motions in the Universe*, Volume 151 of *Astrophysics and Space Science Library*, pp. 3–17.
- Gill, S. P. D., A. Knebe, and B. K. Gibson (2004, June). The evolution of substructure - I. A new identification method. *MNRAS* 351, 399–409.
- Gill, S. P. D., A. Knebe, and B. K. Gibson (2005, February). The evolution of substructure - III. The outskirts of clusters. *MNRAS* 356, 1327–1332.
- Giovanelli, R. and M. P. Haynes (1985, May). Gas deficiency in cluster galaxies - A comparison of nine clusters. *ApJ* 292, 404–425.
- Gnedin, N. Y. (2000, October). Effect of Reionization on Structure Formation in the Universe. *ApJ* 542, 535–541.
- Gregory, S. A. and L. A. Thompson (1978, June). The Coma/A1367 supercluster and its environs. *ApJ* 222, 784–799.

- Hamilton, A. J. S. (1993, November). Toward Better Ways to Measure the Galaxy Correlation Function. *ApJ* 417, 19.
- Harker, G., S. Cole, J. Helly, C. Frenk, and A. Jenkins (2006, April). A marked correlation function analysis of halo formation times in the Millennium Simulation. *MNRAS* 367, 1039–1049.
- Hausman, M. A. and J. P. Ostriker (1978, September). Galactic cannibalism. III - The morphological evolution of galaxies and clusters. *ApJ* 224, 320–336.
- Hayashi, E., J. F. Navarro, and V. Springel (2007, May). The shape of the gravitational potential in cold dark matter haloes. *MNRAS* 377, 50–62.
- Helly, J. C., S. Cole, C. S. Frenk, C. M. Baugh, A. Benson, and C. Lacey (2003, February). Galaxy formation using halo merger histories taken from N-body simulations. *MNRAS* 338, 903–912.
- Hernquist, L. and N. Katz (1989, June). TREESPH - A unification of SPH with the hierarchical tree method. *ApJS* 70, 419–446.
- Hewett, P. C. (1982, December). The estimation of galaxy angular correlation functions. *MNRAS* 201, 867–883.
- Heyl, J. S., L. Hernquist, and D. N. Spergel (1994, May). Structure of merger remnants. 4: Isophotal shapes. *ApJ* 427, 165–173.
- Hickson, P. (1982, April). Systematic properties of compact groups of galaxies. *ApJ* 255, 382–391.
- Hickson, P., C. Mendes de Oliveira, J. P. Huchra, and G. G. Palumbo (1992, November). Dynamical properties of compact groups of galaxies. *ApJ* 399, 353–367.

- Hickson, P., D. O. Richstone, and E. L. Turner (1977, April). Galaxy collisions in dense groups. *ApJ* 213, 323–326.
- Hoessel, J. G., W. R. Oegerle, and D. P. Schneider (1987, November). The surface-brightness-effective-size relation for elliptical galaxies in the cores of clusters. *AJ* 94, 1111–1115.
- Hubble, E. P. (1926, December). Extragalactic nebulae. *ApJ* 64, 321–369.
- Huchra, J., M. Davis, D. Latham, and J. Tonry (1983, June). A survey of galaxy redshifts. IV - The data. *ApJS* 52, 89–119.
- Huchra, J. P. and M. J. Geller (1982, June). Groups of galaxies. I - Nearby groups. *ApJ* 257, 423–437.
- Huchra, J. P., M. J. Geller, and H. G. Corwin, Jr. (1995, August). The CfA Redshift Survey: Data for the NGP +36 Zone. *ApJS* 99, 391–+.
- Huchra, J. P., M. J. Geller, V. de Lapparent, and H. G. Corwin, Jr. (1990, March). The CfA redshift survey - Data for the NGP + 30 zone. *ApJS* 72, 433–470.
- Iodice, E. (2010, June). Polar Disk Galaxies as New Way to Study Galaxy Formation: the Case of NGC4650A. Volume 1240 of *American Institute of Physics Conference Series*, pp. 379–382.
- Iodice, E., M. Arnaboldi, F. Bournaud, F. Combes, L. S. Sparke, W. van Driel, and M. Capaccioli (2003, March). Polar Ring Galaxies and the Tully-Fisher Relation: Implications for the Dark Halo Shape. *ApJ* 585, 730–738.
- Iodice, E., M. Arnaboldi, R. P. Saglia, L. S. Sparke, O. Gerhard, J. S. Gallagher, F. Combes, F. Bournaud, M. Capaccioli, and K. C. Freeman (2006, May). Stellar Kinematics for the Central Spheroid in the Polar Disk Galaxy NGC 4650A. *ApJ* 643, 200–209.

- Iodice, E., M. Arnaboldi, L. S. Sparke, R. Buta, K. C. Freeman, and M. Capaccioli (2004, April). Photometric structure of the peculiar galaxy ESO 235-G58. *A&A* 418, 41–52.
- Iodice, E., M. Arnaboldi, L. S. Sparke, and K. C. Freeman (2002, August). Near-Infrared photometry in J, H and Kn bands for polar ring galaxies. II. Global properties. *A&A* 391, 117–126.
- Iodice, E., M. Arnaboldi, L. S. Sparke, J. S. Gallagher, and K. C. Freeman (2002, August). Near-Infrared photometry in the J, H and Kn bands for Polar Ring Galaxies. I. Data, structural parameters. *A&A* 391, 103–115.
- Iovino, A. (2002, November). Detecting Fainter Compact Groups: Results from a New Automated Algorithm. *AJ* 124, 2471–2489.
- Iovino, A., E. Tassi, C. Mendes de Oliveira, P. Hickson, and H. MacGillivray (1999). A New Automated Sample of Compact Groups of Galaxies. In J. E. Barnes & D. B. Sanders (Ed.), *Galaxy Interactions at Low and High Redshift*, Volume 186 of *IAU Symposium*, pp. 412–+.
- Jing, Y. P. (1998, August). Accurate Fitting Formula for the Two-Point Correlation Function of Dark Matter Halos. *ApJL* 503, L9+.
- Jones, C., E. Mandel, J. Schwarz, W. Forman, S. S. Murray, and F. R. Harnden, Jr. (1979, November). The structure and evolution of X-ray clusters. *ApJL* 234, L21–L25.
- Jones, L. R., T. J. Ponman, and D. A. Forbes (2000, February). Multiwavelength observations of an evolved galaxy group: an end-point of galaxy merging? *MNRAS* 312, 139–150.

- Jones, L. R., T. J. Ponman, A. Horton, A. Babul, H. Ebeling, and D. J. Burke (2003, August). The nature and space density of fossil groups of galaxies. *MNRAS* *343*, 627–638.
- Karataeva, G. M., I. O. Drozdovsky, V. A. Hagen-Thorn, V. A. Yakovleva, N. A. Tikhonov, and O. A. Galazutdinova (2004, February). The Stellar Content of the Polar Rings in the Galaxies NGC 2685 and NGC 4650A. *AJ* *127*, 789–797.
- Katz, N. and S. D. M. White (1993, August). Hierarchical galaxy formation - Overmerging and the formation of an X-ray cluster. *ApJ* *412*, 455–478.
- Kauffmann, G. (1996, July). Disc galaxies at  $z=0$  and at high redshift: an explanation of the observed evolution of damped Ly $\alpha$  absorption systems. *MNRAS* *281*, 475–486.
- Kauffmann, G., J. M. Colberg, A. Diaferio, and S. D. M. White (1999, February). Clustering of galaxies in a hierarchical universe - I. Methods and results at  $z=0$ . *MNRAS* *303*, 188–206.
- Kauffmann, G. and M. Haehnelt (2000, January). A unified model for the evolution of galaxies and quasars. *MNRAS* *311*, 576–588.
- Kawata, D. and J. S. Mulchaey (2008, January). Strangulation in Galaxy Groups. *ApJL* *672*, L103–L106.
- Kim, R. S. J., J. V. Kepner, M. Postman, M. A. Strauss, N. A. Bahcall, J. E. Gunn, R. H. Lupton, J. Annis, R. C. Nichol, F. J. Castander, J. Brinkmann, R. J. Brunner, A. Connolly, I. Csabai, R. B. Hindsley, Ž. Ivezić, M. S. Vogele, and D. G. York (2002, January). Detecting Clusters of Galaxies in the Sloan Digital Sky Survey. I. Monte Carlo Comparison of Cluster Detection Algorithms. *AJ* *123*, 20–36.

- Klypin, A., S. Gottlöber, A. V. Kravtsov, and A. M. Khokhlov (1999, May). Galaxies in N-Body Simulations: Overcoming the Overmerging Problem. *ApJ* 516, 530–551.
- Knebe, A., B. Arnold, C. Power, and B. K. Gibson (2008, May). The dynamics of subhaloes in warm dark matter models. *MNRAS* 386, 1029–1037.
- Knebe, A., S. P. D. Gill, B. K. Gibson, G. F. Lewis, R. A. Ibata, and M. A. Dopita (2004, March). Anisotropy in the Distribution of Satellite Galaxy Orbits. *ApJ* 603, 7–11.
- Knebe, A., A. Green, and J. Binney (2001, August). Multi-level adaptive particle mesh (MLAPM): a c code for cosmological simulations. *MNRAS* 325, 845–864.
- Knebe, A., N. I. Libeskind, S. R. Knollmann, G. Yepes, S. Gottlöber, and Y. Hoffman (2010, June). The impact of baryonic physics on the shape and radial alignment of substructures in cosmological dark matter haloes. *MNRAS* 405, 1119–1128.
- Knollmann, S. R. and A. Knebe (2009, June). AHF: Amiga’s Halo Finder. *ApJS* 182, 608–624.
- Kravtsov, A. V., O. Y. Gnedin, and A. A. Klypin (2004, July). The Tumultuous Lives of Galactic Dwarfs and the Missing Satellites Problem. *ApJ* 609, 482–497.
- Kravtsov, A. V., A. A. Klypin, and A. M. Khokhlov (1997, July). Adaptive Refinement Tree: A New High-Resolution N-Body Code for Cosmological Simulations. *ApJS* 111, 73–+.
- Kriessler, J. R. and T. C. Beers (1997, January). Substructure in Galaxy Clusters: A Two Dimensional Approach. *AJ* 113, 80–100.

- Lacey, C. and S. Cole (1993, June). Merger rates in hierarchical models of galaxy formation. *MNRAS* 262, 627–649.
- Lacey, C. and S. Cole (1994, December). Merger Rates in Hierarchical Models of Galaxy Formation - Part Two - Comparison with N-Body Simulations. *MNRAS* 271, 676–+.
- Laine, S., R. P. van der Marel, T. R. Lauer, M. Postman, C. P. O’Dea, and F. N. Owen (2003, February). Hubble Space Telescope Imaging of Brightest Cluster Galaxies. *AJ* 125, 478–505.
- Landy, S. D. and A. S. Szalay (1993, July). Bias and variance of angular correlation functions. *ApJ* 412, 64–71.
- Larson, R. B., B. M. Tinsley, and C. N. Caldwell (1980, May). The evolution of disk galaxies and the origin of S0 galaxies. *ApJ* 237, 692–707.
- Lauer, T. R. (1988, September). Cannibalism by First-Ranked Cluster Galaxies. In *Bulletin of the American Astronomical Society*, Volume 20, pp. 1103–+.
- Lauer, T. R. and M. Postman (1992, December). The Hubble flow from brightest cluster galaxies. *ApJL* 400, L47–L50.
- Lee, J. and P. Erdogdu (2007, December). The Alignments of the Galaxy Spins with the Real-Space Tidal Field Reconstructed from the 2MASS Redshift Survey. *ApJ* 671, 1248–1255.
- Li, Y. and A. Helmi (2008, April). Infall of substructures on to a Milky Way-like dark halo. *MNRAS* 385, 1365–1373.
- Limousin, M., J. Sommer-Larsen, P. Natarajan, and B. Milvang-Jensen (2009, May). Probing the Truncation of Galaxy Dark Matter Halos in High-Density

- Environments from Hydrodynamical N-Body Simulations. *ApJ* 696, 1771–1779.
- Lin, H., R. P. Kirshner, S. A. Shectman, S. D. Landy, A. Oemler, D. L. Tucker, and P. L. Schechter (1996, November). The Power Spectrum of Galaxy Clustering in the Las Campanas Redshift Survey. *ApJ* 471, 617–+.
- Macciò, A. V., B. Moore, and J. Stadel (2006, January). The Origin of Polar Ring Galaxies: Evidence for Galaxy Formation by Cold Accretion. *ApJL* 636, L25–L28.
- Magliocchetti, M. and S. J. Maddox (1999, July). The redshift evolution of clustering in the Hubble Deep Field. *MNRAS* 306, 988–993.
- Mamon, G. A. (2008, July). The nature of the nearest compact group of galaxies from precise distance measurements. *A&A* 486, 113–117.
- Matteucci, F., J. Franco, P. Francois, and M. Treyer (1989, September). Chemical evolution of disk galaxies - Self-consistent structure of the disk. *Revista Mexicana de Astronomia y Astrofisica* 18, 145–152.
- Matteucci, F. and P. Francois (1989, August). Galactic chemical evolution - Abundance gradients of individual elements. *MNRAS* 239, 885–904.
- McCarthy, I. G., C. S. Frenk, A. S. Font, C. G. Lacey, R. G. Bower, N. L. Mitchell, M. L. Balogh, and T. Theuns (2008, January). Ram pressure stripping the hot gaseous haloes of galaxies in groups and clusters. *MNRAS* 383, 593–605.
- McConnachie, A. W., S. L. Ellison, and D. R. Patton (2008, July). Compact groups in theory and practice - I. The spatial properties of compact groups. *MNRAS* 387, 1281–1290.

- McConnachie, A. W., D. R. Patton, S. L. Ellison, and L. Simard (2009, May). Compact groups in theory and practice - III. Compact groups of galaxies in the Sixth Data Release of the Sloan Digital Sky Survey. *MNRAS* 395, 255–268.
- Mendes de Oliveira, C. L., E. S. Cypriano, and L. Sodré, Jr. (2006, January). The Luminosity Function of the Fossil Group RX J1552.2+2013. *AJ* 131, 158–167.
- Merchán, M. E., M. A. G. Maia, and D. G. Lambas (2000, December). Correlation Function of Galaxy Groups. *ApJ* 545, 26–31.
- Miller, C. J., R. C. Nichol, D. Reichart, R. H. Wechsler, A. E. Evrard, J. Annis, T. A. McKay, N. A. Bahcall, M. Bernardi, H. Boehringer, A. J. Connolly, T. Goto, A. Kniazev, D. Lamb, M. Postman, D. P. Schneider, R. K. Sheth, and W. Voges (2005, September). The C4 Clustering Algorithm: Clusters of Galaxies in the Sloan Digital Sky Survey. *AJ* 130, 968–1001.
- Milosavljević, M., C. J. Miller, S. R. Furlanetto, and A. Cooray (2006, January). Cluster Merger Variance and the Luminosity Gap Statistic. *ApJL* 637, L9–L12.
- Mo, H. J., S. Mao, and S. D. M. White (1998, April). The formation of galactic discs. *MNRAS* 295, 319–336.
- Mo, H. J. and S. D. M. White (1996, September). An analytic model for the spatial clustering of dark matter haloes. *MNRAS* 282, 347–361.
- Mo, H. J. and S. D. M. White (2002, October). The abundance and clustering of dark haloes in the standard  $\Lambda$ CDM cosmogony. *MNRAS* 336, 112–118.
- Monaco, P., F. Fontanot, and G. Taffoni (2007, March). The MORGANA model for the rise of galaxies and active nuclei. *MNRAS* 375, 1189–1219.
- Monaghan, J. J. (1992). Smoothed particle hydrodynamics. *ARAAS* 30, 543–574.

- Nagashima, M., H. Yahagi, M. Enoki, Y. Yoshii, and N. Gouda (2005, November). Numerical Galaxy Catalog. I. A Semianalytic Model of Galaxy Formation with N-Body Simulations. *ApJ* 634, 26–50.
- Nagashima, M. and Y. Yoshii (2004, July). Hierarchical Formation of Galaxies with Dynamical Response to Supernova-Induced Gas Removal. *ApJ* 610, 23–44.
- Navarro, J. F., M. G. Abadi, and M. Steinmetz (2004, September). Tidal Torques and the Orientation of Nearby Disk Galaxies. *ApJL* 613, L41–L44.
- Nichol, R. C. (2004). Clusters of Galaxies in the Sloan Digital Sky Survey. In J.S. Mulchaey, A. Dressler, and A. Oemler (Ed.), *Clusters of Galaxies: Probes of Cosmological Structure and Galaxy Evolution*, pp. 24–+. Cambridge University Press.
- Niemi, S., P. Nurmi, P. Heinämäki, and M. Valtonen (2007, December). Are the nearby groups of galaxies gravitationally bound objects? *MNRAS* 382, 1864–1876.
- Oegerle, W. R. and J. M. Hill (2001, December). Dynamics of cD Clusters of Galaxies. IV. Conclusion of a Survey of 25 Abell Clusters. *AJ* 122, 2858–2873.
- Oemler, Jr., A. (1974, November). The Systematic Properties of Clusters of Galaxies. Photometry of 15 Clusters. *ApJ* 194, 1–20.
- Oleak, H., D. Stoll, H. Tiersch, and H. T. MacGillivray (1998, July). The shapes of Shakhbazian compact groups of galaxies. *Astronomische Nachrichten* 319, 235–+.
- Orlov, V. V., A. V. Petrova, and V. G. Tarantaev (2001, July). The intrinsic shapes of galaxy groups. *MNRAS* 325, 133–137.

- Ostriker, J. P. and S. D. Tremaine (1975, December). Another evolutionary correction to the luminosity of giant galaxies. *ApJL* 202, L113–L117.
- Paz, D. J., D. G. Lambas, M. Mercjam, and N. D. Padilla (2006, June). Shapes of Clusters and Groups of Galaxies: Comparison of Observation to Model Predictions. In *Revista Mexicana de Astronomía y Astrofísica Conference Series*, Volume 26 of *Revista Mexicana de Astronomía y Astrofísica*, vol. 27, pp. 195–+.
- Paz, D. J., D. G. Lambas, N. Padilla, and M. Merchán (2006, March). Shapes of clusters and groups of galaxies: comparison of model predictions with observations. *MNRAS* 366, 1503–1510.
- Plionis, M., S. Basilakos, and H. M. Tovmassian (2004, August). The shape of poor groups of galaxies. *MNRAS* 352, 1323–1328.
- Ponman, T. J., P. D. J. Bourner, H. Ebeling, and H. Böhringer (1996, December). A ROSAT survey of Hickson’s compact galaxy groups. *MNRAS* 283, 690–708.
- Press, W. H. and P. Schechter (1974, February). Formation of Galaxies and Clusters of Galaxies by Self-Similar Gravitational Condensation. *ApJ* 187, 425–438.
- Press, W. H., S. A. Teukolsky, W. T. Vetterling, and B. P. Flannery (1992). *Numerical recipes in FORTRAN. The art of scientific computing*. Cambridge: University Press.
- Reshetnikov, V. and N. Sotnikova (1997, September). Global structure and formation of polar-ring galaxies. *A&A* 325, 933–942.
- Reshetnikov, V. P. (2004, March). Photometric structure of polar-ring galaxies. *A&A* 416, 889–900.

- Reshetnikov, V. P., M. Faúndez-Abans, and M. de Oliveira-Abans (2002, February). ESO 603-G21: A strange polar-ring galaxy. *A&A* 383, 390–397.
- Ribeiro, A. L. B., R. R. de Carvalho, H. V. Capelato, and S. E. Zepf (1998, April). Structural and Dynamical Analysis of the Hickson Compact Groups. *ApJ* 497, 72–+.
- Robotham, A., S. Phillipps, and R. De Propris (2008, January). The Shapes of Galaxy Groups: Footballs or Frisbees? *ApJ* 672, 834–848.
- Rubin, V. C. (1994, August). Multi-spin galaxies. *AJ* 108, 456–467.
- Sackett, P. D., H. Rix, B. J. Jarvis, and K. C. Freeman (1994, December). The flattened dark halo of polar ring galaxy NGC 4650A: A conspiracy of shapes? *ApJ* 436, 629–641.
- Sales, L. V., J. F. Navarro, D. G. Lambas, S. D. M. White, and D. J. Croton (2007, December). Satellite galaxies and fossil groups in the Millennium Simulation. *MNRAS* 382, 1901–1916.
- Santos, W. A., C. Mendes de Oliveira, and L. Sodré, Jr. (2007, October). Fossil Groups in the Sloan Digital Sky Survey. *AJ* 134, 1551–+.
- Schechter, P. (1976, January). An analytic expression for the luminosity function for galaxies. *ApJ* 203, 297–306.
- Schombert, J. M. (1987, August). The structure of brightest cluster members. II - Mergers. *ApJS* 64, 643–666.
- Schweizer, F., B. C. Whitmore, and V. C. Rubin (1983, July). Colliding and merging galaxies. II - S0 galaxies with polar rings. *AJ* 88, 909–925.
- Shakhbazyan, R. K. (1973). Compact groups of compact galaxies. *Astrofizika* 9, 495–501.

- Shakhbazyan, R. K. and M. B. Petrosyan (1974). Compact groups of compact galaxies. II. *Astrofizika* 10, 13–20.
- Sheth, R. K., H. J. Mo, and G. Tormen (2001, May). Ellipsoidal collapse and an improved model for the number and spatial distribution of dark matter haloes. *MNRAS* 323, 1–12.
- Sheth, R. K. and G. Tormen (1999, September). Large-scale bias and the peak background split. *MNRAS* 308, 119–126.
- Skibba, R. A., F. C. van den Bosch, X. Yang, S. More, H. Mo, and F. Fontanot (2011, January). Are brightest halo galaxies central galaxies? *MNRAS* 410, 417–431.
- Smith, G. P., H. G. Khosroshahi, A. Dariush, A. J. R. Sanderson, T. J. Ponman, J. P. Stott, C. P. Haines, E. Egami, and D. P. Stark (2010, November). LoCuSS: connecting the dominance and shape of brightest cluster galaxies with the assembly history of massive clusters. *MNRAS* 409, 169–183.
- Sommer-Larsen, J. (2006, June). Properties of intra-group stars and galaxies in galaxy groups: ‘normal’ versus ‘fossil’ groups. *MNRAS* 369, 958–968.
- Sparke, L. S. and A. L. Cox (2000). New Observations of Polar Ring Galaxies. In F. Combes, G. A. Mamon, & V. Charmandaris (Ed.), *Dynamics of Galaxies: from the Early Universe to the Present*, Volume 197 of *Astronomical Society of the Pacific Conference Series*, pp. 119–+.
- Spavone, M., E. Iodice, M. Arnaboldi, O. Gerhard, R. Saglia, and G. Longo (2010, May). Chemical Abundances in the Polar Disk of NGC 4650A: Implications for Cold Accretion Scenario. *ApJ* 714, 1081–1095.
- Spergel, D. N., R. Bean, O. Doré, M. R. Nolta, C. L. Bennett, J. Dunkley, G. Hinshaw, N. Jarosik, E. Komatsu, L. Page, H. V. Peiris, L. Verde, M. Halpern,

- R. S. Hill, A. Kogut, M. Limon, S. S. Meyer, N. Odegard, G. S. Tucker, J. L. Weiland, E. Wollack, and E. L. Wright (2007, June). Three-Year Wilkinson Microwave Anisotropy Probe (WMAP) Observations: Implications for Cosmology. *ApJS* 170, 377–408.
- Spergel, D. N., L. Verde, H. V. Peiris, E. Komatsu, M. R.olta, C. L. Bennett, M. Halpern, G. Hinshaw, N. Jarosik, A. Kogut, M. Limon, S. S. Meyer, L. Page, G. S. Tucker, J. L. Weiland, E. Wollack, and E. L. Wright (2003, September). First-Year Wilkinson Microwave Anisotropy Probe (WMAP) Observations: Determination of Cosmological Parameters. *ApJS* 148, 175–194.
- Springel, V., S. D. M. White, A. Jenkins, C. S. Frenk, N. Yoshida, L. Gao, J. Navarro, R. Thacker, D. Croton, J. Helly, J. A. Peacock, S. Cole, P. Thomas, H. Couchman, A. Evrard, J. Colberg, and F. Pearce (2005, June). Simulations of the formation, evolution and clustering of galaxies and quasars. *NATURE* 435, 629–636.
- Springel, V., S. D. M. White, G. Tormen, and G. Kauffmann (2001, December). Populating a cluster of galaxies - I. Results at  $z=0$ . *MNRAS* 328, 726–750.
- Stinson, G., A. Seth, N. Katz, J. Wadsley, F. Governato, and T. Quinn (2006, December). Star formation and feedback in smoothed particle hydrodynamic simulations - I. Isolated galaxies. *MNRAS* 373, 1074–1090.
- Strauss, M. A. and J. A. Willick (1995). The density and peculiar velocity fields of nearby galaxies. *PhysRep* 261, 271–431.
- Tago, E., J. Einasto, E. Saar, E. Tempel, M. Einasto, J. Vennik, and V. Müller (2008, March). Groups of galaxies in the SDSS Data Release 5. A group-finder and a catalogue. *A&A* 479, 927–937.

- Tago, E., E. Saar, E. Tempel, J. Einasto, M. Einasto, P. Nurmi, and P. Heinämäki (2010, May). Groups of galaxies in the SDSS Data Release 7 . Flux- and volume-limited samples. *A&A* 514, A102+.
- Teyssier, R. (2002, April). Cosmological hydrodynamics with adaptive mesh refinement. A new high resolution code called RAMSES. *A&A* 385, 337–364.
- Tovmassian, H., M. Plionis, and J. P. Torres-Papaqui (2006, September). Physical properties of Hickson compact groups and of the loose groups within which they are embedded. *A&A* 456, 839–846.
- Tovmassian, H. M., O. Yam, and H. Tiersch (2001, October). Hickson Compact Groups: The Cores of Elongated Loose Groups. *Revista Mexicana de Astronomia y Astrofisica* 37, 173–177.
- Tremaine, S. and Q. Yu (2000, November). Resonant capture, counter-rotating discs, and polar rings. *MNRAS* 319, 1–7.
- Tucker, D. L., A. Oemler, Jr., Y. Hashimoto, S. A. Sackett, R. P. Kirshner, H. Lin, S. D. Landy, P. L. Schechter, and S. S. Allam (2000, October). Loose Groups of Galaxies in the Las Campanas Redshift Survey. *ApJS* 130, 237–265.
- Vale, A. and J. P. Ostriker (2006, September). The non-parametric model for linking galaxy luminosity with halo/subhalo mass. *MNRAS* 371, 1173–1187.
- Vale, A. and J. P. Ostriker (2008, January). A non-parametric model for linking galaxy luminosity with halo/subhalo mass: are brightest cluster galaxies special? *MNRAS* 383, 355–368.
- van den Bosch, F. C., X. Yang, H. J. Mo, S. M. Weinmann, A. V. Macciò, S. More, M. Cacciato, R. Skibba, and X. Kang (2007, April). Towards a concordant model of halo occupation statistics. *MNRAS* 376, 841–860.

- van Driel, W., M. Arnaboldi, F. Combes, and L. S. Sparke (2000, February). A neutral hydrogen survey of polar ring galaxies. III. Nançay observations and comparison with published data. *A&AS* *141*, 385–408.
- van Driel, W., F. Combes, F. Casoli, M. Gerin, N. Nakai, T. Miyaji, M. Hamabe, Y. Sofue, T. Ichikawa, S. Yoshida, Y. Kobayashi, F. Geng, T. Minezaki, N. Arimoto, T. Kodama, P. Goudfrooij, P. S. Mulder, K. Wakamatsu, and K. Yanagisawa (1995, March). Polar ring spiral galaxy NGC 660. *AJ* *109*, 942–959.
- van Gorkom, J. H., P. L. Schechter, and J. Kristian (1987, March). H I maps of S0 galaxies with polar rings. *ApJ* *314*, 457–475.
- Vikhlinin, A., B. R. McNamara, A. Hornstrup, H. Quintana, W. Forman, C. Jones, and M. Way (1999, July). X-Ray Overluminous Elliptical Galaxies: A New Class of Mass Concentrations in the Universe? *ApJL* *520*, L1–L4.
- von Benda-Beckmann, A. M., E. D’Onghia, S. Gottlöber, M. Hoeft, A. Khalatyan, A. Klypin, and V. Müller (2008, June). The fossil phase in the life of a galaxy group. *MNRAS* *386*, 2345–2352.
- von der Linden, A., P. N. Best, G. Kauffmann, and S. D. M. White (2007, August). How special are brightest group and cluster galaxies? *MNRAS* *379*, 867–893.
- von Neumann, J. and R. D. Richtmyer (1950). A method for the numerical calculation of hydrodynamic shocks. *Journal of Applied Physics* *21*, 232.
- Wadsley, J. W., J. Stadel, and T. Quinn (2004, February). Gasoline: a flexible, parallel implementation of TreeSPH. *NewA* *9*, 137–158.
- Wainer, H. and D. Thissen (1976). Three steps towards robust regression. *Psychometrika* *41*, 9–34. 10.1007/BF02291695.

- Warnick, K., A. Knebe, and C. Power (2008, April). The tidal streams of disrupting subhaloes in cosmological dark matter haloes. *MNRAS* *385*, 1859–1883.
- Wechsler, R. H., J. S. Bullock, J. R. Primack, A. V. Kravtsov, and A. Dekel (2002, March). Concentrations of Dark Halos from Their Assembly Histories. *ApJ* *568*, 52–70.
- Weinberg, D. H., L. Hernquist, and N. Katz (2002, May). High-Redshift Galaxies in Cold Dark Matter Models. *ApJ* *571*, 15–29.
- Weinmann, S. M., F. C. van den Bosch, X. Yang, H. J. Mo, D. J. Croton, and B. Moore (2006, November). Properties of galaxy groups in the Sloan Digital Sky Survey - II. Active galactic nucleus feedback and star formation truncation. *MNRAS* *372*, 1161–1174.
- White, S. D. M. and M. J. Rees (1978, May). Core condensation in heavy halos - A two-stage theory for galaxy formation and clustering. *MNRAS* *183*, 341–358.
- Whitmore, B. C., R. A. Lucas, D. B. McElroy, T. Y. Steiman-Cameron, P. D. Sackett, and R. P. Olling (1990, November). New observations and a photographic atlas of polar-ring galaxies. *AJ* *100*, 1489–1522.
- Yahagi, H. and Y. Yoshii (2001, September). N-Body Code with Adaptive Mesh Refinement. *ApJ* *558*, 463–475.
- Yahil, A. and N. V. Vidal (1977, June). The Velocity Distribution of Galaxies in Clusters. *ApJ* *214*, 347–350.
- Yang, X., H. J. Mo, and F. C. van den Bosch (2008, March). Galaxy Groups in the SDSS DR4. II. Halo Occupation Statistics. *ApJ* *676*, 248–261.
- Yang, X., H. J. Mo, F. C. van den Bosch, and Y. P. Jing (2005, February). A

- halo-based galaxy group finder: calibration and application to the 2dFGRS. *MNRAS* *356*, 1293–1307.
- Yang, X., H. J. Mo, F. C. van den Bosch, A. Pasquali, C. Li, and M. Barden (2007, December). Galaxy Groups in the SDSS DR4. I. The Catalog and Basic Properties. *ApJ* *671*, 153–170.
- Zabludoff, A. I., M. J. Geller, J. P. Huchra, and M. S. Vogeley (1993, October). The kinematics of dense clusters of galaxies. I - The data. *AJ* *106*, 1273–1300.
- Zabludoff, A. I. and J. S. Mulchaey (1998, May). Hierarchical Evolution in Poor Groups of Galaxies. *ApJL* *498*, L5+.
- Zel'Dovich, Y. B. (1970, April). Fragmentation of a homogeneous medium under the action of gravitation. *Astrophysics* *6*, 164–174.
- Zibetti, S., D. Pierini, and G. W. Pratt (2009, January). Are fossil groups a challenge of the cold dark matter paradigm? *MNRAS* *392*, 525–536.
- Zwicky, F. (1933). Die Rotverschiebung von extragalaktischen Nebeln. *Helvetica Physica Acta* *6*, 110–127.
- Zwicky, F. (1937, October). On the Masses of Nebulae and of Clusters of Nebulae. *ApJ* *86*, 217–+.